The interaction between a sonic transverse jet and an oblique shock wave in a supersonic crossflow.

An experimental study.

Giulio Dacome

Technische Universiteit Delft

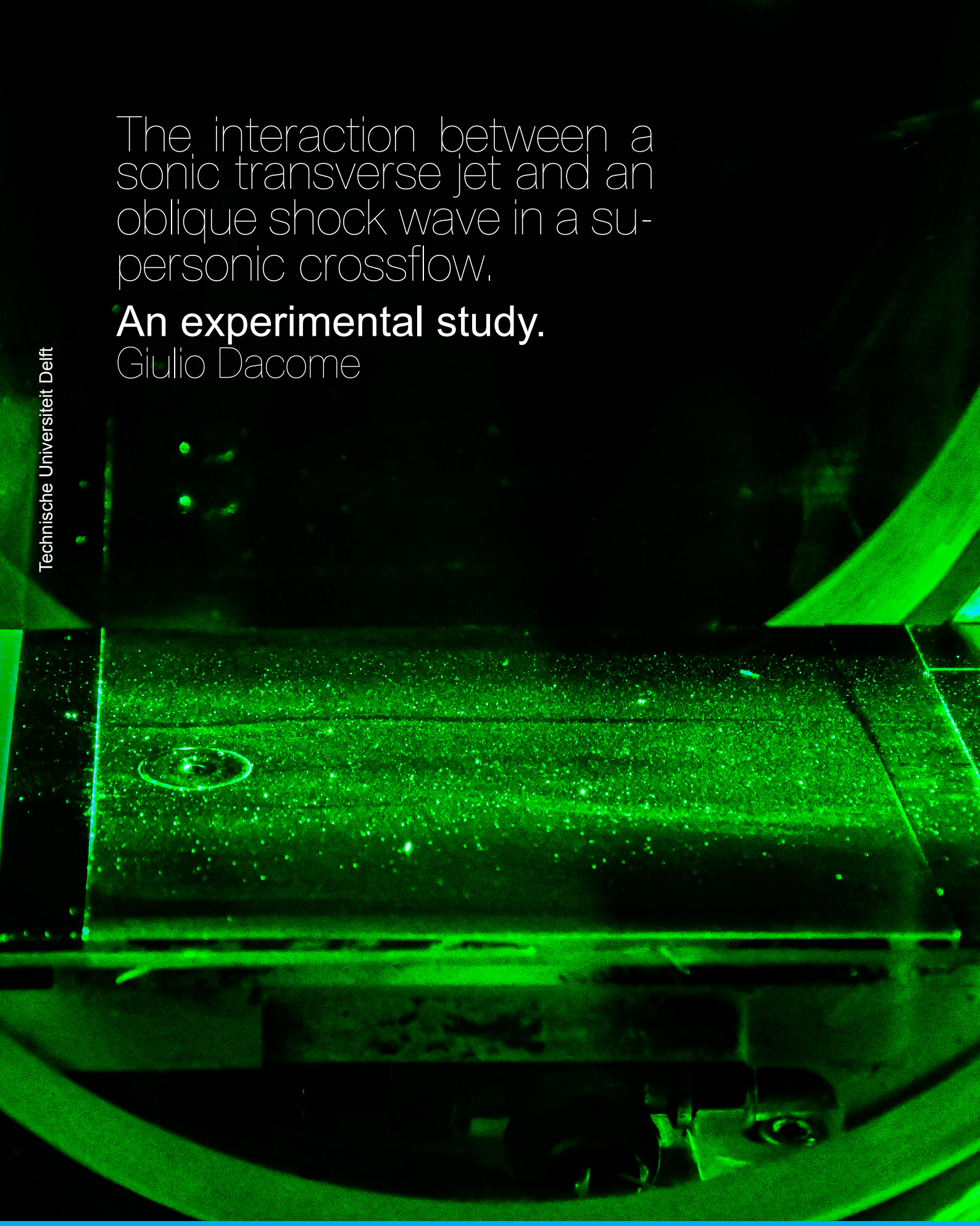

TU Delft

The interaction between a sonic transverse jet and an oblique shock wave in a supersonic crossflow.

An experimental study.

by

Giulio Dacome

to obtain the degree of Master of Science
at the Delft University of Technology,
to be publicly defended on 25th February 2021

Student number: 4476867
Date completed: 25th February 2021
Thesis Supervisors: Dr.ir. F. F. J. Schrijer, TU Delft
Dr.ir. B. W. van Oudheusden, TU Delft

TU Delft

Executive Summary

As air-breathing propulsion is promising to make its appearance in high-speed transport and orbital insertion, SCramjet engines offer the highest efficiency at the flight regime these vehicles will operate in: hypersonic flight. One of the most effective combustion chamber designs that has been considered in legacy work and recent literature is one of the simplest concepts: a jet in (supersonic) crossflow. With virtually no moving parts and the enthalpy of the incoming supersonic stream allowing for auto-ignition and spontaneous combustion, this system promises to provide the best performance. To obtain combustion, though, fuel and air need to be mixed to the proper mass ratio. Momentum-driven effects being prominent in the near-field and diffusion-driven ones in the far-field, literature has proven this design over and over again. A way to enhance entrainment and, consequently, mixing of the two perpendicular fluids is the introduction of an oblique shock wave impinging on the jet plume. The goal of this research project is to investigate the performance of such combustor design in an attempt to quantify the counter-playing effects of increased mixing performance against the generation of a shock-wave boundary-layer interaction inside the combustion chamber itself.

An experimental campaign was carried out in the experimental facilities of the High-Speed Laboratory at the Faculty of Aerospace Engineering at TU Delft. The ST-15 supersonic tunnel was used with a freestream Mach number of $M_\infty = 2$. A transverse flow was injected at sonic conditions and varying momentum flux ratio. A strong and a weak oblique shock ($\theta = 12\,\text{deg}$ and $\theta = 9\,\text{deg}$, respectively) were introduced inside the test section at two different impingement positions downstream of the jet orifice: $x_{\text{shock}}/d_{\text{jet}} = 13$ and $x_{\text{shock}}/d_{\text{jet}} = 16$. Schlieren and shadowgraphy measurements as well as oil flow visualization were conducted in order to quantify the basic geometric properties of the complex flow field emerging from the interaction. Additionally, stereo particle image velocimetry measurements were acquired both on wall-normal and wall-parallel planes.

As air from the transverse jet enters the test section, it is enveloped in a barrel shock that terminates with a Mach disk. This last feature is of utmost importance for momentum-driven mixing in the near-field and its position above the wall is a good measure of the mixing performance in this region of the field. Its position was found to rise and shift downstream almost linearly with increasing momentum flux ratio, as expected. Impinging the shock downstream of the injector and being the flow mostly supersonic downstream of the barrel shock, no considerable effect is observed of the shock on the near-field properties, apart from the alteration of the length of the separation zone downstream of the jet. This increases drastically as the shock is inserted into the flow field.

Mixing and entrainment were quantified based on the vertical penetration of the jet into the cross-stream, its lateral expansion and profiles of turbulent kinetic energy, which were obtained from a statistical analysis of instantaneous PIV results. The strong-shock case where the impingement position is the closest to the jet exit shows an increase in vertical penetration of up to 66.3% compared to the no-shock configuration. This is most probably caused by the combined action of the CVP-induced upward-directed velocities and the flow deflection imparted by the compression wave forming upstream of the interaction region

of the boundary layer with the shock. Lateral expansion is also greatly increased by the same flow scenario as much as 59.6%. Also, this configuration sees the formation of large-scale vortices whose axis is oriented normal to the bottom wall. Although these features were seen for all cases with oil flow visualization, stereo PIV highlighted them only for the aforementioned situation. Therefore, it seems as though the shock wave has the effect of spreading the fuel/injectant over a larger area compared to the baseline cases where no shock was present. Indeed, the profiles of turbulent kinetic energy appear less intense, but indeed spread over a wider area. This indicates the possibility of having regions of more lean mixture compared to very fuel-rich regions seen for the “standard” jet in crossflow taken as a baseline.

Concerning combustion and flame holding effects, the shock does provide favourable conditions to promote auto-ignition. In fact, static temperature and static pressure increase whilst the mean transit velocity through the combustion chamber decreases, thereby increasing the residence time of fuel in the combustor. The analysis of instantaneous snapshot verified the fact that fuel packets form, due to the formation of the shear layer above the jet plume. The configuration that showed the most increase in plume expansion is also the one showing the most increase in residence time, reporting a 42.1% gain.

Of course, though, a rather massive interaction region appears due to the SBLI. The size of separated flow bubbles increases drastically as compared to the baseline cases (no-jet configurations). Some cases more than triple the length and height of the recirculation zone, indicating that a more in-depth investigation of losses thereby induced is in order. An increase in wave drag is indeed expected.

Preface

I was told that, apparently, this section should be devoted to thanking my friends and everyone who supported me. So, first of all, I would like to thank *Il Peperoncino* in Delft for the fantastic pizza con speck e burrata. I must say... sensational. Then, I am in dire need of thanking M&M's for their great candies. Especially the crunchy ones. In the lonely hours in the wind tunnel, you provided some of the sweetest moments. If only did I manage to hide them from *someone*... (he knows who he is)

OK. Now seriously.

In some of the motivation letters I wrote in the past I mentioned that I am generally able to plan ahead and be organised with time. But when you start your thesis right when the worst pandemic in recorded history starts raging through Europe, it makes you question whether that is actually true.

During this thesis I was forced to carry out most of the progress meetings with my fantastic supervisors, Ferry and Bas, online. It sucked. I could not get a place in the basement and share my doubts, dilemmas and frustration with fellow thesis-makers. It sucked. I will not be able to defend it in person with my family and friends there to share this moment with. It incredibly just sucks.

Still, I met and worked with some fantastic people along the way. Every one of them contributed to making the thesis experience enjoyable even when working alone from home all the time.

Thank you Ferry and Bas... I really cannot overstate how key they have been in helping me throughout. Always there for my questions. Always there to guide me towards solutions. Always there to share a laugh in the lab (or remotely). Thank you! Thank you to the lab staff as well! Dennis, Frits, Peter, Henk-Jan and Nico. They have been of invaluable help when I got stuck during the experiments and when I needed tips for the manufacturing of parts (I am sorry for blowing up the seeder). Thank you to the PhD candidates in the lab that answered many of my questions, especially Alessandro and Edoardo.

But also my fantastic friends, who were always there. No matter what.

Thank you to all my friends who supported me along the way. *Gracias* José and *dankjewel* Julia for always being close to me and having the right thing to say at the right time. Sorry if I bored you with nerd aerodynamics talk... Thank you Eric for helping me with the runs and, especially, for teaching me how to use the spray paint (I know, I know... it's easy). Thank you Jacopo, Andrea and Enrico for all the laughs we had together in these two years in aerodynamics and all the *disagio* we shared throughout. Thank you Matteo, Federico, Giulia (now with a G), Matilde and Camilla for being such amazing friends and always being there to support me. I cannot thank you enough. *Grazie* Alessandro for never stopping to encourage and motivate me in these *balordi* times.

Thank you to my lovely girlfriend Laura, who was always there to comfort me when I was sad and to laugh with me when I was cheerful. Thank you for allowing me to rant indefinitely and for all the boring wind tunnel tech-talk you like listening to.

Thank you to my fantastic parents, grandparents and family people who supported me during this project and, in general, throughout my studies. It would not have been possible without you!

Grazie a tutti!

Giulio Dacome
Delft, 25th February 2021

Nomenclature

Latin

a	Speed of sound [m/s]
C_f	Friction coefficient [-]
c_p	Isobaric specific heat. At $T = 288.15$ [K], $c_{p,\text{air}} = 1004.8$ [J/(kg·K)]
c_v	Isochoric specific heat. At $T = 288.15$ [K], $c_{v,\text{air}} = 717.7$ [J/(kg·K)]
d	Diameter [m]
e	Entropy [J/K]
f	Focal length [m]
J	Momentum flux ratio [-]
L	Length [m]
M	Mach number [-]
M	Magnification factor. Better indicated as $\overline{M}$ [-]
p	Pressure [Pa]
q	Dynamic Pressure [Pa]
R	Gas constant: $R_{\text{air}} = 287.15$ [J/(kg·K)]
r	Resolution [pixel/m]
$R_{\varphi\varphi}$	Reynolds stress at position φ of tensor [$(\text{m/s})^2$]
Re	Reynolds number [-]
T	Temperature [K]
t	Time [s]
U	Velocity (general) [m/s]
u	Velocity x-component [m/s]
v	Velocity y-component [m/s]
w	Velocity z-component [m/s]
x	Streamwise direction [m]
y	Wall-normal direction [m]
z	Trans-plane direction [m]

Greek

β Shock angle [deg]

γ Specific heat ratio [-]

λ Wave length [m]

μ Dynamic viscosity [kg/(cm·s)]

$\nu(M)$ Prandtl-Meyer angle at given Mach number [deg]

ν Kinematic viscosity [m^2/s]

ω Vorticity [$1/s$]

ρ Density [kg/m^3]

σ Standard deviation [m/s]

τ Shear stress [Pa]

θ Flow deflection angle [deg]

ε Uncertainty [dep.]

Acronyms

CCD Charge Coupled Device

CVP Counter-rotating Vortex Pair

FOV Field Of View

Nd:YAG Neodymium-doped Yttrium Aluminium Garnet (laser)

OSW Oblique Shock Wave

PIV Particle Image Velocimetry

RCS Reaction Control System

SBLI or SWBLI Shock-Wave Boundary-Layer Interaction

SCRamjet Supersonic Combustion Ramjet (engine)

TKE Turbulent Kinetic Energy [J]

Subscripts

∞ Freestream variable

0 Stagnation variable

jet Referring to the jet

pix Pixel characteristic

shock Referring to the impinging oblique shock wave

Contents

1

Introduction

As an alternative to chemical propulsion for sub-orbital flight and trans-atmospheric ascent, high-speed air breathing engines offer a viable and light-weight alternative. The need to carry the oxidizer together with the fuel drastically increases the mass of any given launcher on the pad. It comes to no surprise that many of the concepts developed for space planes and legacy vehicles in the U.S.-based X-program incorporated ramjet or even SCramjet engines in their design. Yet, technical limitations always hindered their full-scale entry into service. Material properties and combustion control issues severely limited the endurance and range of these vehicles. Now, with new advancements in those areas, the sector is seeing new concepts for space planes being rolled out by several parties. It is probably the case that chemical propulsion will never be completely phased out due to its excellent scalability and its vacuum performance. Still, air-breathing propulsion can offer an appealing alternative for the early stage of the climb through the denser atmospheric layers or as a mean to propel high-altitude high-speed transport.

As the flight regimes ticks into hypersonic Mach numbers, performing combustion in a subsonic environment leads to excessive losses in engine thrust. This is the reason why SCramjet engines were developed that allow for supersonic combustion. Given the extremely short residence time of fuel and air in the combustion chamber, it is of utmost importance to achieve the proper mixing of fuel and oxidizer (air). Many mechanisms have been studied in literature but it appears as though the most effective one is also the simplest possible design: injecting fuel on a perpendicular direction with respect to the crossflow in the chamber. As a mean to enhance the mixing and promote ignition, introducing an incident oblique shock wave impinging on the plume has been proven in literature to be rather effective.

The present research work investigates experimentally the interaction of a sonic jet with an incident shock in a supersonic crossflow and how the mixing properties can be enhanced thereby. To provide more in-depth information for the trade-off phase of the design, an investigation is carried out on the detrimental effects the introduction of the shock has on the flow and, potentially, the generation of thrust.

1.1. The jet in crossflow

As fluid flow is injected through an orifice into a stream moving across the port hole, a jet in crossflow results. This interaction is also known as either “secondary” or “transverse”

injection and can be found in several contexts both in nature and in man-made applications. The most standard representation of a jet in crossflow is the configuration whereby the jet enters in the main stream with an angle of 90 degrees to it, as shown in Figure 1.1.

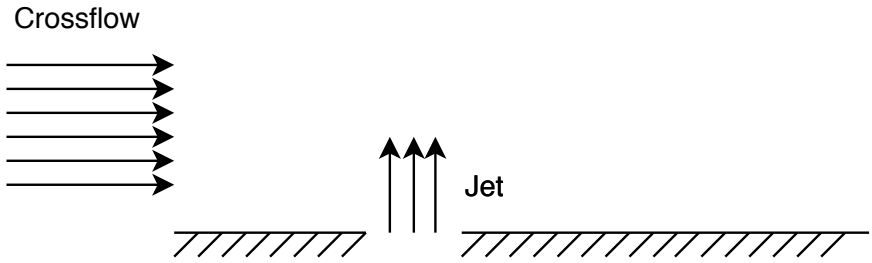

Figure 1.1: Schematic of a jet in crossflow

The interaction between the two fluid flows produces several flow features and coherent structures which will be investigated in the foregoing. The formation and behaviour of these depends on the jet's and external stream's regime, as well the injectant species.

At beginning the 20^{th} century and in the inter-war period, as urbanization started booming, concerns began to arise regarding the location of large industrial plants. The initial interest into the interaction of transverse jets with the flow field arose in an effort to predict the concentration and distribution of chemicals emitted by an industrial plant over a large stretch of land. Sutton (1932) elaborated a theory on the development of eddies in a turbulent atmosphere and their convection and deformation with the wind, which could be applied to the smoke plumes exhausting from chimneys in industrial plants. Bosanquet and Pearson (1936) then set out to determine the concentration at ground level of chemicals emanating from a source at a given height above the ground as, for instance, factory emissions. They concluded that, in the vicinity of the chimney, a rather small concentration could be measured whereas the concentration peaked moving downwind by a distance of about ten times the height of the source. Multi-species considerations were then elaborated on by Sheridan (1966), who created a model to predict air-water entrainment arising from the interaction of a water jet with the surrounding air (e.g. a geyser).

Volcanic eruptions also represent a well-know example for the present flow in nature. Be it a violent eruption, where hot gases are expelled from a crater or just sulfuric emissions "puffing" from a dormant volcano into the wind, they both are instances of subsonic jets in a subsonic crossflow. Following the same principles, underwater vents form a similar flow pattern as incandescent gases are exhausted from submerged chimneys into streaming deep-sea currents near oceanic ridges. Aubry et al. (2017) conducted an investigation on the behaviour of volcanic plume and, in particular, the conditions which lead to its collapse and the ones leading to it reaching the stratosphere.

1.2. Engineering applications

Regarding man-made applications, several are the fields where a jet in crossflow can be found. Historically, these started to emerge towards the end of the Second World War, when technical developments in aeronautics were pushing in the direction of jet propulsion with turbojets and rockets. In the context of the former, a subsonic jet is injected into a subsonic compressible stream. Modern advances in the field, in fact, involve the use of jets originating on orifices along the turbine blades, which allows for film cooling. Here, cooler air is bled from the compressor stages and fed to the turbine blades, the operating

temperature of which would cause them to melt. Air blown through the orifices effectively creates a lower-temperature sheet (i.e. film) enveloping the blades. Film cooling is also studied for temperature control of the outer skin of hypersonic vehicles (for instance in the case of re-entry craft) in order to mitigate heating from skin friction. Here, however, the interaction is with a compressible, supersonic stream.

It is in this flight regime that most of the engineering applications of such interaction can be found. In trans-atmospheric flight, aerodynamic control surfaces become ineffective at high altitude due to the low dynamic pressure. It is for this reason that side reaction control thrusters are used to provide attitude corrections. As the jet fires to the side of the direction of flight, the plume interacts with the surrounding compressible stream. Figure 1.2a and 1.2b show two example RCS designs used in space systems. The former shows a snapshot of the firing of the launch escape system of SpaceX's Dragon capsule, while the latter displays the front port thruster assembly on the nose of the Space Shuttle.

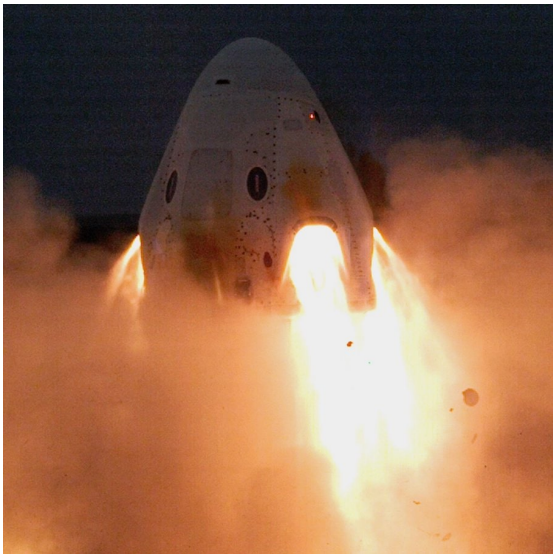

(a) Dragon capsule launch abort system. Copyright-free.

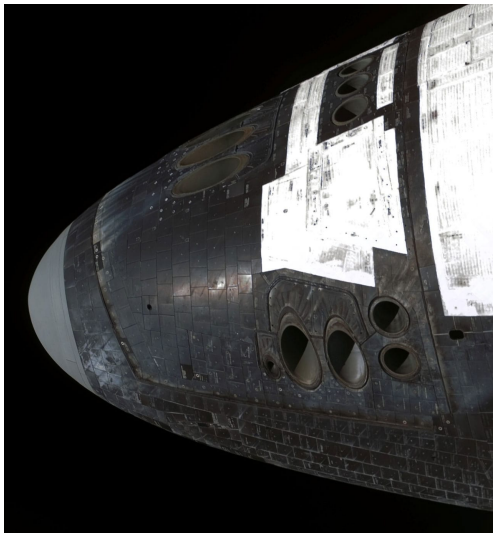

(b) Front port thruster assembly of the Space Shuttle. Copyright-free.

In a compressible regime, the interaction of the jet with the crossflow greatly alters the performance of the single jet firing in still air. This is due to the complex shock structures and compressibility-related flow features that alter pressure distributions around the vehicle, thus affecting thruster performance (Zhang et al. (2012)). As the stream into which the jet is injected becomes, in fact, supersonic, the secondary flow acts as an obstacle to the main one. This causes a bow shock wave to form upstream of the injection location, as illustrated in early works conducted my Morkovin et al. (1952). The flow discontinuity causes alterations in the pressure distribution that affect the performance of the thruster, i.e. the thrust produced by the RCS actuator is greatly affected by its interaction with the cross-stream. It is for this reason that the design of control systems for launch abort systems, orbital launchers and missiles (if not aerodynamic) needs to consider the interaction effects.

Zhang et al. (2012) conducted a study on a body of revolution, whereby they identified the most effective nozzle shape to produce the largest control force. They also discovered that, in case of 3D bodies, the bow shock wraps around the main body, thus reducing the pressure difference and degrading the effectiveness of reaction control. This result was confirmed by Grandhi and Roy (2017), who also found that control performance is highly

sensitive to the vehicle's angle of attack. In the context of flight vehicle design, Ebrahimi (2008) found that transient phenomena occurring during the jet start-up and shutdown create strong structural loads due to abrupt pressure fluctuations caused by the unsteady onset of the bow shock. Further studies also included the analysis of the interaction of a jet with a fin in the case of spin-stabilized rocket (Beresh et al. (2007)). Here, a pair of thrusters fire symmetrically to induce a rotation about the roll axis of the vehicle. Given the rotational nature of the flow field about the body of the rocket, an angle of attack will be induced on a downstream fin, thus causing it to lift. Other analyses were performed on the influence of the jet temperature (i.e. hot versus cold gas thrusters) on the performance of the jet (Stahl et al. (2009)).

In the context of hypersonic vehicle design which, according to Curran (2001), will greatly pick up in the near future due to its numerous applications, the use of jets is crossflow plays a key role. Not only for attitude control, but also for fuel injection into the combustion chamber of a supersonic combustion (SC) ramjet. This type of propulsion system is generally adopted by vehicles flying in the hypersonic regime in virtue of the decay of specific impulse of other propulsive mechanisms, as shown in Figure 1.3.

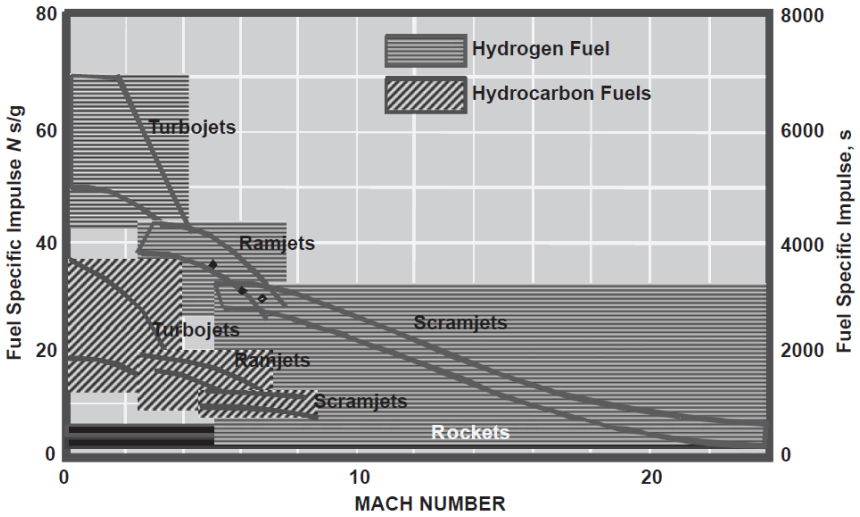

Figure 1.3: Graph showing the typical specific impulses for several types of propulsion systems. Obtained from Segal (2009).

Today, the only vehicle ever to achieve sustained flight using a SCramjet engine has been NASA's X-43a, shown in Figure 1.4a[1] With a typical flight Mach number of $6 < M_\infty < 8$ and the typical longitudinal dimensions of such vehicle on the order of just a few meters, the residence time of air in the combustion chamber reduces to mere milliseconds (Segal (2009)) and remains supersonic throughout. Complex flow interaction occur upstream of combustion, rendering the design of the chamber even more complex (Figure 1.4b[2]). It is for this reason that mixing and combustion need to occur both rapidly and effectively to sustain hypersonic flight. Several configuration for injectors have been studied in the legacy designs, most of which feature a body that is intrusively installed in the middle of the stream in the combustor. Huang (2016) mentions several possible designs, including strut-, ramp- and pylon-type fuel injectors, all featuring the intrusion of bodies into the supersonic stream and, thus, large modifications to the flow field. The work also mentions

[1]Obtained from `nasa.gov/centers/armstrong/history/experimental_aircraft/X-43A` on 9/4/2020.
[2]Obtained from `nasa.gov/centers/langley/news/factsheets/X43A_2006_5` on 9/4/2020.

how the best combination of injection effectiveness, design simplicity and reliability is forcing air into the combustion chamber through a wall-mounted orifice.

(a) NASA's X-43A Hyper-X vehicle.

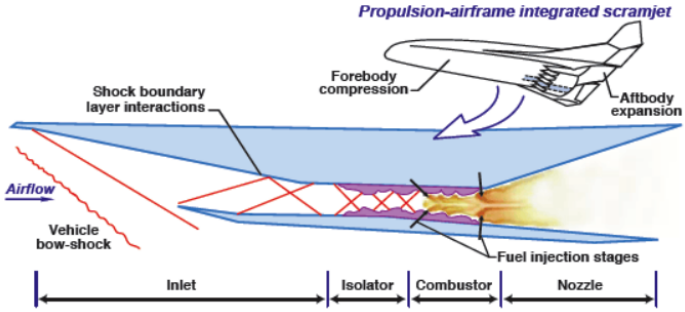

(b) Schematic of flow structures in a SCramjet engine.

Transverse injection provides abrupt momentum transfer in the near-field of the port hole and convects into the counter-rotating vortex pair. This is a flow feature which will be greatly elaborated on in the foregoing, being one of the characteristic signatures of the interaction of a jet in crossflow. It provides velocity gradients favouring entrainment and, thus, mixing of fuel and air. The need for effective combustion becomes clear by examining the expression for thrust of a SCramjet engine in Equation 1.1.

$$T = I_{\mathrm{sp}} \dot{m} g_e \tag{1.1}$$

where I_{sp} is the specific impulse, $\dot{m}$ the mass flow and g_e the gravitational acceleration at sea level (by convention). By turning the above equation around, it is possible to grasp the definition of specific impulse: the ratio of thrust per fuel weight expelled per unit time ($I_{\mathrm{sp}} = T/(\dot{m} g_e)$). Considering the SCramjet's thermodynamic cycle, one can re-write the definition of specific impulse as in Equation 1.2 (Segal (2009)).

$$I_{\mathrm{sp}} = \frac{V}{g}\left[\sqrt{1 + \frac{2}{(\gamma - 1)/M_0^2}(\psi - 1)\left[\eta_c \eta_e \left(\frac{\Delta H_c / H_0}{\psi}\right) - 1\right]} - 1\right] \tag{1.2}$$

where V is the flight velocity, M_0 the flight's Mach number, H_0 the freestream enthalpy, ΔH_c the addition of enthalpy in combustion and η_c and η_e the compression and expansion efficiencies. It is thus clear that higher specific impulse is obtained with higher combustion enthalpy. With a smoother fuel burn, dictated by thorough mixing, combustion efficiency is greatly increased, thus leading to higher enthalpy and, ultimately, greater thrust.

All combustor designs have the goal of maximizing mixing while minimizing pressure losses. It is the case, though, that injection in compressible flow results in the formation of a bow shock wave upstream of the injector, causing total pressure losses. The foregoing work is going to assess whether the introduction of an incident oblique shock can benefit the mixing performance and provide information for future works conducted in the context of SCramjet design.

1.3. The effect of the shock

As an incoming compression wave hitting the jet plume during its development, the shock reportedly induces several effects on the flow field inside the combustion chamber.

The idea is to introduce a new feature in the combustor with the following goals.

- Promote mixing by the introduction of vorticity.
- Enhance entrainment by the formation of a strong shear layer.
- Promote mixing on the small-scale by generating turbulent kinetic energy.
- Increase temperature, pressure and residence time to better promote auto-ignition.

Having a shock impinging on the developing jet plume is also a rather simple technique requiring no active input or moving parts. Its creation can be caused by the addition of a flap upstream of the position of the jet or by simply tailoring the shape of the inlet itself. There are though, some downsides to this technique.

First of all: separation. The introduction of a shock is going to cause large-scale flow separation inside the combustion chamber as air rushes through it. Also, depending on the angle of the flow deflection, a weak or strong interaction can result, with dramatically different effects on the interaction of the discontinuity with the boundary layer. It is possible that a region of unmixed fuel and air can form in the interaction region, hindering the mixing as well. Furthermore, as a result of separation, a drastic increase in wave drag through the test section is expected. Second of all: deterioration of thrust. As just mentioned in the above, especially as a strong interaction occurs, the formation of secondary discontinuities reflecting through the chamber will cause losses the stream's total pressure which will result in thrust reduction. Finally, as illustrated in the work by Kumar et al. (2008), the separated boundary layer can increase the blocking effect in the chamber and unstart the engine.

This research effort will, though, mainly be focused on the effect the shock has on the mixing of the fluids and will address the aspects related to flow separation only briefly.

1.4. Problem statement

Given the research conducted in the field of jets in supersonic crossflow and the capabilities of research facilities in Delft University of Technology, the goal of this thesis is stated below.

The objective of this research project is to quantify the mixing performance of an injector design incorporating an incident oblique shock wave as a mean to further enhance mixing and entrainment.

Effectively, this translates to the analysis of different combinations of incident shock angle, position and jet momentum flux ratio to give an assessment of how the best mixing performance can be obtained and describing the influence of an upstream jet on the SBLI. The momentum flux ratio will have an effect on the trajectory of the jet itself and on its penetration, as will the boundary layer thickness to a lesser extent, as mentioned by Portz and Segal (2006). Both these aspects depend further on the Mach number of the cross stream. The addition of an OSW is expected to greatly enhance the mixing performance by generating vorticity and promoting the formation of small-scale turbulent structures

by forcing flow transition. In general, the presence of an oblique shock impinging on the boundary layer will give rise to well-know flow field. Yet, the interaction with an upstream jet blowing air away from the wall causes relatively unknown effects to the interaction domain of the SBLI. As mentioned by White (2011), blowing air perpendicular to the boundary layer renders it unstable, promoting transition and anticipating separation. Yet, further studies by Yan et al. (2020) analysing the interaction between a recirculation channel (thus resulting in a jet upstream of the shock) show how such configuration can prove beneficial for shortening the length of the separation region caused by the SBLI.

In order to properly define the flow field resulting from the interaction several measurements will be taken. The velocity field is going to be mapped using Particle Image Velocimetry (PIV) technology and compressible flow structures are going to be visualized using Schlieren photography in a preliminary attempt to understand the flow physics. Coupled with oil flow visualization, this techniques is going to allow for selection of the design points to be tested with PIV. Each experimental technique will serve as a tool to understand selected aspects of the flow problem. But what are the parameters in use to control the interaction and potentially in use for a combustor of a SCramjet? The foregoing provides a list of the main control variables.

- **Momentum flux ratio, J**. The ratio of linear momentum of jet and crossflow. It simplifies to the ratio of the corresponding dynamic pressures.
- **Flow deflection angle, θ**. The deflection imparted to the flow causing the oblique shock wave to form.
- **Shock impingement position, x/d**. Defined as the position the shock where would hit the wall in a completely inviscid field.

It is thus possible to identify one main research question, whose answer will be sought throughout the experimental campaigns.

How is the mixing in the near- and mid-field of the jet-shock-crossflow system affected by the variation of the control parameters?

One is then able to further split the main research question into several sub-questions which will be answered separately during the work.

1. How does the presence of the shock influence the mixing of fuel and air?
   (a) As the position of the Mach disk is an indicator for the mixing happening in the near field, what is the effect of a change in the control variables on it?
   (b) What is the effect of changing the control parameters on the vorticity resulting in the flow field and the development of the shear layer between the crossflow and the jet flow?
   (c) What is the effect of the shock properties (i.e. position and strength) on the vertical penetration and lateral expansion of the plume?
   (d) How is the generation of turbulent kinetic energy affected by a change in control variables? Where is the most TKE measured?
   (e) What are the general differences in flow field (i.e. flow structures) depending on the shock characteristics?

(f) How does the introduction of the incident OSW alter the mixing mechanisms in the near and mid fields?

2. How does the jet influence the downstream SBLI?

(a) What differences are there between in flow structures in the interaction region of the SWBLI between the situation with and without an upstream blowing jet?

(b) How do the control parameters affect the interaction length downstream of the shock impingement location? How does the introduction of the shock change the size of the interaction region compared to no-shock configurations?

(c) Which control variable has the greatest influence on the interaction length in the SBLI region?

1.5. Research Methodology

In relation to the research questions presented, it is necessary to define ways in which the main variables are going to be measured. Being an experimental project, the present section contains information on the techniques that will be employed and how they will be used to measure the quantities of interest.

First, images are going to be acquired using Schlieren photography and shadowgraphy. These are a line-of-sight techniques, allowing for the visualization of the field of the density's gradient and second derivative, respectively. It allows for precise identification of flow discontinuities and compressible features. With these, one is able to deduce quantitative information on the evolution of complex flow structures in high-speed flow (Settles and Hargather (2017)). For the present study, these optical techniques are going to be employed in a preliminary quantification of the flow field. Finally, oil flow visualization techniques are going to be used in order to get a grasp on how the behaviour of the boundary layer (i.e. flow separation, incident shock location etc.) such as in the work by Sun et al. (2011).

Regarding flow measurement techniques, stereographic PIV imaging is going to be used to map the velocity field and the complex three-dimensional turbulent structures arising from the interaction of the jet with the supersonic crossflow and the incident shock wave(s). Even though this techniques is not able to fully resolve the three-dimensional velocity gradient tensor, it can reliably measure the out-of-plane velocity component. In a field where 3D effects are prominent, it is considered to be a step ahead compared to planar PIV. Plane-normal velocity data can in fact still be a good indicator for the presence of turbulent structures, if not to complete the set of diagonal elements of the Reynolds stress tensor. The sum of those (i.e. the trace of the tensor) can be used to compute the turbulent kinetic energy, which is a key indicator of fluid mixing. Furthermore, when examining the SBLI, the additional measurable velocity data can provide insight on how the jet and the CVP perturb the "classical" interaction. Data with this technique, in fact, is not only going to be gathered on wall-normal planes, but also on wall-parallel ones. These loci are believed to contain information of (1) the plume's lateral expansion and (2) the turbulent motions at the edge of the boundary layer. Indeed, two wall-parallel planes are going to be imaged, namely one floating 4 [mm] above the wall and the second 8 [mm] from it. The former is expected to capture data right the edge of the incoming boundary layer and well within the separation regions induced by both the jet and the shock. The latter, instead, while still cutting through the large-scale separation zones caused by the incident OSW's, will mostly lie in the external flow.

Table 1.1 in the next section will present how a given flow measurement technique will capture a certain set of variables of the flow field (be it either qualitative or quantitative aspects) and which research question it will provide an answer to. Quantitative techniques include PIV, to a certain extent, Schlieren photography. Qualitative techniques also include Schlieren, together with oil flow visualization and the analysis of flow features from PIV.

1.6. Expected results

Data collected via some of the measurement techniques can provide direct answers. For instance, Schlieren visualization can directly answer questions related to the formation of shock waves and their location in the flow field. Inspection of oil traces on walls can provide insight into the behaviour of the boundary layer with little further elaboration. Some other measurement techniques require processing of the collected data in order to compute certain variables. Table 1.1 presents the output of all measurement equipment in use. The variables in bold are those that require a further processing step to compute them.

Measurement	**Variables measured**
PIV	Velocity, pressure, circulation / vorticity, jet penetration
Line-of-sight	Shock location, jet penetration, boundary/shear layer development
Oil flow	Shock waves, boundary layer separation, near-wall flow features

Table 1.1: Direct or indirect outputs per measurement technique

Introducing a shock wave impinging on the jet plume downstream of the injector location is expected to enhance the mixing performance of the injector system, as shown in several research works in the literature. This, however, will surely downgrade thrust performance for a SCramjet engine given the shock-induced total pressure loss. Yet, this will introduce a flow deflection, vorticity and entropy rise in the jet plume and its shear layer, which is expected to enhance mixing (Lee et al. (1997)).

The expected flow configuration arising from this multi-factor interaction is displayed in Figure 1.5. The flow comes into the figure from the left-hand side with a Mach number of 2. The jet being sonic, its Mach number is unity. As the incoming flow encounters the abrupt momentum transfer caused by transverse injection, effectively acting as an obstacle to the stream, a detached bow shock forms upstream of the orifice. The consequent compression causes mild recirculation at the bow shock foot. Separation is also observed in the immediate downstream vicinity of the jet. The jet exhaust itself is enveloped in a barrel shock, terminating with a Mach disk. The jet flow passing the barrel shock lies within the boundaries marked with the thin black lines. Being the flow highly turbulent at this stage, mixing will be favoured in this region. The impinging oblique shock wave is then introduced into the field from the upper left corner of the figure. As it hits the bottom wall, a reflected shock is also formed. As a consequence of the interaction with the discontinuity with the boundary layer, another recirculation area forms in between the incoming shock foot and the onset of the compression wave. This forms as a result of the weak compression induced by the interaction region.

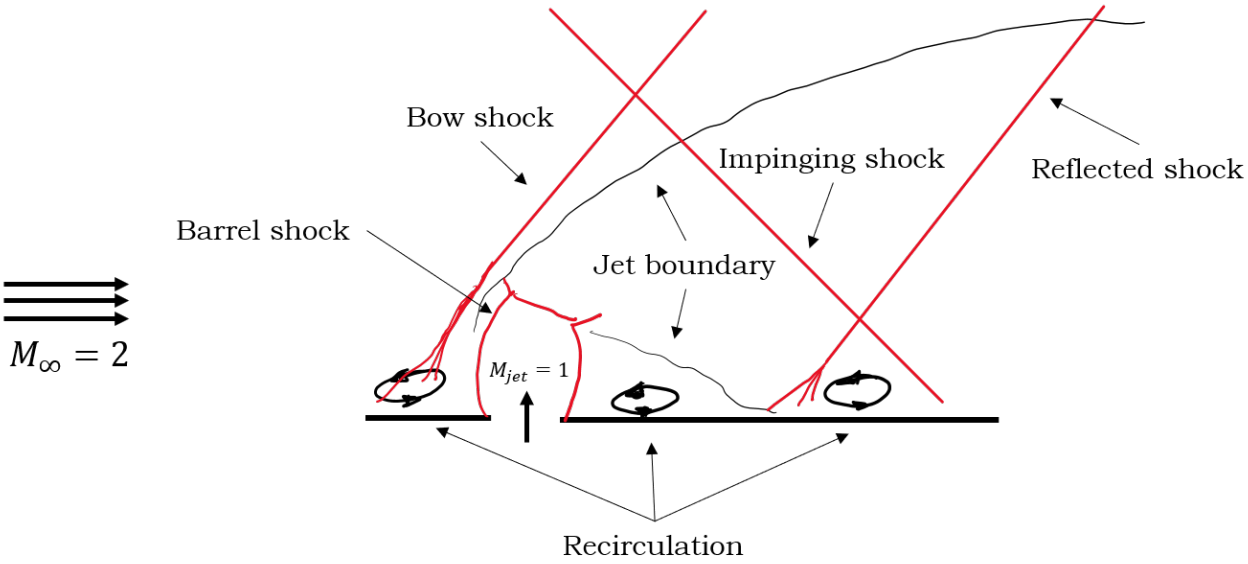

Figure 1.5: Schematic of flow interaction field expected in the experimental work.

1.7. Report outline

As far as the contents of the present report are concerned, an overview is presented hereby. First, Chapter 2 illustrates the most important findings from literature, which this project aims to build on. Chapter 3 then presents the main characteristics of the experimental facility in use for the work together with the model set-up, followed by Chapter 4. This explains in detail all the decisions made regarding the measurement techniques, as well as illustrating the working principles of those. The results are first introduced in Chapter 5, which presents the findings of the preliminary testing campaign comprising the results from line-of-sight techniques and the selection of configurations to be analyzed with PIV. The results of this are then presented in Chapter 6. Finally, Chapter 7 recaps the findings of this research project and suggests some recommendations for future research endeavours in the same area.

2

Theoretical Background

This chapter contains information relating to the literature that will serve as a background to the research conducted in the present work. The digression will set off at the presentation of the dynamics of shock-wave boundary layer interaction, followed by the presentation of the field and flow problems arising from the interaction of a jet in a compressible crossflow. Finally, the mixing augmentation mechanisms are presented, especially the literature investigating the effects of an oblique shock wave impinging on the developing jet plume.

2.1. Shock Wave-Boundary Layer Interactions

The interactions between a shock wave and the boundary layer have several applications in engineering disciplines and can play a critical role in the determination of the performance of a flight vehicle or propulsion system. These phenomena occur, of course, in supersonic flows, where the presence of strong discontinuities interferes with the development of the boundary layer on the wall. In particular, the pressure rise caused by the presence of shock waves causes alterations in the velocity profiles and flow reversals in the near-wall viscous layer. It is possible to distinguish between five main types of shock-wave boundary layer interactions (SBLI), listed below. Most of the foregoing is based on the work by Babinsky and Harvey (2011).

- **Impinging oblique shock wave reflection.** This situation occurs, for instance, in wind tunnels and supersonic channels. Here, an incoming oblique shock wave impacts against the wall and is reflected towards the opposite side of the duct. The flow is deflected by a certain angle, which indeed causes the second shock to form downstream of the first in order to re-align the flow with the centre line. The interaction at the foot of both shocks causes alterations in the development of the boundary layer.

- **Ramp.** As a gas approaches a ramp, a flow deflection needs to occur. This is caused by an oblique shock. As for the previous case, the discontinuity will interact with the boundary layer at its foot.

- **Normal shock.** Rather common in transonic flight, a normal shock might form somewhere in the flow to bring the supersonic region of air back to subsonic conditions to ensure pressure compatibility with the surrounding environment. The foot of the shock is immersed withing the wall boundary layer and alters its behaviour.

- **A pressure jump.** A sudden pressure variation in the flow field causes a shock wave to form to ensure compatibility.
- **A forward facing step.** As air nears a blunt feature along the wall, the resulting unfavourable pressure gradient causes the flow to separate. Acting the separated flow bubble as an "obstacle" to the stream, a shock wave forms just upstream of the separation location. This situation is rather similar to the case where a jet is fired 90 degrees to a supersonic stream.

To describe the behaviour of the boundary layer, it is possible to take the Navier-Stokes equations and only consider the momentum balance in x-direction (streamwise direction) and neglect the wall-normal velocity and wall-normal pressure gradient (Equation 2.1).

$$\frac{\partial}{\partial x}\left(\rho u^2\right) = -\frac{\partial p}{\partial x} + \frac{\partial \tau}{\partial y} \tag{2.1}$$

The boundary layer equation highlights a contrast between the flow's inertial properties (i.e. its momentum) and the pressure gradient. When considering the case where a shock's foot lies somewhere in the flow, the characteristics of the interaction will almost completely be dictated by the resistance of the boundary layer to the pressure rise and adverse pressure gradient. A turbulent velocity profile will be less prone to reaction compared to a laminar boundary layer profile. A key feature for the laminar case is the strong ensemble of shear stresses that will be generated within the layer. Furthermore, the temperature of the wall and the flow upstream of the shock's foot location will also play a role in establishing the interaction characteristics. If the wall is cooled, the speed of sound in its vicinity is greater, thus making the lower section of the boundary layer more "resistant". The opposite happens if the wall is heated.

Weakly interacting flows are those who do not cause flow separation upon interaction with the shock. In general, these can be described by the fact that viscous effects can be neglected and the flow field can be fully described by considering its inviscid characteristics. The two most relevant shock interactions in the context of a jet in supersonic crossflow and its application to the combustion of a SCramjet engine are the are interactions with a incident-reflecting shock system and the case where a normal shock impinges on the wall.

Weak interactions

An incident-reflecting shock system occurs as an oblique shock reaches the wall of a channel. It will impart a deflection to the flow which will cause it to deviate from being parallel to the guide walls. Thus, a second shock must be generated to compensate for the initial deflection to ensure that the flow streams parallel to the walls thereon. Figure 2.1 displays a schematic of the interaction at the wall level. As the shock enters the wall layer, it encounters the typical velocity gradient that ensures the no slip condition at the wall. Thus, as the Mach number progressively decreases, the shock angle will rise due to the $M - \beta - \theta$ relation. Eventually, as the discontinuity reaches the sonic line at the bottom of the layer, the shock is completely smear due to the impossibility of subsonic flow to hold a shock wave. However, the shock still causes a pressure rise downstream of it, causing the flow to slow down in the lower part of the boundary layer. A "bump" is thus created upstream of the incident's shock foot which travels upstream. Acting as a weak ramp to the incoming flow, isentropic compression waves form, which then coalesce into the reflected shock. As shown in Figure 2.2, as in the case for the incident shock case, the same

smearing phenomenon is observed in the case of the normal one. Indeed, the shock loses its strength as it progresses further down into the boundary layer. As the shock causes an increase in pressure and, thus, a decrease in velocity of air downstream of its foot, a perturbation travels upstream. Again, these cause the formation of isentropic compression waves, which then coalesce into the main shock. It can sometimes happen that a set of secondary shocks appear downstream of the main one. This phenomenon is known as a *supersonic tongue* and is produced by the shape of the boundary layer itself. In fact, as air crosses the shock and re-aligns with the main flow, its streamlines expand over the convex shoulder of the wall layer.

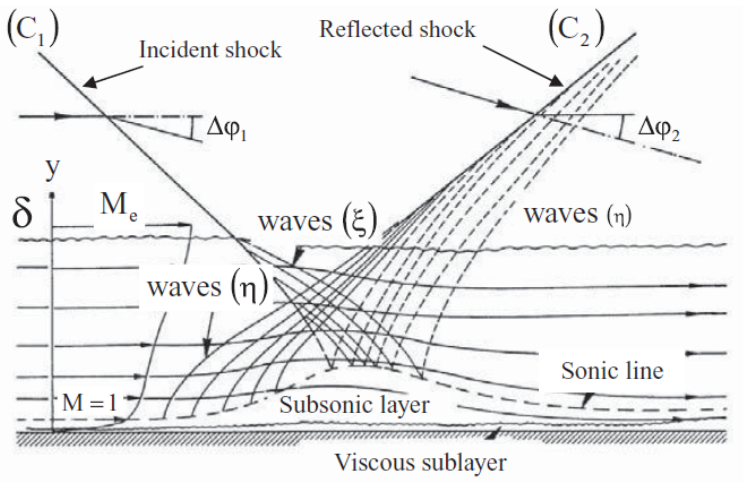

Figure 2.1: Schematic of the interaction between the boundary layer and incident-reflecting shock system. Obtained from Babinsky and Harvey (2011).

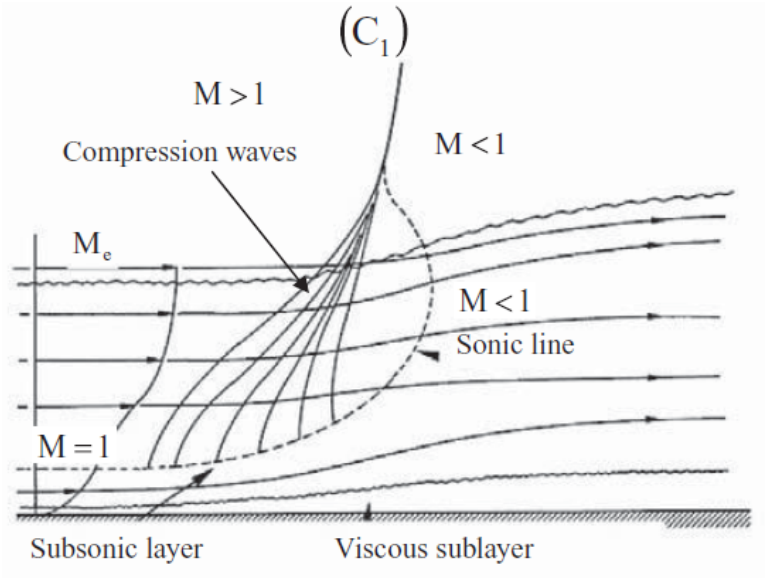

Figure 2.2: Schematic of the interaction between the boundary layer and an normal shock wave. Obtained from Babinsky and Harvey (2011).

Strong interactions

As mentioned in the above, strong SBLI occur when the shock wave causes the boundary layer to separate. The determination of the point of separation is the key to determine if the interaction will indeed be strong, transitional or weak. Free interaction theory provide an expression for the maximum shock strength (pressure ratio) a boundary layer can tolerate without separating. Based on Free Interaction Theory, based on the assumption that flow details are independent of downstream features, Delery and Marvin (1986) provides an expression for the limit pressure ratio at which the boundary layer remains attached to the wall (Equation 2.2).

$$\frac{p - p_0}{q_0} = \mathcal{F}(x - x_0/L)\sqrt{2C_f}(M_0^2 - 1)^{1/4} \tag{2.2}$$

where the $\mathcal{F}$ is assumed to be a universal correlation function. This function increases with the streamwise length x. Recalling the definition of the Reynolds number as in Equation 2.3, one can see how Equation 2.2 is also increasing with increasing Re. This means that higher resistance to separation with a higher Reynolds number. Indeed, the correlation is valid when associating the increase in Reynolds to a fuller velocity profile. The opposite dependency is, instead, observed for the Mach number. An increase in M_0 appears to lead, in fact, to a decrease in limit pressure ratio.

$$Re_x = \frac{\rho V x}{\mu} \tag{2.3}$$

Souverein et al. (2013) also appears to have found a universal criterion to determine the onset of flow separation as a function of the main flow parameters. The criterion is defined using a dimensionless parameter whose definition is presented in Figure 2.4.

$$S_e = k\frac{\Delta P}{q_e} = kg(M_e, \varphi) \tag{2.4}$$

where k and g are a constant and a function depending on the flow parameters, respectively. In particular, k is a constant which solely depends upon the Reynolds number. The flow will separated for $S_e \geq 1$ and remain attached for $S_e < 1$. This scaling appears to be rather precise (at least for a first order estimation) as shown in Figure 2.3. There, the black and grey markers refer to an attached or almost separated flow, respectively. White markers correspond to separated conditions.

Anyway, as the conditions for boundary layer separation are obtained, the flow topology in the boundary layer in the vicinity of the shock's foot is rather different compared to the one for the non-separating flow, as visible in Figure 2.4. The phenomenon of shock smearing still appears in this flow case. However, as the boundary is now no longer attached, many new features arise. The separated flow bubble acts, again, as a micro-ramp generating isentropic compression waves. These impart a small upward deflection angle to the flow. To re-align the flow to the main stream, a second shock leg results downstream of the first, close to where the bubble reattaches to the wall. The result is the generation of the λ-shock structure which is rather typical for the strong interaction with a normal shock wave and that Dickmann and Lu (2009) found also in the region upstream of the bow shock in the interaction of a jet in a supersonic flow. Again, a supersonic tongue can form right downstream of the second leg. The situation is also different in the case of a strong interaction with an incident-reflecting oblique shock (Figure 2.5).

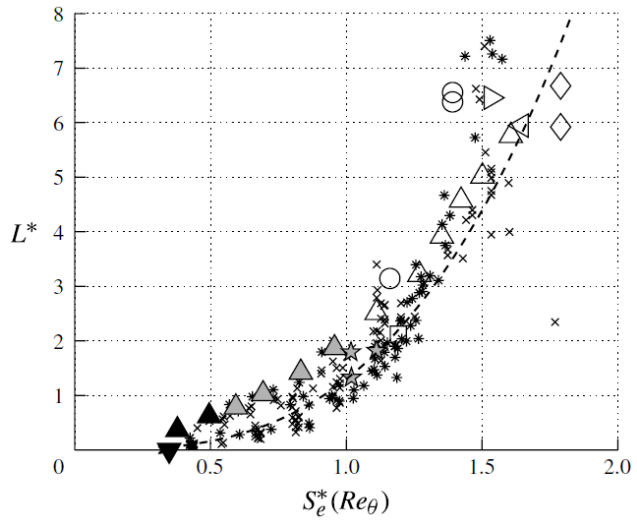

Figure 2.3: Plot showing the separated length scale obtained using Equation 2.4 versus the parameter S_e. Obtained from Souverein et al. (2013).

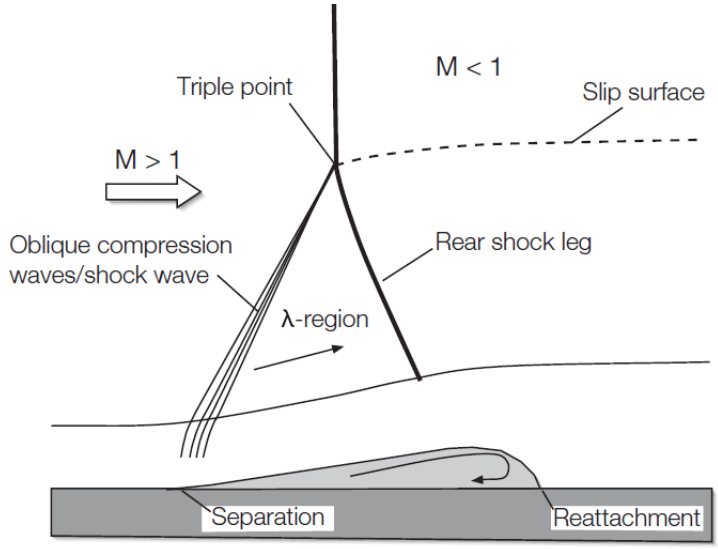

Figure 2.4: Schematic of the strong interaction between a normal shock wave and the boundary layer. Obtained from Babinsky and Harvey (2011).

The separated flow bubble in Figure 2.5 causes the usual coalescing of isentropic compression wave in the upstream shock. As air flows over the bubble and re-attaches again, a second shock forms at the corresponding location. This is usually referred to as a *re-attachment shock*.

Upstream influence

the reader should have clear in mind now that SBLI have an effect on upstream properties through the propagation of information through the subsonic region of the boundary layer close to the wall. Green (1970) determined how the length of the upstream influence region can be scaled according to several parameters: the upstream Mach number M_0, the thickness of the inflow boundary layer δ_0, the Reynolds number based on the thickness Re_δ, the shock strength and the state of the wall layer itself (i.e. laminar or turbulent).

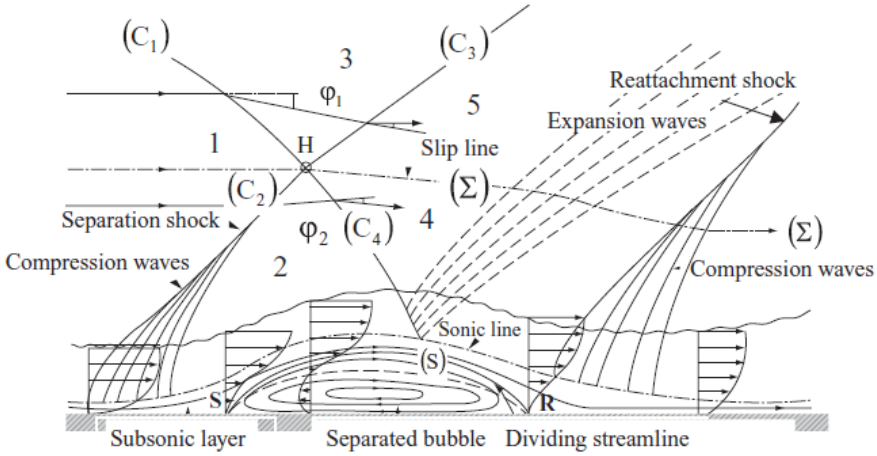

Figure 2.5: Schematic of the strong interaction between an incident-reflecting oblique shock wave and the boundary layer. Obtained from Babinsky and Harvey (2011).

Considering the normalized interaction length L/δ_0, their effect is the following.

- L/δ_0 increases for increasing shock strength and constant Mach number.
- L/δ_0 decreases as the Mach number increases and constant shock strength.
- L/δ_0 increases for an increase in thickness-based Reynolds number.

A note should be made on the last item. In particular, the trend is indeed verified for moderate values for the Reynolds number. However,e around a critical value of about $Re_\delta \approx 10^5$, the trend inverts. Still, an increase in Reynolds number signifies a diminishing of the importance of the viscous factors, which leads to increased resistance against separation.

SBLI control

As strong interactions cause the downstream boundary layer to separate, extensive works in the literature focus on the attempt to control such interaction, as mentioned in a comprehensive review by Huang et al. (2020). In this work the author distinguishes mainly between two types of SBLI control: for internal and for external flows. In the former case, which is also the most applicable to the JICF case in the supersonic scenario, the author recalls solutions such as adaptable-geometry ramps, vortex generators and, indeed, a jet. It is not exactly a jet in the configuration of the present work, but rather a nozzle flow originating from a recirculation channel. The work by Yan et al. (2020) explains this and Figure 2.6 illustrates it. It is necessary to mention that a “standard” JICF does not feature the downstream suction jet. This particular item would, in fact, benefit the boundary layer properties downstream of the interaction zone by delaying separation (White (2011)). Yet, the study shows that suction-blowing configuration shows good potential for control and reduction of flow separation downstream of the shock impingement location. Pasquariello et al. (2014) hints at the fact that beneficial properties are caused more by the downstream suction hole than the upstream blowing port. Nonetheless, these two studies serve as illustrating a potentially new control technique which only relies on existing pressure differences to function (i.e. is passive). Referring back to the study by Huang et al. (2020), an application for jets in crossflow for control of the SBLI properties is found in the use of microjets.

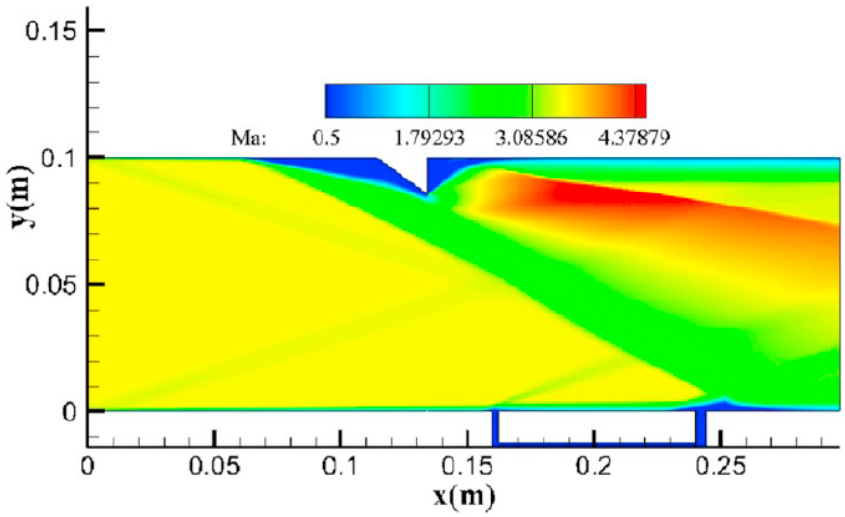

Figure 2.6: Figure displaying the SBLI with the rirculation channel. Taken from Yan et al. (2020).

Ali et al. (2013) conducted experiments on the effects of a microjet placed upstream of ramp-induced SBLI. Their tests show how the upstream jet, by producing a shock upstream, slows air down before meeting the "main" shock system. This allows for a weaker interaction, causing the oblique shock to start smearing farther above the wall than in the no-jet case. Furthermore, pressure change over the streamwise coordinate is shown to be more gradual.

Air jets have been indeed extensively studied in the literature as a mean to control the flow in the interaction region. Yet, the most effective way of exerting control was not found in a configuration similar to the one in study in the present work, but rather with lower mass-flow jets or plasma actuators. For instance, the numerical work conducted by Deshpande and Poggie (2018) mentions how the introduction of a plasma actuator is beneficial in terms of the reduction of the strength of the reflected shock and reducing the separation length.

The need for SBLI control is of particular importance in high-speed propulsion system. Especially when a strong interaction takes place, multiple shocks can form in sequence, thus forming a shock train. Gnani et al. (2016) reports several shock configurations that can emerge depending on the flow Mach number in the duct. Figure 2.7 illustrates this clearly.

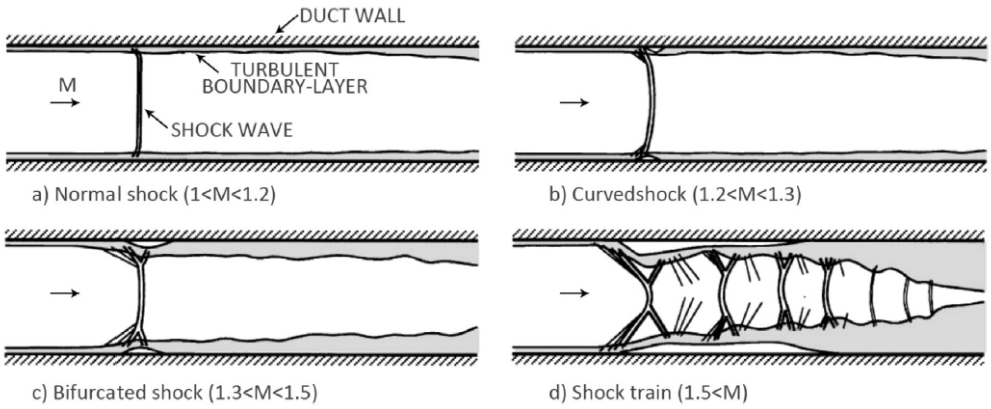

Figure 2.7: Schematic of possible shock patterns inside high-speed ducts. Courtesy of Gnani et al. (2016).

As the flow Mach number surpasses a certain value, in fact, massive separation occurs as a result of the strong shock-wave boundary-layer interaction, leading to high friction losses. A channel of receding shocks effectively forms for the worst-case scenario, indicating the need to enforce some method of control.

2.2. Jet dimensionless parameters

Essential to the discussion presented in the present survey is the definition of Mach number:

$$M = \frac{U}{a} \tag{2.5}$$

where U is the local flow velocity and a the speed of sound ($a^2 = \partial p/\partial \rho = \gamma RT$). The description of the characteristics of a jet is generally described using three dimensionless parameters referring to inertial and viscous behaviours (Mahesh (2013)). The first is the jet's *velocity ratio* r, defined as the ratio of the incoming cross stream's velocity to the jet's (Equation 2.6).

$$r_{\text{jet}} = \frac{U_{\text{jet}}}{U_\infty} \tag{2.6}$$

The second parameter also refers to the inertial properties of the jet and is known as the *momentum flux ratio* J, defined as the ratio of dynamic pressures. Its expression is presented in Equation 2.7.

$$J = \frac{\rho_{\text{jet}} U_{\text{jet}}^2}{\rho_\infty U_\infty^2} \tag{2.7}$$

In compressible flows, dynamic pressure can be reformulated considering the definition of Mach number reported in Equation 2.5. In particular,

$$q = \rho U^2 = \rho \cdot M^2 a^2 = \rho \cdot M^2 \gamma RT \tag{2.8}$$

Thus, substituting the expression back into Equation 2.7, it is possible to obtain a second definition for the momentum flux ratio (Equation 2.9).

$$J = \frac{\rho_{\text{jet}} \gamma_{\text{jet}} M a_{\text{jet}}^2}{\rho_\infty \gamma_\infty M a_\infty^2} \tag{2.9}$$

Early studies by Morkovin et al. (1952) and Orth et al. (1969) mention how J is predominant parameter in the determination of the behaviour of the jet. Beresh et al. (2005) confirms this results experimentally and mentioning how an increase in momentum flux ratio will lead to an increase in jet penetration, which is the same conclusion reached by Portz and Segal (2006) and several other studies.

Concerning the viscous properties of the jet, Mahesh (2013) provides another rather fundamental parameter to observe in this context, which is the jet's Reynolds number, defined as in Equation 2.10.

$$Re_{\text{jet}} = \frac{U_{\text{jet}} d_{\text{jet}}}{\nu_{\text{jet}}} \tag{2.10}$$

Here, the characteristic length is taken as the diameter of the injecting orifice, d_{jet}. ν_{jet} is the kinematic viscosity. A secondary variable playing a role in the penetration of the jet in the crossflow is the incoming boundary layer's thickness. It is generally expressed in its dimensionless form, normalized with the port hole's diameter (δ/D). McClinton (1974) showed how a thicker inflow boundary layer benefits jet penetration. Pizzaia and Rossmann (2018) not only confirmed the results, but also built up on them observing how a greater J also leads to greater lateral expansion of the jet, leading to improved entrainment properties.

2.3. Secondary supersonic injection

This chapter is to serve to the reader as a detailed analysis of the flow structures and the characteristics of the flow field generated by the secondary injection of a jet in supersonic crossflow. Details are going to be provided for the general inviscid flow field induced in the compressible flow domain, as well as the creation and interaction of viscous phenomena with pressure-driven features.

The inviscid flow field

The first studies of secondary jet injection in compressible were conducted by Morkovin et al. (1952), Zukoski and Spaid (1964) and Orth et al. (1969). In particular, the first crude but comprehensive picture of the salient flow structures was published by Morkovin et al. (1952). The authors conducted an experimental campaign to deepen their understanding into this type of flow field. The geometry considered consisted of a cylinder with a conical tip, as shown in Figure 2.8.

To understand the features emerging in such complex flow field, it is first necessary to understand what is happening in the near field of the jet. In the experiments by Morkovin et al. (1952), the jet attains sonic conditions at its exit and emission into the cross stream. The jet is underexpanded, meaning that its pressure is greater than the surrounding environment's. For this reason, as illustrated in the previous chapter, the jet first expands through a Prandtl-Meyer expansion fan. Then, as the jet's pressure drops, its boundary curves towards the centre of the stream to re-compress it. Eventually the compression wave becomes so strong that it forms a *barrel shock* around the main stream of the jet. The barrel shock terminates with a quasi-normal strong shock wave known as *meniscus* or *Mach disk*, as in the case of underexpanded jet in still air. The Mach disk is a key and rather characteristic feature of the flow field induced by a jet in supersonic crossflow and is responsible for most of the mixing in the relatively near field (Kawai and Lele (2009)). As the barrel shock ends, two transmitted shocks form. Schetz et al. (1967) conducted an

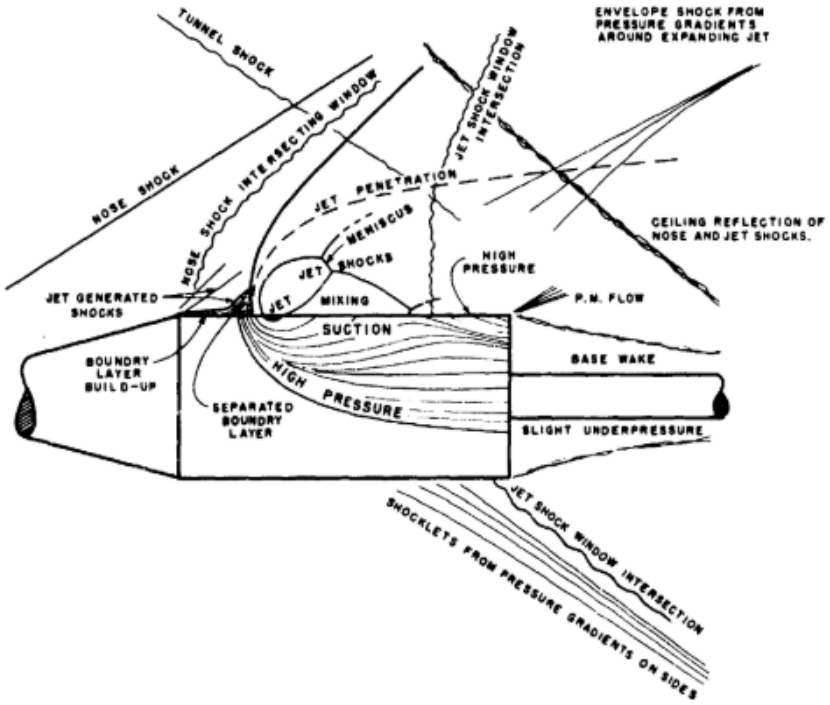

Figure 2.8: Schematic of the experimental model used in the work by Morkovin et al. (1952) and the resulting flow field around ti. Taken from Morkovin et al. (1952).

experimental campaign whereby they attempted a comparison between the case of a jet exhausting in quiescent air and a jet exhausting in a moving stream. First introduced by Schetz and Billig (1966), the concept of *effective back pressure* comes in handy and will be a valuable comparison parameter. The effective back pressure is a value for the jet's back pressure which makes the case of a jet exhausting in crossflow equivalent to the case of the a jet in a stream. Using this definition it was possible for Schetz and Billig (1966) to work on the differences between an "erect" and a jet in a stream. The claim is that the Mach disk height is less in the case of the jet in cross flow but its centre line is made longer by the fact that the jet is bent with the momentum of the stream.

Ahead of the jet a detached bow shock forms. In fact, the jet flow acts as a blunt body forced into the fluid. The bow shock stands just upstream of the jet's orifice and causes an abrupt pressure rise. The strip of high-pressure air flows around the injection location and disperses in the far field. Interesting is the fact that small compression wavelets were observed in front of the jet, slowly coalescing into the strong bow shock upstream of the jet. Downstream of the bow shock and, thus, in the vicinity of the injection location, a region of low pressure air forms. This is caused by what Morkovin et al. (1952) refer to as the "pump effect" of the jet. In fact, being the jet a source of vertically directed momentum, conservation laws call for a drop in pressure on the opposite direction of convection of momentum. The bow shock forming around this type of body of revolution will be found in later developments to be rather undermining for the performance of the jet as a side thruster. For instance, Zhang et al. (2012) found that the bow shock wave "wraps around" a 3D body of revolution, thus decreasing the pressure difference between either side of the vehicle and, hence, the thrust produced by the jet. As the flow convects farther downstream, the rises again due to the sequence of incident and reflecting shocks observed along the wall. In the case of the experiments conducted by Morkovin et al. (1952), the

flow then separates at the base of the cylinder crossing a Prandtl-Meyer fan.

Jet penetration and trajectory

In the later study by Zukoski and Spaid (1964), the authors tested the phenomenon of the jet in crossflow with the goal of finding a scaling parameter to describe the shape of the shock wave and the main features of the interaction. They found that the most appropriate scaling occurred by taking it as equal to the height of the Mach disk above the wall. The authors made an equivalence between the situation of a jet in supersonic crossflow and the interaction of a supersonic stream with a blunt axisymmetric body. By equating drag force produced by the "object" to the rate of change of momentum if the injectant, they were able to obtain an analytical expression for the radius curvature of the equivalent sphere (Equation 2.11).

$$h \propto \left[\sqrt{d(c)}\right](1/M_\infty)(P_{0,j}/P_\infty)^{1/2} \tag{2.11}$$

where $d(c)$ is the equivalent orifice diameter, M_∞ the freestream Mach number and $P_{0,j}/P_\infty$ the ratio of the jet's total pressure to the freestream's static pressure. Figure 2.9 shows the important of such parameter on the estimation of the penetration of the jet into the surrounding stream-

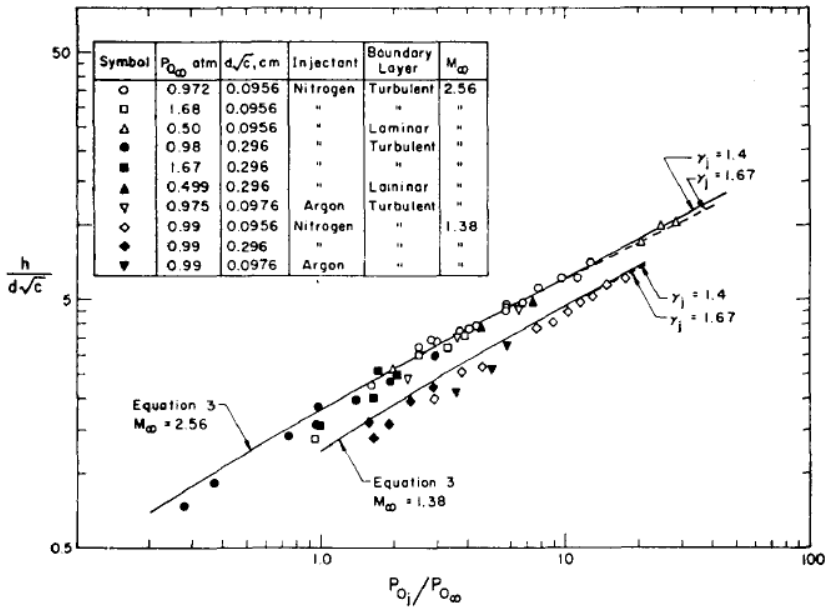

Figure 2.9: Graph of jet penetration versus ratio of jet's total pressure to freestream's static pressure. Log-log scale. Taken from Zukoski and Spaid (1964).

Zukoski and Spaid (1964) also point out how this relation seems to yield reasonable results also in real flows (i.e. viscous flows). This seems to indicate that the influence of the boundary layer in this interaction is rather weak and can be neglected in for a first-order analysis of the flow field. Further work into the derivation of an analytical expression to describe the jet's trajectory was conducted by Orth et al. (1969). Considering a fluid parcel, one can set up the equation for momentum conservation for a control volume of infinitesimal dimensions oriented parallel to the central streamline of the jet. Balancing forces along the element's longitudinal axis, one obtains Equation 2.12.

$$m(du/dt) = -mg\sin\alpha + \Delta\overline{P}A \tag{2.12}$$

where m is the mass of the control volume, du/dt is the time rate of change of the volume's velocity $u = u(s)$, α is the local inclination angle, $\overline{P}$ the average static pressure along the length of the volume and A the cross-sectional area of the control volume. Instead, applying conservation of momentum in a direction perpendicular to the jet's centre line it is possible to obtain Equation 2.13.

$$D + mg\cos\alpha = mu^2/R \tag{2.13}$$

where D is the drag of the element and $R = R(s)$ the local radius of curvature of the jet. Using the definition of the drag force as $D = C_D q_\infty S$ and combining the two equations above, it is possible to obtain an analytical expression of the inclination of the the central streamline with respect to the line coordinate s (Equation 2.14).

$$\frac{\mathrm{d}\alpha}{\mathrm{ds}} = -\frac{C_D h \rho_a u_a^2 \sin^2\alpha}{2\rho_j u_j^2 (A_j^2/A)(\rho_j/\rho)} \tag{2.14}$$

This model can be readily applied if the expression for the density and area of the cross-section are known as a function of the line coordinate s. To estimate those, Orth et al. (1969) provide semi-empirical relations obtained from experimental data. The authors also distinguish four different flow cases depending on whether the jet matches the stream's pressure or not and whether the boundary layer upstream of the jet is thick or thin. As far as inviscid phenomena are concerned, if the pressure at the exit of the jet matches the surrounding's stream pressure, then no shock system will form and nor will a Mach disk appear. This case, though, appears to be rare in most engineering applications involving jets in crossflow and will thus not be taken into account.

Papamoschou and Hubbard (1992) conducted a study trying to define the dependence of jet penetration on several flow parameters. The independent varying parameters were first identified by Broadwell and Breidenthal (1984). In particular, the claim is that the dependence of the jet penetration height, h, can be expressed as the dimensional argument in Equation 2.15.

$$\frac{h}{d} = \frac{h}{d}\left(J, M_1, M_j, \frac{p_j}{p_2}, \frac{Q_j}{Q_2}\right) \tag{2.15}$$

where Q is the density, the subscript 1 refers to the conditions upstream of the bow shock and 2 to the conditions downstream of the bow shock but upstream of the injector. Their conclusion was that the main variable playing a role in the penetration of the jet is the momentum flux ratio, J. A weak dependence was found for the two Mach numbers, the pressure and the density ratio. In particular, they found how an increasing momentum flux ratio allows for greater penetration of the jet into the cross stream.

The claim by Papamoschou and Hubbard (1992) is not new to the field of jets in crossflow. The strong dependence of jet penetration and, in general, of the trajectory on the momentum flux ratio will be reinforced again by Beresh et al. (2005), who analysed the penetration of a supersonic jet in a subsonic flow.

Portz and Segal (2006) conducted a similar study as the ones listed in the above, with the addition of the element of injectant molecular weight, something which was only superficially considered in the study by Papamoschou and Hubbard (1992). There they concluded that the penetration and trajectory of the jet are only mildly dependant on such factor. Furthermore, their work provides a comprehensive summary of several analytical

expression for the trajectory of the jet in s supersonic crossflow. In general, they observe how all trajectory equations assume the generic form shown in Equation 2.16, relating the penetration height P normalized with the nozzle's diameter D.

$$P/D = A(q_j/q_a)^B(x/D + C)^E(\delta/D)^F \cdot (M_j/M_a)^G \tag{2.16}$$

where M is the molecular weight and the constants A,B,C,E,F and G are to be determined from regression considerations of experimental data. The exponential coefficients estimated from several studies are tabulated in Table 2.1, together with the corresponding freestream Mach number at which they were experimentally determined.

	A	B	C	E	F	G	M_∞
Schetz et al. (1967)	1	0.435	0	0.435	0	0	N/A
Falempin (2001)	1.45	0.5	0.5	0.35	0	0	1.5
Hersch et al. (1970)	1.92	0.35	0.5	0.277	0	0	2
Rogers (1971)	3.87	0.3	0	0.143	0	0	4
McClinton (1974)	4.2	0.3	0	0.143	0.057	0	4
Portz and Segal (2006)	1.36	0.568	-1.5	0.276	0.221	-0.0251	1.6

Table 2.1: Table reporting the coefficients for the estimation of the jet plume's trajectory from several studies. Adapted from Portz and Segal (2006).

By inspection of Equation 2.16 and by comparison with Table 2.1, it is apparent that most studies consider the effect of a different molecular species negligible, which will also be confirmed in the work by Gruber et al. (1997). Indeed, also for only case where such aspect is taken into account (Portz and Segal (2006)), the coefficient appears to be rather weak. All authors agrees on the fact that the strongest variable affecting the penetration and the trajectory of the plume is the dynamic pressure ratio (J) (scaled and transformed via coefficients A and B). The exponential coefficient E also appears to be important, as it will define the scaling along the streamwise direction. The ratio of the incoming boundary layer's thickness to the diameter of the injecting orifice is thought to be negligible as well by most.

Shock Structures

Still focusing on the near field of the jet, it is necessary to shed some more light on the nature, the shape and behaviour of three-dimensional flow discontinuities. Figure 2.10 shows the resulting three-dimensional flow discontinuities from the interaction. Figure 2.10a shows a schematic of the several shock structures created during the interaction. As explained in earlier sections, a bow shock forms upstream of the jet, which is enveloped in a barrel shock terminating with a Mach disk. This is followed by a reflected shock and a collision shock originating from air streaming around the barrel (Liang et al. (2018)). Figure 2.10b shows a view from a wall-parallel plane of the contours of density. With these views it is possible to further examine the behaviour of these compressible flow features. The reflected shock propagates downstream with the flow and visibly dissipates in the far field. The collision shock forms right downstream of the jet injection, rather close to the downstream stagnation point. Close to it, a shear layer forms due to the difference in velocity between the two flow regions: port and starboard of the collision shock and aft of the reflected shock and the Mach disk. the most clearly visible feature is, though, the bow shock. It is the strongest discontinuity in the field and its strength determines much of the properties of the interaction.

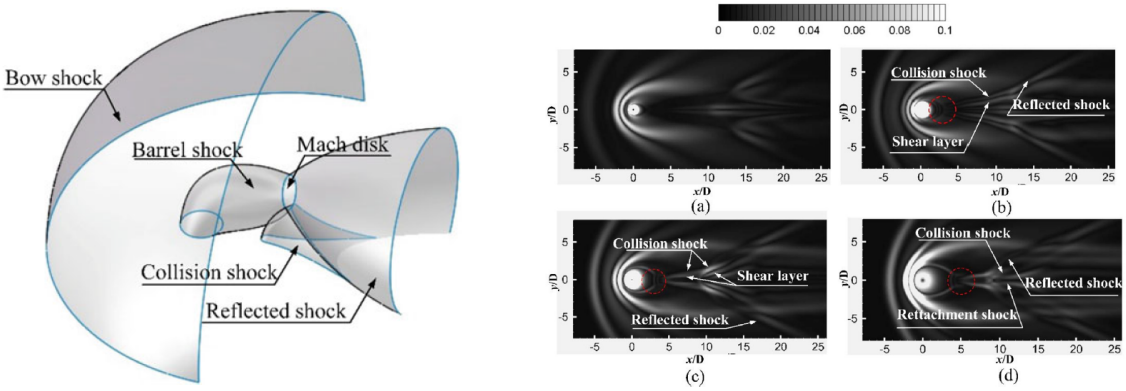

(a) 3D schematic of shock structures in the near field of the jet.

(b) Schlieren-like images of the shock structure viewed from above.

Figure 2.10: Shock structures. From Liang et al. (2018).

A more detailed description of the formation of the collision is provided by Sun and Hu (2018b) in their computational study. In particular, as it will be detailed in a later section, the supersonic boundary layer separates in the region downstream of the port hole. As this happens, the separation bubble distorts into a herringbone-type vortical features. In the meantime, supersonic flow is able to stream around the jet barrel to fill the low-pressure region that follows it. As the supersonic stream encounters the three-dimensional separation zone, a shock wave is formed. The shock is oblique in nature and aligned with the legs of the herringbone region. The oblique shock waves generated on either side of the centre line coalesce at the top to form a conical structure.

The supersonic CVP

As for the subsonic flow case, jets in supersonic crossflows also transform into the counter-rotating vortex pair (CVP) in the far field after being bent by the incoming flow's momentum (Mahesh (2013)). Chai and Mahesh (2011) studied the interaction of a jet in a supersonic stream using computational tools. Visualizing a cross-plane downstream of the injection port further clarifies the formation of the counter-rotating vortex pair (Figure 2.11).

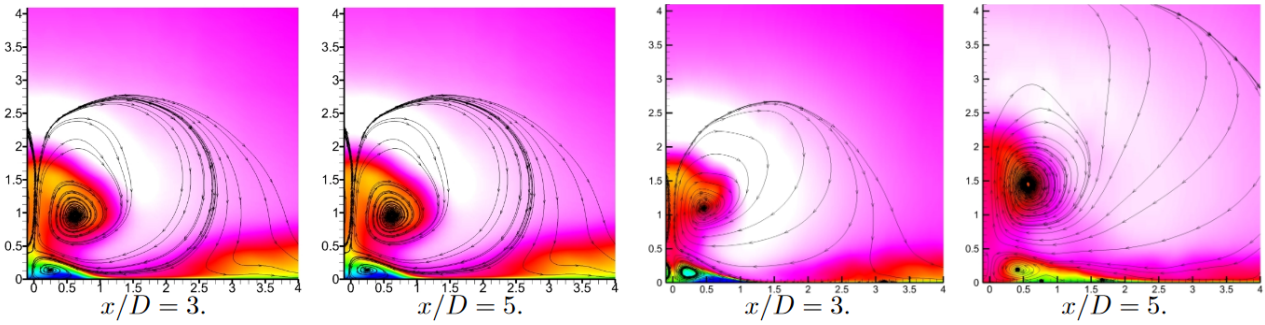

Figure 2.11: Visualization of vorticity contours on downstream planes. Obtained from Chai and Mahesh (2011).

The two snapshots on the left of Figure 2.11 were obtained considering a laminar inflow boundary layer, whereas the ones on the right by considering a turbulent profile. the rise and increase of vorticity in the far field is clear. In particular, as the flow undergoes abrupt deceleration through the Mach disk, the mechanism thanks to which the CVP then forms

is different to the one illustrated by Kelso et al. (1996) for subsonic jets. In particular, the mechanism for the formation of the vortex pair, whose nature is mainly time-averaged, relies in the instantaneous flow properties. Sun and Hu (2018b) also shed some light on the physical origin of such feature. In particular, the claim is that streamlines recirculate in the separation zone downstream of the jet, rise by the plume's lee and initiate a rotary motion propagating downstream as the main CVP.

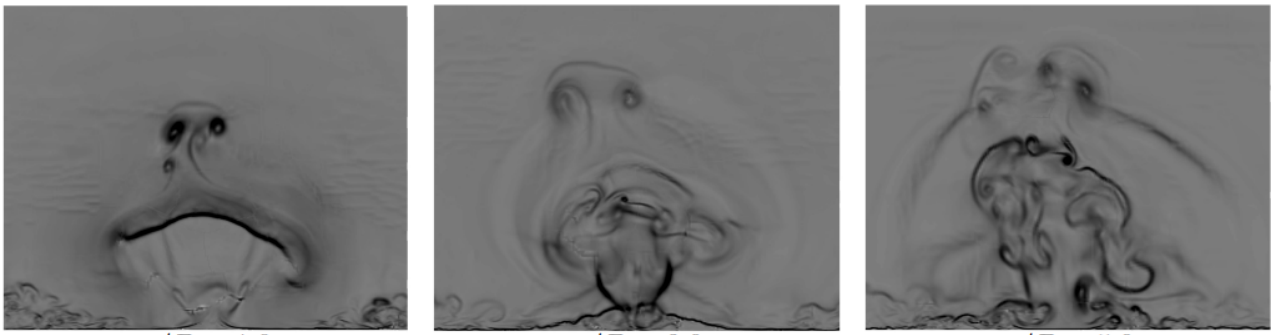

Figure 2.12: Instantaneous field on downstream cross-planes. Taken from Chai and Mahesh (2011).

Figure 2.12 displays how the jet penetrates into the surrounding environment via visualization of density gradient magnitude contours. Apart from mechanical considerations regarding the progressive increase of the vertical height above the wall, clearly discernible instantaneous features appear at every downstream station. In particular, two shear layers are forming in this interaction in supersonic streams. These originate as the flow crosses the Mach disk. The first is created between the region of air flowing through the Mach disk and the region just crossing the windward side of the transmitted barrel shock (above the disk). The second shear layer is, instead, forming due to the difference in velocity between the air crossing the Mach disk and the fluid entrained in the plume's lee. These coherent structures quickly break down (for real flows) due to Kelvin-Helmoltz instabilities. Taking the time-averaged statistic of these structures, the CVP results (Chai and Mahesh (2011)). A similar observation was claimed by Gruber et al. (1997).

As it propagates downstream, the counter-rotating vortex pair leaves a gap where the fuel concentration is extremely weak between the lower edge of the vortex pair and the wall. This gap is highlighted with a purple line in the figure and gets greater and greater as the momentum flux ratio J is increased. The gap appears to be smeared as the observing station shifts downstream. Viscous phenomena take over and dissipate large-scale vorticity introduced by the CVP. Part of the reason why the pressure in the region downstream of the jet is low, as pointed out in the legacy study by Morkovin et al. (1952), is the presence of the CVP itself. In fact, not only upward directed flow momentum calls for a decrease in pressure in such region, but also the induced velocity field of both column vortices appears to recall air from the wall, thus causing static pressure to further reduce.

Historically, the formation of such feature appeared mysterious for most legacy workers in the field. As Kamotani and Greber (1972) observed how the single column jet then transformed into a pair of vortices, many have tried to explain the mechanism underlying its formation. Broadwell and Breidenthal (1984) theorized how the jet acts as impulsive source of momentum and, as a three-dimensional finite wing, it causes two counter-rotating structures at its edges. A key difference with respect to the subsonic jet case is the fact that, whereas the subsonic CVP starts forming in the immediate near field of the

injection (Coelho and Hunt (1989)), the supersonic case first needs to wait for the injectant to cross the Mach disk and only stabilizes in the mid- to far field.

As remarked by Sun and Hu (2018b), the interaction with the CVP and the shock structures can give rise to four different flow patterns.

1. Streamlines flow around the jet barrel, do not interact with the herringbone-shaped separation-induced vortical structures, to then rise up into the main CVP due to the suction generated by it.

2. Streamlines go over the separation region and into the re-attachment valley. Here, the wings of the herringbone form tunnels in which streamlines can swirl, forming the primary trailing counter-rotating pair (TCVP).

3. The flow interacts with the collision shock formed by the wings of the herringbone themselves and enter a rotating pattern downstream of the reattachment point in the separation valley. This forms a secondary TCVP.

4. The stream glows around the barrel, over the separation region and eventually joins the secondary TCVP downstream of its formation point. The secondary TCVP dies out due to downstream local dissipation and to the progressive disappearance of the herringbone region.

Interaction with the boundary layer

Dickmann and Lu (2009) performed detailed studies on the flow structures emerging from the interaction of transverse jets with viscous phenomena. Just upstream of the jet injection location a bow shock wave forms. Indeed, the injectant acts as an obstacle to the incoming flow, thus generating a flow discontinuity. Being the bow shock's foot quasi-normal at the wall's stagnation point, a λ-shock structure forms at that location (Babinsky and Harvey (2011)). Due to its interaction with the incoming boundary layer, the shock is smeared into the viscous layer and flow separation occurs. The plume (usually underexpanded) itself is enveloped in a barrel shock, which terminates with the typical Mach disk: a circular normal shock. The plume then flows into a high-vorticity region characterized by powerful wake vortices: the counter-rotating vortex pair (CVP). On the wall's surface just downstream of the nozzle, two horseshoe vortices form along with a smaller recirculating flow bubble which will give rise to a shock upon reattachment.

Figure 2.13 reports a schematic of the main flow features resulting from the interaction. Necessary is the mention that flow separation is caused upstream of the bow shock due to the unfavourable pressure gradient induced through the subsonic section of the boundary layer in the vicinity of the wall. It is also possible to analyse how the wall boundary layer behaves as air goes around the injecting nozzle. Apart from the re-circulation zone ahead of the injection, a smaller separated flow bubble also forms in the vicinity of the jet's lee on the wall. The re-attachment of this second reversed flow causes a secondary shock to form, which will eventually dissipate in the far field. Figure 2.14a provides more insight into the flow pattern on a wall- and flow-parallel plane positioned on the wall in the near field of the orifice.

Figure 2.14a highlights all flow phenomena mentioned in the above. Considering an imaginary axis going through the centre of the orifice and parallel to the outer flow, it is possible to identify several interesting points.

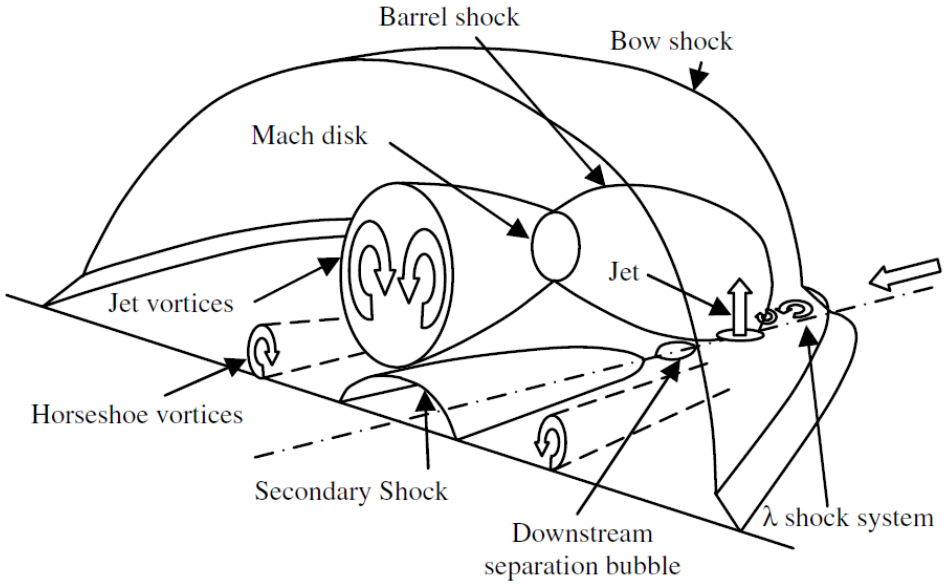

Figure 2.13: Schematic of flow structures generated by a jet in supersonic crossflow

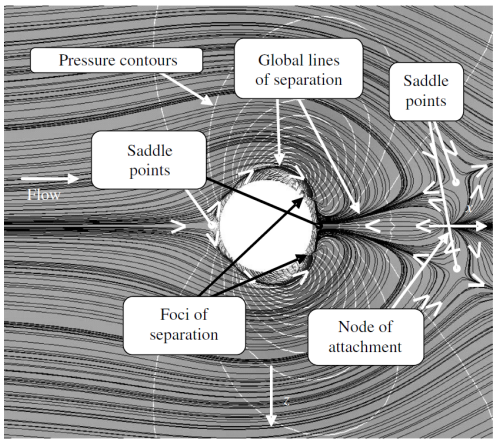

(a) Friction lines on the wall in the near field of the jet.

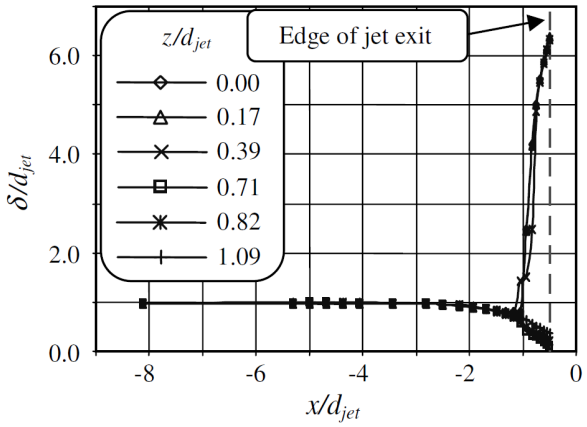

(b) Boundary layer thickness upstream of the bow shock.

Figure 2.14: Orifice's near field: friction lines and boundary layer thickness. From Dickmann and Lu (2009).

- **Stagnation points.** Two stagnation points are visible up- and downstream of the port hole, where the velocity of the streaming air will go to zero.
- **Reattachment points.** One reattachment points is present where the separated flow bubble rejoins the main flow along the wall. It is shown just downstream of the hole, where the bubble terminates.
- **Foci of separation.** These points are characteristic identifiers of three-dimensional separation as mentioned in Lighthill (1963).
- **Saddle points.** These are locations where the flow velocity is virtually zero, and where the velocity vector is not defined, as it would point in several directions at the same time.

Interesting to note in Figure 2.14a is also the fact that the flow is reversed in the im-

mediate vicinity of the jet, downstream of it. This is caused by flow separation indeed. Figure 2.14b enables a deeper understanding of the behaviour of the boundary layer just upstream of the bow shock's foot. In particular, it appears that its thickness, δ_{99}, initially decreases. As the shock foot is progressively approached, the thickness spikes: a clear sign of flow separation.

The incoming flow's boundary layer thickness is a parameter which has been greatly considered in literature as one of the secondary drivers for flow penetration and mixing in the far field. Usually normalized with the port hole's diameter as in Figure 2.14b, it is the subject of several parametric studies. The first was conducted by McClinton (1974), who found that jet penetration increases with boundary layer thickness as in Equation 2.17.

$$\frac{h}{D} \propto \left(\frac{\delta}{D}\right)^{0.0574} \tag{2.17}$$

where δ is the thickness of the wall layer normalized by the orifice's diameter, D. The above expression indicates that the dependency of jet penetration on boundary layer thickness is weak, as demonstrated by the exponent's value close to null. A more accurate approximation is provided in the work by Povinelli and Povinelli (1971). They provide a rather comprehensive expression which, however, depends on the boundary layer's momentum thickness (Equation 2.18).

$$\frac{h}{D} = 2.96\left(\frac{p_{0,j}}{p_{eb}}\right)^{0.405} M_J^{0.163}\left(\frac{x}{d^*} + 0.5\right)^{0.204}\left(\frac{\theta}{d^*}\right)^{0.141} \tag{2.18}$$

where $d^* = D\sqrt{C_D}$ is the effective jet diameter, p_{eb} the effective back pressure and θ the momentum thickness. As mentioned in an earlier section, another approximation is also available from the work of Rogers (1971).

The explanation as to why a laminar and thinner wall layer inhibit penetration is that, according to Muppidi and Mahesh (2005), the thin boundary layer case (as for the laminar one) sees more streamwise momentum concentrated close to the jet exit. This bends the plume "early" into the stream. A fuller turbulent velocity profile, which would also be more isotropic in nature, would distribute the streamwise momentum over a larger vertical distance, thus causing less bending in the vicinity of the port hole.

2.4. Jet entrainement and mixing

It was shown that, to achieve optimal combustion conditions, flame-holding considerations are of second order, meaning that flow-related considerations leading to enhancements in mixing are to be optimized for first, as demonstrated by Lee et al. (1997). Two main factors have to be designed for: plume penetration and mixing. The jet plume needs to spread away from the wall such that wall heating from combustion is kept low (Li et al. (2017)). Beresh et al. (2005) proved that greater penetration is achieved for greater momentum flux ratio, which also leads to the creation of a stronger counter-rotating vortex pair (CVP). McClinton (1974) also showed how an increasing ratio of boundary layer thickness to jet diameter δ/D is beneficial to increase jet penetration height. Furthermore, according to Beresh et al. (2003), for an equivalent momentum flux ratio, a decreasing Mach number in the crossflow benefits penetration as well.

Apart from considerations on penetration height, several mixing strategies have been considered in the past to achieve an effective blend between fuel and air. It is key to

establish which parameters and mechanisms contribute to mixing. For subsonic flow, mixing in the near field is dominated by abrupt momentum transfer between the jet and the surrounding fluid, whereas far-field mixing is mostly characterized by molecular diffusion. VanLerberghe et al. (2000) claim that in high-speed jets, instead, near-field mixing is not that effective. Most mixing happens as the jet core crosses the normal shock (the Mach disk) and enters the rotational regime of the CVP, also noticing regions of unmixed fuel in the jet. Kawai and Lele (2009) also assert the importance of the normal shock on mixing and observed an increase in mixing the further downstream from the location of the Mach disk. Gruber et al. (1997) conducted studies on the turbulent eddy scales encountered in such interactions and states that mixing is highly dependent on the formation of smaller-scale coherent structure which entrain the flow and promote molecular diffusion.

In the context of transverse injection techniques, several ideas have been tested to increase the fuel-air blending properties. Murugappan et al. (2005) considered the injection of fuel in pulses. Through an experimental campaign, they proved that mixing is greatly enhanced and that higher frequency could force a faster break-up of the plume into smaller turbulent structures. Zhang et al. (2016) also proved enhancement in mixing by generating a vortex with micro-ramps. Improvements in performance were observed for both upstream and downstream locations of the ramp with respect to the jet. Many studies have also been conducted on dual injection: having two wall orifices. Lee (2006) studied the case where two nozzles are placed in a tandem configuration. There, it is the case that the upstream nozzle generates a region of lower velocity, where the plume of the second jet can penetrate more easily and higher. The second plume also imparts more vorticity to the fluid, thus increasing its mixing potential. Being the overall total pressure losses similar to the single-jet scenario, dual injection is a rather appealing configuration to consider. Excellent mixing was also observed by Anazadehsayed et al. (2017) by placing a downstream air port hole. This is not the case, though, for multiple parallel injections. In this situation, the upstream bow shocks unite to form a stronger discontinuity, which induces great losses (Sun et al. (2011)).

All of the strategies to achieve proper fuel and air mixing in the combustion chamber of a SCramjet engine will be considered elaborated upon in the present chapter.

Quantifying mixing

Air and fuel mix according to two main mechanisms (Lee et al. (1997)).

- **Convection.** The transport of fluid across the flow domain allows it to blend with the injectant and other species.
- **Diffusion.** Process occurring on the molecular scale, directly caused by atomic segregation.

The first is dominated by velocity differences across the domain and its vorticity. A non-dimensional flow parameter exists which expresses the ratio of mixing by convection to diffusivity: the *Peclet number*, defined in Equation 2.19.

$$Pe = \frac{\int_y \int_z \rho_{\text{fuel}} \frac{u\sqrt{v^2+w^2}h}{r} \mathrm{d}y\mathrm{d}z}{\int_y \int_z \rho_{\text{fuel}} u \mathrm{d}y\mathrm{d}z} \tag{2.19}$$

where r is the fuel's effective radius and h the height of the injector. A high Peclet number indicates that convection is the dominant mixing mechanisms, whereas a low one indicates that diffusion is the primary mechanism.

Mixing mechanisms: the importance of coherent structures

Given the rather short residence time of fuel inside the combustion chamber of a SCramjet engine, it is essential to obtain rapid and effective mixing of fuel and surrounding air. Morgenthaler (1967) performed experimental work on radial (i.e. transverse) injection a supersonic stream. this technique is known to cause a drop in total pressure due to loss of axial momentum. However, this loss is generally compensated by the enthalpy addition during combustion. For this process to be successful, the achievement of proper fuel-to-air ratio is paramount. Axial fuel injection, although seemingly attractive from a propulsive standpoint, is not able to allow for great fuel penetration. For this reason, transverse injection appears to be an interesting solution.

As mentioned in Kawai and Lele (2009), the Mach disk plays a crucial role in the mixing process. More on this phenomenon will be explained in the foregoing. It is essential to also point out how entrainment behaviour is dominated by the formation of several coherent structures (Mahesh (2013)). In particular, one of the most comprehensive studies detailing the formation and characteristics of the several coherent structures forming in the flow was performed by Fric and Roshko (1994). They document the formation of four main vortical features.

- **The shear layer vortices.** These are generated periodically due to Kelvin-Helmoltz instabilities due to adjacent regions of fluids at different velocities.
- **The CVP in the far field.** The strong counter-rotating vortex pair.
- **The horseshoe vortices.** As the flow approaches the bow shock and separates, it will continue flowing alongside the jet's wake to form this feature.
- **The wake vortices.** These generate as a result of the vorticity of the horseshoe vortices, forming vertical features from the wall to the Mach disk.

A later study by Yuan et al. (1999) made use of large-eddy simulation computational tools to analyse the formation and shedding of several vortical structures in the near field of the injection. Figure 2.15a shows the observed patterns, as compared to the experimental work conducted by Kelso et al. (1996) (Figure 2.15b).

Figure 2.15a highlights the formation of three distinct coherent structure in the proximity of the injectant nozzle. In particular, spanwise vortices form "tubes" of high vorticity which roll up on the windward side of the plume. These are also marked with red dye in Figure 2.15b. Vertical streaks also form, only to dissipate soon after their formation. Hanging vortices form at the jet exit. These are quasi-steady features oriented in the streamwise direction which oscillate around a fixed location. Yuan et al. (1999) also remark how these can be periodically shed into the crossflow and be immediately replaced by a new such vortex. Their observation is that both feature originate in the Kelvin-Helmoltz instability that are created as the jet penetrates the cross stream and will be the main responsible feature for the formation of the CVP.

Ben-Yakar et al. (2006) observes how the near field mixing is dominated by the stretching and entrainment of the jet plume. Stretching is in fact responsible for the increase in contact area between the injectant and the surrounding fluid, leading to the promotion of mixing on a molecular level. Gruber et al. (1997) had already observed how the mixing in high-speed freestream condition is predominantly achieved as coherent structures travel

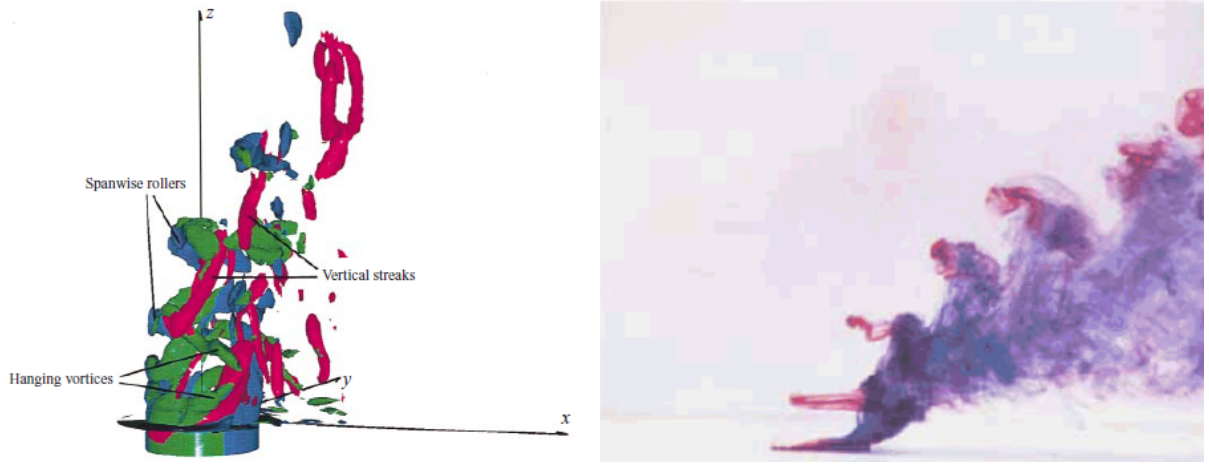

(a) Result of LES simulations by Yuan et al. (1999).

(b) Experiment with liquid dye by Kelso et al. (1996).

Figure 2.15: Comparison between computational and experimental results of the formation of vortices in the near field of the injection.

downstream and engage in molecular mixing with air. This, however, is rather slow process and can be detrimental for the efficiency and effectiveness for the performance of the combustion chamber of a SCramjet engine. The question is thus in regards as to how the small-scale structures contribute to the mixing process and how it can be controlled and accelerated in the near field.

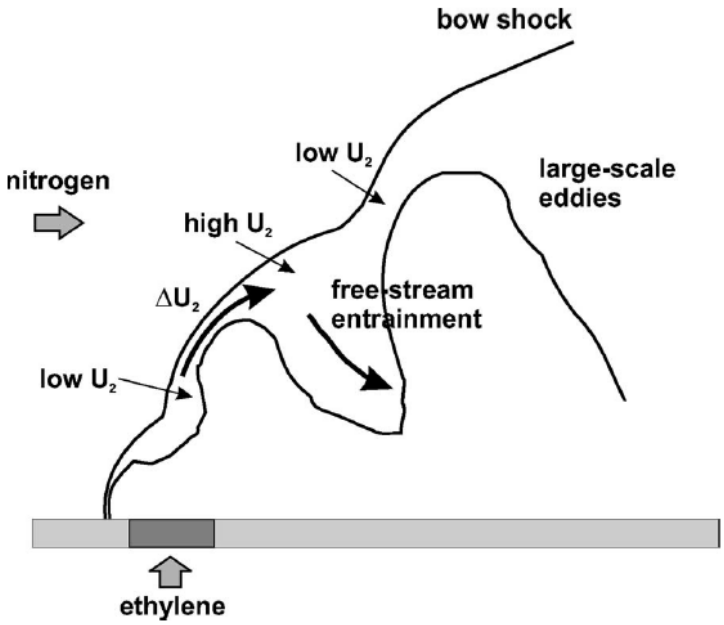

Figure 2.16: Schematic of the behaviour of the shear layer and bow shock wave dynamics. From Ben-Yakar et al. (2006).

Figure 2.16 displays the motion of the large-scale ethylene structures according to the deformation of the bow shock upstream of the jet's plume. The velocity fields induced by the moving eddies cause differences in the convection speed as a function of the distance from the wall. Given the nature of the shock wave, this causes the bow shock to bend

according to the local convective velocity. In particular, it will be steeper in regions of low flow speed and more shallow where its velocity magnitude is greater. This allows for a differences in shear stresses all along the jet's shear layer, which conversely lead to large deformation of the plume. This is what ultimately causes entrainment and, finally, mixing.

The importance of the Mach disk

As opposed to the subsonic case, where strong near-field mixing can be achieved by momentum-driven fluid exchange, the supersonic jet in crossflow sees little to no mixing in the near field of its injector port. As mentioned by VanLerberghe et al. (2000), in fact, mixing becomes more and more effective with increasing downstream distance from the location of the Mach disk. Figure 2.17 shows an instantaneous snapshot of the flow field in the vicinity of the injection port hole. The image intensity (i.e. luminosity) is indicative of the level of injectant density at the corresponding location. A brighter signal points to a denser medium, where the opposite holds for a dark one. By a first inspection one can notice how the Mach disk location is roughly unchanged between the three snapshots. Yet, some degree of unsteadiness is visible in the outer shape of the barrel shock and, of course, a much greater degree of temporal instability can be observed in the plume's shear layer.

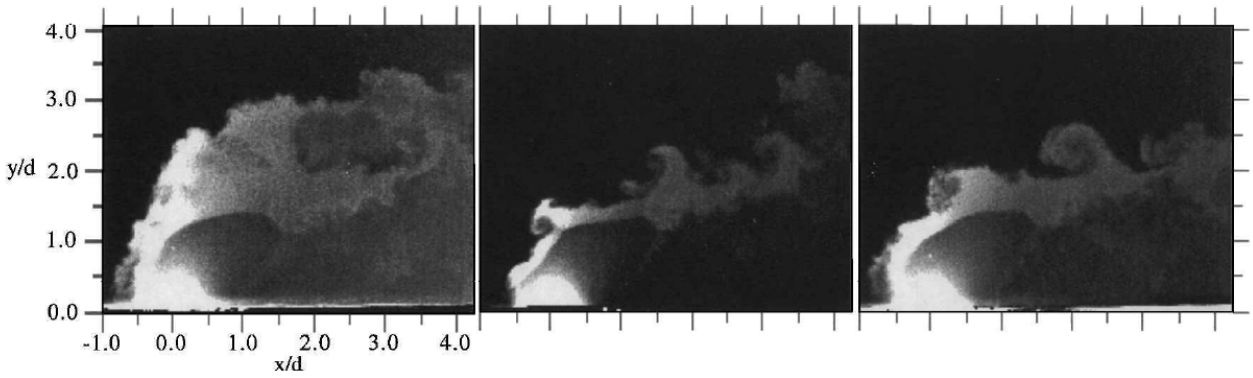

Figure 2.17: Instantaneous PLIF images of the barrel shock region. Presented by VanLerberghe et al. (2000).

Figure 2.17 shows three instantaneous snapshots of the region of the barrel shock and Mach disk. A highly bright signal is visible in the close vicinity of the jet exit, indicating high-density fluid. As the jet is further expanded by lip-centered expansion waves, the density rapidly decreases up to the position of the Mach disk. A relatively large volume of fluid also appears to completely avoid the barrel shock. As this gas mass did not flow through neither the barrel shock nor the Mach disk, it still retains much of its original momentum. This allows it to penetrate deeper into the stream to heights up to two or three times larger than the one of the meniscus (VanLerberghe et al. (2000)). A net contrast in density (i.e. signal intensity) is also visible right at the border of the barrel shock. This is, of course, cause by the rapid re-compression imparted by this flow feature. As fluid is slowed down by the shock it gets entrained into the adjacent stream. The eddy structures convecting downstream of the disk, with their induced velocity field, have the potential to induce higher entrainment. Thus, the wake region is by far the one where the most mixing occurs. Yet, if it were not for the presence of the Mach disk, the flow's vorticity would be lower, and so its mixing potential.

Kawai and Lele (2009) performed computational work on a similar configuration as the one by VanLerberghe et al. (2000). By employing Large Eddy Simulation (LES) techniques,

they were also able to draw conclusions on the shear layer dynamics, instabilities and resulting effects on the mixing effort of the fluid. Their work underlines the importance of the turbulent kinetic energy (the trace of the Reynolds stress tensor: Equation 2.20) in identifying regions of intense mixing.

$$k = \frac{\overline{u'u'} + \overline{v'v'} + \overline{w'w'}}{2U_\infty} \tag{2.20}$$

Regions where the turbulent kinetic energy are the ones where the presence of most turbulent eddies can be recorded and, hence, the ones responsible for the most mixing. This is a factor empirically proven in Figure 2.18. The upper part of the image indeed contains contours of turbulent kinetic energy on wall-normal, flow-normal planes. The bottom part, instead, is coloured by scalar concentration of injectant fluid. By inspections and comparison of the two parts of the figure, it is possible to deduce how regions with large k are also the ones where the most dilution will occur, pointing to better mixing. The regions where k peaks are the edges of the shear layer (due to the formation of instabilities) and especially behind the Mach disk. This is, in fact, the region where fluid gets entrained the quickest and diluted faster as the shift is moved downstream.

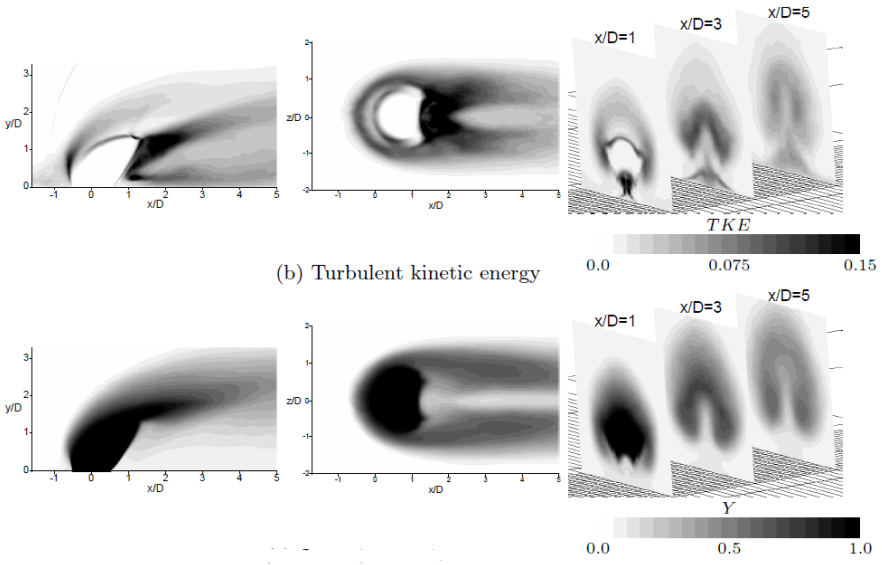

Figure 2.18: Contours of turbulent kinetic energy (top) and scalar fluid concentration (bottom). Obtained from Kawai and Lele (2009).

The vorticity created by the crossing of the Mach disk causes greater instability of the jet's shear layer boundaries, leading a quick breakdown of both the windward and leeward sides of the jet plume, as shown in Figure 2.17.

Far-field mixing: entrainment by the CVP

It has been shown in numerous studies, the CVP possesses great velocity gradients which dominate the behaviour of the interaction in the far field. In order to better quantify the mixing potential, the notion of circulation and streamwise vorticity should be introduced, as mentioned in Santiago and Dutton (1997). In particular, Equation 2.21, reports the mathematical definition of the streamwise vorticity.

$$\frac{\zeta_x}{U_c/d} = \frac{d}{U_c}\left(\frac{\partial W}{\partial y} - \frac{\partial V}{\partial z}\right) \tag{2.21}$$

where V and W are the wall-normal and spanwise velocity components, respectively. Then, the definition of the integrated vorticity (i.e. circulation) is provided in Equation 2.22 for each single vortex.

$$\Gamma = \int_0^{2\pi} \int_0^{\infty} \zeta(r,\theta) r \mathrm{d}r\mathrm{d}\theta \tag{2.22}$$

The most dominant flow feature at a distance relatively far downstream is the counter-rotating vortex pair. Furthermore, as it is the one with the highest vorticity, it is clear that it is the feature contributing the most mixing potential. As it also turns out in a computational study by Sun and Hu (2018a), the CVP is the key feature for mixing fluid in the near-wall region. In particular, as mentioned in the above, a "gap" between the forming CVP branches creates. This gap progressively reduces until complete dissipation in the far field. Up until the point where this region fades, it possesses some interesting properties when it comes to mechanical entrainment of surrounding gases. In particular, it is convenient to refer to this region as *Region I* and to the rest of the flow field as *Region II*, as suggested in Sun and Hu (2018a).

Region I is a section of the field where mixing is rather low. The injectant concentration is almost null due to the blockage effect of the barrel shock, which defines the upstream border of this section. It spans the space between the leeward separation zone and the termination of the gap between the CVP branches. As the momentum flux ratio increases, this region expands. Yet, as far as injectant mass fraction (i.e. concentration) is concerned, higher values are obtained for increasing *J*. This suggests that better entrainment in region I occurs for low momentum flux ratios. High concentration is, however, found in the near-wall far field for an increasing J, suggestion the possibility of flame extinction far downstream.

As mentioned in the above, the concentration of fuel in the proximity of the wall is higher for lower momentum flux ratio due to the blockage effect caused by the barrel shock. As the attention is shifted towards the downstream far field, the "pumping" effect of the CVP becomes apparent. Its large induced velocity gradient in fact drains fluid from the near-wall layers and brings them up into the core of the plume. This is the reason why, for both momentum flux ratios, the distribution of fuel appears to become more uniform over the considered wall-normal distance. For higher J, the peak concentration appears to be farther away from the wall compared to the low-J case. Moving downstream, an increasing in near-wall concentration becomes apparent, pointing at the possibility of lean combustion and, eventually, flame extinction towards the outlet of the flow domain.

Furthermore, as shown in several literature studies (such as Zukoski and Spaid (1964) and Schetz et al. (1967)), the height of the Mach disk is also an parameter which gives indications as to the degree of mixing in the field. The higher the Mach disk, the better the mixing.

Shock-enhanced mixing

In compressible flow, the vorticity equation sees a strong source term in its baroclinic vorticity term, defined in Equation 2.23.

$$S_{\text{baroclinic}} = \frac{1}{p_\infty \rho_\infty} \int_y \int_z |\nabla\rho \times \nabla p| \mathrm{d}z\mathrm{d}y \tag{2.23}$$

Variations of both pressure and density will be reflected into the cross product of the gradient of both state variables. In incompressible fluids, this component is almost null, given the almost complete lack of density variations. Gradients of both states get rather strong in the presence of flow discontinuities and, in particular of shock waves. It is for this reason that the study of how to increase fluid mixing using shock waves is a rather promising one due to strong vorticity induced by those.

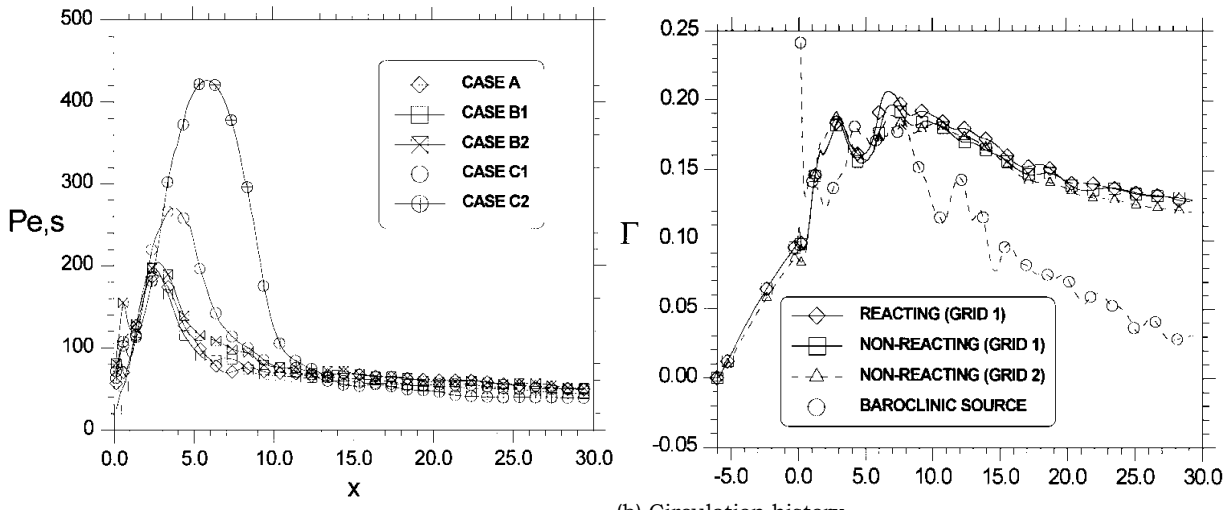

(a) Peclet number history

(b) Circulation history

Figure 2.19: Plot displaying the evolution of circulation and Peclet number and circulations as a function of downstream distance. Courtesy of Lee et al. (1997).

Figure 2.19a displays a peak in its value in the near field of the injection, which then decreases smoothly all the way down towards the far field. By comparison with Figure 2.19b, the trend is similar. In fact, a high Peclet ratio points in the direction of high mixing by convection instead of diffusion. The peaks in Figure 2.19a rise approximately with the Mach number considered in the simulations by Lee et al. (1997). An interesting consideration can be made in regards to the difference between the circulation distribution of reacting and non-reacting flow cases (Figure 2.19b). The curves show a good match all the way to the outlet. Furthermore, the same plot also displays the circulation induced by the baroclinic source, which appears to spike in the vicinity of the shock wave, to then ease out downstream.

Even though based on the study of parallel injection, the work by Nedungadi and Lewis (2000) sheds some more light on the mechanisms of mixing augmentation using an incident shock wave. Their study focuses on the simulation of the three-dimensional injection of a helium jet encountering a ramp, which acts as a shock generator. The authors studied the effect of a jet with swirl compared to a jet with no swirl and how the vorticity would thereby change. the change in vorticity was defined through the parameter *enstrophy*, whose definition is provided in Equation 2.24.

$$E = \int\int \overline{\omega}^2 \mathrm{d}\overline{A} \tag{2.24}$$

where jet plume area A and vorticity are normalized by the factor $2V_\infty/d_j$ and A_j, respectively. This is a parameter in use to describe the change in integrated vorticity over the jet plume's area. Figure 2.20b and 2.20a show the evolution of the jet according to the level of swirl and downstream distance.

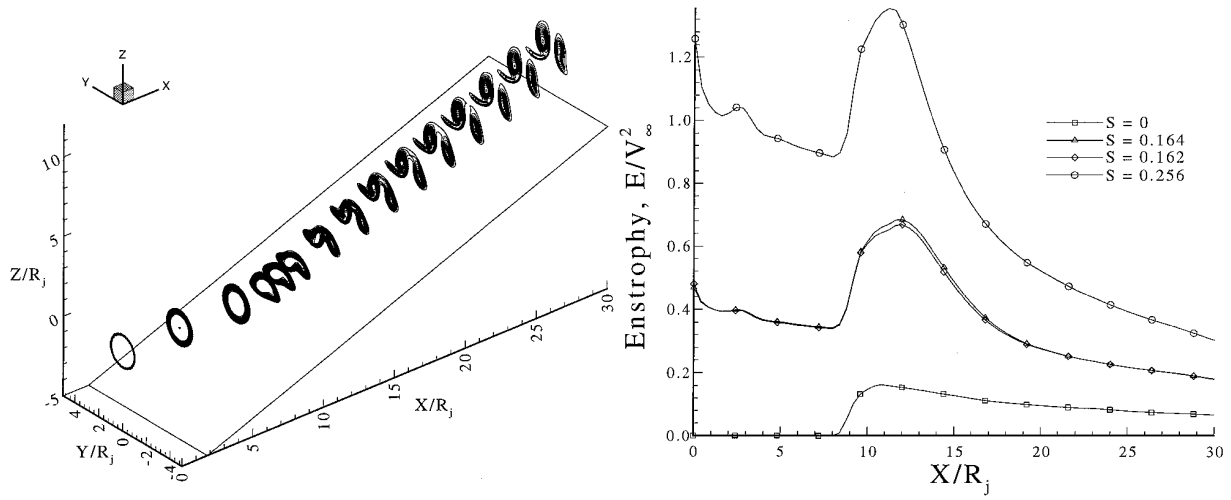

(a) Jet plume deformation

(b) Variation of enstrophy

Figure 2.20: Evolution of the jet plume area and enstrophy variation with increasing downstream distance. Courtesy of Nedungadi and Lewis (2000).

Figure 2.20a shows a qualitative view of the way the jet plume deforms as it propagates downstream. The jet in the figure is a swirling one. The cross-section maintains its symmetrical shape up until the position of the shock wave. There, it becomes elongated and more compressed on the right-hand side (due to its swirling direction). Given the baroclinic source of vorticity induced by the shock, the jet enters a regime whereby two counter-rotating streamwise vortices trail towards the outlet. This behaviour was also observed in the case of a non-swirling parallel jet, even though with lower intensity. The downstream behaviour thus remains asymmetric in nature. The addition of swirl proves to be beneficial for the parameter E: the enstrophy. Figure 2.20b shows the variation of such variable with increasing normalized downstream distance. Addition of swirl is clearly beneficial, highly increasing the maximum observed peak.

Needless to say that the counter-rotating vortex structure found by Nedungadi and Lewis (2000) is rather similar to the CVP formed by the injection of a jet in crossflow. Pourhashem et al. (2018) conducted an experiment to investigate the behaviour of the interaction of a bow shock wave with an incident vortex. A similar experiment had been conducted by Smart and Kalkhoran (1995). In that occasion, the authors generated a vortex by placing an upstream semi-wing. By placing the fin at an angle of attack, they were able to generate a vortex due to the fin itself being finite. By inclining the profile either at $\alpha = 5°$ and $\alpha = 10°$, they were able to generate two types of interactions: strong and weak. The shock was generated by placing a ramp into the stream. As the incident vortex crosses the oblique shock wave, it gets deflected upwards with the main stream. As the pressure in the vortex core is minimal, an attempt was made to predict where the point of minimum pressure would lie on the ramp itself. The point was found to lie where along a line directed towards the ramp from the point of contact with the shock directed at an angle of μ (the Mach angle) towards the ramp with respect to the deflected fluid. With regards to the differences between the weak and strong interactions, they can be found in mainly two aspects of the flow.

1. **Pressure on the ramp.** A weak interaction causes small and almost negligible pressure variations along the ramp, with a small dip observed in the region where the

low pressure hits the ramp. A strong interaction, instead, causes a major drop in pressure.

2. **The shock structure.** As the vortex hits the shock, two different patterns emerge at the point of contact. If, in fact, the weak interaction produces no visible change in the structure of the shock, the strong vortex does smear the shock in the proximity of the point of contact.

Nakamura et al. (2008) performed experimental studies on the jet in crossflow whose mixing properties are to be enhanced thanks to the presence of an incident oblique shock. Their goal was to investigate how the position of the incident shock could affect the combustion process by leading to better entrainment. Their experiment was further enhanced in Nakamura et al. (2009), where measurements were acquired with particle tracking velocimetry (PTV) technology. The oblique shock was created thanks to a shock generator mounted on movable arm on the upper guide wall of the tunnel. The qualitative difference between the cases where the oblique impinges either up- or downstream of the injector port are shown in Figure 2.21.

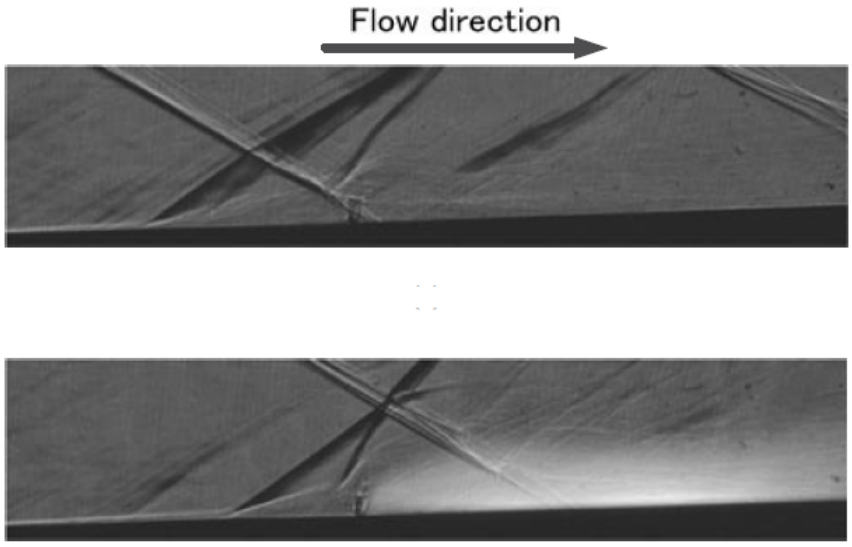

Figure 2.21: Schlieren chemiluminescent images displaying the situation where the oblique shock impinges upstream (top) and downstream (bottom) of the injection nozzle. Obtained from Nakamura et al. (2008).

The top image in Figure 2.21 shows how the incident oblique shock forms a structure similar to the one caused during the shock wave boundary interaction. The incident shock's foot is smeared in the vicinity of the jet exhaust an part of the shock is reflected at that location. The boundary layer separation zone upstream of the jet expands as compared to the jet with no shock scenario. Instead, by inspection of the bottom image, it is possible to observe how several phenomena occur. Amongst all, the chemiluminescent Schlieren technique highlights a large region of combustion just downstream of the jet port. This demonstrates that, as the shock impinges directly on the jet plume downstream of the injection it brings favourable properties for combustion. Ignition is, in fact, achieved right downstream of the port and flameholding was confirmed downstream. Furthermore, the bow shock appears to be quasi-normal at the injector's location, whereas for the upstream shock case it appeared to be more oblique in nature.

The reason for an accelerated ignition is twofold. First, as known from theory of inter-

actions between shock waves and boundary layers, the large and abrupt pressure jump caused by the shock results in a subsonic region towards the bottom of the boundary layer. This thus increases the average residence time of a fluid molecule in the region. This slows the fluid down and allows it to better mix with the surroundings. Moreover, the effect is also beneficial for the outer flow outside the wall layer, as it allows for further mixing due to the introduction of baroclinic vorticity.

The results by Nakamura et al. (2008) were confirmed and expanded upon by their successive work: Nakamura et al. (2009). Using particle tracking velocimetry techniques, the authors were also able to track the residence time of particles in the recirculation zone, which appeared to expand with increasingly downstream location of the shock. In particular, the residence time was defined as in Equation 2.25 as the ratio of the length of the re-circulation zone to the average speed of the fluid in such area.

$$\tau_{\mathrm{f}} = \frac{L}{u_{\mathrm{avg}}} \tag{2.25}$$

Figure 2.22 plots the average measured residence time versus the position of the incident shock.

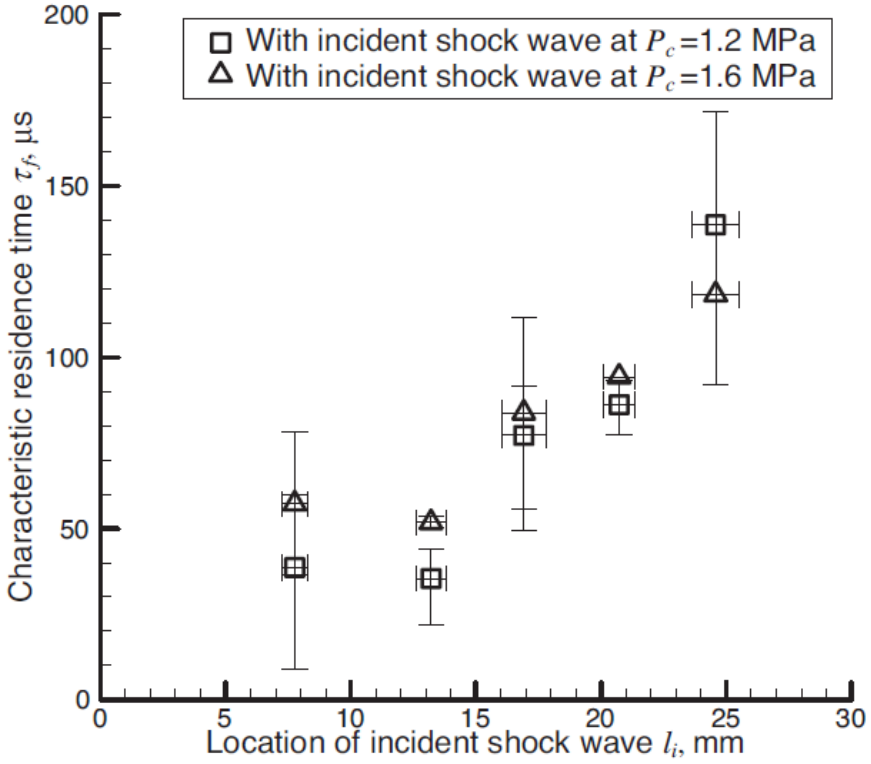

Figure 2.22: Plot of average fluid residence time in the re-circulation zone versus the shock position. Obtained from Nakamura et al. (2009).

An almost monotonic increase in residence time is observed as a function of increasing downstream position of the incident shock wave. As mentioned in the above, in fact, as the shock moves further downstream, the length of the downstream separation region increases. If the average convection speed of the flow remains roughly constant (which it does), then the residence time clearly increases. As the re-circulation zone is one where

vorticity and swirl are high, the flow has the opportunity to thoroughly mix with air and ignite.

As a combination of the studies of mixing enhancements by adding multiple ports and by using a shock wave, the study by Barzegar Gerdroodbary et al. (2015) analyzes the configuration where a cascade combustor design is enhanced by the presence of a shock wave. Figures 2.23a and 2.23b show some results of their study.

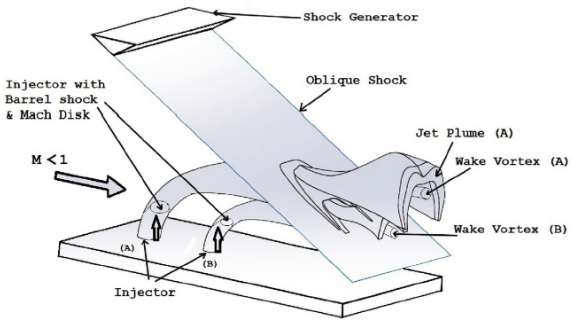

(a) Schematic of flow structures

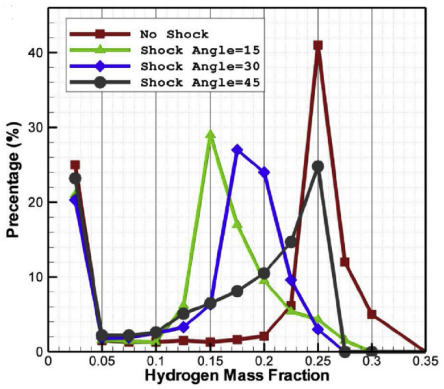

(b) Plot of mass distribution at $x/D = 80$

Figure 2.23: Visualizations of flow structures generated by the interaction of the jet plume and an incident oblique shock wave. Courtesy of Barzegar Gerdroodbary et al. (2015).

Figure 2.23a shows a schematic of the flow structures that generate upon interaction with an incident oblique shock wave. the development of the plume follows the standard process of transformation from a cylindrical vorticity tube to the CVP up until the plane of contact with the shock wave. There, the shock introduces a severe disturbance to the flow field, distorting and deforming the edges of the plume. The core of the CVP remains relatively intact, but the outer structure looses its shape. Figure 2.23b, instead, shows the mass distribution far downstream. the percentage scale indicates the relative fraction of unmixed fuel (in this case, hydrogen) over the total fluid mass at the given streamwise location. In particular, the scenario where no shock is introduced into the domain shows a sharp peak at about 40%, where the rest of the fluid mass is somewhat “untouched” by the mixing of hydrogen. The cases where the shock wave is inserted, though, show milder gradients and lower peaks. Shock-induced vorticity has indeed entrained the flow and enabled thorough mixing. thus, the conclusion can be drawn that entrainment sees a benefit as the shock angle increases, which makes the shock strength greater.

3

Experimental Methodology

Given the multiple parameters that play a role in the definition of the jet-shock-crossflow system, it is necessary to choose the most relevant parameters for testing beforehand. A reduced set of governing parameters will be chosen. The choice is reported in Table 3.1. The jet will be inserted into the test section by means a nozzle mounted flush with the lower wall of the chamber. The total pressure of the air source feeding the secondary flow can be varied to achieve the desired momentum flux ratio. A shock generator is then mounted on the top wall of the tunnel to generate the impinging oblique shocks. Initial runs were conducted with a set-up that did not allow for free positioning of the compression wedge. This caused the issue of not being able to position the shock wave at the same location for two different shock angles (corresponding to the two different flow deflections). Thus, the supports of the shock generators were re-designed to allow for arbitrary positioning.

Parameter	**Symbol**	**Value**	**Units**
Momentum flux ratio	J	1 - 2	[-]
Flow deflection angle	θ	9 - 12	[deg]
Shock strength	$\xi = p_2/p_1$	1.62 - 1.89	[-]
Shock position *	$x_{\text{shock}}/d_{\text{jet}}$	13 - 16	[-]

Table 3.1: Table reporting the chosen experimental control parameters and their range. The shock position value (*) refers to the shock impingement position on the bottom wall if the flow field were completely inviscid.

Two experimental test campaigns were set up and executed throughout the thesis project. The first had the goal to investigate the basic characteristics of the jet in cross-flow and its interaction with an incident oblique shock using simple flow measurement techniques. These consisted of Schlieren, shadowgraphy and oil flow visualization. The second experimental campaign was, instead, used to characterize the two-dimensional velocity field, together with an estimation of the out-of-plane velocity component. This was achieved by employing stereo particle image velocity. This second campaign entailed the imaging of two different planar loci. Wall-normal planes were imaged to gather insight into the plume penetration in elevation from the wall, the velocity field thereby formed and the development of shear layers as a result of the interaction with the incident OSW. Additionally, wall-parallel planes, shone a few [mm] off the bottom wall, provided information on the characteristics of the laterally expanding plume and the near-wall flow.

Table 3.2 summarizes the characteristics of both experimental campaigns conducted. Specifically, it recaps their goal, the techniques in use and the variables each one of them

provided as “output”.

Campaign	Objective	Techniques	Output
1	Obtain an understanding of the effect of control variables	Schlieren, shadowgraphy, oil flow visualization	General flow field, separation zones, Mach disk position, barrel shock shape
2	Full quantification of the interaction field	Stereo PIV	$u, v, w, \omega_z, \nabla \cdot V, TKE$, $R_{\varphi\varphi}$, $\tau, l_{\text{separation}}$, vortex structures, mean flow

Table 3.2: Table reporting the outlook on both experimental campaigns.

The test matrices executed for each test campaign are presented in Appendix B. It is necessary to mention that the variables listed in Table 3.2 refer to the ones that can be obtained both directly and indirectly (i.e. with further processing required). For instance, vorticity and circulation are not a direct output of PIV measurements, but rather a variable which results from a differential mapping of the velocity field.

3.1. ST-15

All experimental campaigns were conducted in the ST-15 supersonic facility at the Aerospace Engineering laboratory of the Faculty of Aerospace Engineering at Delft University of Technology. ST-15 is a blow-down wind tunnel. It is fed air from a high-pressure reservoir and can achieve Mach numbers all the way between the transonic regime to Mach 3, depending on the geometric profile of the guide walls. The external reservoir holds approximately 40 [atm] of air, with each run using between 0.5 and 1.5 [atm], depending on runtime. Therefore, the number of runs to be executed in a single day is more limited by the turn-around time between one run and the next than by the available air pressure in the reservoir. The main flow parameters in use for all runs are listed in Table 3.3.

Parameter	Symbol	Value	Units
Total pressure	p_0	2	[bar]
Total temperature	T_0	290	[K]
Mach number	M_∞	2	[-]
Jet Reynolds number	Re_{jet}	59,323	[-]
Jet diameter	d_{jet}	4	[mm]
Jet Mach number	M_{jet}	1	[-]
Jet total temperature	$T_{0,\text{jet}}$	295	[K]
Boundary layer thickness	δ_0	5	[mm]

Table 3.3: Table specifying the main test conditions in ST-15.

Figure 3.1 shows a cross-section view of the facility. Air blowing down from the high-pressure tank enters the facility from the left-hand side, where the arrow is present. The settling chamber (station 1) receives and stabilizes the flow before the test section contraction. Here, a gauge measures total pressure. In the case a PIV system is in place, the seeder hose is connected to the bottom wall of this segment of the tunnel and a particles are injected via a seeding rake placed in the chamber. Air then is accelerated through the

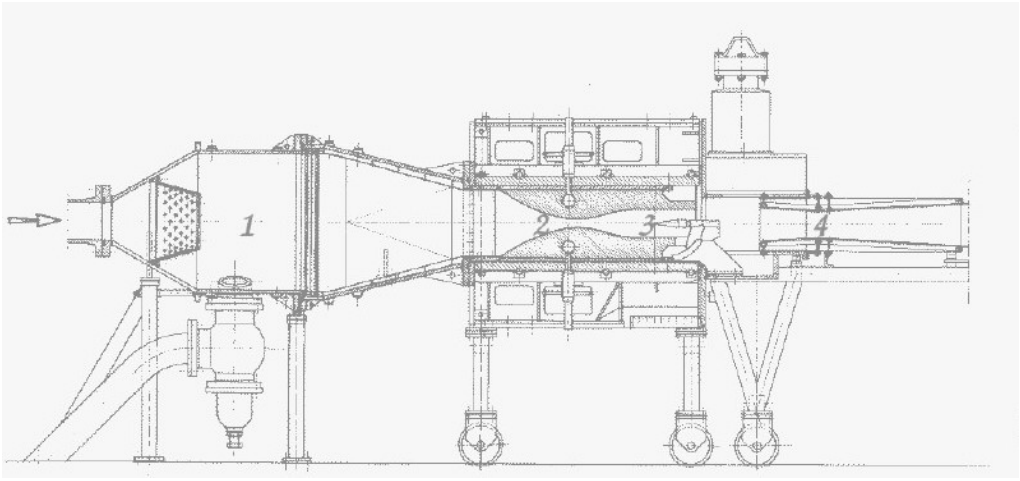

Figure 3.1: View of a streamwise cross-section of the ST-15 supersonic experimental facility.

converging portion of the nozzle (station 2), upon termination of which the flow becomes sonic in the throat.

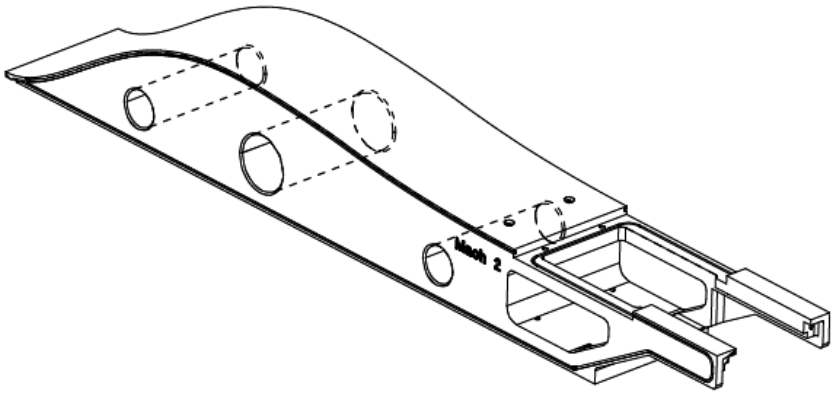

Figure 3.2: Bottom guide wall of the Mach-2 laval nozzle in use for testing

The diverging section of the nozzle allows for geometrical achievement of the test Mach number, which is reached at station 3, which is also where the model is installed. For the tests described in the foregoing at $M_\infty = 2$, the upper guide wall is equipped with slots supporting the mounting of shock generators. The bottom liner (shown in Figure 3.2), instead, features the possibility to install a multi-purpose plate which, for the testing described in this work, accommodates the nozzle of the transverse jet. More details on these parts will follow in Section 3.2. Finally, the accelerated air is diffused to atmospheric conditions after station 4. Figure 3.3 shows the tunnel with parts labeled.

3.2. Wind tunnel set-up

This section illustrates in detail the design of the model test set-up and the various components. As the goal of this research project project is to study the interaction between a secondary jet in crossflow and an incident oblique shock, the two main assemblies in the test section have the goal to re-create each of the two flow features: the shock and the jet.

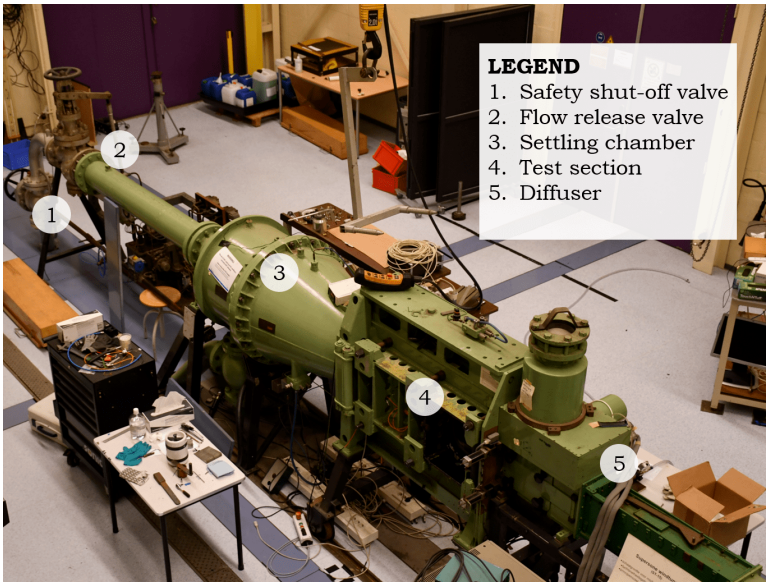

Figure 3.3: Photograph illustrating ST-15.

The nozzle generating the actual jet in crossflow is mounted to the multi-purpose plate mentioned above, where the test section Mach number is geometrically expanded to $M_\infty = 2$, see Figure 3.4.

Figure 3.4: Photograph showing the Mach-2 converging-diverging nozzle with the position of the jet nozzle highlighted in red.

3.2.1. Secondary injector

Figure 3.5 displays a schematic of the injector assembly along with its piping, designed and manufactured during the research work conducted by Pazhev (2020).

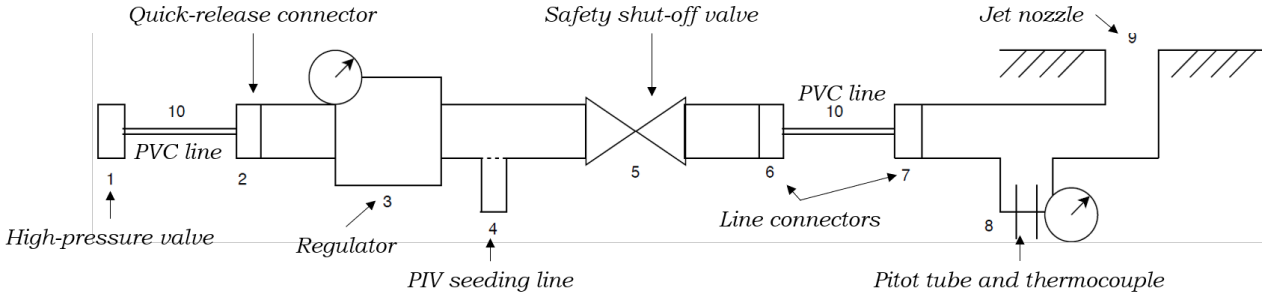

Figure 3.5: Assembly of the injector assembly. See text below for label description.

The schematic shows all of the components which the injection systems consists of. Starting from the left-hand side of the diagram (1), air is fed into the system via a high-pressure valve. High-pressure air is then connected to the first of two assemblies in the system (the upstream one) through a PVC hose (10), which latches onto a quick release mechanism (2). The total pressure in the system is manually set thanks to the gauge-equipped regulator (3). Each combination of jet Mach number and momentum flux ratio requires a specific total pressure. In case a PIV system is used, tracer particles are injected into the system via a secondary hose (4). For safety purposes, a shut-off valve is incorporated in the upstream assembly (5). The two assemblies are connected with a PVC hose between points 6 and 7. A thermocouple and a Pitot tube (8) are connected to the downstream assembly, just upstream of the 90-degree bend exhausting into the cross stream (9). The sonic nozzle's profile, along with the specification of other components of the test set-up, are provided in Appendix A. The installation of the system requires the upstream assembly to be located outside the tunnel (as shown in Figure 3.6a), whereas the downstream one inside of it, right below the nozzle plate (see Figure 3.6b).

(a) Upstream assembly (pressure regulator, PIV seeding line and safety shut-off valve).

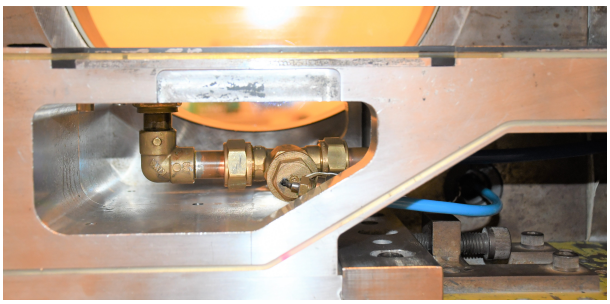

(b) Downstream assembly (thermocouple and Pitot tube and sonic nozzle).

Figure 3.6: Photographs of both parts in the injection system installed for operation in ST-15.

The air feed lines have dedicated insertion slots to the interior of the test section. Air gets fed from the upstream to the downstream assembly through a line which enters a 90-degree connector located on the side wall of the tunnel diffuser. From there, another line reaches to the downstream assembly, which is connected underneath the injection

plate. A third and final line exits the test section through a flexible hole in the side door of the tunnel. This is the feed line connecting to the pressure transducer for the Pitot tube.

Technical drawings of the components in use for the measurements are presented in Appendix A. Upon completion of the first experimental run, some modifications were performed. With regards to the plate and its nozzle, this translated to ensuring that the nozzle plane was flush with the plate itself. Oil flow visualizations show, in fact, perturbations in the near-wall flow. This is caused by the fact that the plate design was created to allow for quick replacement of the nozzle by screwing it into the plate itself. To solve the issue, as it was decided to only perform measurements with the sonic nozzle, it was established to thoroughly tighten the nozzle to the plate to render it as flush as possible with the bottom guide wall. The microscopic gaps between the plug and the threading are going to be filled with resin to make the system airtight and create a smooth wall which air can flow over.

3.2.2. Shock generator

The shock generator is a simple wedge-like ramps that is installed and tightened to the upper guide wall of the wind tunnel, as illustrated in Figure 3.7.

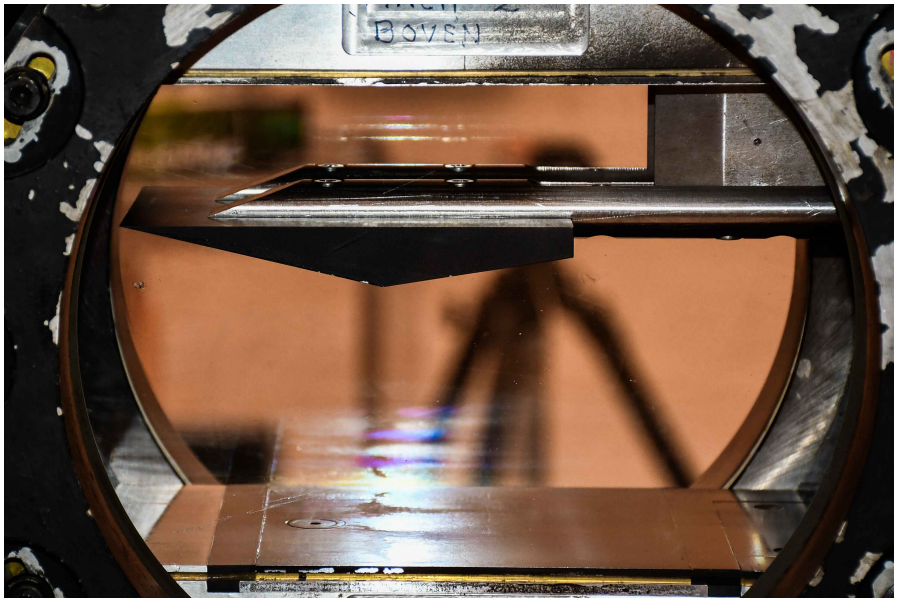

Figure 3.7: Shock generator for $\theta = 12$ deg installed in ST-15's test section along the upper guide wall.

The figure also shows how the shock generator is mounted to the upper liner by means of two parallel pylons which themselves connect to cylindrical support rods extending upstream. The pylon and connector allow for two streamwise positions, depending on the relative bolt positioning. This effectively introduced a slight offset in the results of the first experimental campaign. Different positions are also obtainable by shifting the location of the bolts at the point of attachment to the upper guide wall, where the pylons meet the liner. There, a total of eight bolt holes are present, which effectively allow for two different streamwise positions. For the present studies, though, only the most upstream position was selected, as the other position would have led the shock to impinge too far downstream.

Given the two different shock angles induced by the two different deflection angles imposed by the two ramps, the inviscid shock impingement location was different for either case. This means that a direct comparison cannot be drawn between the runs with varying

shock angle, as their impingement location will differ every time. Ultimately, this was the factor which called for a re-design of the struts supporting the wedges. The new design allows the supports to slide such that a precise positioning of the shock generators can be achieved. It is shown in Figure 3.8.

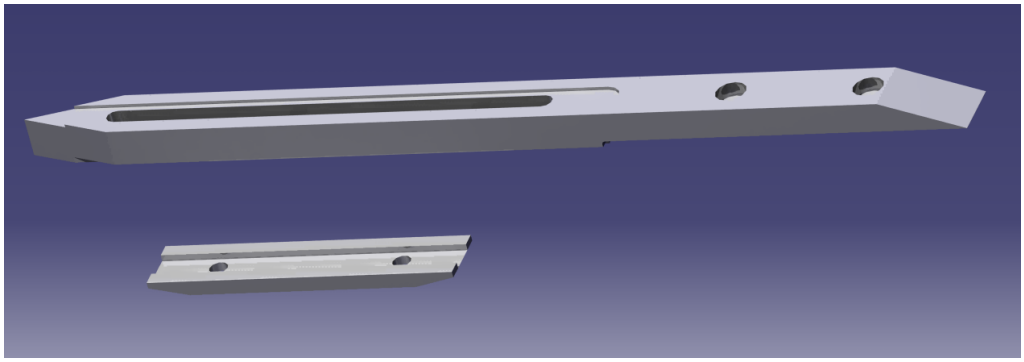

Figure 3.8: Rendering from CATIA V5 displaying the newly manufactured supports for the shock generators.

The requirements behind the design of the new supports were several.

- To allow for an inviscid shock impingement position ranging from 10 x/d_{jet} to 16 x/d_{jet} for both shock flow deflection angles taken into consideration: $\theta = 9\,\text{deg}$ and $\theta = 12\,\text{deg}$.
- To ensure sufficient stiffness during tunnel start-up and shutdown, which are the most unsteady moments of a run.
- To avoid blunt angles exposed to the flow: to avoid the formation of a detached shock in the vicinity of the strut. This translates to $\theta_{\text{max}} \leq \theta_{\text{detached}}$.
- To be compatible with the current shock generators and the same bolts in use for the old design.

The old design for the supports featured four holes drilled into the supports which effectively only allowed for two different positions of the shock generator. As the shock angles are different, there was no way to make the shock hit at the position on the bottom wall. Thus, the new design features a slot running through part of the length of the strut to make sure the support's position can be accurately tailored. As the long slot is estimated to cause a decrease in the bending stiffness of the design due to a reduced second moment of area, a slider was added to the design, shown in the bottom-left portion of Figure 3.8. This particular feature was added with the intention of providing extra lateral structural integrity to the strut. The bolt holes are spaced so to accommodate the two bolts holding the strut to the pylons attached to the upper wall.

The combination of transverse jet and shock generator is expected to produce a flow field rich with both inviscid and viscous flow phenomena. Figure 3.9 shows a schematic of it. Starting from the top-left corner of Figure 3.9, several flow features are expected to be visible in the experimental runs. The shock generator will induce an oblique shock directed towards the bottom guide wall of the tunnel, together with an expansion fan at its trailing edge. Along its way, it will meet and interact with the bow shock created by the jet itself. In fact, acting the jet as an obstacle, the flow will adapt by creating a bow shock wave upstream of the barrel shock. This last feature refers to a discontinuity which envelopes the

jet flow just outside its exit and terminates with the Mach disk. Both up- and downstream of the barrel shock, two recirculation zones will appear. The upstream one is caused by the interaction of the normal shock with the boundary layer, which causes a pressure rise through the subsonic portion of the wall layer. The downstream one, instead, is induced by the high curvature of streamlines behind the barrel shock. Finally, a last separation zone is visible as a result of the interaction of the incident shock with the boundary layer. If the interaction is strong enough, then the velocity layer will separate. A reflected shock is produced from weak compression wave coalescing into a stronger discontinuity due to the "bump" caused by the interaction.

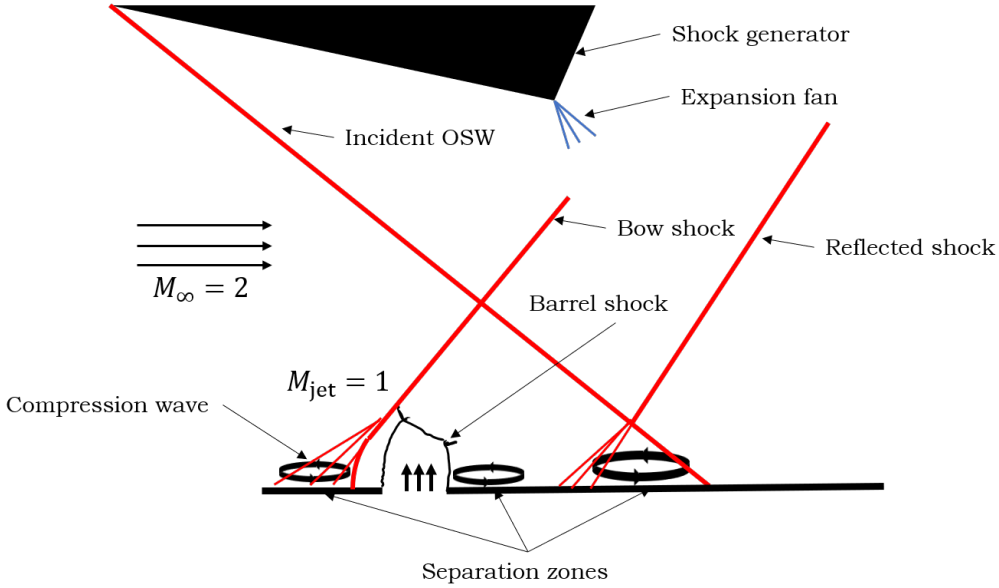

Figure 3.9: Schematic of the flow field generated by the presence of both a transverse jet and an incident oblique shock wave. Similar to the field studied by Nakamura et al. (2009).

3.2.3. Influence of the set-up on the flow

Figure 3.10 shows flow discontinuities created within the test section by the experimental set-up itself. These are not induced by the interaction with the jet nor by willingly installed shock generators. They are simply due to deflection angle changes caused by the installation of the tunnel liners and their inserts.

Ignoring, for the moment, imperfections on optical access windows, several compression waves are visible in the field. The Schlieren knife-edge filter was oriented vertically with the obstruction on the left-hand side (as seen from the perspective of the incoming light ray). Compression waves will thus appear as dark streaks, whereas expansion fans will result white. The two main perturbing features are the two shocks generated in the bottom left corner of the test sections. The fastening insert at that location induces a slight change in elevation of the test section's lower wall. Thus, effectively, a deflection angle results. The first shock is followed by a brief expansion as the elevation is brought back to the baseline level, finally closed by a compression wave as the flow re-aligns with the wall. Another, but weaker, shock enters the flow field after being generated along the upper guide wall. This was caused by imperfectly closed screw holes along such liner. At the downstream end of the figure, two expansion-compression features appear. Again, these are generated by the fastening insert (at the downstream edge of the jet's plate). Finally,

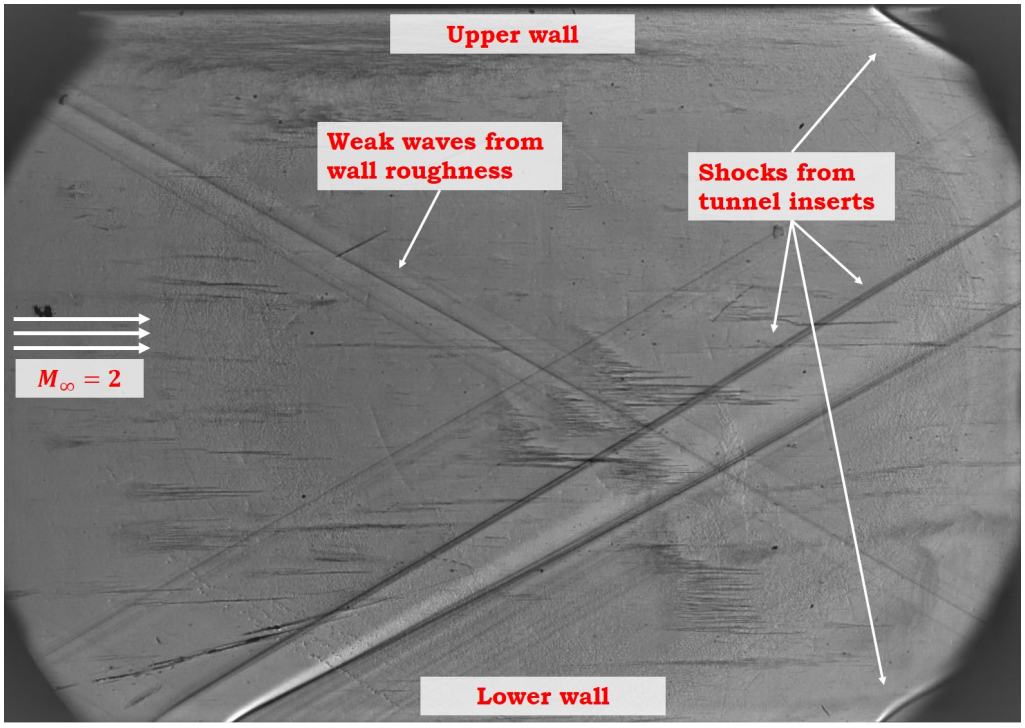

Figure 3.10: Schlieren image of test section without oblique shock and with jet deactivated. Acquired with a focal length of $f = 200$ [mm]

.

several rather weak compression waves are seen all throughout the field and are caused by imperceptible imperfection and/or roughness along the upper and lower liners.

3.3. Coordinate System

The coordinate system in use for all experimental campaigns is a Cartesian right-handed one. Its origin is centred at the jet exit. With the x-axis pointing in the downstream direction and the y-axis pointing away from the jet, the z-axis completes the system by pointing in the direction of the port window of the tunnel. The system is shown in Figure 3.11. The z-axis is directed towards the reader. As mentioned in the above, the positive direction of the z-axis will also be referred to as the port side and the negative one as starboard.

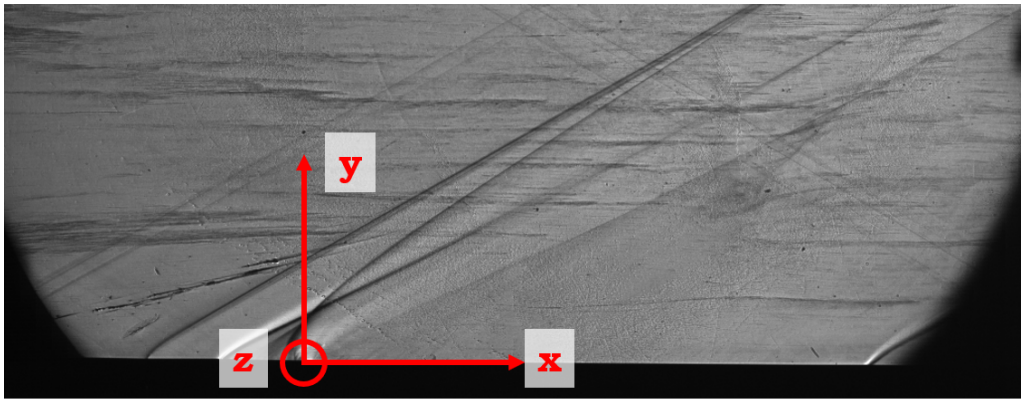

Figure 3.11: Coordinate system for the jet in crossflow flow case

4

Measurement Techniques

This chapter contains detailed information about the measurement set-up that was selected and employed throughout the two experimental test campaigns. As mentioned in previous chapters, it was decided to split the measurement challenges in two different campaigns, each one having the goal to measure different aspects of the flow and employing different measurement techniques.

4.1. Line of sight techniques

Schlieren and shadowgraphy were employed to visualize the flow field and shock waves in the test section. A schematic of the configuration is shown in Figure 4.1. It consists of a Z-type system, with a LED light as a source and Photron Fastcam as the acquisition device. The Z-type Schlieren configuration is already installed an tuned into ST-15's shop, with the exception of the various lenses along the light path, the light source and, of course, the camera system. The configuration can also be switched to shadowgraph mode as the knife-edge is removed and the camera lens brought out of focus from the test section's mid-plane, as mentioned in the review work by Settles and Hargather (2017).

Before delving into the specifics of the Schlieren system installed in ST-15, it is necessary to backtrack and explain the working principle of this imaging technology. Understanding it can shed more light onto the observations. Most of the discussion that follows is based on the work of Settles (2001). In general, Schlieren and shadowgraphy exploit the laws of refraction. As an electromagnetic waves crosses interfaces between media having different densities, it undergoes an angular deflection which is proportional to the change in the *index of refraction* (n), defined as in Equation 4.1.

$$n = \frac{c}{v} \tag{4.1}$$

where c is the speed of light in vacuum and v the speed of light in the local medium. As mentioned above, n changes with the density of the medium. Its change is governed by the Gladstone-Dale relation (Equation 4.2).

$$n = 1 + K\rho \tag{4.2}$$

being K the Gladstone-Dale constant ($K_{\text{air}} = 2.25\ [m^3/kg]$). To get more valuable results, it is necessary here to introduce one of the most fundamental laws in optics: the ray equation: Equation 4.3.

$$\frac{\partial}{\partial s}\left(n\frac{\partial x}{\partial s}\right) = \nabla n \tag{4.3}$$

The ray equation describes the variation the light beam undergoes depending on the local refraction index variation. In particular, it shows how the alteration of the light path is proportional to the gradient of the refraction index and, thus, the density. This means that any light beam will curve into a region of higher density and away from a more rarefied field. For the case in consideration, meaning density variations caused by compressible flow features, the light will only undergo a deviation inside the test section. Referring back to the ray equation, assuming unit n ($n_{\text{air}} = 1.000273$) and small displacement ($\mathrm{d}s = \mathrm{d}z$), it is possible to write Equation 4.4. It holds as light is only refracted inside the test section (thus along the z-axis) having a finite width W,

$$\varepsilon_x = \frac{\partial x}{\partial z} = \int_0^W \frac{\partial n}{\partial x}\mathrm{d}z = K\int_0^W \frac{\partial \rho}{\partial x}\mathrm{d}z \tag{4.4}$$

where ε (in this context) is the displacement of the light ray and the Gladstone-Dale equation was substituted in place of the refraction index. For a shadowgraph system in a one-dimensional context, the light intensity is measured as in Equation 4.5, where x and y are the coordinates normal to the direction of propagation of light (z).

$$\frac{\Delta I}{I_0} = LK\int_0^W \left(\frac{\partial^2 \rho}{\partial x^2} + \frac{\partial^2 \rho}{\partial y^2}\right)\mathrm{d}z \tag{4.5}$$

Equation 4.5 reveals the actual nature of shadowgraph measurements, which corresponds to the measurement of the two-dimensional scalar Laplacian. The measurement therefore does not contain any directional indication whatsoever. Additionally, the second derivative is integrated over the width of the test section. A shock wave in a shadowgraphy image is going to appear a bright light strip followed by a dark one. For a Schlieren image, instead, the observation is going to be rather different. In fact, instead of light concentrating where the second derivative of density is the greatest, the knife-edge filter will block part of light on its way to reach the sensor. The filter will also have the consequence of making the Schlieren images darker compared to the shadowgraph ones, due to less light being able to reach the camera sensor. Regarding quantification of this effect, it is possible to define of light that bypasses the obstruction to the total amount of light, simply based the geometrical area of the filter exposed to light. Being a the area of the knife-edge open to light and d the added deflection along the light path, it is possible to write the following

$$\frac{I}{I_0} = \frac{a+d}{a} = 1 + \frac{f\varepsilon_y}{a} \tag{4.6}$$

where f is the focal length, the distance between the filter and the sensor. Then, the variation of light intensity, analogously to Equation 4.5 is given by,

$$\frac{\Delta I}{I_0} = \frac{f\varepsilon_y}{a} = \frac{f}{a}\int_0^W \frac{\partial n}{\partial y}\mathrm{d}z = \frac{fK}{a}\int_0^W \frac{\partial \rho}{\partial y}\mathrm{d}z \tag{4.7}$$

Schlieren images thus measure the integral through the test section width of the derivative of density, thus providing some directional insight as to the direction of intensifying and rarefying flow. Depending on the orientation of the dark half of the knife-edge filter, shocks will either appear as bright or dark stripes. Keeping in mind that light deflects towards region of higher density, in the present study the dark half of the knife-edge is

placed on the right-hand side of the sensor, with air moving from left to right of the images. Thus, shocks will appear as dark areas, whereas expansion fans will seems brighter.

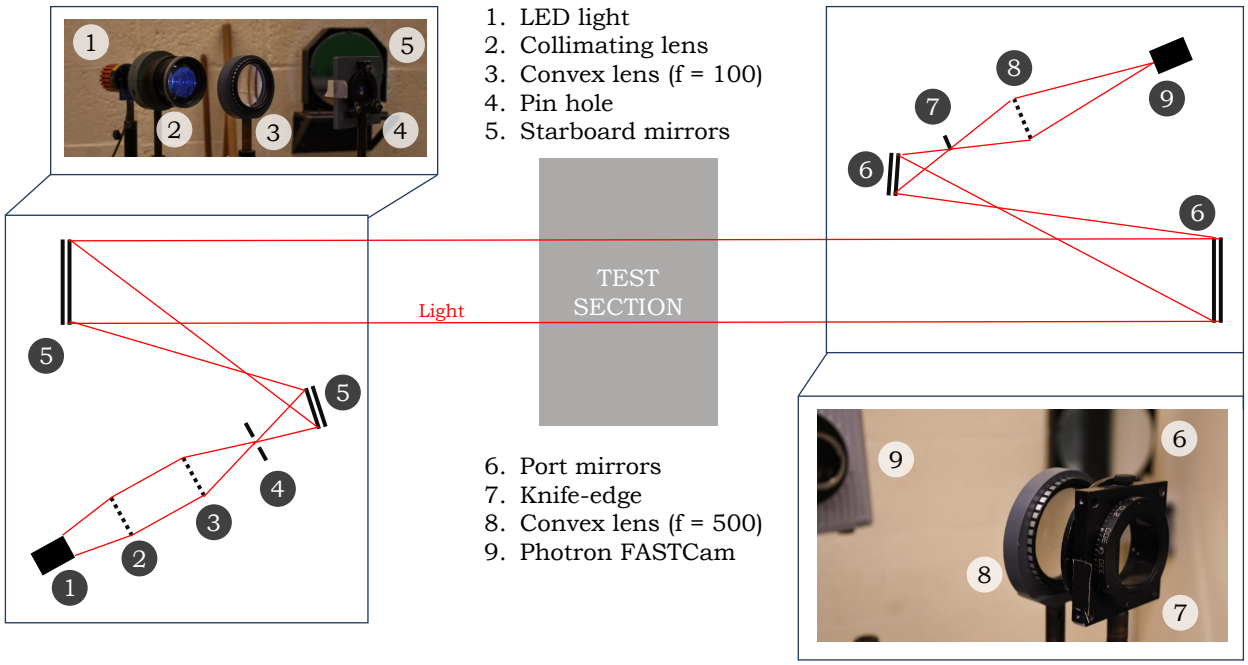

Figure 4.1: Schematic of the Schlieren in the Z-configuration with all of its component labelled.

#	Item	Description
1	Light source	LED THORLBAS MCWHLP1: 405 [nm] light, 1200 [mW] power, THORLABS-LEDD1B controller
2	Collimating lens	F2.5 f = 178 [mm]
3	Convex lens	f = 150 [mm]
5,6	Mirrors	Parabolic mirrors parallel to the test section
8	Convex lens	Variable focal length. Selected f = 500 [mm] for most runs
9	Camera	Photron Fastcam SA1.1

Table 4.1: Detailed list of equipment in use for Schlieren photography

Table 4.1 shows the specifications of each component chosen for the Schlieren and shadowgraphy measurements. The way the imaging system was switched from shadowgraphy mode to Schlieren mode and viceversa was by removing the knife-edge filter and de-focusing the camera such that the new plane of focus would be between 10 and 20 [mm] away from the centre line of the test section.

4.2. Oil flow visualization

As a mean to gather additional information into the behaviour of the flow near the wall and the formation of near-wall structures, oil flow visualization comes in with proven capabilities to obtain a (mostly) qualitative understanding of the flow.

The technique relies on the application of a thin layer of oil onto the surface of interest. The air flow will exert a friction force on the interface between it and the oil layer, which will

cause the oil to move along with it. However, as the viscosity of the oil is high, its Reynolds number brings the oil to flow in Stokes regime, meaning viscous forces are considerably higher than inertial ones, which are now negligible. The velocity profile within the oil layer will be linear, resulting in *Couette flow* (Equation 4.8 and Figure 4.2[1]).

$$\tau_{\text{wall}} = \mu_{\text{oil}} \left(\frac{\partial u_{\text{oil}}}{\partial y} \right)_{y=0} = \mu_{\text{oil}} \cdot k = \tau_{\text{interface}} \tag{4.8}$$

with k being the constant value of the velocity gradient.

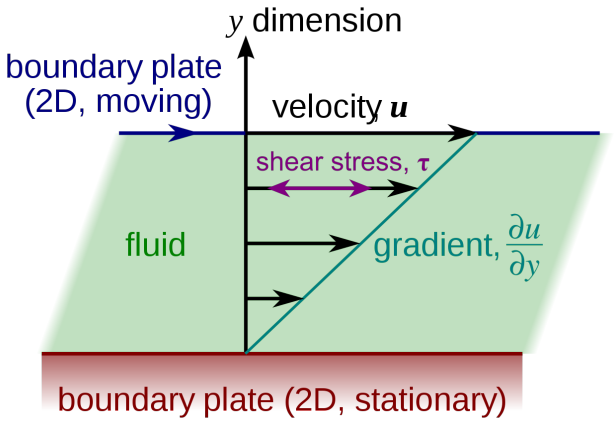

Figure 4.2: Schematic representation of Couette flow.

Shifting the attention towards the interface between air and oil, it is possible to write the friction that the air exterts on the oil as

$$\tau_{\text{interface}} = \mu_{\text{air}} \left(\frac{\partial u_{\text{air}}}{\partial y} \right)_{y=\delta_{\text{oil}}} = \mu_{\text{oil}} \cdot k \tag{4.9}$$

or,

$$\left(\frac{\partial u_{\text{air}}}{\partial y} \right)_{y=\delta_{\text{oil}}} = \frac{\mu_{\text{oil}}}{\mu_{\text{air}}} \cdot k \tag{4.10}$$

where δ_{oil} is the thickness of the oil layer. In the Stokes regime, as the prevailing term is the viscous one, it is possible to ignore the contribution of the inertial terms in the Navier-Stokes equations, such that the pressure gradient is only balanced by the viscous term, as shown below.

$$\nabla p = \mu \nabla^2 \mathbf{u} \tag{4.11}$$

Following the work of Merzkirch (1987) paraphrasing the analysis of Squire (1961), the velocity of oil at the interface is given by Equation 4.12.

$$u_{\text{oil}}(y = \delta_{\text{oil}}) = \frac{\mu_{\text{air}}}{\mu_{\text{oil}}} \left(-\frac{\delta_{\text{oil}}^2}{2\mu_{\text{air}}} \frac{\partial p}{\partial x} + \delta_{\text{oil}} \left(\frac{\partial u_{\text{air}}}{\partial y} \right)_{y=\delta_{\text{oil}}} \right) \tag{4.12}$$

As the thickness of the oil layer is considered to be small, together with the ratio of viscosities, the oil velocity is small as well. A word of caution needs to be mentioned, though,

[1]Obtained from `https://en.wikipedia.org/wiki/Couette_flow#/media/File:Laminar_shear.svg` on 14/09/2020

as this analysis holds for relatively small pressure gradients. Thus, near separation, the oil pattern needs to be interpreted with caution. The more recent work by Yang (2001) suggests, instead, that oil can be quite accurate in tracking the presence of separation and re-attachment regions.

In the context of the present work, the oil applied to the surface of the wind tunnel is mixed with titanium dioxide particles (TiO_2) and has a white colour. The procedure for measurement and testing is as follows.

1. The oil-particles mixture is pre-mixed for approximately 30 minutes before application onto the tunnel guide wall.
2. A thin uniform layer of oil is manually applied onto the surface of interest.
3. The tunnel is run for 10 [s].
4. Upon termination of run, the resulting oil patterns are photographed with a reflex camera (Nikon D7500).
5. Pictures are post-processed to compensate for eventual perspective error and contrast.

The results of the oil measurements are presented in Chapter 5.

4.3. Particle Image Velocimetry

It is clear that the flow field resulting from the interaction of a sonic jet with a supersonic crossflow is highly three-dimensional in nature (see Chapter 2). Thus, a simple planar imaging technique might fail in the attempt to capture all relevant flow phenomena. In the realm of particle image velocimetry, one should turn to the employment of 3C-techniques. Ideally, also given the unsteady nature of the interaction, having a technique enabling the measurement of both space and time components (4C-PIV) would be desired. Tomographic time-resolved measurements would provide exhaustive information about the interaction, yet hardware availability and the complexity of the technique rule this option out, along with a significant time delay that would be introduced on the project.

Stereo PIV, instead, is seen as a feasible and complete enough measurement technique to gather the necessary information. In particular, it is though that this can be achieved by combining information present on multiple imaging planes. Both streamwise wall-normal and wall-parallel planes are going to be imaged during the experimental campaign. In particular:

- $\mathbf{z/d_{jet}} = 0$. This is the symmetry plane of the test section: it "cuts" the jet orifice through its centre line, extending both up- and downstream.
- $\mathbf{z/d_{jet}} = 2$. Just as the previous plane, this too is a wall-normal locus, but shifted off the centre line by two jet diameters. The reason for this offset will be clarified in Chapter 5.
- $\mathbf{y/d_{jet}} = 1$. Right at the edge of the incoming boundary layer, this wall-parallel plane will have the goal to capture the evolution of the jet plume in the spanwise direction.
- $\mathbf{y/d_{jet}} = 2$. With the same purpose as the previous plane, this location is believed to enclose more information about the mid-to-far-field mixing mechanisms and the results of the interaction with the incident oblique shock wave.

For both configurations (wall-normal and wall-parallel), the list of equipment is provided in Table 4.2.

Item	Quantity	Details
CMOS cameras	2x	LaVision imager sCMOS.
Laser	1x	EverGreen laser. $\lambda = 532$ [nm]
Programmable Timing Unit	1x	LaVision PTU
Camera lenses	2x	Nikkor 105 [mm] and 60 [mm]
Scheimpflug adapters	2x	Single-axis adapters
Acquisition machine	1x	Running DaVis v8.4
Seeders	2x	1x for settling chamber and 1x for jet

Table 4.2: List of equipment in use for the PIV experiments. Valid for both wall-normal and wall-parallel.

Of particular interest due to their direct effect on the PIV measurement and its setup are the characteristics of the cameras in use. Table 4.3 reports the most relevant features of the imagers and the lenses. The data of the camera was taken from LaVision's technical specifications [2].

LaVision Imager sCMOS		
Property	**Symbol**	**Value**
Resolution	r	2560 x 2160 [pix]
Pixel size	l_{pix}	6.5 x 6.5 [μm]
Frame rate	f_{im}	50 [Hz]
Exposure time	t_{im}	15 [mics] - 100 [ms]
Digital output	-	16 [bit]
Lenses		
Property	**Symbol**	**Value (f105 / f60)**
Focal length	f	105 [mm] / 60 [mm]
Aperture range	$f_{\#,\text{min}} - f_{\#,\text{max}}$	2.4-32 / 2.8-32

Table 4.3: Table reporting technical specifications of imaging equipment.

4.3.1. Governing parameters

The tuning of the single parameters to ensure good quality of the measurements is governed by several relations. First and foremost, it is necessary to introduce the definition of some fundamental parameters. The geometrical features of any thin lens are governed by the *thin lens equation* (Equation 4.13).

$$\frac{1}{f} = \frac{1}{d_o} + \frac{1}{d_i} \tag{4.13}$$

where the image distance d_i is defined as the distance between the lens and the sensor and d_o the one between the lens and the imaged subject (see Figure 4.3 [3]).

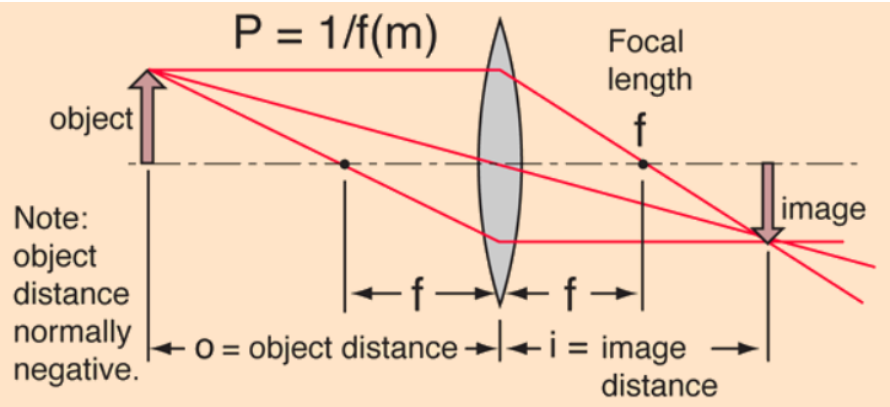

Figure 4.3: Schematic illustrating graphically the definitions of object and image distances.

Then, it is possible to introduce the *magnification factor*: the ratio of the image distance to the object distance. Alternatively, due to geometric considerations and by the definition

[2] https://www.lavision.de/en/products/cameras/cameras-for-piv/. Last accessed on 22/11/2020.
[3] http://hyperphysics.phy-astr.gsu.edu/hbase/geoopt/lenseq.html. Last accessed on 23/11/2020.

of the distances, it is possible to re-write the definition as the ratio of the size of the field of view to the size of the sensor. Both versions are presented in Equation 4.14.

$$\overline{M} = \frac{d_i}{d_o} = \frac{N_{\text{pix}} l_{\text{pix}}}{l_{\text{fov}}} \tag{4.14}$$

where l_{fov} is the size of the desired field of view. In the context of the design of a PIV experiment, the size of the field of view is known. Upon selection of the desired lens (thus the focal length), the thin lens equation only allows for one resulting image distance, which corresponds to the distance from the imaging plane where the camera should be positioned. Of course, when the time comes to actually install the equipment, hardware limitations will impose further restrictions. This means that the precise object distance will not be enforced precisely. However, a correction can be applied with the focus ring integrated on the lens itself. The focus characteristics of the imager also depend on the f-stop: the ratio between the focal length and the camera's diaphragm aperture (Equation 4.15).

$$f_\# = \frac{f}{d_{\text{lens}}} \tag{4.15}$$

where d_{lens} is the aperture of the diaphragm. The higher the f-stop, in fact, the higher the depth of field (or focal depth) δz, as expressed in Equation 4.16.

$$\delta z = 4.88 \lambda f_\#^2 \left(\frac{\overline{M} + 1}{\overline{M}} \right)^2 \tag{4.16}$$

For the purposes of a PIV set-up, it is essential for the focal depth to be at least equal to the thickness of the laser sheet, to ensure that all particles within the field of view. This poses the first of three requirements on the definition of the required f-stop. The second property that the aperture needs to ensure is, of course, that there is enough light reaching the sensor to avoid under-exposing the images. However, given the high power of the laser and the active image corrections performed in real time by the acquisition software DaVis, this is deemed not critical. The final condition that needs to be met, though, requires more attention: the particle image diameter. As the aperture is relatively small, diffraction comes into play, limiting the particle diameter to the expression in Equation 4.17.

$$d_{\text{diff}} = 2.44 \lambda (1 + \overline{M}) f_\# \tag{4.17}$$

Additionally, the geometrically imaged particle diameter is equal to $d_{\text{geom}} = \overline{M} d_{\text{p}}$, with d_{p} being the physical particle diameter. An approximation to the particle image diameter (d_τ) can then be found in Equation 4.18.

$$d_\tau = \sqrt{d_{\text{geom}}^2 + d_{\text{diff}}^2} = \sqrt{(\overline{M} d_{\text{p}})^2 + d_{\text{diff}}^2} \tag{4.18}$$

If a particle is imaged to be smaller than the size of the single pixel, then peak locking errors can occur. This results from a situation where the particle does not move enough within the image plane and is captured by the same pixel in both counterparts of the same pair, leading to a virtually null displacement. Ideally, then, one would aim at imaging a particle to be 2-3 pixel wide. To enforce this condition, Equation 4.18 can be used, imposing $d_\tau > 3 l_{\text{pix}}$. By comparing the three requirements for the f-stop setting and selecting the most critical one, it was found that $f_\# \geq 10.5$ which, given the specific lenses, resulted in $\mathbf{f_\# = 11}$.

The last parameter that needs to be tuned is the time separation between laser pulses which, in return, determines the time interval between images in a pair. In general, one should abide by the "quarter rule": select a dt such that the displacement does not exceed one quarter of the interrogation window size in processing. Upon conversation with the experimental supervisor and experience with the tunnel configuration, it was decided to select the time separation based on the notion that the particle's average displacement should be about 12 pixels (see Equation 4.19).

$$\mathrm{d}t = \frac{s_{\mathrm{pix}} l_{\mathrm{pix}} / \overline{M}}{u_\infty} \tag{4.19}$$

where the imposed displacement is $s_{\mathrm{pix}} \approx 12$. This resulted in $\mathrm{d}t = 0.6\mu s$. Image pairs are acquired at the maximum frequency allowable by the laser system, which is 15 [Hz]. Please note that this configuration, therefore, does not allow for a full time resolution of the flow, such as in Beresh et al. (2016).

4.3.2. Imaging configuration

Based on the results of the Schlieren measurement elucidated in detail in Chapter 5, it was decided to image the following portions of the flow field. Wall-normal imaging is to be conducted on a rectangular window ranging from $x = -2.5d_{\mathrm{jet}}$ to $x = 17.5d_{\mathrm{jet}}$ and $y = 0$ to $y = 10d_{\mathrm{jet}}$. For the wall-parallel case, instead, the window extends from $x = -2d_{\mathrm{jet}}$ to $x = 14d_{\mathrm{jet}}$ and from $z = -6d_{\mathrm{jet}}$ to $z = 6d_{\mathrm{jet}}$. See Figures 4.4a and 4.4b.

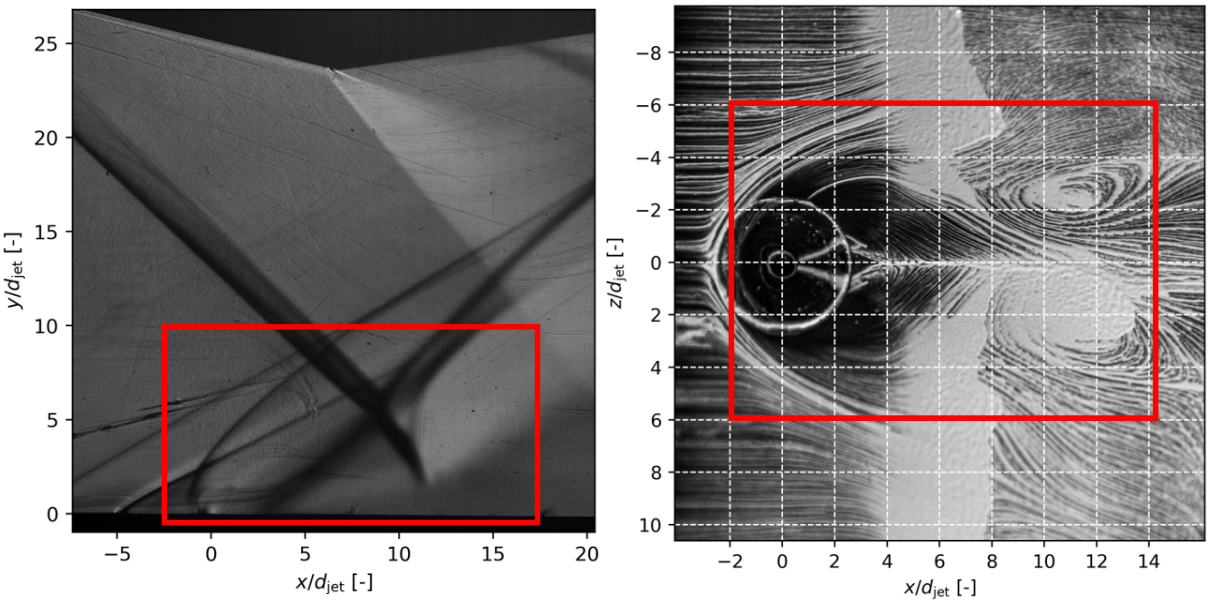

(a) Wall-normal FoV

(b) Wall-parallel FoV

Figure 4.4: Fields of view for PIV imaging.

For both imaging planes considered in this work different lenses and camera positions have been adopted. As illustrated by the work Prasad (2000), two main configurations exist for the placement of cameras in stereo PIV experiments. The *translational* configuration involves placing the two imagers in such a way such that their main optical axes are parallel to each other. While simple both for calibration and successive processing, a large error is shown to exist in the estimation in the out-of-plane component given the inherent limitation in the half-angle that can be achieved between viewing direction. Given the

highly three-dimensional nature of the flow case at hand, the reduction of the out-of-plane error is paramount. Thus, the *rotational* configuration is the one sounding more appealing.

Referring back to Figure 3.11, it is possible to define a set of three angle to determine the angular position of each of the cameras. In particular, the following angles are defined (positive following the right-hand rule convention).

- ξ about the x-axis.
- υ about the y-axis.
- ζ about the z-axis.

Table 4.4 reports the geometric coordinates of the both cameras for both imaging configurations. It is necessary to note how the actual distance from the physical plane is larger than the predicted distance by the thin lens equation. This is because, given accessibility requirements needed to access and maintain the test section, the cameras had to be placed further away than established by theory. This was corrected for by compensating with the focus ring on the lens.

	Wall-normal	**Wall-parallel**
$\overline{M}$ [mm]	0.28	0.27
f [mm]	105	60
d_o [cm] (from Eq. 4.13)	48.36	27.63
$\xi_1/\upsilon_1/\zeta_1$ [deg]	1.8 / 0 / -18.78	42.10 / 15.24 / 0
$d_{o,1}$ [cm]	52.80	40.74
$\xi_2/\upsilon_2/\zeta_2$ [deg]	1.8 / 0 / 29.09	-42.10 / 15.24 / 0
$d_{o,2}$ [cm]	57.22	40.74
Imaging angle [deg]	**47.87**	**84.20**

Table 4.4: Table containing information about the positioning of the cameras and the subtended angles. The subscripts 1 and 2 refer to properties of cameras 1 and 2, respectively.

Now, since the lens plane inherently possesses an offset angle with respect to the image plane, a Scheimpflug adapter was added to the lens system to enforce the *Scheimpflug condition*. This imposes that the field of view, the lens plane and the observer (i.e. sensor) plane must collinear. In reality it was not possible to ensure perfect collinearity such that the entire field of view would be in focus. Thus, a mild Scheimpflug angle was set to be roughly 10 degrees for all configurations and manually adjusted to ensure proper focus throughout the entire field of view. The final adjustment for focus was then the setting of a high-enough f-stop.

The camera and lens configuration is displayed in Figure 4.5. Then, Figures 4.6a and 4.6b display how the cameras have been set up for imaging of wall-normal and wall-parallel planes, respectively.

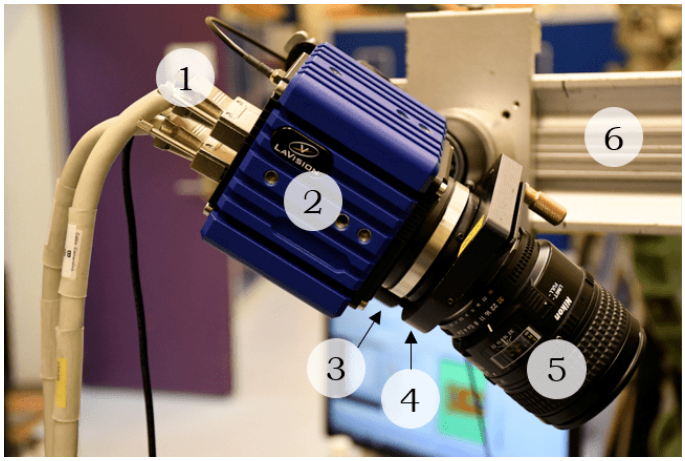

1. Data cables
2. LaVision imager sCMOS
3. Offset lens adapters
4. Scheimpflug adapter
5. Lens
6. Support structure

Figure 4.5: Photograph of lens configuration

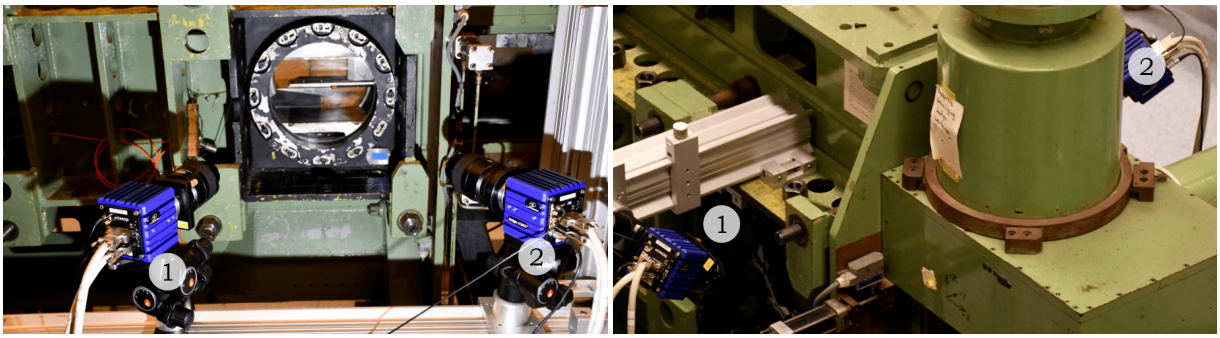

(a) Wall-normal imaging (b) Wall-parallel imaging

Figure 4.6: Camera configurations for PIV imaging. The numbers indicate the camera cardinality.

4.3.3. Seeding and illumination

Having discussed optical techniques and imaging configurations, it is now necessary to delve deeper into the details of how the particles are introduced into the test section and how they are illuminated with the laser. First, the seeding.

For a particle to be a proper tracer for PIV applications, it is necessary for it to have a minimal lag compared to the actual "real" flow in study and the alterations it causes in the flow should be kept to a minimum. Formally, assuming spherical particles having a low enough Reynolds number for them to move in Stokes regime ($Re \to 0$), the evolution of the velocity vector in time can be expressed as in Equation 4.20 (where the subscript p refers to particle properties).

$$\frac{\mathrm{d}\mathbf{V}}{\mathrm{d}t} = -\frac{3}{4} C_D Re_p \frac{\mu}{\rho_p d_p^2} (\mathbf{V} - \mathbf{U}) \tag{4.20}$$

with $\mathbf{V}$ and $\mathbf{U}$ being the particle's and the flow's velocities, respectively. The solution to the above equation of motion is an exponentially decaying particle's velocity with a change in flow speed. Physically, this means that the particle will always lag the flow characteristics by a certain time constant τ_p. Of course, one would aim at keeping the lag time as low as possible, in order to achieve the highest possible fidelity. From experience with the use of ST-15 and its experimental apparatus, the organic DEHS oil produces acceptable results. When atomized, the particle diameter lies around 1 [μm]. The work

by Ragni et al. (2011) analyses the dynamic behaviour of the tracers in response to a step change in velocity (i.e. a shock wave). Keeping in mind that the solution to equation 4.20 assumes the form:

$$V(t) = C_1 + C_2 \exp(-t/\tau_p)$$

it is possible to calculate the value for the time constant. For DEHS particles, it was found that $\tau_p = 2$ [μs].

Particles are injected into the test section through two different channels. One seeding line is introduced inside the tunnel's settling chamber, where a seeding rake is present to allow for uniform seeding density in the field of view. The second line is through the jet itself. In fact, given the strong momentum carried by and with the jet normal to the wall, the risk is that little to no seeding is visible in the downstream near field of the nozzle (which remains problematic nonetheless). Concerning hardware, the PIVTech PIVPART 45 seeder (Figure 4.7) and the other seeder were used to seed the jet and the settling chamber, respectively. Both operated with 1 [bar] of over-pressure relative to the flow they were injecting particles into.

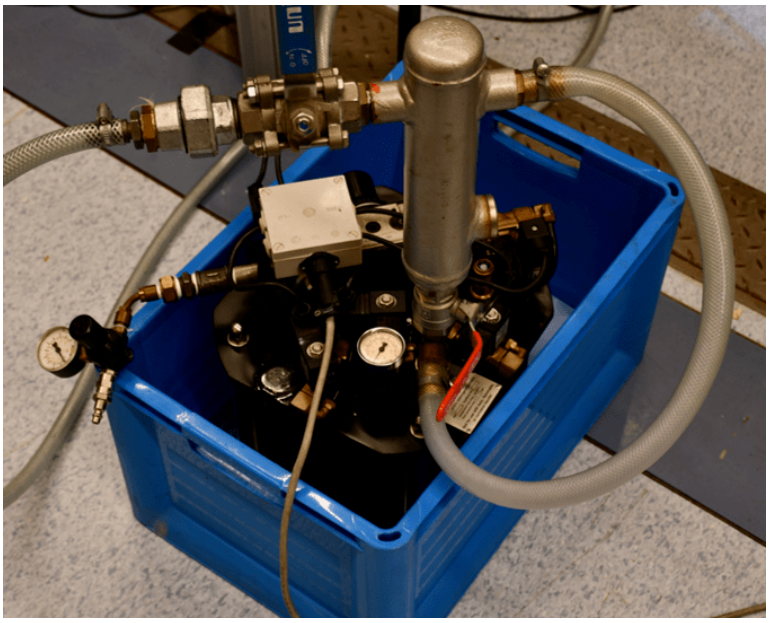

Figure 4.7: PIVTech PIVPART 45 seeder. In use for the jet.

Whereas these first two requirement translate into a particle having as little volume and mass as possible, the constraint of visibility upon imaging tends to lead the selection of the tracer towards bigger mean diameters. Yet, the 1 [μm] diameter of the selected DEHS oil is deemed sufficient for proper illumination. Indeed, the Nd:YAG EverGreen Big Sky laser provides enough energy per pulse to achieve sufficient light scattering. Then, it is necessary to determine how the laser sheet shall be introduced inside the test section. The configuration varies between the wall-parallel and wall-normal imaging set-ups. Both rely on the same probe to project the beam forward into the section towards the jet, shown in Figure 4.8.

For both imaging scenarios, the probe is fastened to the diffuser in predefined slots. For the wall normal case, the probe is inserted through the side of the tunnel, with the

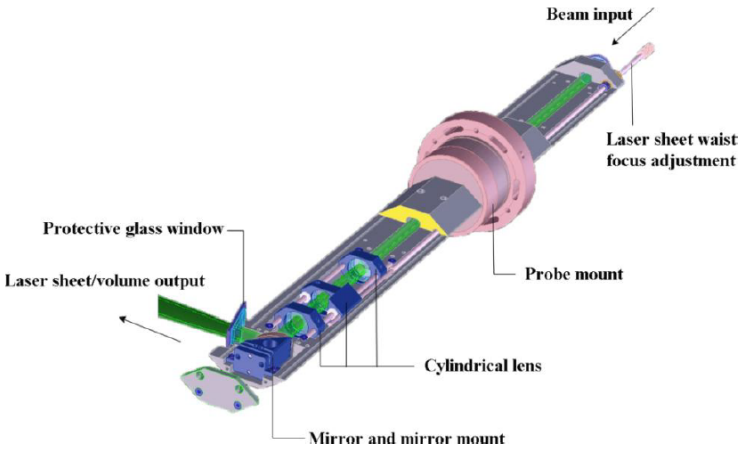

Figure 4.8: Schematic of the laser probe in use. Taken from Donker Duyvis (2005).

jet's air line introduced from the bottom flange. Spherical lenses are positioned right at the exit of the laser head to ensure sufficient height of the sheet (see Figure 4.9a). For the second imaging scenario (wall-parallel planes), the probe is introduced from the bottom flange, with the laser placed parallel to the stream and a mirror reflecting the beam upward towards the diffuser and the probe (Figure 4.9b).

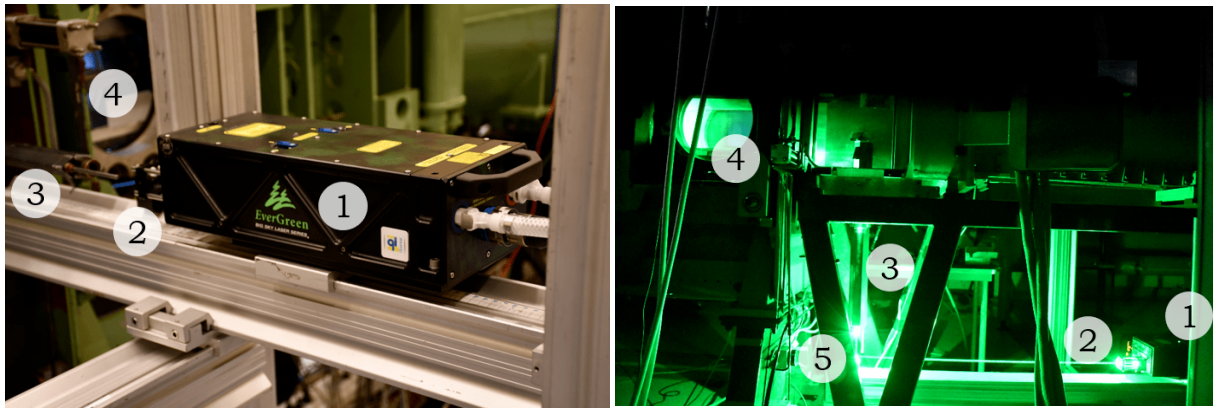

(a) Wall-normal imaging (b) Wall-parallel imaging

Figure 4.9: Laser configurations for PIV imaging. Pointers: (1) laser head, (2) spherical lenses, (3) laser probe of 4.8, (4) test section and (5) planar mirror.

4.3.4. Image processing

The set-up described up to this point allows for the acquisition of digital black and white images of the particle field. Image processing techniques have to be applied in order for the raw images to be transformed into velocity data. To understand how an image is processed from an intensity field to velocity data, it is first needed to delve deeper into how a particle is actually captured by the imaging system. Each individual tracer scatters light along all directions, but not in an isotropic manner.

In PIV application, most of the light captured by the cameras comes from side scattering. Depending on the angle of the system with respect to the laser sheet plane, some forward or backward scattering may occur as well. Now, due to diffraction effects caused by the lenses in the imagers, each particle never actually gets imaged as a perfect circle, but

rather as a decaying intensity pattern showing alternating bright and dark regions. This characteristic pattern is known as an *Airy disk*, from the name of the researcher who first discovered it. It is an important parameter playing a role in the determination of the proper f-stop for acquisition.

The reason for the introduction of the reader to this phenomenon will become clear in a short while. In fact, to reconstruct the velocity field, cross-correlation is performed. The image data of generic shape ($M \times N$) is divided into several smaller "interrogation windows". For each individual window, cross-correlation is performed between images of the same pair. As each window, generally containing the same particles, will be displaced between one image and the next in the pair, the computation of such displacement in the image space can be translated into a displacement in the physical space. Coupling this with the chosen δt, one is readily able to find the local velocity vector that allowed such motion. Performing this for all windows in the image, the entire velocity field can be reconstructed. Mathematically, the correlation coefficient (ϕ) following a displacement of $\mathbf{d} = [m, n]^T$ is given by,

$$\phi(m,n) = \frac{\sum_{i=1}^{M}\sum_{j=1}^{N}[I_1(i,j) - \overline{I_1}][I_2(i+m, j+n) - \overline{I_2}]}{\sigma_1 \sigma_2} \tag{4.21}$$

where I refers to the intensity and the overline to the average estimator. σ is the standard deviation. The subscripts refer to the first (1) and second (2) image of the pair. In order to be able to achieve velocity values not only at the pixel locations, but also on the sub-pixel scale, an interpolation scheme becomes necessary. Raffel et al. (2018) propose the use of a three-point Gaussian fit, which stands for a fair approximation of the Airy disk characteristics .

Being the above the core of PIV image processing, more steps are taken in the present work to obtain the velocity field. These are listed below.

1. **Image pre-processing and filtering.** This is a step entailing a preliminary preparation of the image. Three main options were investigated for use.
   (a) *Background subtraction.* The background intensity field is subtracted to all images based on a pre-acquired set.
   (b) *Minimum filtering.* Per pixel, this operation subtracts the minimum intensity encountered over a pre-defined time interval.
   (c) *Butterworth filtering.* A type of high-pass filtering with a predefined length (i.e. number of images).
2. **Masking.** Although several types of masking exist, only geometric masking is utilized in this work. This "hides" the regions which are deemed invalid for processing (such as the walls of the tunnel) or which the laser sheet does not cover. Other masking techniques are not considered as their action is already covered by the previous step.
3. **Vector calculation.** The core of PIV processing: the cross-correlation transforming the bitmap to velocity field. Several parameters can be modified to enhance the quality of the results.
   (a) *Window size.* An increasing window reduces noise but also resolution, as it effectively approximates the local velocity vector to the average one in the window. Anyway, a bigger window also leads to shorter processing time.

(b) *Window shape.* A circular window shape ensures a smoother transition between one position and the next, whereas a square is more robust.

(c) *Number of passes.* The more passes the correlation kernel makes over the image the better the quality. Of course, the more passes the worse it is for runtime. Usually, this is performed by first using a large window, to then decrease its size for later passes.

4. **Statistics.** This step is used to determine the average field, its standard deviation along with all second-order statistics, such as Reynolds stresses.

5. **Image post-processing.** Some regions might have been too corrupt for the cross-correlation filter to get any data out of them. Hence, a subsequent smoothing of images, together with interpolation in the noisy/invalid regions was applied.

4.4. Uncertainty Analysis

In the present work, it is usually the case that the average result (either from the Schlieren image sequence or the PIV image pairs) is analyzed. Yet, the average relies on an underlying data set comprising several instantaneous acquisitions. Each experimental techniques is characterized by inherent pitfalls, which are going to be discussed in the foregoing.

4.4.1. Line-of-sight techniques

Sources of error for line-of-sight techniques are inherent mainly in the optical system in use. In particular, hardware limitations lead to the following possible issues.

- **Integration along the line-of-sight.** Probably the predominant causes of error, this makes Schlieren photography and shadowgraphy a tool to be relegated for the preliminary experimental phases only (for the present work). Any given light ray cruising across the imaging system undergoes distortions caused by all features it encounters along its path. This means that, effectively, the camera only sees an “averaged” result of the phenomena that actually occur inside the test section.

- **Optical aberrations.** Along its path, light crosses several lenses, mirrors, tunnel windows and, of course, the test section. Slight misalignment in the imaging equipment, dust on lenses, windows and sensor can all lead to inaccuracies when the time comes to digitally reconstruct the image. Even though thorough effort was made to ensure cleanliness and alignment of all equipment in use, it is deemed unavoidable to have a slight deterioration due to these imperfections.

- **Unsteadiness in the flow.** This error source is related to the fact that brightness is integrated along the line of sight. In fact, as the flow is highly unsteady (especially in the cases with the active jet), the motion of the feature causes it to appear larger than it actually is on the final ensemble averaged image. This is clearly visible on, for instance, the imaging of the oblique shock impinging on the jet plume. Its front, in fact, appears rather wide in the Schlieren image. In this respect, shadowgraphy helps as it effectively only maps variations of the second derivative of density, which occur in shorter spaces and with steeper gradients. However, this technique does not provide any directional information.

4.4.2. Oil flow

Little to no quantitative information can be derived from the analysis of an oil flow picture. Flow features arising in near-wall regions can be readily analysed and serve as input

for definition of future experiments employing techniques of a more quantitative nature (such as PIV), but the extraction of quantitative information is challenging at the least. Error sources have a varied origin. Start-up and shut-down loads on the flow cause the oil to suddenly shift as the tunnel is started and then stopped. In the foregoing, all results displaying oil flow consist of images of the oil taken as tunnel got back to a standstill. Furthermore, different pressure gradients lead the oil in different directions, making different regions have different streamline resolutions. For instance, a region where oil accumulates can be overfilled with oil, whereas one where oil rarefies can see too poor of a resolution.

4.4.3. Stereo PIV

Depending on the specific phase of a PIV experiment, different uncertainties arise from the processes involved in the acquisition.

Statistical uncertainty

Given the imaging half-angle between the two cameras, it is possible to estimate the relative error in the estimation of the out-of-plane component as compared to the in-plane one. For this, Figure 4.10 comes in practical.

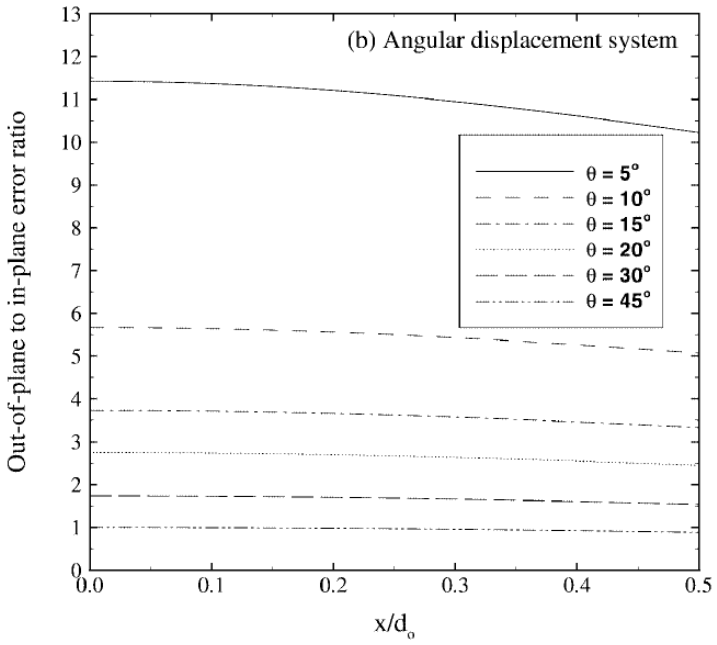

Figure 4.10: Plot displaying the relative error ratio versus position along the field of view, normalized by object distance, for various imaging half-angles. Taken from Prasad (2000).

From the figure one can infer how the relative error ratio is going to be between 2 and 3 for the imaging of wall-normal planes and close to unity for imaging of wall-parallel sections. However, a word of caution needs to be mentioned as for the wall-parallel measurement. Given the highly warped optical arrangement, self-calibration sometimes failed or gave poor results. Furthermore, given the proximity of the laser sheet to the wall and the possible accumulation of seeding oil or dust, bright spot appeared constantly throughout the acquisitions, locally degrading the quality.

By making use of statistical relations, it is possible to come up with the necessary number of samples (i.e. image pairs) that need to be generated to ensure statistical convergence

up to a certain margin of error. According to error propagation theory, it is possible to estimate the uncertainty on the mean velocity, the velocity RMS and the vorticity as in Equations 4.22, 4.23 and 4.24, respectively.

$$\varepsilon_{\overline{u}} = \frac{\sqrt{\overline{u'^2}}}{\sqrt{N}} \tag{4.22}$$

$$\varepsilon_{\langle u' \rangle} = \frac{\sqrt{\overline{u'^2}}}{\sqrt{2N}} \tag{4.23}$$

$$\varepsilon_{\omega} = \frac{\sqrt{2}\varepsilon_{\overline{u}}}{\Delta x} \tag{4.24}$$

According to Benedict and Gould (1996), the oscillations of the flow are related to the standard deviation (σ) as follows: $\sqrt{\overline{u'^2}} = \sigma$.

Particle slip uncertainty

As PIV relies on the representation of the flow by the tracing of particles, a good measure of the fidelity with which the flow is reconstructed lies in the particles slip velocity. It is a measure of the difference between the flow's and the tracer's speed through the field of view. In particular, it is possible to estimated the particle's slip velocity as,

$$\mathbf{u}_{\text{slip}} = \mathbf{u_p} - \mathbf{u_f} = \tau_p \cdot \mathbf{a_p} \tag{4.25}$$

with τ_p being the particle response time and $\mathbf{a_p}$ the particle's acceleration. Assuming the particle's motion is in the Stokes regime (i.e. the viscous forces dominate and $Re << 1$). In steady flow, the acceleration of a given particle is given by the dot product of velocity with its gradient, as shown in Equation 4.26.

$$a_p = \mathbf{V} \cdot \nabla \mathbf{V} \tag{4.26}$$

which, substituted back into Equation 4.25, gives

$$\mathbf{u}_{\text{slip}} = \tau_p \left(\mathbf{V} \cdot \nabla \mathbf{V}\right) = \tau_p \mathbf{V} \cdot \left(\frac{\partial u}{\partial x} + \frac{\partial v}{\partial y}\right) \tag{4.27}$$

It is clear that this error source will be higher in the regions with the steepest gradients of velocity. For high speed flows, this clearly coincides with the locations whose flow is dominated by shocks. The uncertainty can be estimated to be equal to the modulo of the slip velocity:

$$\varepsilon_{\text{slip}} \approx ||\mathbf{u}_{\text{slip}}|| \tag{4.28}$$

Interrogation window size uncertainty

The size of the interrogation window used in processing determines the extent of the smallest feature that can be properly imaged and reconstructed. The smaller the window, the higher the resolution. On the other hand, a small window also leads to an increase in the probability of incurring in loss-of-pair errors. The uncertainty relating to this parameter can be expressed as mentioned in Schrijer and Scarano (2008),

$$\varepsilon_{\text{ws}} = \text{sinc}\left(\frac{l_{\text{window}}}{\lambda}\right) \tag{4.29}$$

where l_{window} is the window size.

Cross-correlation uncertainty

The cross-correlation operator that allows the transformation from bitmap pair to velocity field is, itself, uncertain. The expression for the error deriving from this operation can be taken from Raffel et al. (2018).

$$\varepsilon_{cc} = \frac{\varepsilon_{corr} l_{pix}}{M \Delta t} \tag{4.30}$$

being ε_{corr} the correlation uncertainty. According to Raffel et al. (2018), this values equals 0.2 [pix] for the worst case scenario (tomographic PIV).

Uncertainty in numbers

To recap and conclude this chapter, Table 4.5 presents the calculated uncertainty values caused by all phenomena explained in the above.

Error source	Symbol	Equation	Wall-normal	Wall-parallel
u-component	ε_u	4.22	<0.088 [m/s]	<0.521 [m/s]
v-component	ε_v	4.22	<0.121 [m/s]	<0.623 [m/s]*
w-component	ε_w	4.22	<0.198 [m/s]*	<0.523 [m/s]
RMS - u	$\varepsilon_{u'}$	4.23	<0.067 [m/s]	<0.260 [m/s]
Vorticity	ε_ω	4.24	<23.8 [1/s]	<31.6 [1/s]
Particle slip	ε_{slip}	4.28	<3.01 [m/s]	<7.54 [m/s]
Window size	ε_{ws}	4.29	<-3.64E-4 [m/s]	<3.64E-4 [m/s]
Cross-correlation	ε_{cc}	4.30	<7.73 [m/s]	<8.02 [m/s]

Table 4.5: Table reporting the uncertainty values. Values marked by (*) refer to the out-of-plane velocity.

5

Analysis of the effects of the control parameters on flow structures

This chapter will present results of a preliminary study (i.e. test campaign) of the chosen control variables on the flow field. First, baseline results will be introduced in Section 5.1. Then, the more interesting configurations with the impinging oblique shock wave will be discussed in Section 5.2. This section is further divided into several main sub-sections, whereby the effect of the control parameters is analysed. The general flow field structure is discussed (i.e. shock structures, vortices etc.), followed by the effects of the impinging shock on the Mach disk and its geometry. Compression zone onset and interaction region properties are then discussed, followed by a presentation of the effect that the downstream shock impingement location has on the field. The chapter is finally closed by the discussion of an attempt to quantify the unsteadiness of the jet-shock-crossflow system.

By using line of sight techniques, it possible to quantify some of the main geometric parameters which characterize the interaction of the jet with a supersonic crossflow and with an incident oblique shock wave. Furthermore, it is possible to compare the scenario where the jet is turned on to the ones where the jet is off. This results in an attempt to evaluate how the presence of the jet affects the properties of the supersonic SBLI. Referring back to table 1.1, the main outcome of this first experimental phase is the basic characterization of the jet. In particular, four geometric parameters are going to be taken as quantities of interest in this preliminary phase of the work.

1. **Barrel shock shape.** The shape of the barrel is observed to vary depending on whether the shock is present or not and depending on the local conditions.

2. **Mach disk location.** The location of the Mach disk (especially its height above the injection point) can be correlated to the level of mixing between the primary and secondary flows.

3. **Upstream separation point.** Upstream separation is induced by the bow shock upstream of the jet.

4. **Downstream compression shock foot.** The compression wave forms upstream of the location where the oblique shock reaches the ground. The “upstream influence length” is expected to vary depending on the shock and jet conditions.

In addition, friction lines obtained from oil flow visualization allow for the description and identification of the flow behaviour in the near-wall region. This techniques allows for finding zones of boundary layer separation, re-attachment, shock impingement and more. In general, this technique will serve for the explanation of the behaviour of the boundary layer. Using oil mixed with titanium dioxide particles (TiO_2), it was possible to obtain various flow patterns. The runtime is set to 10 seconds. As can be seen in the graph in Figures 5.1a and 5.1b, the chosen run time allows for steady state conditions to be reached.

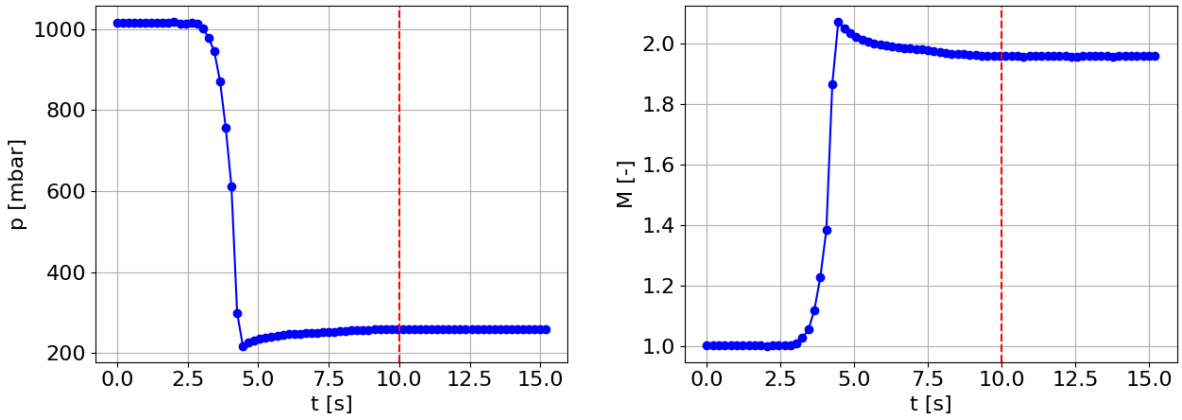

(a) Static pressure in the test section

(b) Mach number in the test section

Figure 5.1: Curves displaying main flow variables and their transient behaviour at the start of the run. The curves above refer to the situation where $M = 1$, $J = 1$ and $\theta = 9\,\text{deg}$. A similar behaviour was noted for all data points. The dashed red line corresponds to the chose run time, after which a wind tunnel run is stopped (when performing oil flow measurements).

Concerning Figure 5.1, the pressure curve was directly obtained from the pressure transducer on the side of the test section, whereas the Mach number was derived by applying the isentropic relations.

5.1. Baseline runs

This section comprises the description of the tests that were conducted in order to establish a baseline. This aspect is twofold. On the one hand, it is necessary to establish the characteristics and flow properties of the scenarios where no shock impinges on the jet plume. On the other hand, the opposite scenario can also be tested: with the jet turned off, one can characterize the flow field created by the presence of the sole shock.

5.1.1. Jet with no shock

First, the near-wall flow field is presented for the case of the jet in crossflow without any incident shock impinging on the plume (see Figure 5.2). The main flow features as illustrated by Dickmann and Lu (2009) also appear rather clear cut in this picture. In particular, the upstream saddle point of separation can be clearly seen in the figure. Furthermore, horseshoe vortices form downstream of the injector port, their swirl being imparted mainly by the change in velocity between the upstream post-shock flow and the downstream separated region. These flow between the bow shock and the collision shock in Figure 5.3. The downstream wall friction lines hint at the presence of a re-attachment zone as mentioned in Liu et al. (2018). The flow then becomes uniform again in the far field downstream. Perturbations appear in the vicinity of the of the jet exit at the onset of the plug's chamfer.

These are not due to interactions of the jet with the surroundings, but are rather given by the change in elevation caused by the chamfer itself. Shifting the focus downstream, oblique separation lines appear visible. Figure 5.3 shows the detail of the several flow discontinuities.

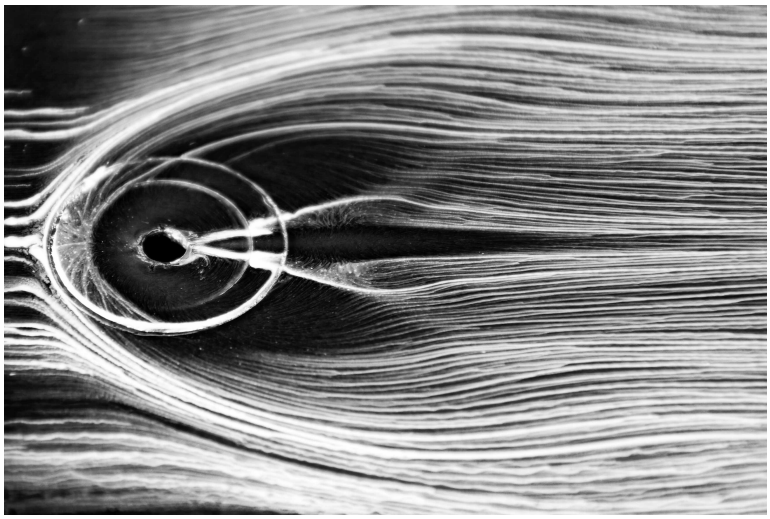

Figure 5.2: Oil flow visualization of jet in crossflow with no incident shock wave. $M = 1$ and $J = 2$.

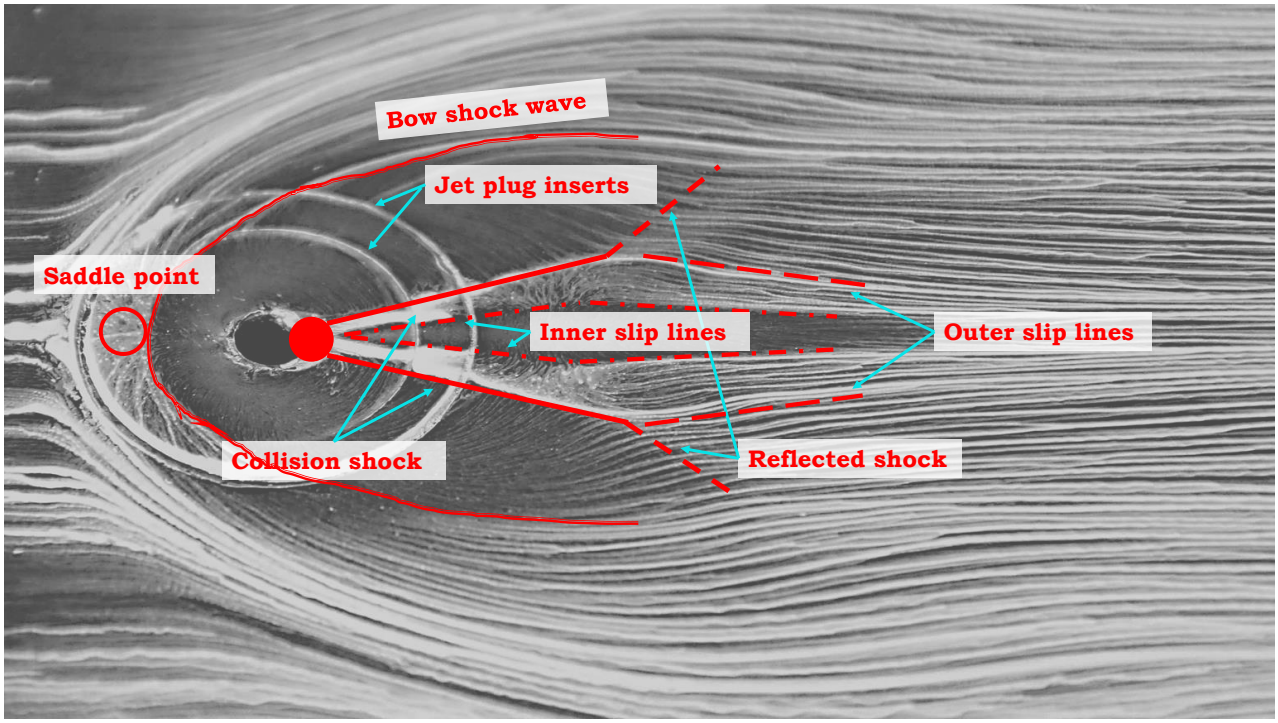

Figure 5.3: Jet in crossflow with $M = 1$ and $J = 2$. Highlighting near-wall flow discontinuities.

The region in between the inner and outer slip lines is the oblique flow separation zones contained between the legs of the herringbone vortical features, as explained by Dickmann and Lu (2009). In the downstream far field oil still seems to leave a gap in the centre. This is caused by the counter-rotating vortex pair (CVP), which recalls air for the near-wall region in an upward-directed current (Sun and Hu (2018a)).

It is also possible to study the flow field in a wall-normal, flow-parallel plane. The interactions on this locus can be investigated by means of line-of-sight techniques. Figure 5.4 displays a Schlieren image of the situation where the jet is sonic and $J = 2$. All canonical features of the interaction of a jet with a supersonic crossflow are clearly visible, as illustrated by Morkovin et al. (1952), Zukoski and Spaid (1964), Beresh et al. (2005) and many more works from the same author, Mahesh (2013) and several more literature publications. The most clear-cut feature is certainly the barrel shock enveloping the jet exhausting from the port hole on the bottom surface, located at (0,0). The barrel shock is curved downstream given the streamwise momentum of the incoming crossflow. This three-dimensional discontinuity terminates into the so-called *Mach disk*: a normal shock which is round in shape and closes off the envelope around the barrel. Upstream of the injection zone a bow shock forms due to the effective obstruction to the main stream produced by the jet exhaust. Upstream of the shock, given its interaction with the boundary layer, the flow separates and compression waves form. These will then coalesce into the bow shock wave itself, as mentioned in Dickmann and Lu (2009). It is necessary to note that a second shock wave also appears, but is not caused by the jet. Instead, as shown in Figure 3.10, it is generated by a change in elevation of the test section's surface due to the presence of a fastening insert.

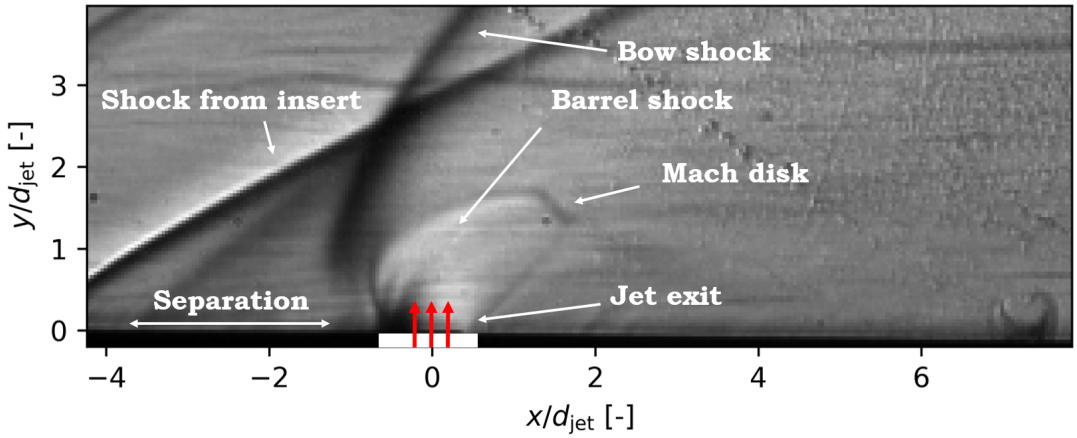

Figure 5.4: Jet in supersonic crossflow with $M_j = 1$ and $J = 2$. Highlighting notable features.

The momentum flux ratio is one of the key parameters for the determination of the trajectory of the plume, the extent of the up- and downstream separation zones and many more flow field features. Therefore, it was decided to test three different J values and observe what their effect would be on the overall flow field. Figure 5.5 illustrates the comparison.

As expected, an increase in J, which translates to an increase in momentum of the transversely injected flow, results in a shift in the position of the Mach disk. In particular, it shifts further away from the location of the orifice. The jet momentum flux ratio, also comparable to the jet-to-crossflow pressure ratio, is indeed one the main variables (together with the jet inclination angle) contributing to the height of the Mach disk above the wall, as mentioned by Yan et al. (2016). Furthermore, the height of such feature is of key importance for the mixing of the two fluid flows. Kawai and Lele (2009) explain how, in fact, the height of the disk can be directly correlated to the level of mixing in the fluid domain. For the present cases, the height of the Mach disk was plotted versus its corresponding J

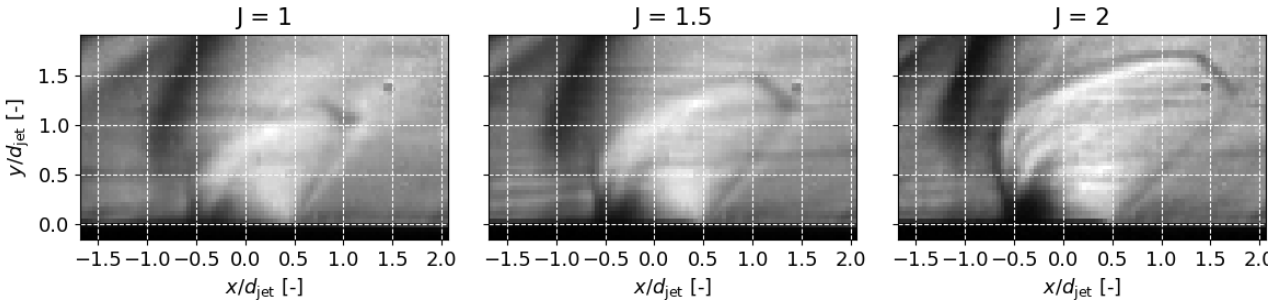

Figure 5.5: Comparison between the barrel shock of the sonic jet at various J values.

in Figures 5.6a and 5.6b, which show the quantification of the location of the middle point of the Mach disk, as interpreted from Figure 5.5.

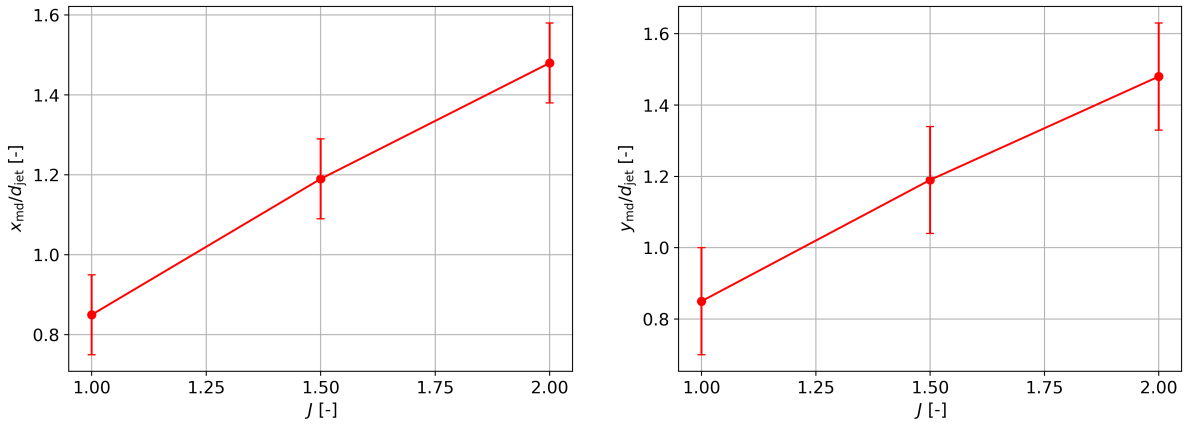

(a) x_{md} vs. J

(b) y_{md} vs. J

Figure 5.6: Position in x- and y-coordinates of the Mach disk middle point.

A word on the uncertainty. Plotted values refer to the mean position of the middle point of the Mach disk as seen from the digital image. Due to unsteadiness in the jet, the barrel shock always move throughout the acquisition, and so does the disk. The uncertainty values reported in the caption of all figures containing data of positions of flow features are taken as the most extreme positions observed during the run. For example, if $\varepsilon_y = \pm 0.2$, it means that the plotted position varies in the interval $[y - 0.2, y + 0.2]$.

5.1.2. Shock with no jet

Having presented the baseline case of the jet purely interacting with the supersonic cross-flow, it is now necessary to present the case of the shock wave with no jet present.

The flow case in Figure 5.7 was obtained by deactivating the jet and by mounting the 9-degree shock generator. The shock impingement line is visible as an accumulation of oil along the flow-normal direction. The most oil is concentrated between the actual shock foot and the onset of the compression waves caused by the recirculating flow in the upstream region of it (Babinsky and Harvey (2011)). Just downstream of this particular feature, oil rarefaction region is seen. In particular, a re-attachment line is present. That is where the flow, after undergoing separation in the interaction region, finally reattaches to the surface. It was decided not to present the near-wall flow for the case of the sole shock with $\theta = 12\,\text{deg}$, as the field resulted to be rather similar, the sole difference being in the

streamwise extent of the separated flow region between the compression shock and shock shock feet. The same description will be carried out for the description of the flow features on wall-normal, flow-parallel planes (visualized with Schlieren photography) in Figures 5.8, 5.9a and 5.9b.

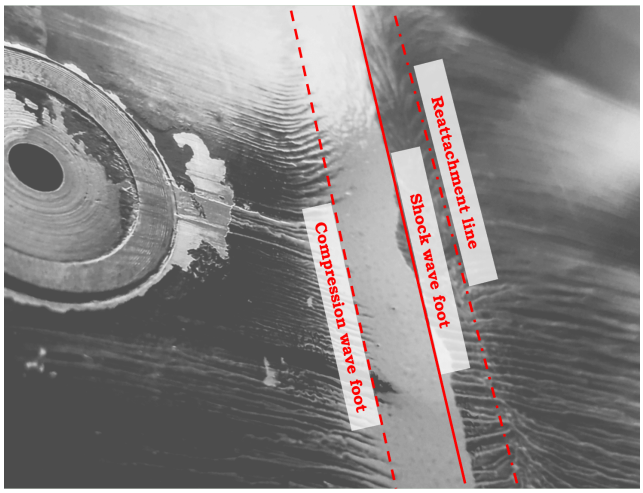

Figure 5.7: Oil flow visualization of flow case of shock with $\theta = 9\,\text{deg}$ and highlight of relevant flow artefacts.

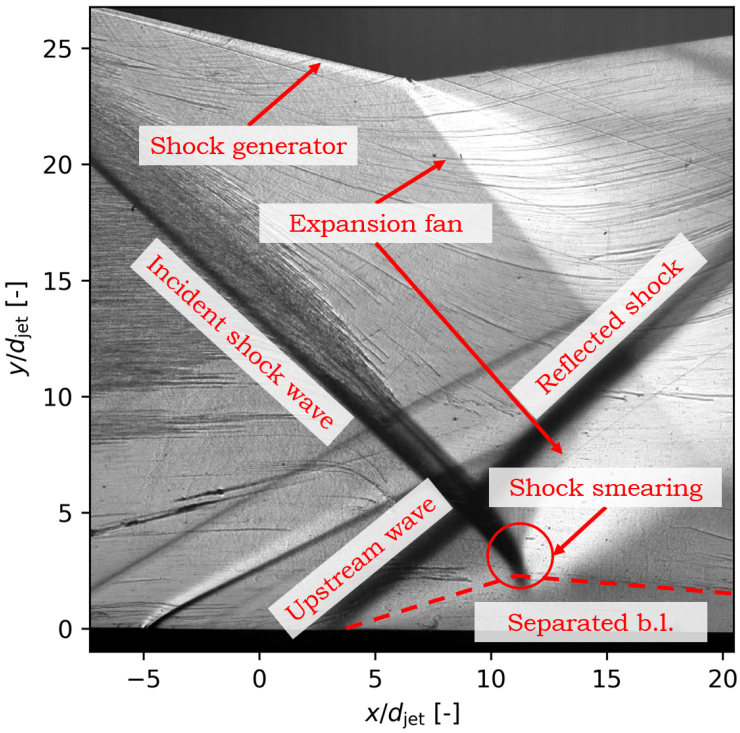

Figure 5.8: Schlieren image of SBLI field with $\theta = 12\,\text{deg}$. Highlighting notable features.

As two deflection angles were used for the ramps in use to generate the shocks ($\theta = 9\,\text{deg}$ and $\theta = 12\,\text{deg}$), two different fields will result, given the different geometries of the corresponding ramps. First, though, it is convenient to present one single flow case: $\theta = 12\,\text{deg}$ (Figure 5.8). The incident oblique shock enters the field of view from the top left corner of the photograph. As it approaches the wall, it interacts with the upstream compression

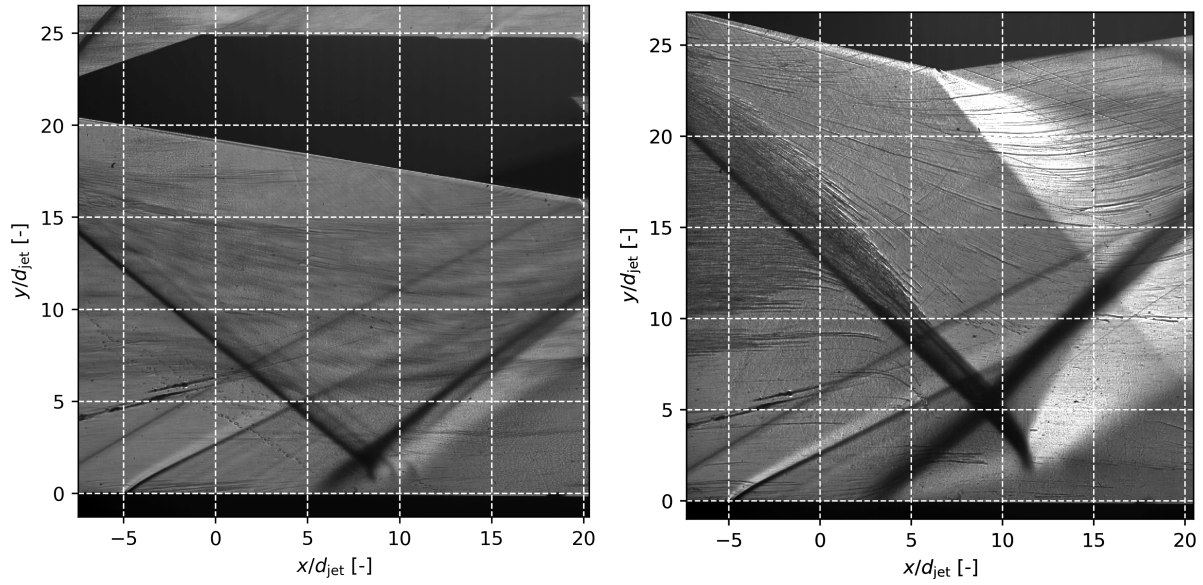

(a) $\theta = 9\,\text{deg}$ (b) $\theta = 12\,\text{deg}$

Figure 5.9: Schlieren images of flow field generated at $M_\infty = 2$ by shock waves with different deflection angles, θ.

wave generated by the interaction of itself with the boundary layer. In particular, as the wall region is inherently characterized by a velocity gradient, the shock angle will become more and more normal the closer to the wall until the sonic line is reached. Given the rise in pressure in the proximity of the shock foot, an adverse pressure gradient is present. Thus, fluid recirculates forming a "bulge" in the boundary layer. Effectively acting as a ramp, compression waves form that coalesce into the upstream shock wave. As it interacts with the incident wave, it gets refracted an its angle changes. Finally, two expansion fans are visible in the field. The one in the upper side of the image is generated by a kink in the shock generator itself, whereas the lower one is due to flow expansion in the post-shock region upon termination of the λ-structure (Babinsky and Harvey (2011)). Large-scale separation can be intuitively observed downstream of the shock impingement location. The case of $\theta = 12\,\text{deg}$ is, in fact, an example strong SBLI, causing the boundary layer to depart from the wall. Large-scale separation such as visible here is the object of study of several works in literature and its control is of major importance for engineering applications, as mentioned in Huang et al. (2020). The introduction of the jet into the field upstream of the interaction point is thought to reduce the extent of such region, as it would appear from a study by Yan et al. (2020). This, however, cannot be proven with the current experimental set-up and measurement techniques employed, as Schlieren imaging effectively carries out an integration of the light intensity along the line of sigh. Yet, with further experimentation, it is deemed possible to quantify this effect (i.e. by employing stereo PIV).

Figure 5.9a and 5.9b show, instead, the comparison between the interactions generated by the two different shock generators. Due to limitations of the test set-up, the shock generators can only be placed at a few discrete locations. It is not possible to vary the shock location as the user pleases. To ensure that the shock would impinge at positions relatively close to the jet exit, given the different shock angles, the ramps were placed at different heights above the bottom guide wall. The shock strength is, of course, different for both cases. The result is that the strongest shock will generate a larger upstream influence region and create a stronger interaction, forcing the boundary to visibly separate. Even

though separation is visible also in the case of Figure 5.9a, it appears to be weaker, if present at all. A detail worth mentioning is the apparent “triple” shock in the 9-degree case. The weak downstream shocks are caused by imperfections in the ramp itself.

5.2. Impinging oblique shock wave

This section will illustrate the effects, of the shock angle on the flow field. First, a general overlook of the two different cases is presented.

5.2.1. General flow field

Figure 5.10a and 5.10b illustrate the flow cases showing the interaction under study. It is possible to identify all key features of both the interaction of the jet with the supersonic crossflow and the SBLI. It is also worth mentioning that, in the case of the stronger, 12-degree shock, the upstream bow shock gets refracted upon interaction with the incident wave. This is not as visible in the 9-degree scenario, as the shock strength is lower.

Given the fact that Schlieren (and shadowgraphy) are line of sight techniques, they are not able to reveal the specific flow features in the proximity of the jet exit and on the nozzle plane. Yet, these techniques offer valuable information. The reader is invited, for instance, to notice the expansion fan that is generated downstream of the interaction zone in Figures 5.10a and 5.10b. This is generated by air streaming through the shock system and accelerating again over the shoulder of the recovering boundary layer.

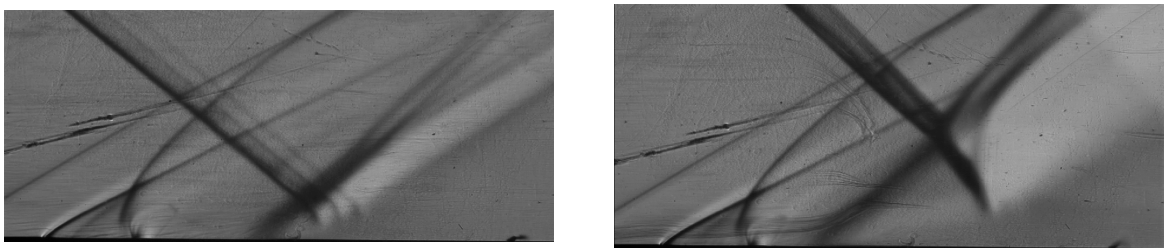

(a) $\theta = 9\,\mathrm{deg}$ (b) $\theta = 12\,\mathrm{deg}$

Figure 5.10: Schlieren images of flow field generated by the incident OSW interacting with the sonic jet at $J = 2$.

In the foregoing a more accurate representation of the boundary layer behaviour will be provided with the discussion of surface oil flow patterns: Figures 5.11a, 5.11b, 5.12a and 5.12b.

Common to all four situations in the figures is the fact that the incident shocks foot is distorted by the interaction with the jet. By inspecting Figure 5.7, clear differences appear. The uniform shock foot front is now interrupted directly downstream of the jet. The port and starboard lobes of the jet, in fact, interact with the incoming shock to create a region of lower speed flow in the proximity of the jet. Furthermore, several new vortical structures seem to appear in the proximity of the oblique shock foot.

The reader is first invited to focus on cases where $\theta = 9\,\mathrm{deg}$ (Figures 5.11a and 5.12a). In particular, especially for the unity momentum flux ratio, two large inward-rotating vortices form just downstream of the smeared foot ($8 < x/d_{\mathrm{jet}} < 10$). Their onset is at the location where the reflected wave from the collision shock meets the compression shock onset. These appear just as a pure accumulation of oil in the case where J is doubled, simply due to the higher intensity of momentum transfer. Two air stream seems to appear as a

result of different deceleration patterns across the shock system, separated by a slip line which connects with its symmetrical counterpart in the downstream far field. The inner section corresponds to the flow which has crossed both the bow shock and the reflected shock from the collision wave (see Figure 5.3). The second region comprises air which has only crossed the incident oblique shock. Due to the velocity difference between the two, a vortex forms. Given the accumulation of oil in the core of the vortex, the conclusion can be made that it rotates in an inward fashion. This means that airspeed is higher in the outer regions, which makes sense given the stronger nature of the quasi-normal bow shock in the near-wall region plus the necessary crossing of the reflected wave. Figure 5.12a, though, reveals two more symmetrical vortices forming within the inner region ($4 < x/d_{\text{jet}} < 6$). The reason for the formation of these is thought to be related to shock wave blockage effects. For an increase in J, the barrel shock increases in size, which acts a greater obstacle to the flow crossing the bow shock. Now, as the incident shock also acts as a barrier, a channel of air forms between the edges of the barrel and the smeared foot edges. Since the intensity of the interaction is higher for $J = 2$ compared to $J = 1$, air is rushed through the channel at greater speeds. As it comes to the downstream end and rejoins air from within the oblique separation region, a vortex forms.

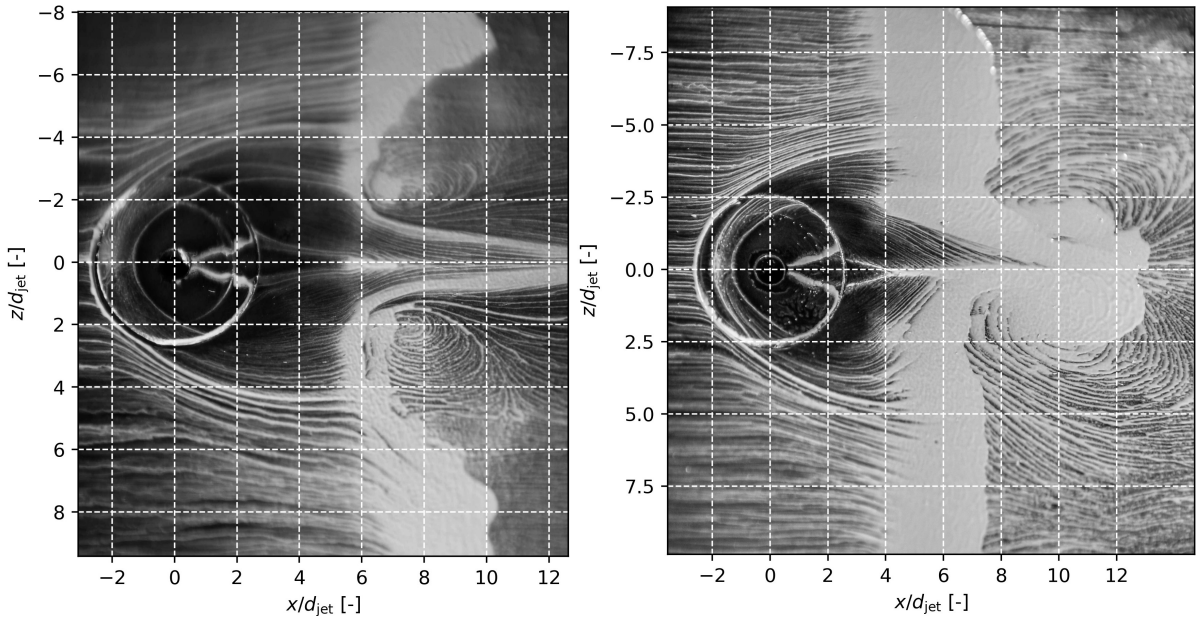

(a) θ = 9 deg (b) θ = 12 deg

Figure 5.11: Oil near-wall flow field generated by the incident OSW interacting with the sonic jet at J = 1.

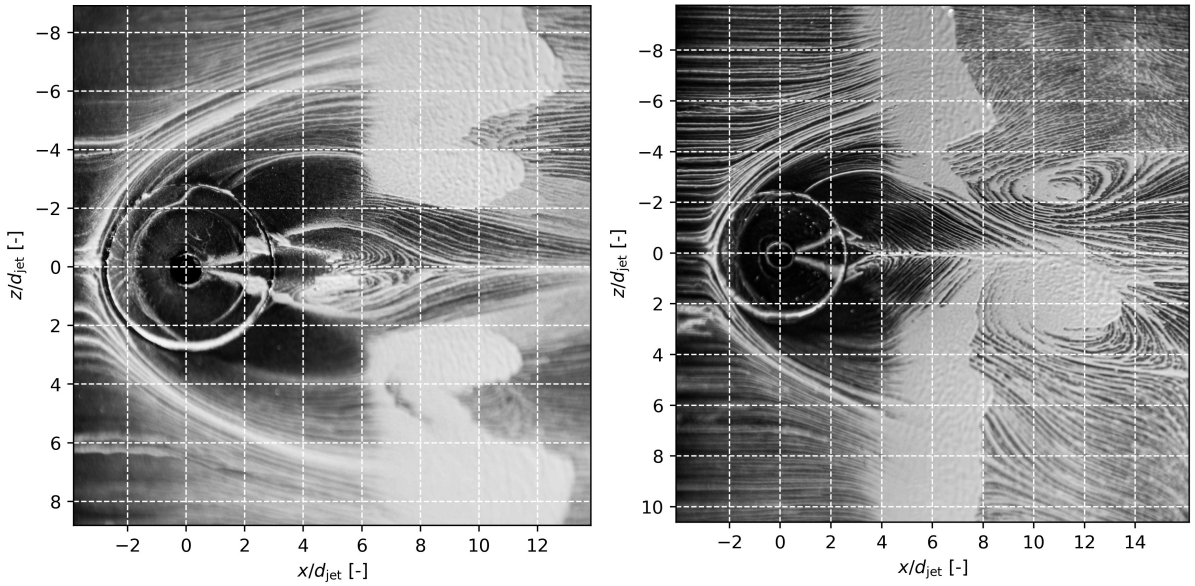

(a) $\theta = 9\,\text{deg}$ (b) $\theta = 12\,\text{deg}$

Figure 5.12: Oil near-wall flow field generated by the incident OSW interacting with the sonic jet at $J = 2$.

A different scenario is observed, instead, for the 12-degree ramp (Figures 5.11b and 5.12b). Both figures show a different downstream pattern compared to the one observed for the weaker shock. In particular, friction lines converge onto a single centre line which continues towards the far field. The counter-rotating vortex pair (CVP) is deemed responsible for this phenomenon. In fact, the CVP induces a velocity field directed towards the symmetry plane on the near-wall region. Moving downstream, the CVP also rises above the wall, rendering its influence weaker and weaker. The higher the J, the higher is the jet plume and, thus, the CVP. For this reason, when $J = 1$, as the incident shock foot is reached, this breaks up the vortex and the interaction produces two vortices whose cores lie on a wall-parallel, flow-parallel plane. When $J = 2$, instead, the CVP is higher above the surface and, thus, no visible effect is visible on the oil flow.

5.2.2. Barrel shock and Mach disk

Given the key role that the barrel shock and Mach disk play in the mixing of the secondary channel flow with the surroundings, more details will be hereby provided into the effects of the introduction of the shock into the field.

Figures 5.13a and 5.13b show the streamwise and wall-normal position of the Mach disk, respectively, as a function of the momentum flux ratio. As the shock is introduced into the field, the Mach disk appears to lie more upstream and at a higher location above the wall with respect to the orifice than with no impinging shock.

The effect of the presence of the shock was also observed to be the modification of the barrel shock shape. As illustrated in Figure 5.14, a slight difference in the shape of the barrel can be observed if the images from Figures 5.14 and 5.5. In particular, looking at the downstream edge, it appears to possess a more concave shape in comparison to the flow field purely generated by the jet. Similar observations can be made for the 12-degree case. This result hints at the fact that there might be further upstream influence, possibly given that the flow naturally separates and recirculates downstream of the injecting orifice. This lastly mentioned region does not appear to be visible from the acquired data. Yet, the following subsection will present more results relating to recirculation zones.

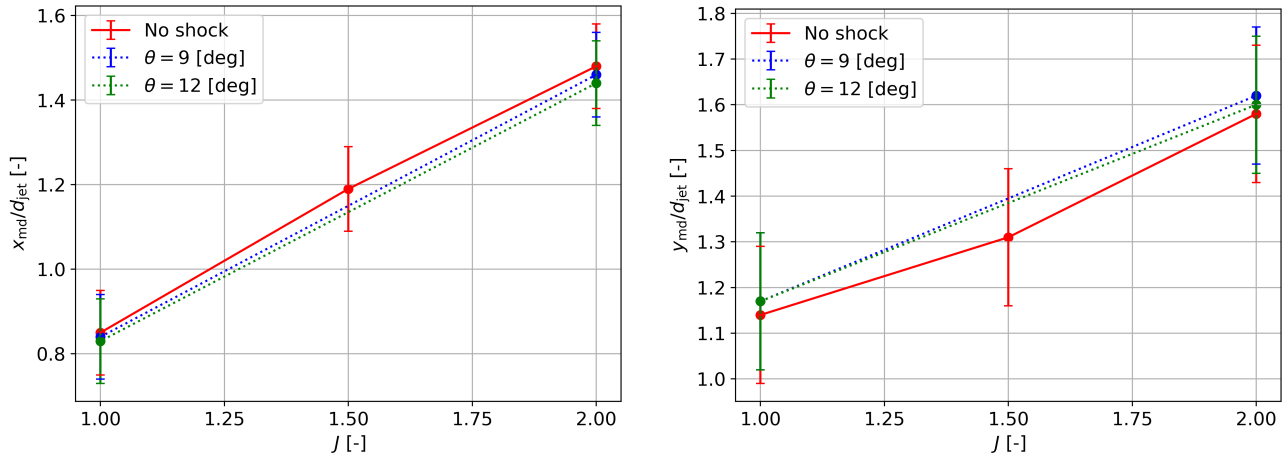

(a) x-coordinate of Mach disk middle point

(b) y-coordinate of Mach disk middle point

Figure 5.13: Plots reporting the position of the middle point of the Mach disk, extracted from Schlieren photographs.

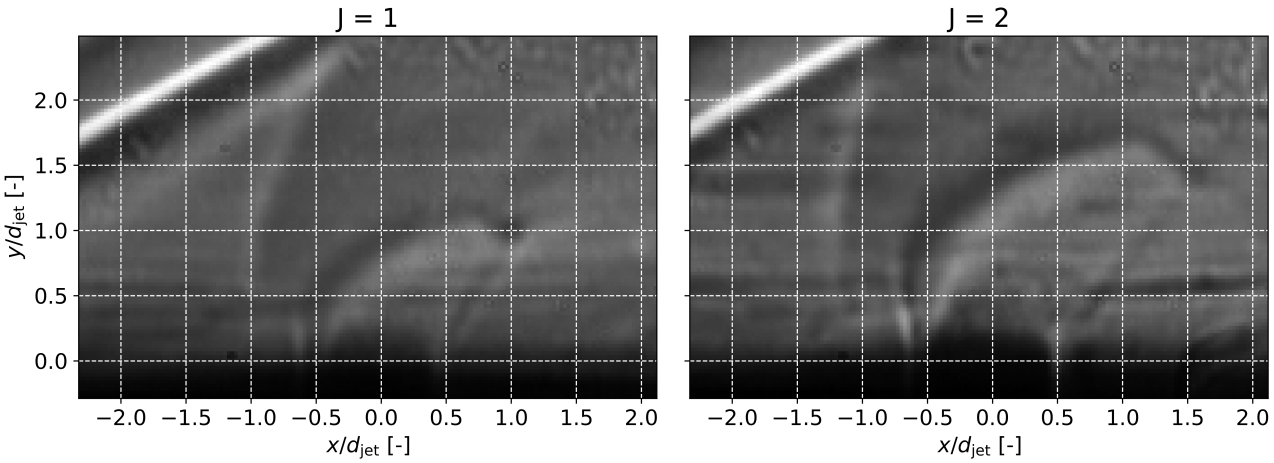

Figure 5.14: Shadowgraph images showing comparison between the barrel shock shape at two J values with the incident shock generated for θ = 9 deg. Similar figures could be obtained for the 12-degree case, which is thus not presented.

5.2.3. Flow separation

A jet exhausting in a supersonic crossflow, due to the abrupt momentum transfer which is thereby caused, generates several separation zones. As illustrated in Figure 5.4, a clear example of such area is the one generated right upstream of the bow shock as a result of the interaction with the freestream boundary layer and formation of a small-scale λ-shock structure. According to literature (Dickmann and Lu (2009) and Sun and Hu (2018b), among others), a second region of recirculation exists right downstream of the port hole. However, it was not possible to capture it with the current imaging set-up. Nonetheless, as the shock is introduced into the test section, it was possible to track the displacement of the compression shock onset upstream of the incident shock foot. In fact, as the upstream separation zone length remains largely unaltered (as expected) with the introduction of the shock, the shock foot location slightly varies, shifting upstream. Figures 5.15a and 5.15b show the results.

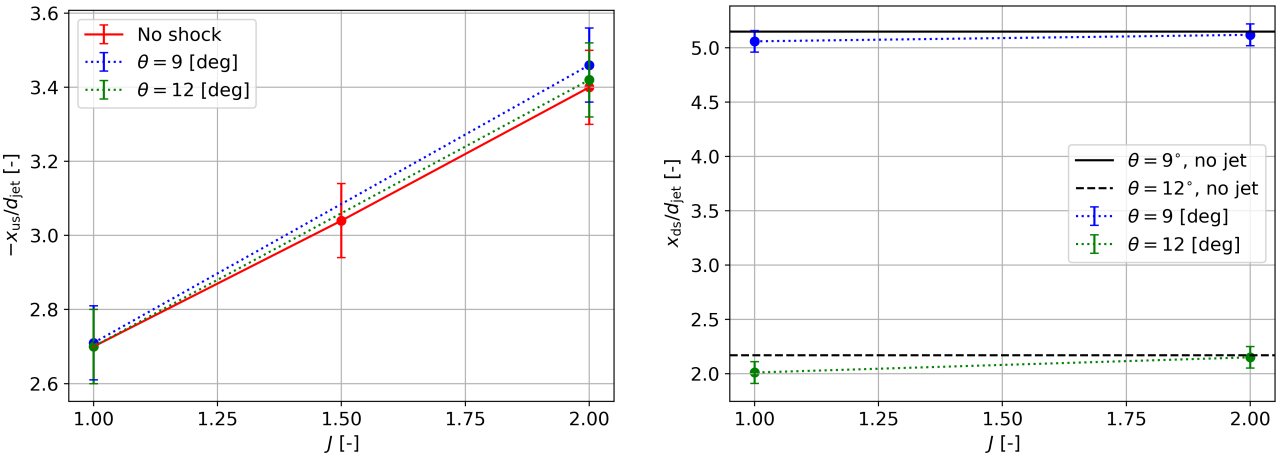

(a) Upstream separation point position

(b) Downstream compression onset position

Figure 5.15: Plots reporting the position of the upstream point of the upstream and downstream separation zones.

Figures 5.16, 5.17 and 5.18 illustrate the flow field on the captured with Schlieren.

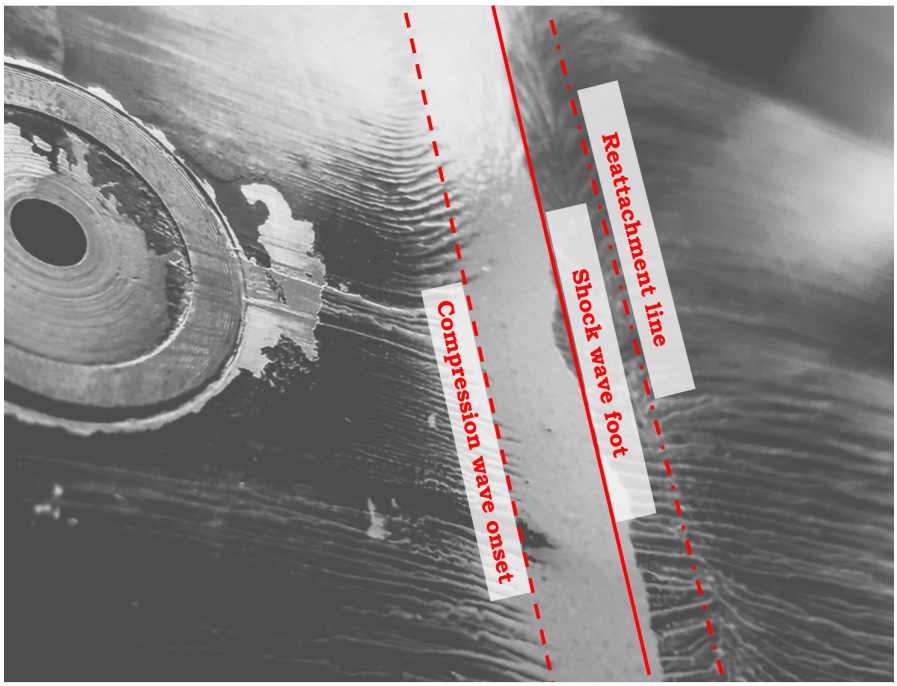

Figure 5.16: Schlieren image of case with no jet and shock generated by $\theta = 9$ deg.

By visual inspection, it indeed appears that no visible changes occur to the onset of separation regions. Of course, the imaging system is unable to focus purely on the interaction in the proximity of the jet. Integration occurs along the line of sight. In addition, the jet-induced bow shock is only present in a fraction of the test section's width. Thus, any interaction of such wave with the incident one will not be visible by means of Schlieren or shadowgraphy. Said bow shock is also much weaker in nature than the incident oblique one. The latter is thus dominant in the determination of the field. Similar results were found for $\theta = 12$ deg, which is thus not presented in this section.

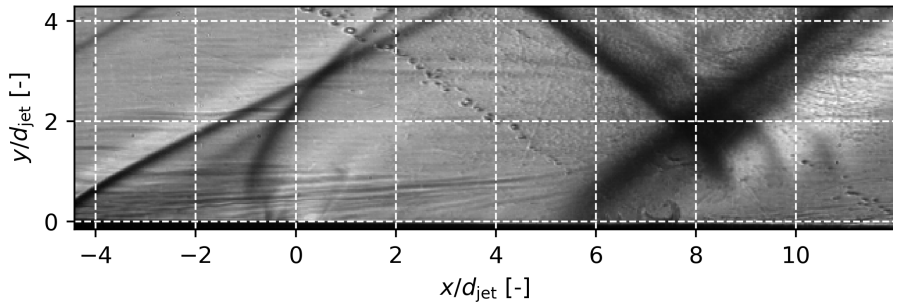

Figure 5.17: Schlieren image of case with sonic jet at $J = 1$ and shock generated by $\theta = 9\,\text{deg}$.

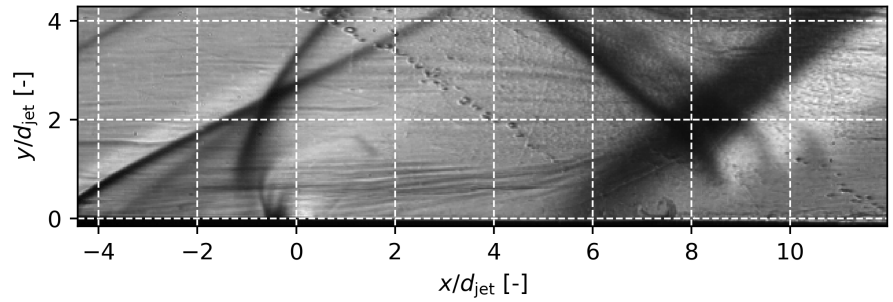

Figure 5.18: Schlieren image of case with sonic jet at $J = 2$ and shock generated by $\theta = 9\,\text{deg}$.

5.2.4. Effect of shock location

As a secondary variable to test, it was decided to investigate the effect of the streamwise position of the shock generator and, thus, of the shock impingement location. In general, it was noticed that the interaction was rendered weaker for all variables but for the onset of the downstream compression wave resulting from the SBLI. First, though, Figures 5.19a and 5.19b illustrate the flow field captured with Schlieren photography. Little to no difference is visible in the images apart from the onset of the weakly visible compression wave, as mentioned in the above. In particular, it seems that the location of separation moves upstream for an increasing momentum flux ratio (see Figure 5.20). As far as the upstream field is concerned (in the vicinity of the jet exit), the barrel shock seems to return to the undisturbed shape, losing the concavity in the downstream wall that was observed in the case where the shock hit more upstream.

The position of the Mach disk also does not seems to be affected by the position of the impinging shock, see Figure 5.21. The downstream ramp causes the Mach disk to sit $\approx 0.2d_{\text{jet}}$ lower above the wall compared to the situation with no impinging shock, whereas the opposite happens with the upstream one. There, a weal increase in elevation of the Mach disk middle point was observed. Still, it can be said that the shock has no considerable effect on the position of the Mach disk and, in general, on the mixing properties driven by the barrel shock itself. It is indeed an expected result, as the flow expected to be supersonic throughout the region of interest. Navier-Stokes being parabolic in the area, no upstream influence is present. Still, some influence ca n be exerted if a disturbance travels through the subsonic portion of the boundary layer with increasing interaction length of the SWBLI. Still, the presence of the shock and, especially, its position compared to the jet's is expected to alter the mechanisms behind near- and mid-field mixing by the generation of large velocity gradients (i.e. shear layers).

Finally, Figures 5.22a and 5.22b show the near-wall flow organization. Compared to the

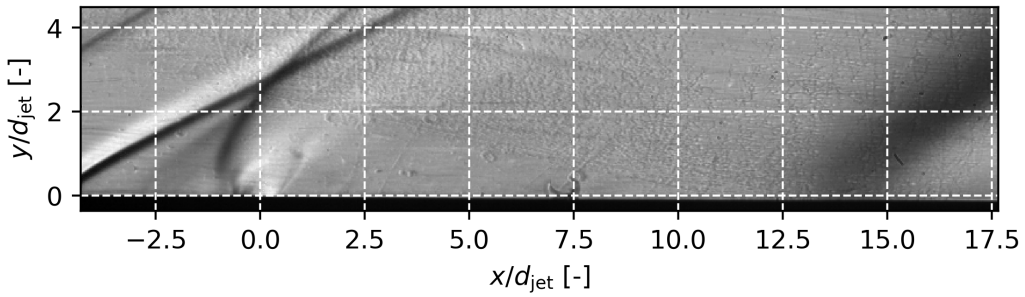

(a) $J = 1$

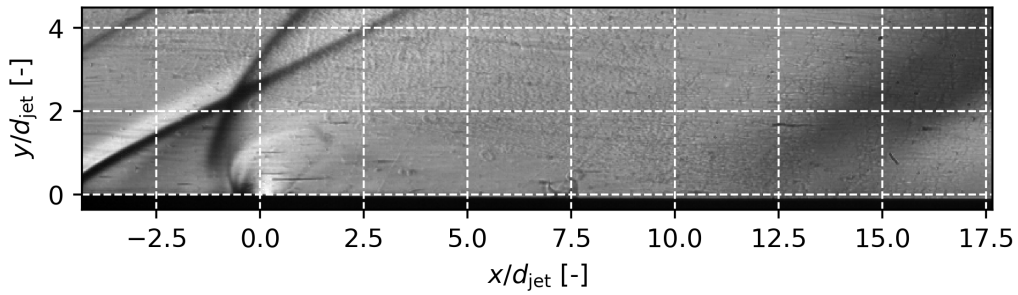

(b) $J = 2$

Figure 5.19: Schlieren image of the flow field generated by the sonic jet interacting with the shock from the 12-degree ramp impinging at $x/d = 20$. Similar observations could be drawn from the 9-degree case, which is thus not presented here.

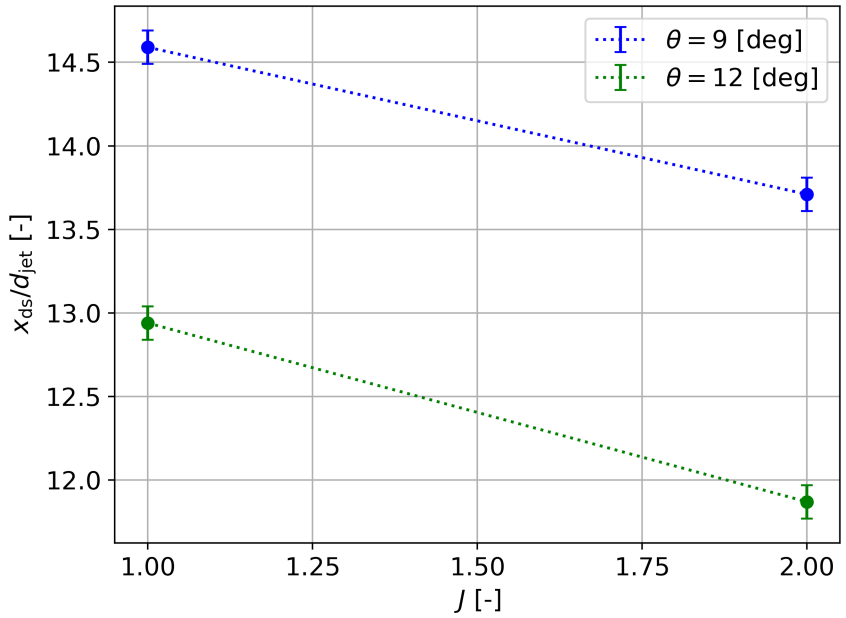

Figure 5.20: Comparison between the onset of the compression wave between the two shocks impinging at the downstream location ($x/d = 18$ for $\theta = 9$ deg and $x/d = 20$ for $\theta = 12$ deg).

situations where the shock was impinging on the surface closer to the nozzle, the pattern here appears to be much more similar to the "undisturbed" jet. Clear friction lines diverge into the oblique separation zone to then re-align with the main stream before hitting the shock front. There, lower-speed flow from the region behind the bow shock interacts with

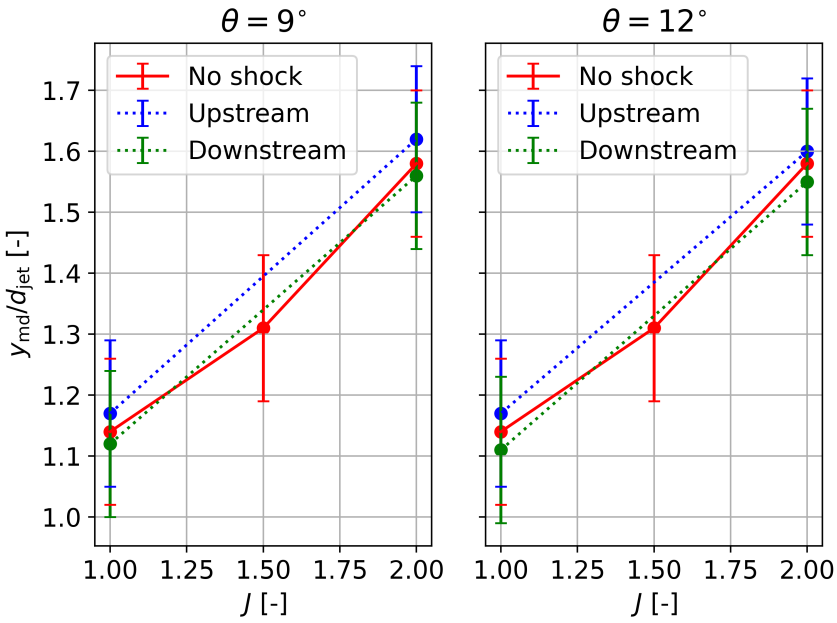

Figure 5.21: Comparison between the position of the Mach disk for varying J when the shock generator is placed at the downstream position (x/d = 18 for θ = 9 deg and x/d = 20 for θ = 12 deg).

the outer flow, smearing the shock and forming vortices. The stronger the shock, the stronger the vortices, as can be evinced from Figure 5.22b. All vortical features that were characterizing the interference flow field when the shock was closer do not appear in the present situation.

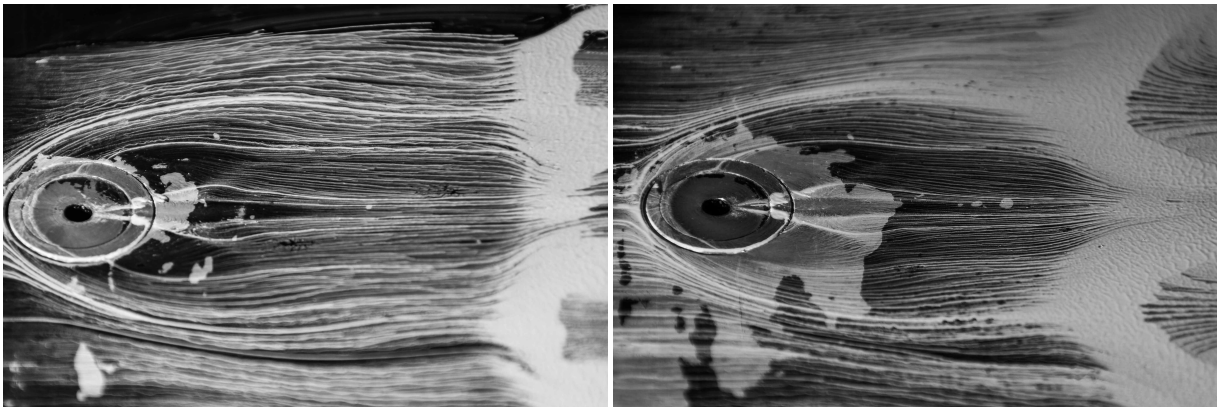

(a) θ = 9 deg (b) θ = 12 deg

Figure 5.22: Oil flow images of the sonic jet at J = 2 with impinging shock at downstream position.

5.3. High-speed Schlieren and shadowgraphy

An attempt was made to capture the evolution of the flow field at very high frequency by augmenting the acquisition frequency of the high-speed camera. The goal of this part of the work is to acquire information relative to the shedding frequency of the vortices at the interface between the jet exit and the crossflow. These are generated by instabilities whose mechanism is similar to a Kelvin-Helmoltz one in nature and is thought to be the main cause of the CVP. In order to have sufficient resolution, the frequency was set in such a

way such a feature travelling along the imaging plane would not move for more than 1 [mm] between one frame and the next. To estimate the acquisition frequency, a uniform flow velocity is assumed behind the bow shock upstream of the jet and equivalent to a Mach 2 flow (Equation 5.1), accounting for the temperature change across the bow shock itself.

$$u = M_\infty \cdot a_2 = M_\infty \cdot \sqrt{\gamma R T_2} \tag{5.1}$$

where the subscript 2 refers to the conditions post-shock. In order to impose a sampling, it is necessary to compute the reciprocal of the estimated transit time of an arbitrary flow feature across the 1 [mm] reference (Equation 5.2).

$$f_s = t^{-1} = \left(\frac{s_{\text{ref}}}{u}\right)^{-1} \tag{5.2}$$

where $s_{\text{ref}} = 1[mm]$. This yields a sampling frequency of $f_s = 125,000[Hz]$. Even at the high frequency, individually shed vortices do not appear to be visible. The reason for this is twofold. On the one hand, their rather small scale renders their detection challenging to begin with. On the other hand, integration of the light beam along its path does not allow for high resolution on the center plane in the test section. Coupled together, the above two factors make the detection of such features on the verge of impossible. Thus, another method needs to be found in order to detect periodic features.

By inspection of the acquired frames, it appears that the barrel shock deforms. Furthermore, the deformation appears to be periodic across several frames. Before drawing any meaningful conclusions, though, it comes in handy to analyze the possible sources of unsteadiness that cause brief alterations in the shape of the barrel shock.

- **Unsteadiness in the nozzle flow.** Twisting in the piping feeding air to the sonic nozzle can generate small-scale vortices which introduce oscillation at the site of the jet exit. Additionally, unsteadiness can be introduced in the jet by the feed flow itself (i.e. not being fed by a uniform reservoir pressure). This factor, however, is ruled out by inspection of images of the free nozzle jet (i.e. without crossflow).

- **Unsteadiness in upstream SBLI.** Inherent transient phenomena in the shock-wave-boundary-layer interaction of the upstream bow shock with the wall layer can never be ruled out completely. Nonetheless, its scale can be compared to the actual motion of the barrel shock appearing from the Schlieren images. Again by inspection of line-of-sight images, such motion does not appear to be relevant in comparison to the extent of the motion of the barrel shock.

- **Kelvin-Helomltz instabilities.** Having rules out all other possible sources of unsteadiness, the only remaining option is, indeed, instability caused by differential velocities and shear stress between the jet and the crossflow.

Coming to the concept first introduced in the above, it was thought to track the motion of the barrel shock in the frequency domain to track the characteristic frequency of the interaction. Figure 5.23 reports some of the stages of the deformation of the barrel throughout approximately one period.

A few observations can be made regarding the evolution of the shape of the barrel shock throughout one estimated period. First, one can spot how the part of the shock deforming

(a) $t = 0$ (b) $t \approx T/2$ (c) $t \approx T$

Figure 5.23: Shadowgraph images of the sonic jet at $J = 2$ at high frame rate, focused on the barrel shock.

the most is the upstream "segment". The downstream one remains relatively steady. The deforming leg arches inward toward the centre line of the jet flow. The perturbations then spreads to the upper segments of the shock wave in a progressive manner (i.e. in a wave-like fashion) until it reaches the edges of the Mach disk and the motion repeats.

To perform a frequency analysis on the images, cross-correlation is performed across bitmaps. The procedure in use is the following.

1. Post-process the images in order to obtain a new one with increased contrast and brightness.
2. Isolate the area of interest within the picture itself. This can correspond to the whole barrel shock or just a specific portion of it. The pros and cons of selecting either the whole barrel or a smaller sample will be discussed in the foregoing.
3. Identify a "quantity of interest": a parameter to be tracked across all time instants whose time series will be mapped onto the frequency domain at a later step.
4. Perform correlation of the individual snapshots in time with a baseline image (i.e. taken virtually at $t = 0$).

Before delving into the results, Equation 5.3 reports the definition of cross-correlation for a one-dimensional signal.

$$\rho = c(u) = (f * g)(u) = \int_{\infty}^{\infty} f(x)g(x+u)\mathrm{d}x \tag{5.3}$$

where the variable ρ is the *correlation coefficient*. In the case where $f = g$, the operation is termed *autocorrelation*. The discrete version of Equation 5.3 is shown in Equation 5.4.

$$\rho = c[l] = \sum_{j=-\infty}^{+\infty} f[l]g[l+j] \tag{5.4}$$

where l is an integer number. Extending this reasoning to a two-dimensional discrete signal, such as an image bitmap, the cross-correlation coefficient can be re-written as in Equation 5.5.

$$c[l_1, l_2] = \sum_{j_1=-\infty}^{+\infty} \sum_{j_2=-\infty}^{+\infty} f[l_1, l_2]g[l_1 + j_1, l_2 + j_2] \tag{5.5}$$

The choice of the correlation window is critical. In fact, a too large window leads to inconclusive results due to large noise introduced by the pseudo-random oscillations in

brightness level of individual pixels across the bitmap. A too small window, instead, could reveal local characteristic frequencies which, however, are not representative of the actual periodic behaviour. The window size should just be the result of a trade-off between being able to identify the characteristic frequency (presumably the one with highest power spectral density) without having a signal engulfed in noise. Several window sizes and shapes were put to the test and are shown in Figure 5.24. A first attempt was made by taking, as correlation window, the rectangle circumscribing the barrel (—). A more localized, still two-dimensional, window was then tested in the region where the shock was observed to deform the most (- - -). The quantity of interest for both cases was taken as the maximum of the correlation coefficient between one frame and the next. Upon gathering the poor results provided by either method, it was decided to go for a one-dimensional window (i.e. a line) instead. The tracked quantity here changed as the "displacement" of the shock instead. Both horizontal (- - -) and vertical (—) were tested. More details on this procedure are going to be presented in the foregoing.

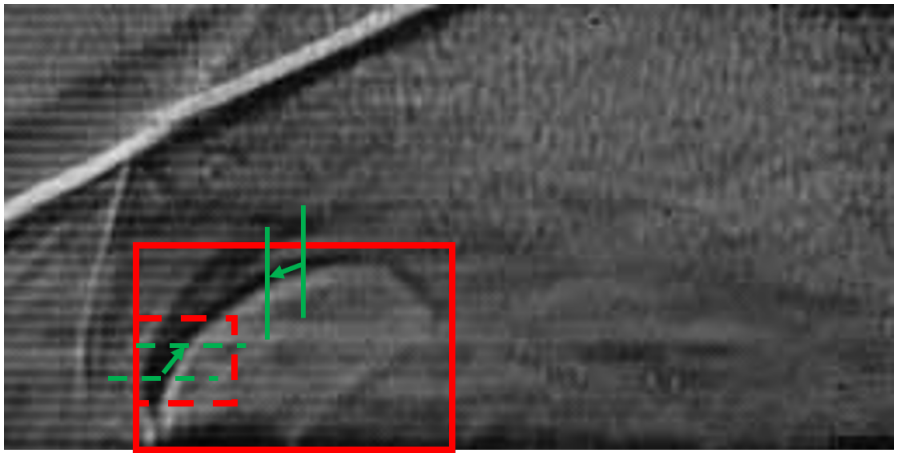

Figure 5.24: Various methods of selection of correlation windows.

In the case of the line window, it is necessary for its middle point to coincide almost exactly with the location of the shock at that instant. Therefore, if the segment is not "aligned", it will have to translate in order to have its centre coincide with the point of maximum brightness of the signal. Figure 5.25 reports the three plots generated by the analysis: the baseline, instantaneous and correlation signals for the case of horizontal traversing. This serves as an example to illustrate the methodology followed for the processing of this data.

The top plot and the middle plot in Figure 5.25 both show a peak roughly in the centre of the domain. This brightness high-point coincides with (approximately, ± 2 [pix]), the location of the barrel shock at the station. The shift between those two reveals the displacement in time. As the resolution of the imaging system with the given lens is known (9 [pix/mm]), it is readily possible to compute the distance "travelled" by the shock frame between one frame and the next by comparing the location of the peak of the correlation signal. Before displaying a full comparison in the results generated by one type of window compared to the other, a secondary consideration must be made. The algorithm of the correlation function has a time complexity of $\mathcal{O}(N_i \cdot N_j)$, being N_i and N_j the number of sample points (in this case, pixels) in either set. This means that, for the case where the sample is one-dimensional (i.e. traversing techniques), the runtime is going to be much shorter.

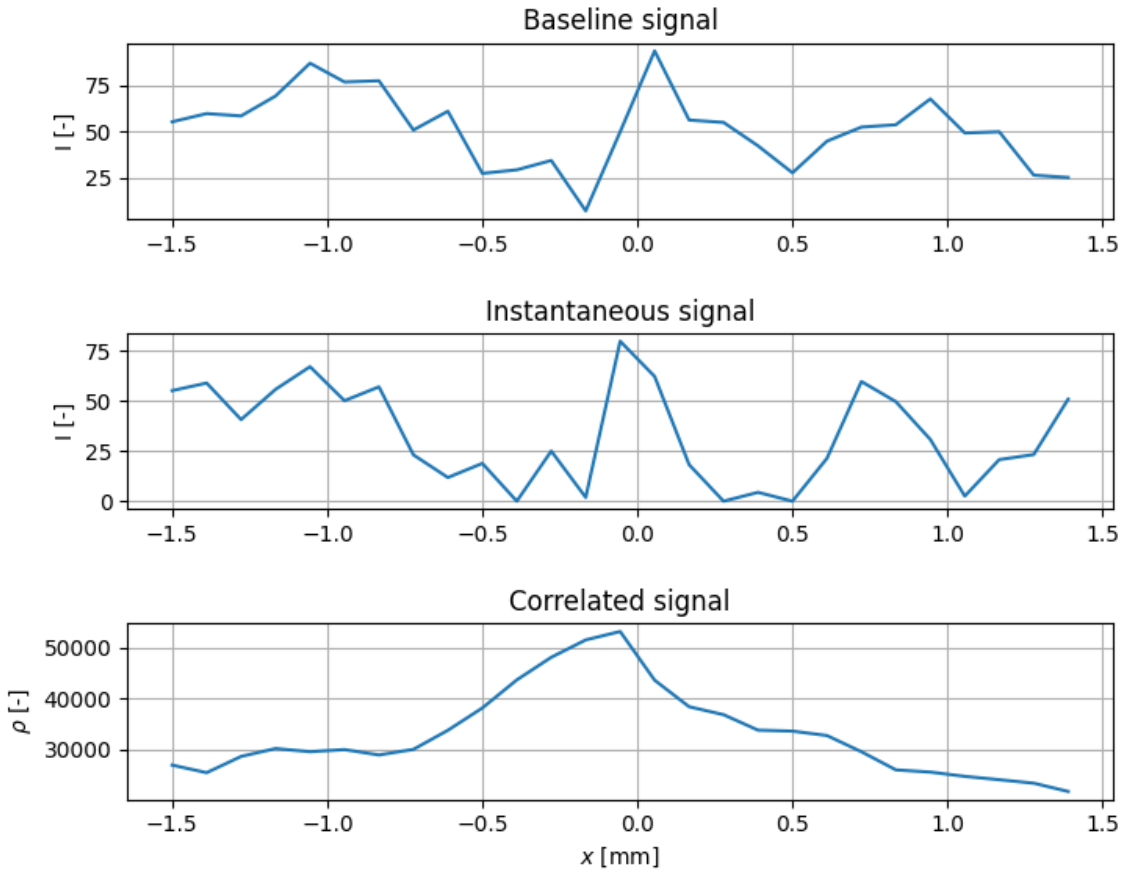

Figure 5.25: Baseline (top), instantaneous (middle) and correlation coefficient (bottom) signals for horizontal traversing of high-speed shadowgraphy images of the sonic jet with $J = 2$.

Figure 5.26 presents the results arising from the comparison of the methods for selecting the correlation window as described in the above. To properly read the plots, the definition of the Strouhal number is reminded in Equation 5.6.

$$St = \frac{fL}{u} = \frac{f d_{\text{jet}}}{a_\infty M_\infty} \tag{5.6}$$

where f is the characteristic frequency, L a reference length (here taken as the diameter of the nozzle, $L = 4$ [mm]) and u is a reference flow velocity (here taken as the freestream velocity $u = u_\infty = 509.11$ [m/s]). The first factor that strikes the eye is certainly the scatter of the data points, also at the same momentum flux ratio. The plots only appear to provide conclusive evidence relating to the order of magnitude of the characteristic frequency (Strouhal number), which appears to lie in a vast range between 0.05 and 0.25 for all cases. When comparing horizontal and vertical traversing techniques, it also appears that the vertical analysis shows less spread than its horizontal counterpart. The reason for this lies in the motion of the barrel shock, which indeed displays more tone in the wall-parallel direction.

The highly scattered result do not come as a complete surprise. Indeed, experiments from literature report a rather different configuration of the measurement technique. From Gruber et al. (1997) who performed PLIF measurements to Ben-Yakar and Hanson (2002) using ultra-high-speed Schlieren techniques. By reading the latter work in detail, it is able

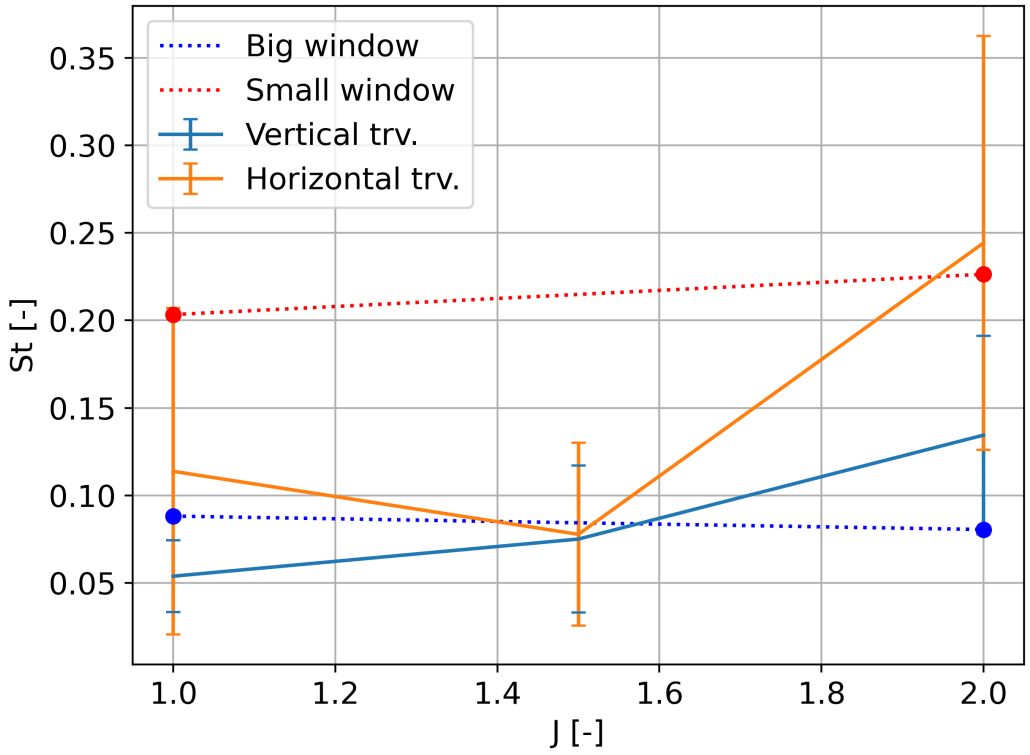

Figure 5.26: Plot showing a comparison between the frequency analyses performed using the several methods described in the above for the selection of the correlation window. Plotting Strouhal number versus J.

to draw some conclusion as to why the current Schlieren technique and data processing method might not be successful.

- **Eddy tracing.** The way the authors are able to track the fundamental frequency of eddy shedding at the leading edge of the orifice is by identifying and mapping the course of each individual eddy as they are expelled into the crossflow. The shedding mechanism does not appear to be directly correlated to the deformation of the windward side of the barrel shock.
- **Jet species.** To obtain the needed image contrast to be able to "see" the eddies, jet and crossflow species were not the same. The former was air and the latter hydrogen. This means that the different density allows the Schlieren system to acquire large density variations, leading to greater contrast.
- **Frame rate.** The frame rate in use for imaging in the work by Ben-Yakar and Hanson (2002) is on the order of [MHz], whereas the one used for the present work is only 125 [kHz], thus lacking several orders of magnitude. The current is not even able to achieve such high acquisition frequencies without cropping the image to a level where no relevant information can be extracted.

5.4. Recap

This first test campaign was carried out in order to evaluate the available test set-up, as well as to obtain preliminary results concerning the interaction of a sonic jet with a supersonic crossflow and an incident oblique shock wave. The goal is now to perform modifications to

the parts as a mean to improve the quality of the obtained results. The main limitations and disadvantages of this first test round are listed below.

- **Limitations of the measurement techniques.** Being Schlieren and shadowgraphy line of sight techniques, integration of the optical properties is inherently performed along the light path. This results in images which do not provide sufficient insight into the features on the plane of the jet's orifice. It is this location that sees the most flow features being created from the resulting interaction. It is therefore deemed necessary to perform further investigation implementing more local flow measurement techniques. Stereo particle image velocimetry is thought to be a technique with a more sound potential.

- **The test set-up.** Some issues concerning the test set-up itself were also noticed from the first round of testing. The installation of the nozzle plug is performed by screwing it onto the plate on the lower guide wall of the tunnel. This leads to small but noticeable discontinuities on the plate's surface. Oil flow visualization reveals that small-scale vortical features arise as a result of the interaction, such as in Figure 5.22b.

- **The shock generator.** Two more issues are related to the design and the mounting of the shock generator. The first is that, between the chosen angles of $\theta = 9\,\text{deg}$ and $\theta = 12\,\text{deg}$, it is not possible to replicate the exact same shock impingement location. This, of course, generates disparities in the results and renders the comparison somewhat more challenging. For this reason, a new sliding support for the ramp was designed for the next experimental campaign.

Still, this preliminary test round was useful in the determination of some first result and the confirmation of some expected findings. Additionally, the set-up was proven effective and in good conditions. No blockage effects have been observed the most critical cases: high-J injection with strong oblique shock wave. Of course, PIV measurements require a probe to be inserted in the stream to reflect the laser beam towards the region of interest. However, the set-up has been proven also for other experiments with even stronger shocks in ST-15 and the bow shock is a rather weak wave. Thus, no critical issue in terms of blockage is expected to occur.

The conclusion that were extracted from this campaign are the following.

- **Momentum-driven features in the near field remain unchanged.** The addition of shock of the shock wave does not seem to alter the position of the Mach disk by significant features, as the variations, also considering uncertainty, all lie within the same range.

- **The shock position influences separation.** Although not fully quantifiable due to integration along the line of sight performed by optical methods, it was understood that the shock position affects the separation length. Still not clear how the interplay evolves between the separation caused by the jet and the one caused by the SBLI, it is something that will be more thoroughly investigated with PIV.

- **Flow structures.** Schlieren, shadowgraphy and oil flow revealed insight into the flow structures emerging from the interaction. Of course, a full resolution of the flow structures such as was performed in Liang et al. (2018) is not possible at this stage.

- **Near-wall vortices.** Oil flow visualization reveals the presence of vortices in the boundary layer whose axis is normal to the wall when the oblique shock wave impinges on the plume. These are thought to have a key role in the mixing of the flow in the near-field.
- **The effect of *J*.** An increasing momentum flux ratio was observed to cause an increase in the size of the barrel shock and its position above the wall and downstream. As shown by Erdem et al. (2012), the increase in Mach disk height would abide by a power law. The increase was observed to be linear, which is indeed expected given the small J-range in use. Slight effects have been reported for the onset of the compression wave as well.

Given the above conclusions, it is necessary to decide which configurations are going to be tested using PIV. First, of course, baseline measurement are deemed unavoidable to quantify the field before the introduction of the perturbing element: the shock. The same goes for the quantification of the field with a shock but without the jet. Then, the variables that will be tested using PIV are going to be: the momentum flux ratio, flow deflection angle and downstream impingement position. Two values for each parameter are going to be chosen. Additionally, wall-parallel measurements are going to be acquired in an attempt to gather more information on the development of the near-wall vortices mentioned in the above.

6

Quantification of the interaction field by means of PIV

The purpose of this chapter is to present the results gathered using PIV techniques and their towards the answering of the research questions in Chapter 1. In addition, the initial part of the chapter will be dedicated to the presentation of the preliminary results.

6.1. Image acquisition

Following imaging parameters established in Chapter 4, Section 4.3.1, it is necessary to check the quality of the acquisition before delving into further processing. First, the field of view is presented, with pointers to the various features, in Figure 6.1a and 6.1b.

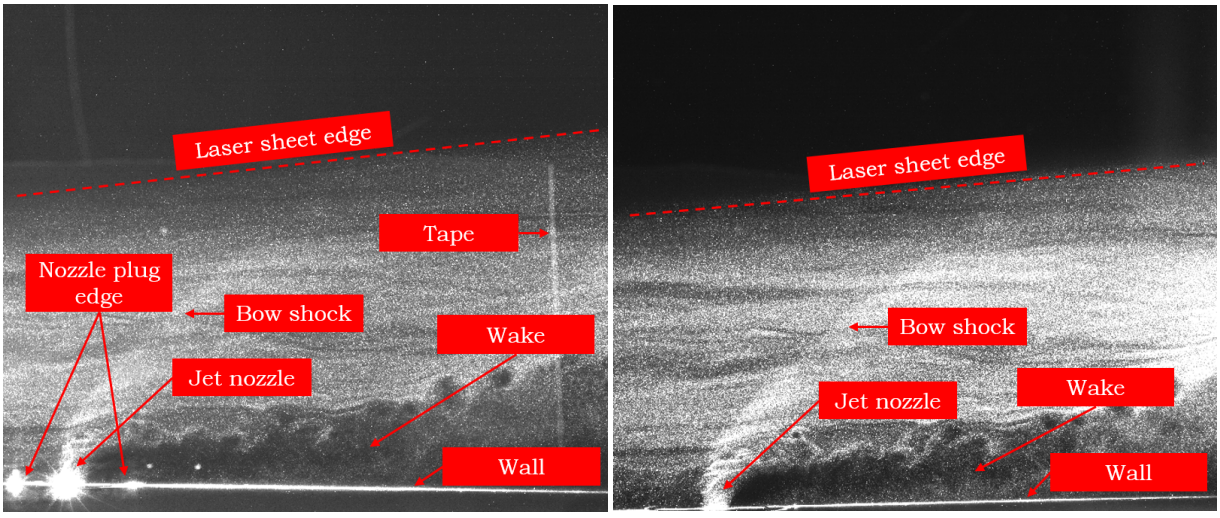

(a) Downstream camera (b) Upstream camera

Figure 6.1: Views of upstream and downstream cameras with pointers to specific features. Images acquired during a run with $J = 1$ with no oblique shock impinging.

A few observations need to be made to clarify the properties of some of the features in the images. First and foremost: the laser sheet. By inspection of Figure 4.9a, one can deduce how the probe is inserted in the stream with an vertical offset to the lower wall of half the test section's height. To ensure complete illumination of the region of interest (i.e. the jet), the probe had to be turned downwards, thus resulting in a sloped edge of

the sheet. Still, the height of the laser-captured area is always more that 4 cm (or 10 x/d), which is more than enough to capture all necessary flow features. Several reflection are, unfortunately, present during acquisition. The brightest of these is certainly the one caused by the jet nozzle. In an attempt to reduce its brightness, the whole setup was repainted black, including the inside of the nozzle and the entire holding plate. However, it was not possible to remove them completely. Additionally, a piece of tape was glued to the port window (visible in Figure 6.1a) to absorb more of the light reflected by the glass. During processing, the most problematic areas in terms of malevolent light reflection are masked, at the expense of the quality in the immediate vicinity of degraded area. Finally, the particle images give an initial impression of the flow features themselves. For instance, the bow shock induced by the jet is clearly visible from these photographs, as well as the vastly turbulent region in the wake of the injection.

Regarding the quality of seeding, the images in Figure 6.1a and 6.1b highlight two different regions characterized by two different source densities (i.e. the fraction of the field of view occupied by particles). A more uniform seeding distribution can be found in the undisturbed freestream, where the effects of the momentum transfer caused by the normal injection give way to the uniformity inherent to the freestream flow. A second region where seeding is more rarefied can be, instead, seen downstream of the nozzle's position. There, flow separation couples with the momentum transfer away from the wall caused by the jet, causing a rather sparse distribution of oil droplets. It must be mentioned that the seeding was observed to vary widely from image pair to image pair, due to the seeding rake in the settling chamber being rather unsteady. The seeding in the jet, instead, remains steady throughout the run due to it being on a direct line to the seeder.

Considering the two regions (wake and undisturbed flow), it was possible to compute the number of particles per pixels by applying a local maximum filter to the brightness bitmap. The number of maximum peaks found by this method was then divided by the total number of pixels inside the specific regions to get the particles density (per pixel), expressed in particles per pixel ([ppp]). Figure 6.2 shows which regions were considered for this analysis.

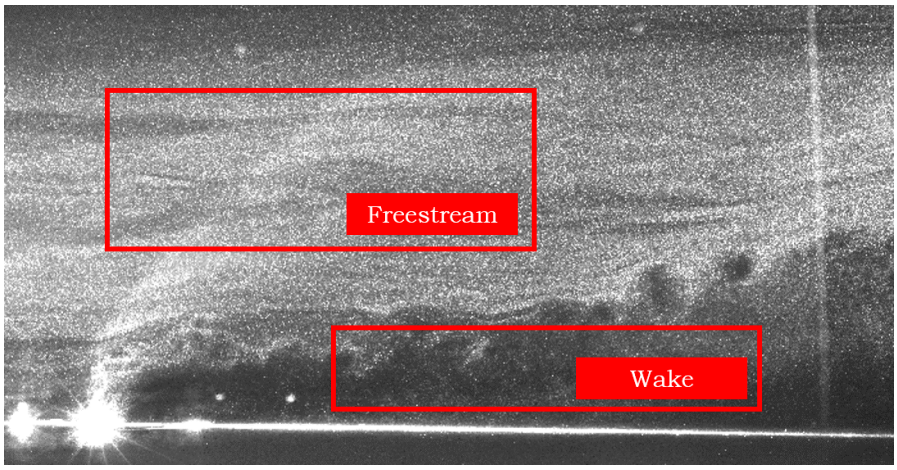

Figure 6.2: Schematic of how the field can be divided according to its particle density.

By computation with the above method, it was found that the freestream region has a particle density of 0.080 [ppp], whereas the wake of 0.073 [ppp]. These values lie well within the range of particle density that literature (Raffel et al. (2018)) and experience

consider acceptable and in the optimal range for cross correlation to operate on the particle images. The chosen wake region is not the most critical one, though. The one in the immediate near field downstream of the injection could not be processed properly due to large noise. Still, the density is still deemed good enough for further processing with DaVis, even though it is expected that the standard deviation of the measurement in the area is going to be significantly higher than in the rest of the field. A second wall-normal plane was also imaged (z/d = 2). This location was chosen because of the offset with respect to the centre line of the test section and the fact that the jet's momentum transfer is reduced at this position and thus the difference in source densities is reduced. Due to the bright reflections and higher uncertainty in the boundary layer, it is the case that a "strip" of data will be neglected in the near-wall region. In particular, the height of this region varies between one and two interrogation window heights and it appears as a data-less strip in the bottom of the velocity fields presented in the foregoing.

An analogous process can be followed for the wall-parallel imaging. There, the difference between wake and freestream regions are less evident. In fact, as the laser sheet effectively "floats" above the wall, its seeding is less sensitive to the momentum transfer caused by the jet. Figures 6.3a and 6.3b show the camera view and the selected region of interest, respectively.

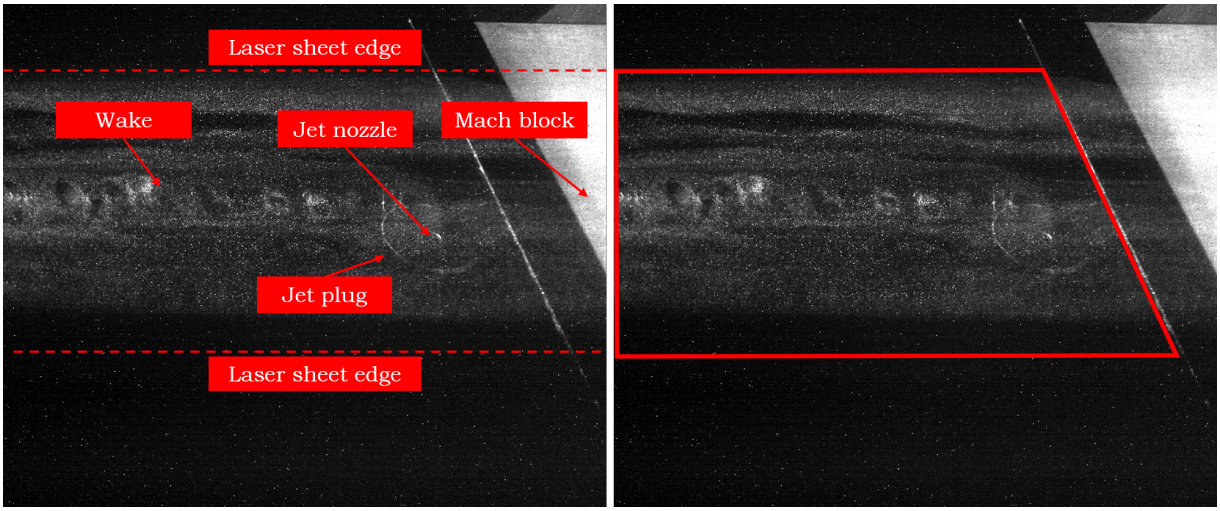

(a) Overall view and pointers to specific features (b) Field of view selected

Figure 6.3: View and selected region of interested for wall-parallel imaging. Shown is the plane $z/d = 2$, but analogous figures can be produced for $z/d = 1$. Views from camera 1.

Using the same principle in the above for the computation of the number of particles per pixels, it was found that the tracer density for this imaging configuration is slightly higher than for the previous imaging plane: 0.081 particles per pixel. A word of caution must be mentioned. In fact, as the laser sheet shines parallel to the wall, any dust particles that lies on the wall itself or particle tracers that get stuck to it during the tunnel run will reflect enough light for the software to detect them as actual PIV particles. This introduces an error in the results. A poor quality of imaging is, in fact, observed for the imaging of this plane. This effect becomes less of an issue for the plane at $z = 2d$ as the background wall is then less sharp, due to the focal plane being higher.

Prior to acquisition, calibration had to be performed. This was a twofold procedure. The first step is the *geometric* calibration. As the stereo system is composed of two cameras

looking at the test section from two different viewing directions, images appear distorted due to perspective. A de-warping procedure is applied the views of either camera by identifying a set of common points along physically orthogonal directions. A calibration plate has to be used (DaVis Type 10). By matching the same features on both views, the image field is reconstructed either by fitting the information to optical distortion laws or by creating a third-order polynomial approximation of the pixel map. The former method is more robust, as it holds also in areas outside the calibration, effectively mapping the whole camera view to a new field. The latter, although generally seen to be of higher quality, only holds in the part of the image covered by the calibration plate (it is a polynomial fitting). Now, if the geometric calibration were 100% accurate, producing a net 0 error, then the procedure would be complete. In practice, however, this is seldom achieved. Hence, a second calibration step, known as *self*-calibration, has to be executed. In this procedure, the algorithm looks for displacement between the camera views after the geometric calibration is complete. The displacement is caused by image optical misalignment. To identify and correct for this, cross-correlation is performed between the views of either camera. Generally, a constant translation is found between the images. Applying this correction iteratively progressively leads to a negligible error between images, indicating that calibration is complete and acquisition can start. The second calibration step is of particular importance for stereo imaging. In fact, as the error in the estimation of the out-of-plane component is sensitive to the viewing angle of the cameras, a misalignment given by poor calibration leads to an amplification of the uncertainty in the computation of such component. For the present study, self-calibration reduced the RMS error due to misalignment to values of $\mathcal{O}(10^{-4})$. The only instance where this procedure failed was for wall-normal imaging at $y/d_{\mathrm{jet}} = 1$, where noise is thought to be a determining factor in degrading the quality (see above).

Finally, before introducing the actual results, it is necessary to report the steps taken and the parameters in use during processing. In particular.

1. **Image pre-processing.** A Butterworth filter was applied to all particle images with a window length of 7 frames. This is meant to sharpen the image and improve particle contrast with respect to the background. It is a type of low-pass filter that allows for a de-noising effect, blocking high-frequency features of the image and allowing lower-frequency ones to remain. Also operates as a smoothing filter.

2. **Image masking.** This operation serves as a way to “neglect” the part of the image that is outside the region of interest or the laser sheet or houses quality-degrading reflections.

3. **Vector calculation.** A multi-pass correlation method is applied to compute the vector field. First, a single pass with a circular window with size 64x64 is performed, followed by two additional passes with smaller 32x32 interrogation windows.

4. **Vector validation.** Effectively a sub-part of the previous step. This process checks for faulty vectors in the output of the multi-pass correlation. It detects outliers outside of the 3σ bounds, it deletes them and replaces them with an interpolated vectors from the neighbouring region.

5. **Statistics.** Once the field is computed over all 900 images, the mean distribution, the standard deviation along with uncertainties and Reynolds stresses is generated.

6.2. Baseline results

Following the same rationale as for the presentation of the results for line of sight techniques, it is first necessary to introduce the baseline results. These correspond to the scenario of having a jet with no impinging oblique shock wave and, conversely, of a shock without the interference of the jet.

6.2.1. Jet with no shock

Figures 6.4a and 6.4b display the streamwise and flow-normal velocity components, respectively.

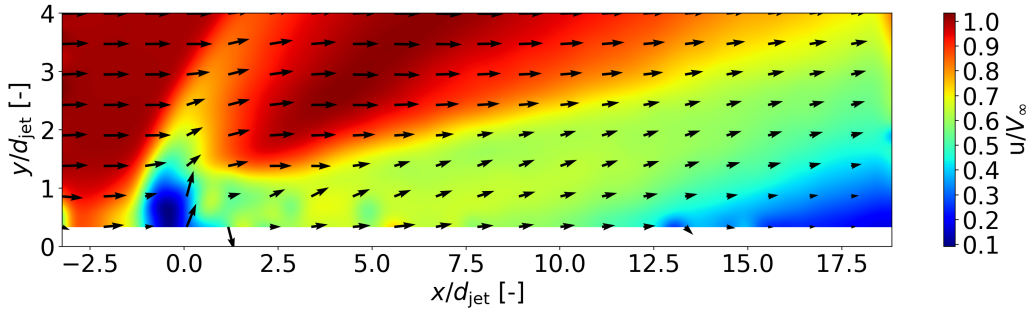

(a) Streamwise component (u)

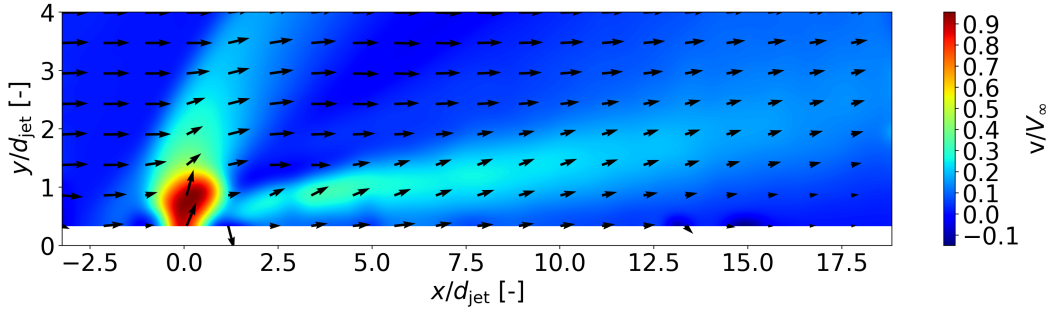

(b) Vertical in-plane component (v)

Figure 6.4: J = 1. Coloured by x- and y- components of velocity.

Already from the distribution of the u-component of velocity one can readily identify the most relevant features of the interaction of transverse sonic jet with a supersonic crossflow. For instance, the bow shock appears extremely sharp across the flow field, becoming weaker and weaker as the y-coordinate increases. Also, the separation zone downstream of the jet location is rather clear, with the velocity close to the wall decreasing further and further as the x-coordinate shifts towards the exit of the field of view. A secondary, weak oblique shock wave also appears towards the downstream end of the image. As mentioned in several works of literature Sun and Hu (2018b), Dickmann and Lu (2009), the separated bubble creates an obstacle to the incoming flow. As far as the velocity distribution is concerned, the u-component drops from about 500 m/s in the freestream to almost 0 at the nozzle location, to recuperate partially in the separation zone. The vertical component, instead, remains mostly null, apart in the neighbourhood of the bow shock and the separated region, where a weak updraft pulls the flow from the wall. In the case of the jet wake, this is caused by the combined action of the CVP and the flow deflection imparted by the developing boundary layer. The region where this component is the highest is, obviously,

the actual jet, whereby the position of the barrel shock and Mach disk is clearly visible.

A comparison can be also drawn between the two momentum flux ratios in testing: $J = 1$ (Figure 6.5a and 6.5b).

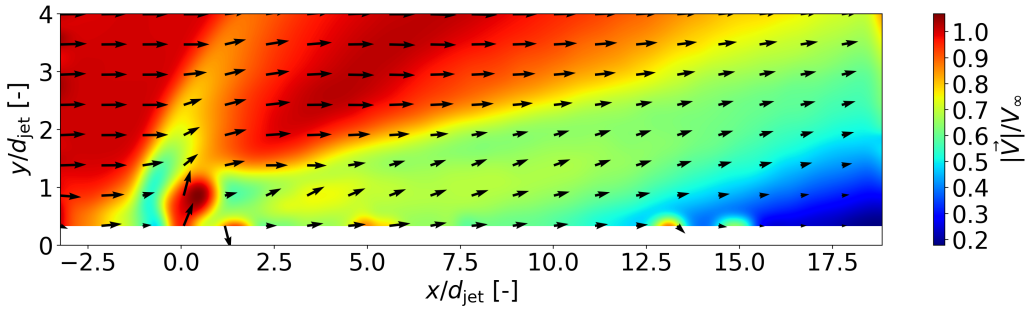

(a) Lowest momentum flux ratio, $J = 1$

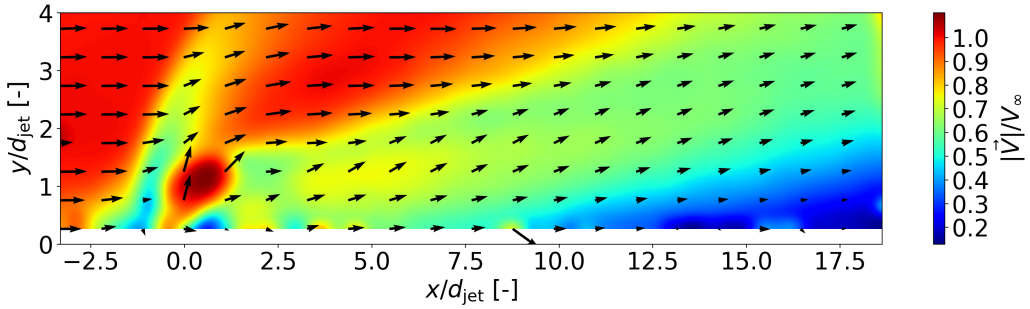

(b) Highest momentum flux ratio, $J = 2$

Figure 6.5: Baseline results with J = 1,2. Coloured by norm of velocity.

The result observed in the figures above is consistent with the observations performed with the Schlieren measurements described in Chapter 5. In particular, the size of the barrel shock and the length of the Mach disk increase when increasing J from unity to 2. Also, the extent of the separation zone appears to be larger for the larger-J case.

Finally, some observations can be made on the out-of-plane component, shown in Figures 6.6a and 6.6b. The regions where flow should be essentially undisturbed still show a non-zero (and slightly negative) value for the out-of-plane component w. This is to be blamed potentially on a slight misalignment of the laser sheet to one side or an error in the self-calibration procedure. Still, the value of velocity measured lies between 10-20 m/s, which brings the measurement within 4% of the freestream velocity. Anyhow, the regions where most fluctuations occur is reportedly the one in the downstream near-field of the jet injection point due to flow separation.

It is now possible to focus on the results of the wall-parallel imaging. The reader is reminded that the Pitot tube inside the jet injection assembly failed during one of the runs. To ensure consistency in the measurements, it was decided to only run the set-up with one momentum flux ratio. Given the newly weakened set-up, the lowest pressure was opted for: $J = 1$.

Figure 6.7a and 6.7b display the vector field coloured by the velocity magnitude. The comparison of the two vector fields highlights, of course, the same flow features that could

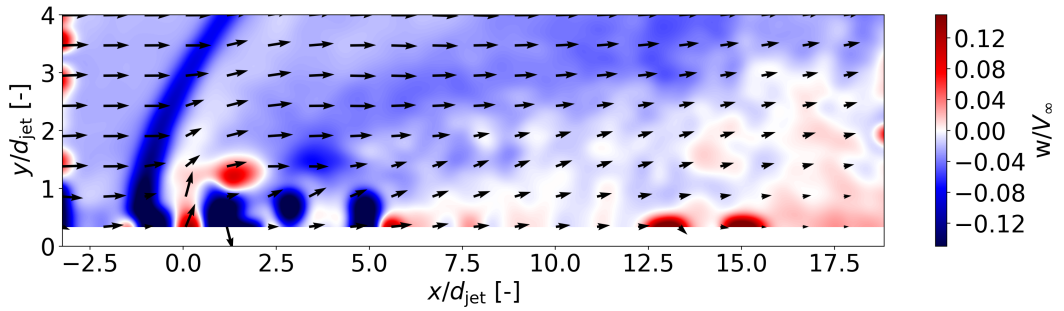

(a) $J = 1$

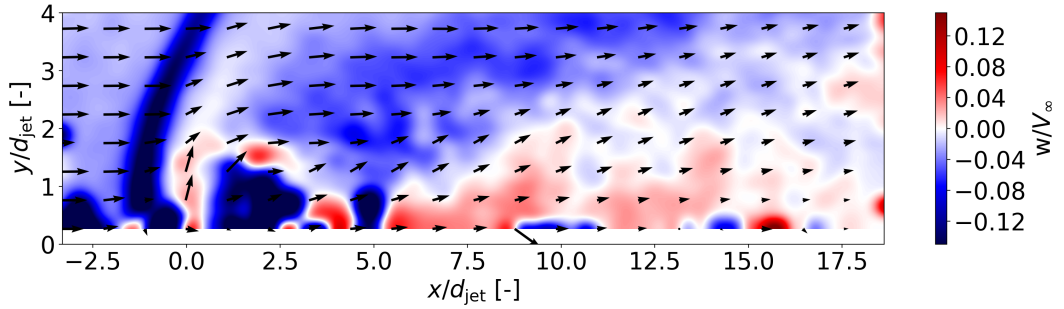

(b) $J = 2$

Figure 6.6: J = 1,2. Coloured by w-component of velocity.

be observed for wall-normal imaging. First, a few observation can be noted on the general quality of wall-parallel measurements. First, again: the reflections. Albeit the paint on the tunnel wall and the masking of the most critical portions of the region of interest, light reflections off the jet's plug and the inside of the jet nozzle caused interference in the determination of the vector cross-correlation in their vicinity. Further processing contributed to rendering the field smoother than the actual raw output of the image cross-correlation, but local quality degradation is still visible nonetheless. Of particular nuisance is the rim of the plug containing the nozzle. Given the sharpness of the edge, it causes bright reflections, which DaVis interprets as low-velocity streaks, given their constancy throughout the run. Also, due to field of view of the cameras, the runs imaging the plane at $y/d = 2$ display an asymmetric region of interest (i.e. instead of ranging from -6 to 6, they range from -4 to 6 z/d).

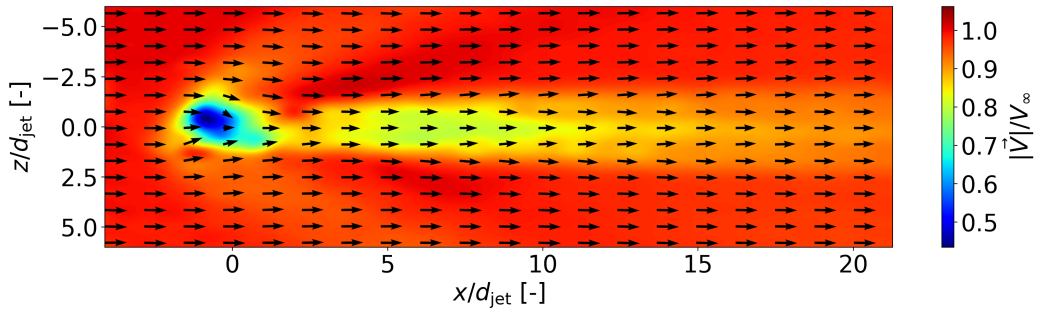

(a) $y = d_{\text{jet}}$

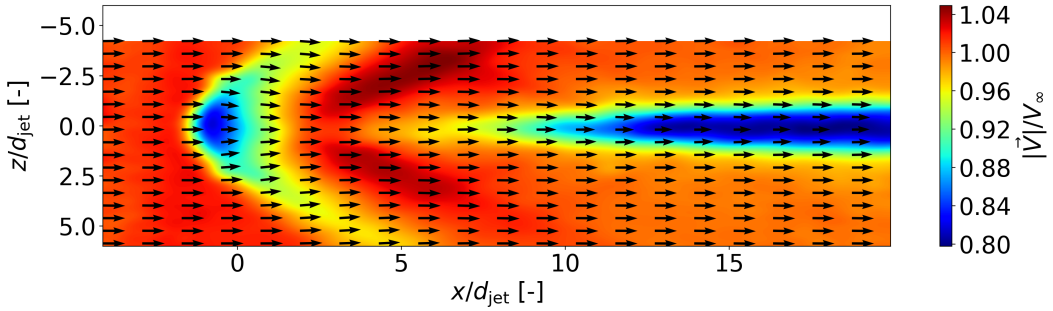

(b) $y = 2d_{jet}$

Figure 6.7: J = 1. Coloured by velocity magnitude.

Considering now the flow features that are visible off Figures 6.7a and 6.7b, readers can immediately spot the bow shock forming upstream of the jet exit, as well as the expanding wake. The reader is reminded that the plane $y/d = 2$ is located a approximately 2 mm above the termination of the barrel shock (i.e. the Mach disk), whereas the plane $y/d = 1$ "cuts through" the barrel shock. Figure 6.7a shows a large lower-speed region in the vicinity of the (0,0) coordinate, coinciding with the jet exhaust in the crossflow. Furthermore, as the plane lies 4 mm above the wall, which also coincides with the average thickness of the boundary in the test section, the freestream velocity does not match the expected value for $M_\infty = 2$ flow. Indeed, deceleration caused by the wall layer still influences the flow at that specific height above the wall. Of course, this is no longer visible where, instead, $y = 2d$, lying well outside the influence of the boundary layer. As far as the jet is concerned, on this higher plane the momentum transfer caused by the exhaust in the near field is no longer visible. Instead, the far wake "emerges" above the laser sheet at a downstream distance of roughly 8 jet diameters, where the most of the jet-related abrupt momentum transfer has already occurred. In fact, the velocity in the wake appears to be much larger in Figure 6.7b than in Figure 6.7a. Similar conclusions can be drawn from the display of the w-component (Figures 6.9a and 6.9b) and the out-of-plane component (now v) in Figures 6.8a and 6.8b.

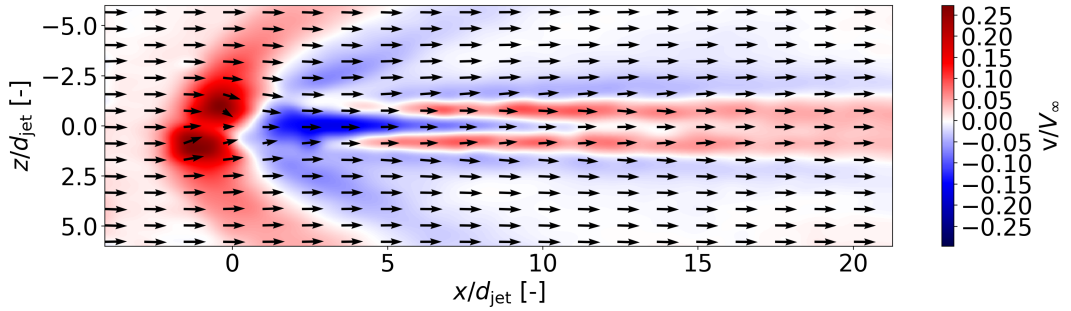

(a) $y = d_{\text{jet}}$

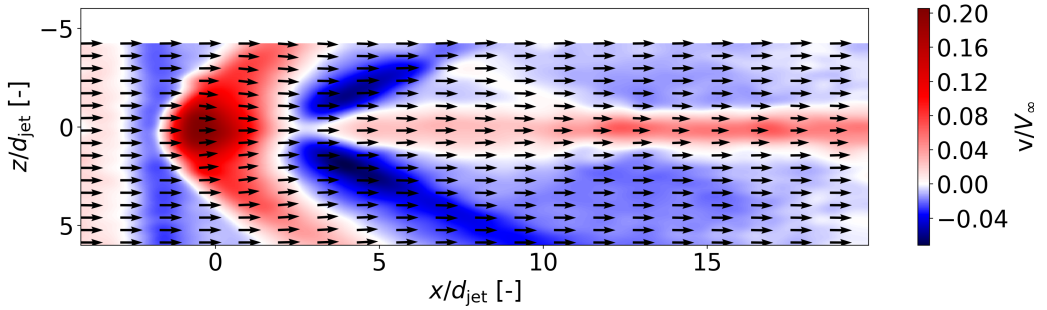

(b) $y = 2d_{\text{jet}}$

Figure 6.8: J = 1,2. Coloured by v-component of velocity (out-of-plane).

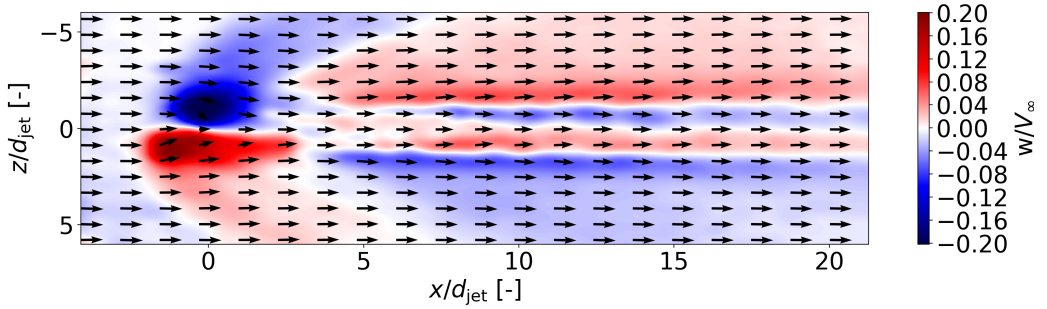

(a) $y = d_{\text{jet}}$

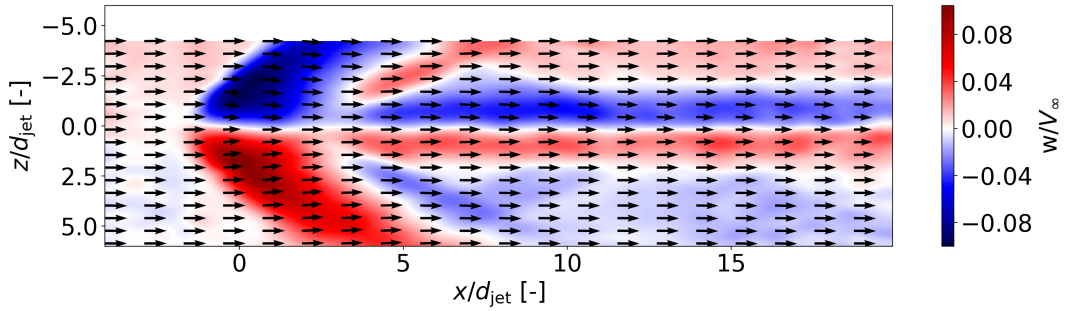

(b) $y = 2d_{\text{jet}}$

Figure 6.9: J = 1,2. Coloured by w-component of velocity (“across”-plane).

Of particular interest from the images taken at the lower plane is the evident demarcation of the counter-rotating vortex pair (CVP). The CVP rotating clockwise on the starboard branch and anti-clockwise on the port one (as viewed from downstream), it induces a velocity field having opposite sign for for the case of the v- and w-components. In the case of Figure 6.8a, the out-plane component is positive (towards the reader) around the centre line and negative on the outboard streaks. The absolute value of the positive and negative velocity regions is, however, not the same. This is because, overall, air is rising from above the wall given the combined action of the CVP itself and the secondary shock forming over the separation region. A rather large dip in velocity is observed immediately downstream of the jet, in the vicinity of the point where air reattaches to the wall. The same trend is visible in Figure 6.8b, even though it appears more "diffused" due to the increased height from the wall, as also mentioned in Sun and Hu (2018a).

The distribution of the w-component is also consistent with the observations noted for the v-component. In particular, Figure 6.9a shows how the two branches of the CVP rotate in opposing directions, thus pushing air to either side of the centre line. The low pressure in the core of the vortices brings air from the outboard regions in towards the middle of the test section. A large deflection from the centre plane is also caused by the bow shock in the vicinity of the jet exhaust. Again, the same effects are visible on the higher plane (Figure 6.9b) but diffused.

6.2.2. Shock with no jet

The foregoing introduces the flow field resulting from the interaction of an impinging oblique shock wave with the boundary layer. A quantification of the velocity field was, in fact, not possible in Chapter 5. A comparison between wall-normal and wall-parallel images is proposed for $\theta = 9\,\text{deg}$ and $\theta = 12\,\text{deg}$ in Figures 6.10 and 6.11.

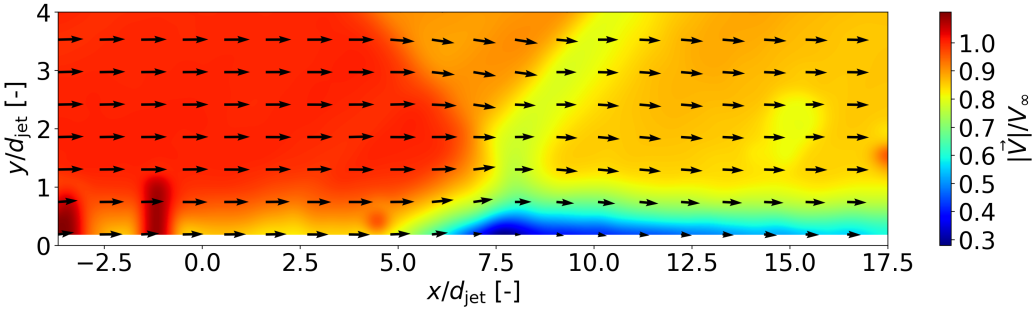

Figure 6.10: $\theta = 9\,\text{deg}$. Jet off. Coloured by velocity magnitude.

The immediate difference that should strike the eye of the reader is the difference in the extent of the low-speed (possibly separation) zone caused by the impinging shock. The case of the lower deflection only sees a small portion of the flow departing from the bottom wall, where the 12-degree case sees a considerable part of the flow separating. Also, the images capture the incident-reflecting shock system proper of the SWBLI, whereby the separated flow bubble acts as obstacle, generating compression waves which coalesce into the reflected oblique shock wave. Wall-parallel measurements show an expected deceleration of the flow due to the shock. Of course, the deceleration caused by the 12-degree case is more abrupt than the 9-degree one. Due to the mounting of the shock generator in the tunnel, the shock front appears slanted, see Figure 6.12. The new supports of the shock generator were manufactured with a lower tolerance than expected, meaning that

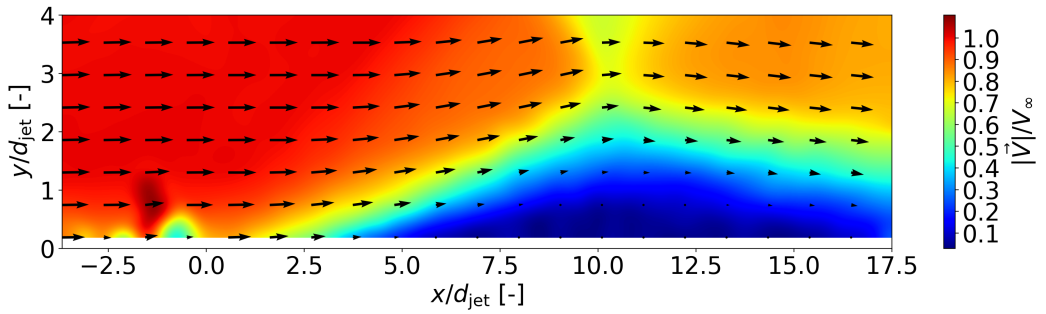

Figure 6.11: θ = 12 deg. Jet off. Coloured by velocity magnitude.

the symmetric row of bolt holes in the 9-degree wedge could not be used. Instead, it had to be mounted closer to the port side of the tunnel, meaning that a spanwise effect is now affecting the results for this configuration. The clearance was 4 mm on the port side and ≈ 2 cm on starboard.

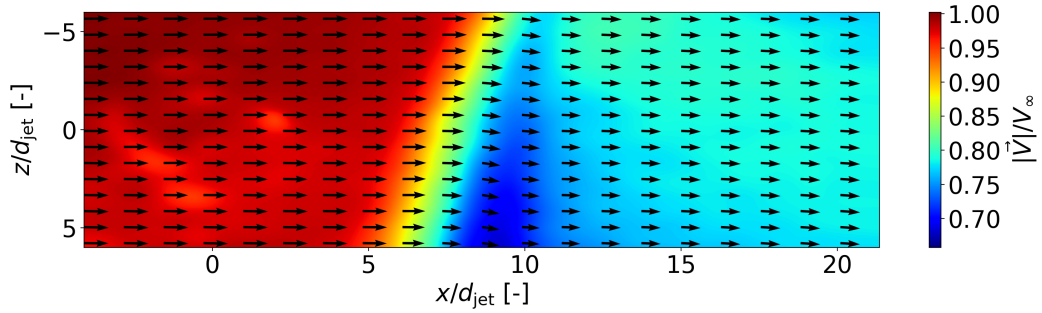

Figure 6.12: θ = 9 deg. Jet off. Imaged at y/d_{jet} = 1. Coloured by velocity magnitude.

6.2.3. Mixing and entrainment

As an introduction to the quantification of mixing and entrainment, it is decided to report the distribution of vorticity across the flow field for both the wall-normal and wall-parallel planes, as well as the ones for Reynolds stresses. First, the reader is reminded of the definition of vorticity in Equation 6.1.

$$\overline{\omega} = \nabla \times \overline{V} = \left(\frac{\partial v}{\partial z} - \frac{\partial w}{\partial y}\right)\overline{i} + \left(\frac{\partial w}{\partial x} - \frac{\partial w}{\partial y}\right)\overline{j} + \left(\frac{\partial u}{\partial y} - \frac{\partial v}{\partial x}\right)\overline{k} \tag{6.1}$$

Now, since stereo PIV is able to measure the out-of-plane velocity component but not the full velocity gradient tensor, the “stereo” vorticity is equal to the planar vorticity, for which,

$$\overline{\omega} = \omega_z\overline{k} = \left(\frac{\partial u}{\partial y} - \frac{\partial v}{\partial x}\right)\overline{k}$$

with $\overline{k}$ being the out-of-plane component of vorticity. Furthermore, values of vorticity are scaled with respect to the governing scaling parameters: the jet diameter for length and the freestream velocity for speed. Being the units of vorticity the reciprocal of time, the normalization reads as in Equation 6.2

$$\omega_{\text{norm}} = \omega \cdot \frac{d_{\text{jet}}}{u_\infty} \tag{6.2}$$

Furthermore, as mentioned at the beginning of the section, it is necessary to examine the Reynolds stresses to get a better grasp on the mixing mechanisms of the flow. These are components of the Reynolds stress tensor:

$$\tau''_{ij} = \overline{u'_i u'_j} \tag{6.3}$$

which is then normalized with the square of the freestream velocity as

$$\tau''_{ij,\text{norm}} = \frac{\tau''_{ij}}{u_\infty^2}$$

The sum of the diagonal components of the Reynolds stress tensor (i.e. its trace) corresponds to the Turbulent Kinetic Energy (TKE):

$$TKE = R_{xx} + R_{yy} + R_{zz} \tag{6.4}$$

To begin with, Figure 6.13 displays the distribution of the out-of-plane component of vorticity for the wall-normal plane for the case where $J = 1$.

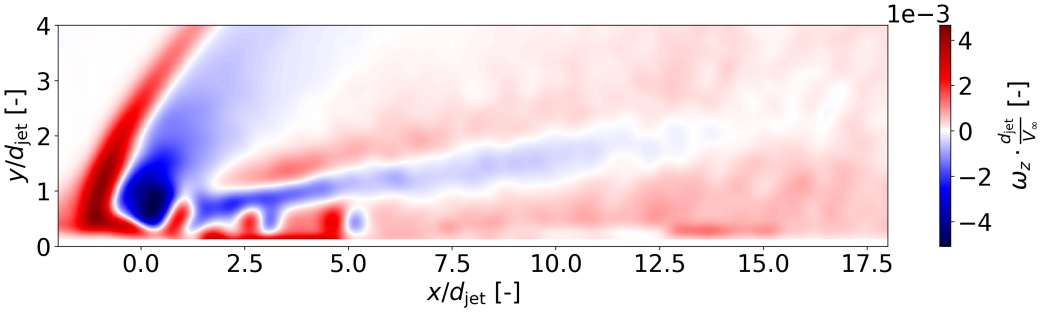

Figure 6.13: Average vorticity field for $J = 1$. No shock impinging on the field.

One can readily see that the areas where the most vorticity is present are, of course, in proximity of the bow shock and in the developing wake. The shear layer resulting from the interfacing jet and crossflow streams is also clearly visible as two contrasting “streaks” of positive and negative vorticity. This statement can be further corroborated by Figures 6.14a and 6.14b.

The former shows how, for an increasing distance above the wall, the vorticity change induced by the bow shock fades and how, as expected, it gets stronger for increasing momentum flux ratio. The changing J has also the effect of anticipating the vorticity peak for an increase in its value. The bow shock being stronger, in fact, results in it having a steeper angle to the horizontal. The vorticity trend across the shock is one whereby an initial sharp increase can observed, followed by a gradual recuperation to freestream conditions (where $\omega \approx 0$). Figure 6.14b, instead, maps vorticity on wall-normal slices, thus cutting through the jet wake. Whereas in the previous it was observed that higher J lead to higher vorticity, here it is the opposite. The difference resides in the different flow driver in the two regions. The properties of the outer flow crossing the shock are mainly momentum driven, and dominated by total pressure losses imparted by the discontinuity.

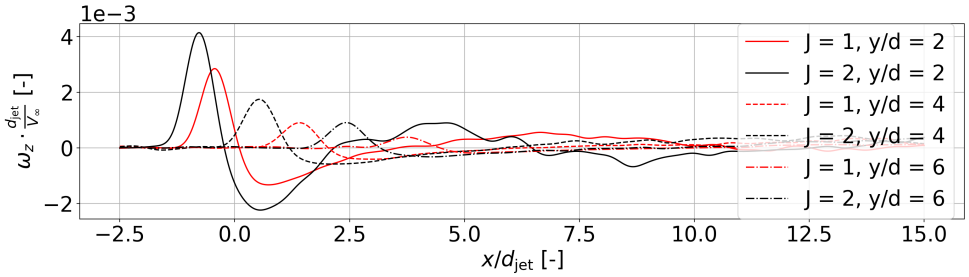

(a) Horizontal slices

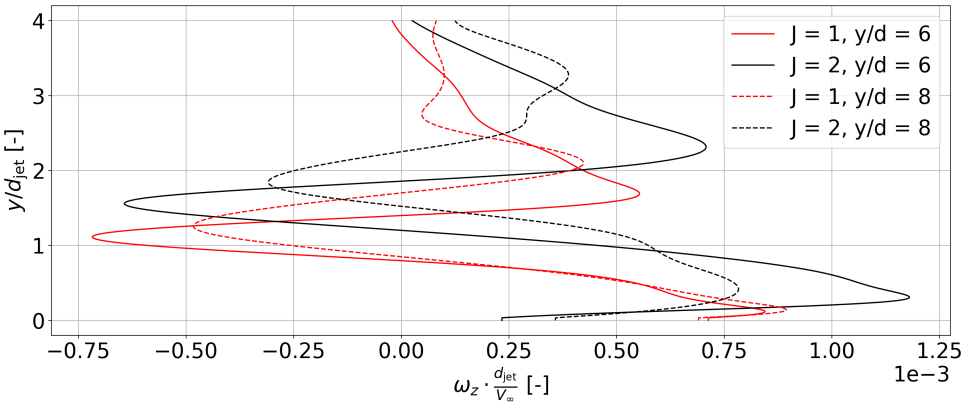

(b) Vertical slices

Figure 6.14: Plots showing the distribution the distribution of vorticity on chosen slices.

The wake, instead, sees this occurring only in the very near field. As the focus shifts downstream, diffusion-driven phenomena take the lead and the near-wall wake is deprived of momentum. This phenomenon will become particularly evident in the display of the Reynolds stresses.

Vorticity mainly represents an inviscid phenomenon, whereby changes in velocity in all coordinate directions are mapped to a curl of the velocity field. Reynolds stresses, instead, arising from the Reynolds decomposition of the velocity field, perform better at the characterization of the turbulent patterns in the flow. Decomposing the velocity as $u = \overline{u}+u'$, in fact, allows one to capture the inherently random velocity fluctuations that are typical of turbulence. Thus, it will be possible to observe how Reynolds stress are mostly null in the parts of the field mostly characterized by pressure phenomena (i.e. inviscid) whereas they will appear mostly where the viscous effects are predominant. To begin the discussion on this variable, Figures 6.15a and 6.15b show a comparison of the Reynolds stress R_{xx}.

As mentioned in the above, the scalar field for R_{xx} is mostly null in the inviscid part of the domain. Not even the bow shock upstream of the jet is visible. As the flow transitions to a more turbulent regime, for instance in the wake of the jet, then appreciable variations of the stress appear. Also, the different mixing mechanisms are visible between the different values of J. Whereas most of the mixing in the lower-J case occurs rather close to the wall in the separated region, for the higher one the actual jet plume developing above the wall takes a more solid role. Further, one can see how the immediate near field of the jet creates higher Reynolds stresses in the higher-J case. In this region, though, the presence

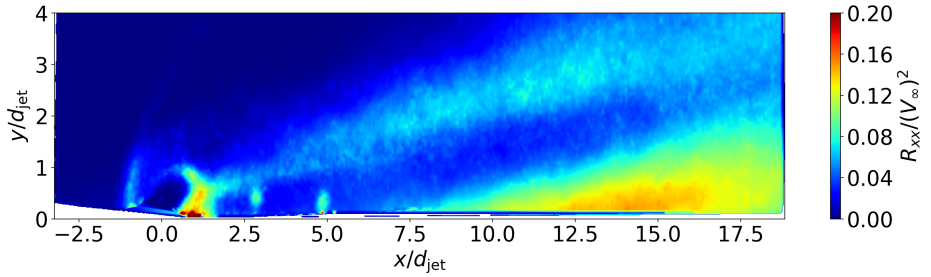

(a) Lowest momentum flux ratio, $J = 1$

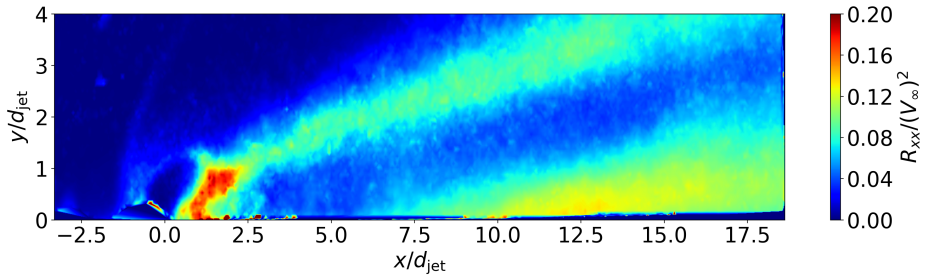

(b) Highest momentum flux ratio, $J = 2$

Figure 6.15: Plots showing the distribution of the Reynolds stress R_{xx}.

of sharp stresses is not a cause for mixing, but rather a result of the highly separated and unsteady air rushing around the barrel shock. Anyhow, it is well-known fact reported in several pieces of literature that a higher momentum flux ratio leads to greater plume penetration and, thus, a more relevant role of the plume itself and CVP in mixing, Finally, the distribution of Reynolds stress on a wall-parallel plane is mostly interesting at the lowest imaged position: $y/d = 1$, shown in Figure 6.16.

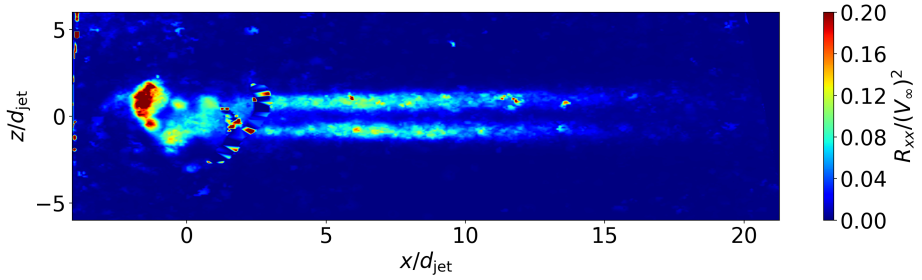

Figure 6.16: Contour plot showing the distribution of the Reynolds stress R_{xx} at $y/d = 1$.

The figure shows clearly how the main mixing mechanism on this plane is provided by the CVP. By drawing air from the outboard regions of the domain and from the near-wall segments, this vortical structure is able to form entrain the flow mostly in the near field. Partly because the trajectory of the CVP brings it above the current laser sheet and partly because of diffusion processes, the vortices fade in the wake, giving way to the familiar dark-blue null field. Indeed, the display of the same variable on the higher horizontal plane at $y/d = 2$ (not shown here) does not reveal any relevant flow feature, indicating how the oscillatory momentum causing a bright flash in Reynolds stress on the lower plane vanishes in the far field captured by the raised laser sheet.

By combining the three diagonal components of the Reynolds stress tensor in a sum, it is possible to obtain a more realistic indication of mixing, as the sum effectively equals the turbulent kinetic energy (Equation 2.18). The distribution for this scalar quantity is shown in Figure 6.17.

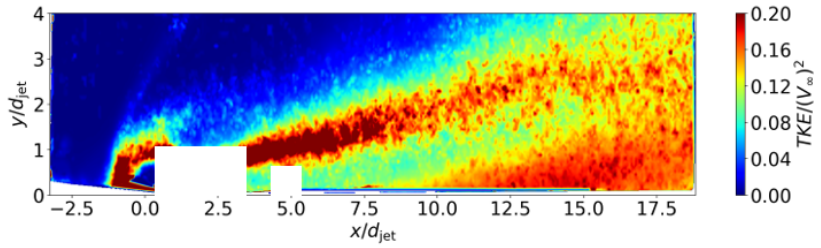

Figure 6.17: Contour plot of turbulent kinetic energy normalized with the square of the freestream velocity. Case for $J = 1$.

The contour plot brightens up in the vicinity of the jet nozzle, indicating the formation of turbulent eddies. There, in fact, flow coming from around the barrel shock and air crossing the Mach disk combine, forming a region characterized by rather high shear. The region in the wake's far field downstream of 10 jet diameters is less evident than in the field for R_{xx}, suggesting how the x-component of the Reynolds stress might be the dominant one in the region. Indeed, as the flow in the area is mostly wall-parallel, the main oscillation are expected to be recorded on the same axial direction. A greater contribution from the other two diagonal components of the tensor is, on the contrary, more visible in the developing plume, where the induced velocities by the CVP diffuse air from other directions.

Figure 6.18 reports the vertical penetration of the jet's plume based on its centre streamline.

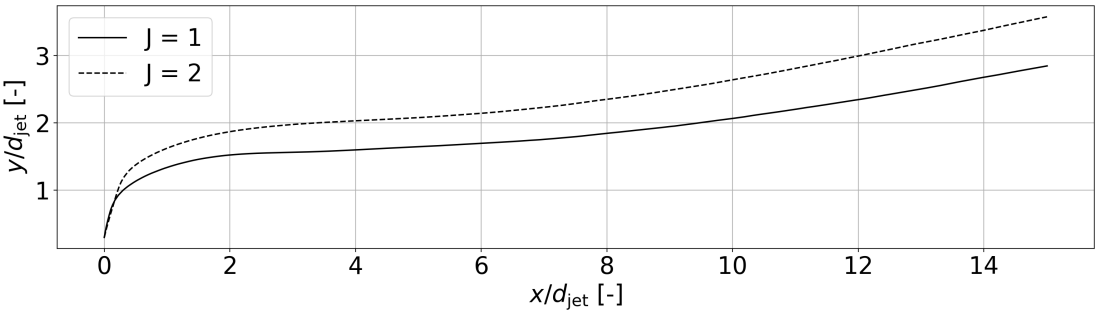

Figure 6.18: Comparison between the plume's centre streamline's trajectory for the two J's in study.

The trajectory was computed using a space-stepping method. The calculation was initialised a position above the wall, at $x = 0$: the centre of the jet nozzle exhausting in the crossflow. As the velocity field is known and the ability to interpolate to sub-pixel accuracy, the velocity data for that exact point was computed. Having the two components u and v, one can calculate the local angle of the plume with respect to the horizon as $\varphi = \arctan v/u$. Given a certain step size ds, the new local position is recomputed simply adding the step size multiplied by either the cosine or sine for the horizontal and vertical directions, respectively. The method was shown to be convergent for decreasing step size, proving its robustness (see Figure 6.19).

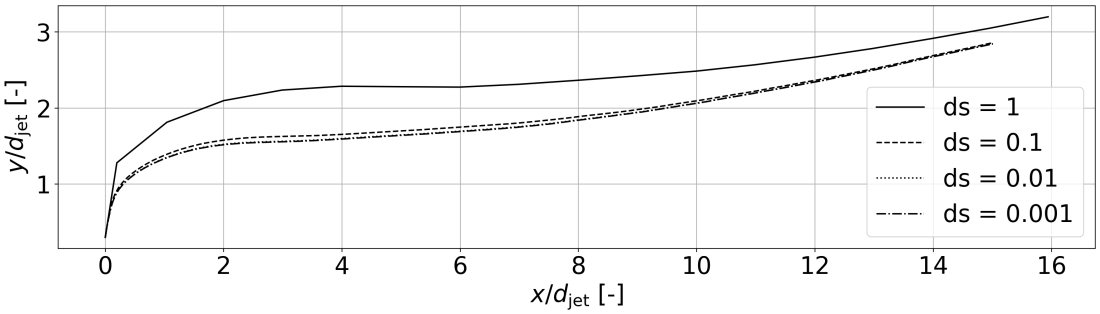

Figure 6.19: Plot showing the computed trajectory for various chosen step sizes, ds. $J = 1$.

To close the discussion on the jet plume's penetration into the crossflow, Figure 6.20 shows how the trajectory computed in the present work compares to other research efforts in the literature.

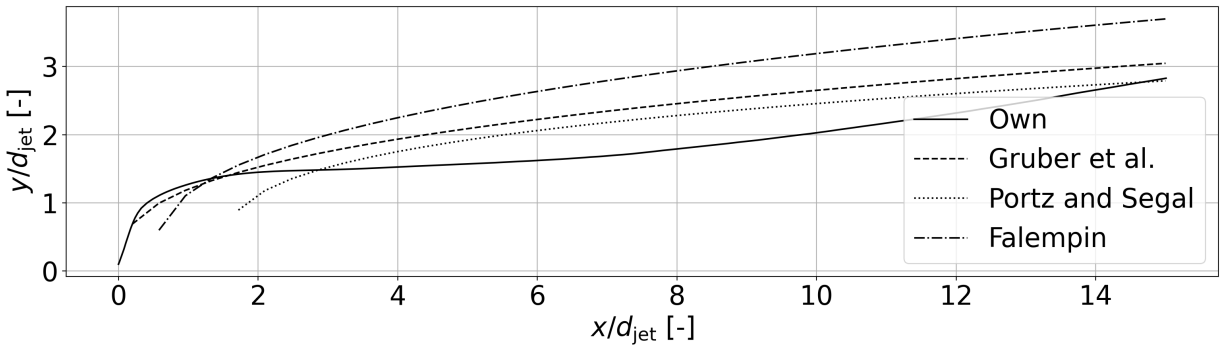

Figure 6.20: Comparison of trajectory computed in this work for $J = 1$ to the one by Gruber et al. (1997), Portz and Segal (2006) and Falempin (2001).

It immediately appears as though the computation of the plume's vertical penetration somewhat underestimates the elevation of the rising wake. However, the reader must be warned that there are some critical differences between this work and the literature. First, the definition itself of the trajectory. All studies reported in the above define jet penetration at a certain streamwise location as the point where outermost edge of the plume is located. It, therefore, makes sense that the solid black curve lies below the other three in the mid-field. Several can be the reasons for the mismatch in the near-field as well. From particle slip affecting PIV-based plume tracking to partial inapplicabilities of the literature equations to the present work. Indeed, it is the case that all three authors listed in the above conducted studies with a different injectant species such as hydrogen or helium. Additionally, the considered range of momentum flux ratios is considerably higher than the one in consideration here.

6.3. Impinging oblique shock

As for the second and main set of measurements that are required to answer the research questions, PIV runs have been conducted to study the interaction between a supersonic crossflow, the sonic jet and an incident oblique shock. The reader is reminded of the main parameters that define the flow case: apart from, of course, the the momentum flux ratio, new variables describing the shock's behaviour are the shock's downstream impingement position and the shock angle. Table 6.1 reports the position o the impingement location of the oblique shock and the location of the onset of the upstream compression wave resulting from the SWBLI.

θ [deg]	β [deg]	$x_{i,1}/d_{\text{jet}}$	$x_{ds,1}/d_{\text{jet}}$	$x_{i,2}/d_{\text{jet}}$	$x_{ds,2}/d_{\text{jet}}$	ε [x/d]
9	38.24	13	4	16	6	$\pm$ 0.5
12	41.58	13	5	16	7	$\pm$ 0.5

Table 6.1: Table showing the impingement location of the incident oblique shock

In the above table, the subscripts 1 and 2 refer to configuration 1 and 2, respectively, where each configuration is intended as a different downstream impingement location. The column for ε reports the error in the setting of the shock position. An error will be present due to to, for instance, slight misplacement of the shock generator or accidental sliding of the wedge due to tunnel vibrations. First, the reader shall be introduced to the typical flow field arising from such complex interactions without delay in Figure 6.21.

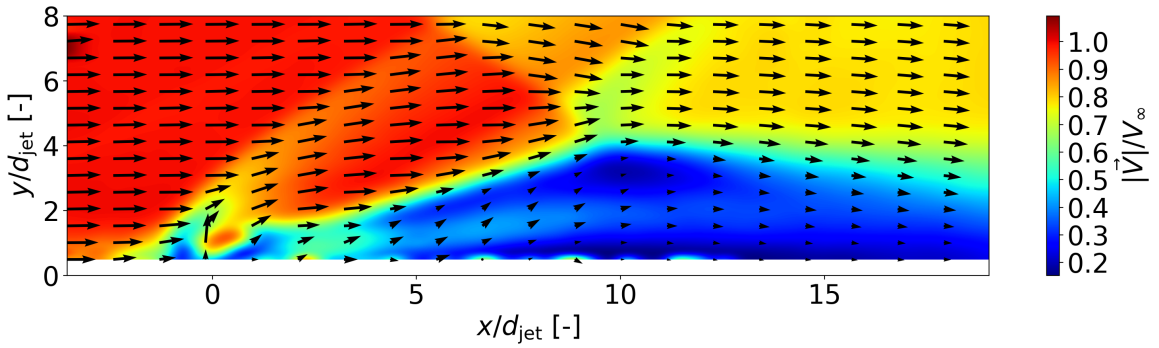

Figure 6.21: Vector field of flow configuration with $J = 1$, $\theta = 12$ deg and $x_{i,1}/d_{\text{jet}} = 12$. Coloured by velocity magnitude.

The field resulting from the interaction is one containing both the typical features of the interaction of the jet with the crossflow and of the SWBLI. These will be (for now) presented as unrelated to each other. The relational analysis will be performed in the foregoing. First, then, one can easily spot the bow shock upstream of the jet, whose strength remains vastly unchanged compared to the "no-shock" scenario up until the point where it crosses paths with the incoming oblique shock. Yet, its strength waivers in comparison to the one of the much stronger oblique shock. This last features causes a rather large-scale separation region that gets amplified even more by the present of the jet. Bordering this region on the upstream side a compression wave forming into a shock wave can be spotted, causing a small flow region to experience a sharp deceleration right downstream of where these two features meet. The separated flow bubble then seems to diminish in size and, potentially, reattach to the wall outside the current field of view. The same features are visible in the field generated by the 9-degree wedge (displayed in Figure 6.22).

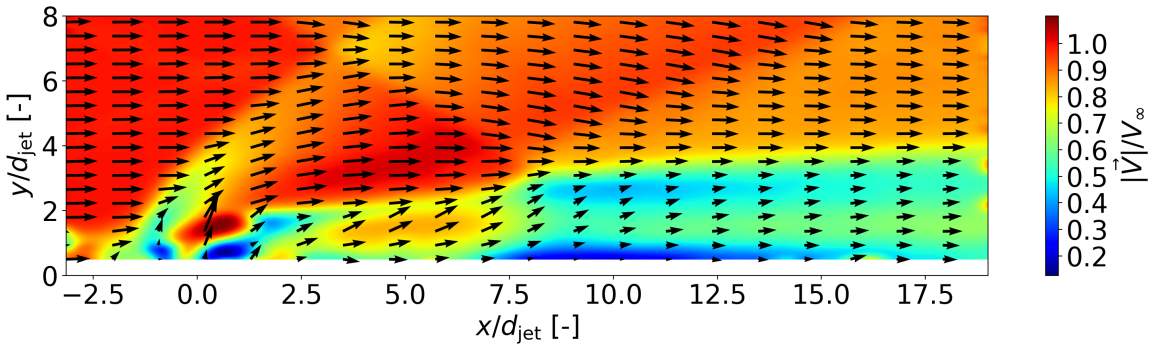

Figure 6.22: Vector field of flow configuration with $J = 1$, $\theta = 9\,\text{deg}$ and $x_{i,1}/d_{jet} = 13$. Coloured by velocity magnitude.

One can still see all relevant features of the interaction, such as the bow shock and the SBLI, but this time the extent of the interaction region is shorter. Indeed, the shock strength is lower, pushing towards a "less adverse" pressure gradient and causing milder effects. The boundary layer's thickness, though, does not appear to diminish as in the previous case, but stays constant from the point of contact with the OSW all the way to the downstream end of the field.

A brief comparison can then be drawn as to what the effect is of changing shock angle, both a SWBLI control perspective and from a point of view of flows mixing. In regards to the former, a stronger shock definitely leads to more separation, thus rendering the effects of an already widely separated field even worse. The latter phenomenon, instead, sees improvements as to the generation of baroclinic vorticity induced by the shock. Further figures to back this statement up will be introduced in the foregoing.

As the shock structures and the interactions between discontinuities are deemed rather complicated, the visualization of the divergence field can help in shedding more light into their interaction, bringing more stark contrast in the visualizations of the shocks. This is displayed in Figure 6.23.

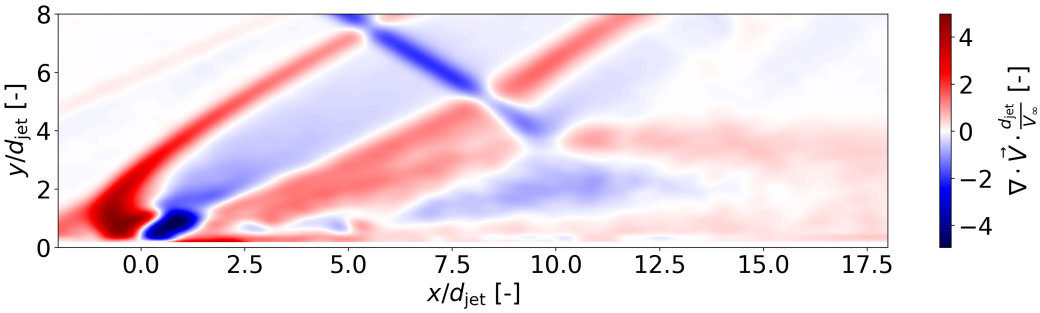

Figure 6.23: Divergence of velocity field for $J = 1$, $\theta = 12\,\text{deg}$ impinging at $x/d = 13$.

First of all, the reader is reminded the definition of the divergence of velocity in Equation 6.5.

$$\nabla \cdot \vec{V} = \frac{\partial u}{\partial x} + \frac{\partial v}{\partial y} + \frac{\partial w}{\partial z} \tag{6.5}$$

Back to the divergence field: from up- to downstream. Traversing the field from left to right one first encounters the weak shock generated by the fastening metal strip upstream of the jet holding plate. This feature was also visible in the Schlieren runs and is rather weak in nature. Moving downstream, the jet-induced bow shock appears, which crosses paths with the incoming oblique shock, shown with opposite sign. The last shock to be crossed is the one reflected off the boundary layer as a result of the SWBLI. This visualization allows also to see how the incident oblique shock is smeared within the large-scale interaction region in the near-to-far field.

Concerning the measurement of this configuration on wall-parallel planes, instead, it is possible to grasp an immediate match will the oil flow visualization data gathered and illustrated in Chapter 5. First, the lowest imaging plane is displayed in Figure 6.24. The plot shows the typical velocity distribution up to the position of the normal jet, with the bow shock forming upstream of it, the deviation of the main flow to the sides and the deceleration caused by the bow shock itself. Then, radical changes can be seen from there towards the downstream end of the field. First, it is possible to spot the emerging onto the laser sheet, followed by curvy shock front, which owes its shape most probably to the two large-scale low-velocity regions forming aft (vortices). These appear on symmetric positions with respect to the centre line and their diameter extends for about 5 jet diameters. By direct comparison with Figure 5.11b, one can see how these features have shifted downstream throughout the 4 [mm] boundary layer, convected backwards by the flow's momentum. It is though that these vortices will enhance mixing by bringing the main wake of the jet towards the outboard regions.

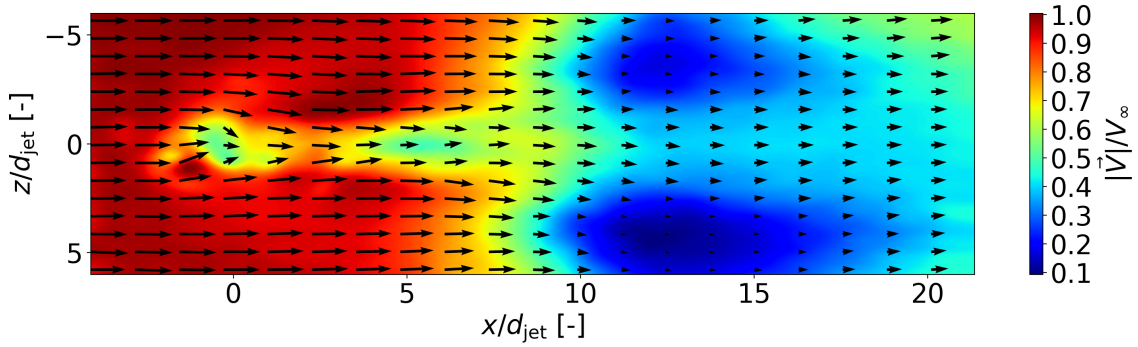

Figure 6.24: Velocity field generated with $J = 1$, $\theta = 12$ deg impinging at $x_i/d = 12$ imaged at $y/d = 1$. Coloured by velocity magnitude.

6.3.1. Mixing: equal shock location

Figures 6.24a and 6.24b report the variability of vorticity on the normal planes when the OSW was generated by a 12-degree deflection to reach the bottom wall at $x/d = 13$.

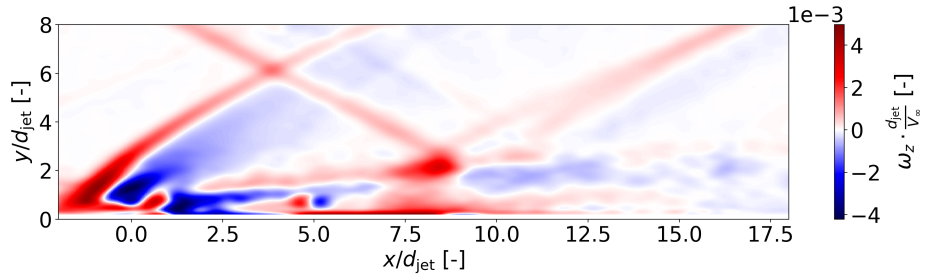

(a) $\theta = 9\,\text{deg}$

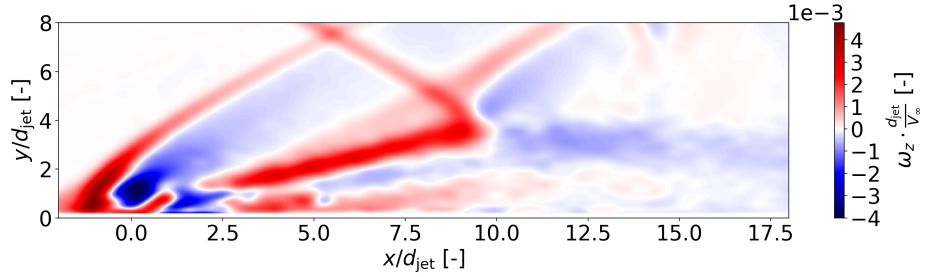

(b) $\theta = 12\,\text{deg}$

Figure 6.24: Contour plots reporting the vorticity field $J = 1$ and shock impingement position of $x/d = 13$.

The development of a strong shear layer appears evident for both shock strengths. The 12-degree case does, however, show greater absolute value for vorticity in the region downstream of the jet. In fact, the weak case shows a similar vorticity field compared to baseline no-shock case shown in Figure 6.13, only to be interrupted by the formation of the SBLI interaction region in the mid-field. The strong case, instead, immediately shows a different development pattern in the immediate downstream vicinity of the jet. This suggests a possible different interaction mechanism and it is reasonable to speculate that this case will cause a greater interaction region compared to the baseline. This aspect will be investigated more thoroughly in Section 6.3.3. Vorticity is also shown to “spread” over a wider area in the present case compared to the baseline cases.

The question is now to analyse how the presence of the shock affects the penetration of the plume into the crossflow. This, in turn, will bring more “fuel” towards the centre of the combustion chamber (i.e. the test section) allowing for better mixing. A comparison between the cases seen so far is displayed in Figure 6.25. The baseline cases where the jet underwent no interference from the incident oblique shock are shown as solid lines. They show a steady increase in “wall altitude” right after injection. This trend is then briefly interrupted in a plateau which then resumes its increase at about $x/d = 6$. The weak shock cases ($\theta = 9\,\text{deg}$) shows marginal to null improvement with respect to the baseline. The curve for $J = 1$ even appears to have a lower penetration compared to its baseline counterpart. The higher-J case, instead, features a marginally higher elevation up until the location where the plume meets the incoming shock. From there on, the flow is again mostly parallel to the wall, as the effect of the CVP is interrupted by the oblique shock. Sharp is the increase in plume elevation for the strong shock cases. The combined effect

of the CVP and the compression wave instilled by the separation region bring the plume to rise abruptly in the near field. It can be speculated that the dominating effect here is not the CVP's action, but rather the upstream shock resulting from the SWBLI. Indeed, as the large-scale interaction region joins the incoming shock, the v-component of velocity becomes negative, forcing the plume back down towards the wall.

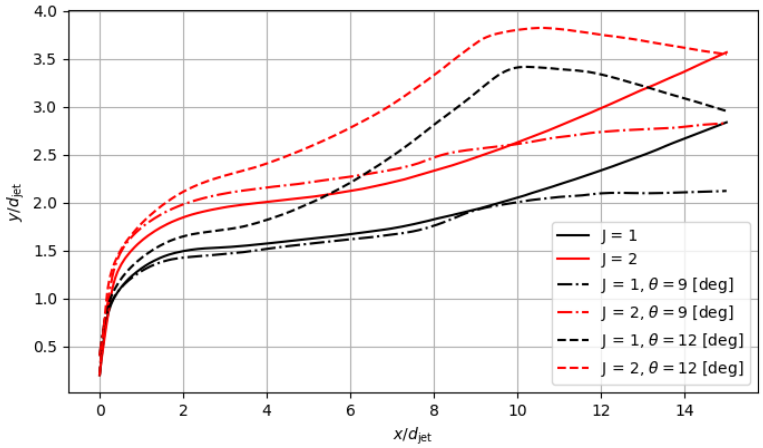

Figure 6.25: Comparison of plume's centre line trajectory: showing cases with no shock and for $\theta = 9$ [deg] and $\theta = 12$ [deg] impinging at $x/d = 12$. Varying J.

A word of caution thus needs to be mentioned upon observation of the curves in the figure above. Being the field of view "limited" to the near- and mid-fields, one cannot know how the flow will evolve past the downstream end of the plot. It is expected that the 12-degree scenario will see a stabilization in the degrading plume as x shifts downstream. Yet, studies such as the one by Nedungadi and Lewis (2000) show how the development of a vortex is abruptly interrupted by the encounter with a shock. This effect is rather evident when the interaction occurs with the 9-degree flow deflection. There, as the flow is effectively drawn to return parallel to the tunnel walls, the CVP looses completely its effect, apart from a rather mild action. The issue with the curve corresponding to the 12-degree shock configurations is also that the streamline also crosses into the interaction region, where large velocity vector variations are usually present, thus making for a less precise determination of the plume's trajectory.

More information about the mixing performance is provided by the contour plots for the Reynolds stresses in Figures 6.26 and 6.27.

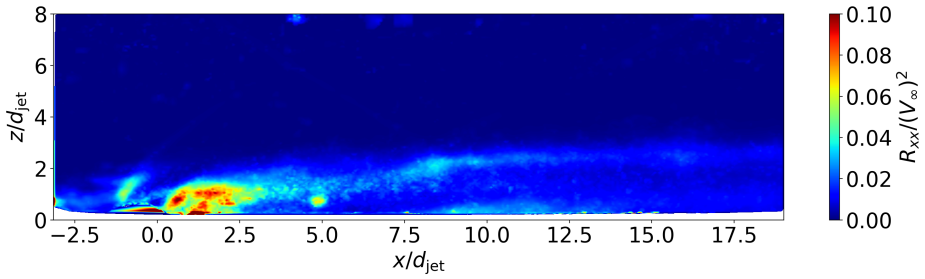

(a) R_{xx}

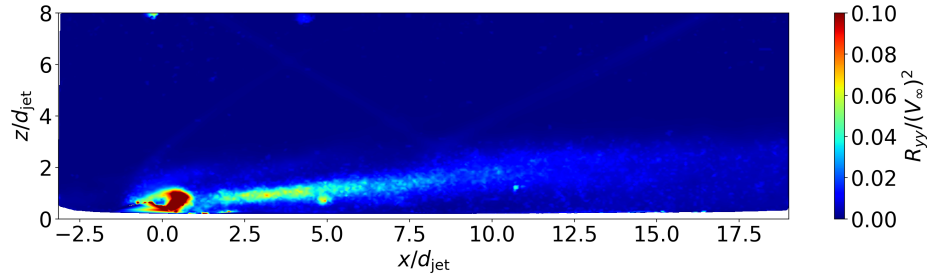

(b) R_{yy}

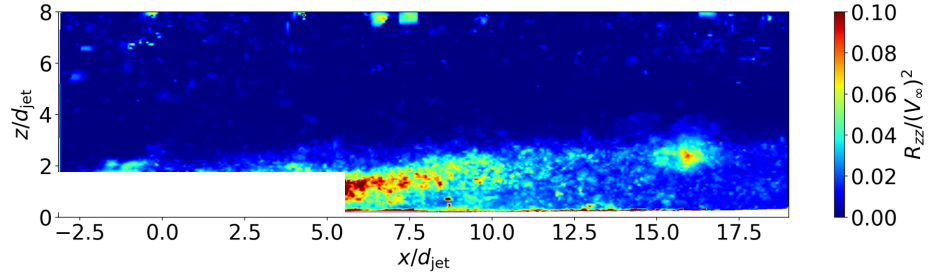

(c) R_{zz}

Figure 6.26: Contour plots reporting the scalar field of the diagonal components of the Reynolds stress tensor for $J = 1$ and shock impingement position of $x/d = 13$. $\theta = 9\,\text{deg}$.

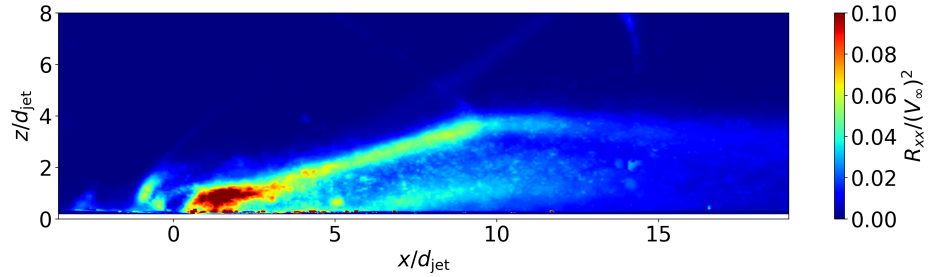

(a) R_{xx}

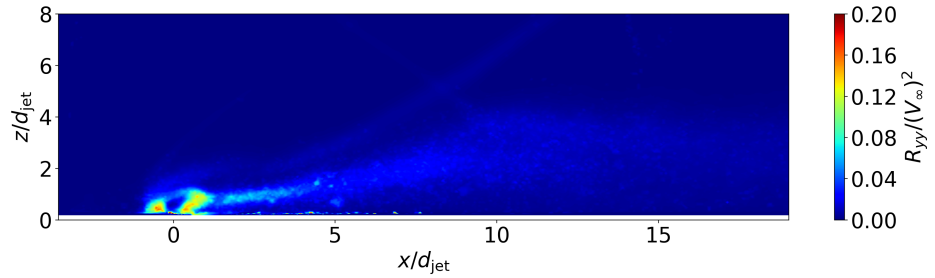

(b) R_{yy}

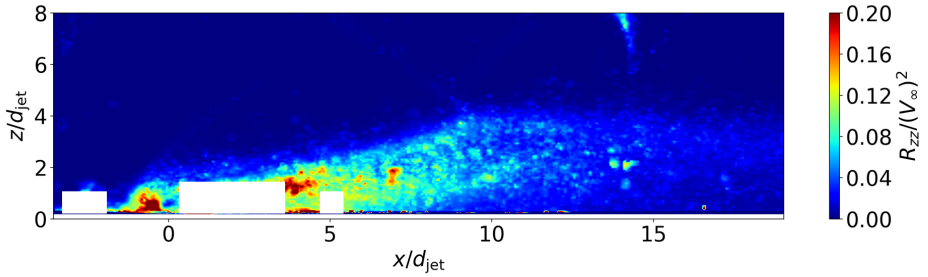

(c) R_{zz}

Figure 6.27: Contour plots reporting the scalar field of the diagonal components of the Reynolds stress tensor for $J = 1$ and shock impingement position of $x/d = 13$. $\theta = 12$ deg.

The comparison of the contours for turbulent kinetic energy reveal insight for the mixing mechanisms of the two flows. The compression wave has the effect of bringing injectant high above the wall. However, if for the strong shock case this translates into a widespread diffusion of kinetic energy over a large area, for the 9-degree case the spread is less impacting. Compared to the flow configuration with no impinging shock in Figure 6.17, it appears like higher Reynolds stresses persist further downstream. However, being the velocity lower downstream of the shock, the longer residence time of fuel in a highly turbulent region plays in favour of mixing. As shown in Figure 6.28, however, mixing does not spread much further than the centre-line. Indeed, as show in the above, Reynolds stresses and turbulent kinetic energy are mostly concentrated in the developing branches of the CVP. However, at the plane's position of $z/d = \pm 2$ there appears to be rather little residual stress. The plot indeed reports the highest concentration where the expanding oblique shock is present in the wake. The bow quickly loses its intensity as the plane shifts away from the symmetry centre line and, thus, it plays no key role in the off-centre mixing. However, the expanding wake downstream of the injection does contributes to mixing.

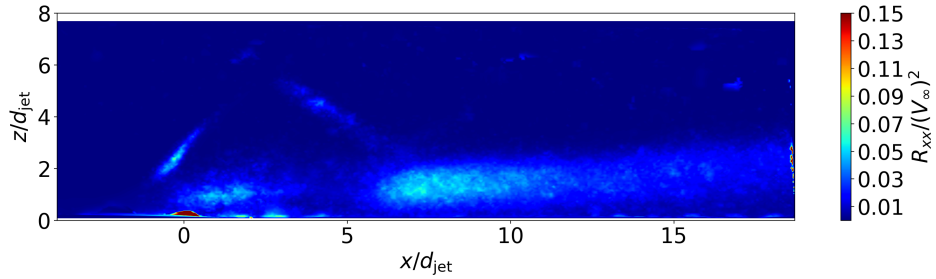

Figure 6.28: Contour plot of Reynolds stress R_{xx} taken on the plane $z/d = -2$ for the case where $J = 1$, $\theta = 9$ deg and $x/d = 13$.

6.3.2. Mixing: varying shock position

If, in the previous analysis, the goal was to analyse the effect of the different shock angle (i.e. shock strength), now the objective is to get an understanding of the effect of the impingement position of the shock. First, referring back to Table 6.1, the flow field for the more downstream impingement position is introduced in Figure 6.29.

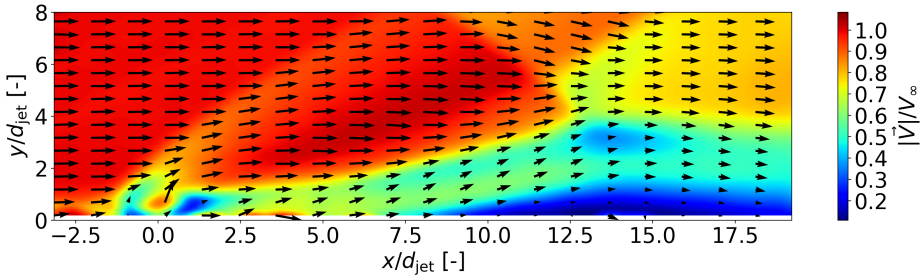

Figure 6.29: Velocity vector field for $J = 1$, $\theta = 12$ deg impinging at $x/d = 16$. Coloured by velocity magnitude.

By comparison with Figure 6.21, it is possible to comment on the qualitative differences between the two flow configurations. If, for the case where the shock hit the wall closer to the jet, the separation region created downstream of the jet "connected" with the one induced by the SBLI, this phenomenon is less abrupt in this case. Separation is still rather large, yet the deceleration underwent by the flow appears less severe. Figure 6.30 shows the velocity distribution along lines perpendicular to the wall. The plots have been generated along wall-normal lines centred at streamwise position where the incident shock meets with the upstream compression wave for each case, i.e. $x/d = 10$ and $x/d = 13$ for the upstream and downstream locations, respectively. By inspection of the figure above, it is possible to notice how the more upstream case causes a greater deceleration of the flow, given the greater size of the separation region downstream of the jet.

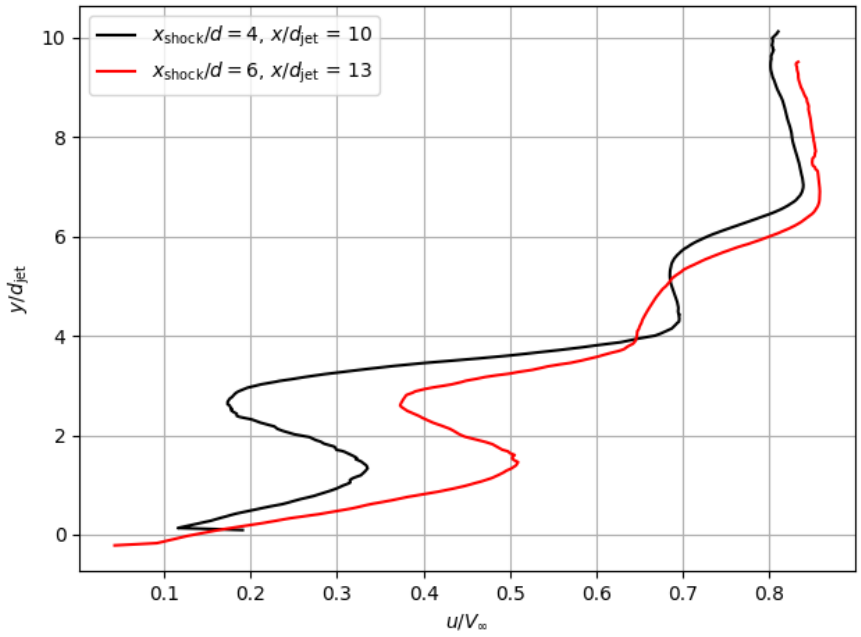

Figure 6.30: u-component of velocity distribution along vertical lines at $x/d = 10$ and $x/d = 13$. $\theta = 12$ deg

Concerning the penetration of the jet plume into the crossflow, Figure 6.31 shows a comparison between several of the cases that have been analyzed so far. The case where the shock impinges at the upstream position has been already discuss thoroughly in the previous section. As the shock impingement position moves downstream, the trend is rather different. In the near field of the jet the plume quickly reaches a plateau and remains stable up to the point of formation of the compression wave. Then, similarly to the previous case, it reaches peak elevation where the compression wave meets the incoming strong shock. Even though the joining of separation zone downstream of the jet and the one caused by the SBLI do not merge to form the large-scale interaction observed in the previous case, it is the case that the adverse pressure gradient circulates upstream through the subsonic part of the boundary layer. Hindering the full development of the CVP, the plume is unable to rise far from the wall.

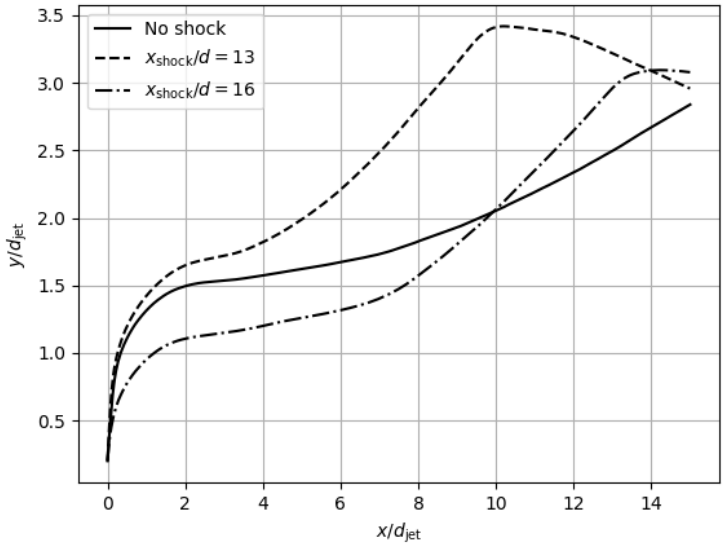

Figure 6.31: Comparison of plume's centre line trajectories for $\theta = 12\,\text{deg}$ and $J = 1$. Comparing baseline configuration to the two different impingement locations.

To conclude, Table 6.2 reports values for the lateral and vertical expansion of the plume for all considered test cases. The figures on the table confirm what has already been delineating in the work conducted so far: the best case for fuel penetration and plume expansion is the strong shock-case with the impingement point closely position downstream of the nozzle. This has a beneficial impact on the mixing and entrainment properties and, thus, the mixing.

The presence of large-scale near-wall vortices and their effect on the fuel penetration and expansion is not yet clear. Their origin can be explained by the fact that a shear layer forms between the air crossing the shock in the undisturbed region (outside the bow shock) and air passing both through the bow shock and again through the OSW. Being the outer air faster, two vortices form at symmetrical positions with respect to the centre line circulating air towards its core (clear from oil flow visualization in Chapter 5). For sure, these allow unmixed fuel from withing the bow shock downstream of the jet to blend more thoroughly with air carried inwards from the external regions of the flow. The newly formed mixture is then convected upwards by the surviving CVP-induced velocity field.

J	θ	x_{shock}/d_{jet}	y/d_{jet} @ $x/d_{jet} = 10$	Δz $y/d_{jet} = 1$	Δz $y/d_{jet} = 2$
1	-		2.05	2.25	2.35
2	-		2.63	-	-
1	9	13	1.98	2.98	3.13
2	9	13	2.58	-	-
1	9	16	1.79	-	3.05
2	9	16	2.24	-	-
1	12	13	3.41	14.25*	3.75
2	12	13	3.80	-	-
1	12	16	2.06	-	3.50
2	12	16	2.89	-	-

Table 6.2: Table reporting the vertical plume penetration and lateral plume expansion. The lateral expansion is defined as the region where the velocity is 80% or less than the undisturbed flow (behind the bow shock). The uncertainty on this measurement is ± 0.1 x/d. The measurement noted by (*) refers to the condition where two large-scale vortices arise.

Figures 6.32a and 6.32b report the distribution of the wall-normal velocity component on the wall-parallel plane located at $y/d = 2$. This is the only plane on which data was acquired for this flow configuration.

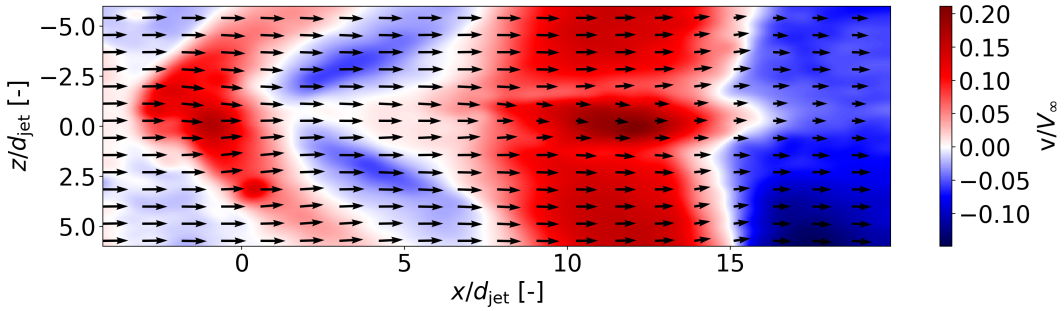

(a) $x/d = 16$

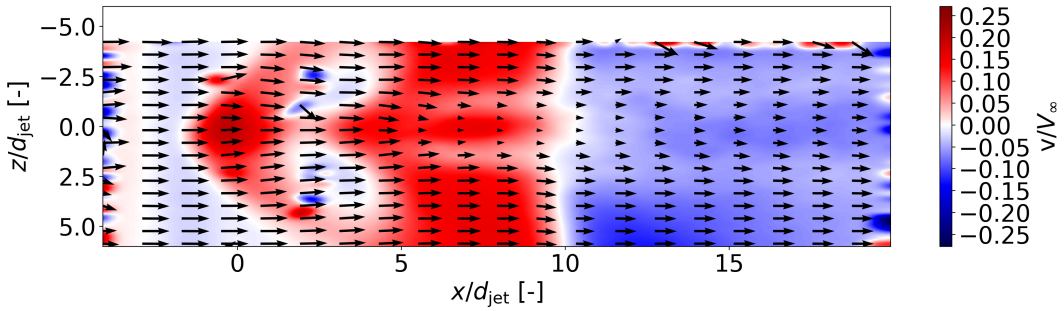

(b) $x/d = 13$

Figure 6.32: Contour plots with velocity v-component (out-of-plane) for $\theta = 12$ deg and $J = 1$.

The comparison between the figures above reports a condition in which the case where the shock hit closer to the jet allows for lifting the flow from the bottom wall starting at a more upstream location compared to the other scenario. In fact, one can see the expansion fan developing from the air rushing around the jet at speed. This feature is in fact not visible from the right-hand side image due to the fact that the shock blocks the full development

of the inviscid features.

The turbulent kinetic energy in Figure 6.33 shows a familiar picture, where the most mixing potential is concentrated in the near field of the jet. Again, most (weaker) potential is observable in the mid- to far-field of the jet, brought high above the wall by the separating air.

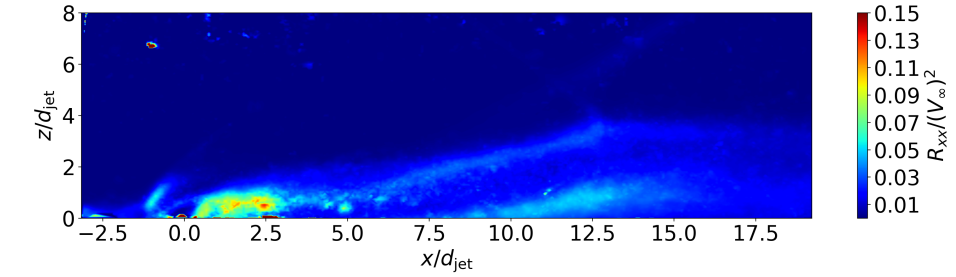

(a) R_{xx}

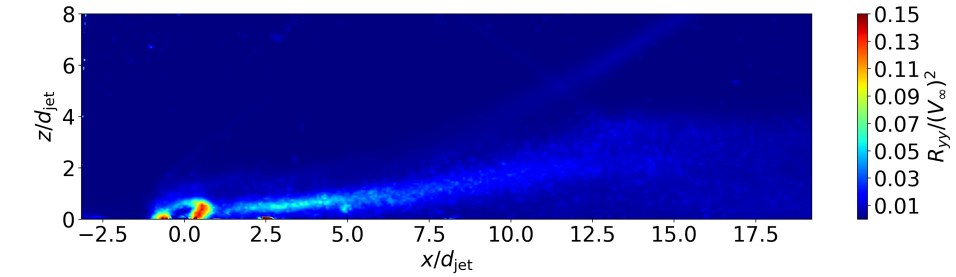

(b) R_{yy}

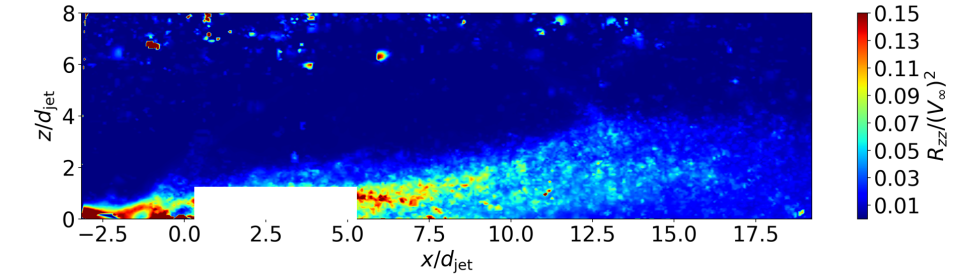

(c) R_{zz}

Figure 6.33: Contour plots reporting the scalar field of the diagonal components of the Reynolds stress tensor for $J = 1$ and shock impingement position of $x/d = 16$. $\theta = 12$ deg.

It was also decided to the test the limit case: the configuration where the shock impinges much farther downstream, right at the edge of the field of view. In particular, it was decided to place the shock impinging position at about $x/d \approx 23$ for the 12-degree wedge and $x/d \approx 26$ for the 9-degree one. The resulting flow fields are shown in Figures 6.34a and 6.34b. The flow configuration arising from the 12-degree wedge is not fundamentally different from the previous cases. It is still possible to see how the separation region downstream of the jet connects with the one induced by the SBLI forming one single long bubble. Instead, considering the weaker shock case, a different flow feature emerges. As the flow appears to reattach in the far field and turns supersonic again, its run is suddenly halted by a normal shock wave forming through the boundary layer. The interference

caused by the incident oblique shock and the subsequent adverse pressure gradient rise cause the acceleration to be discontinued. As the momentum of the flow is also not as strong anymore in the corresponding region, neither an oblique nor a bow shock appear to be able to settle, as a normal shock forms and takes control of the flow's behaviour.

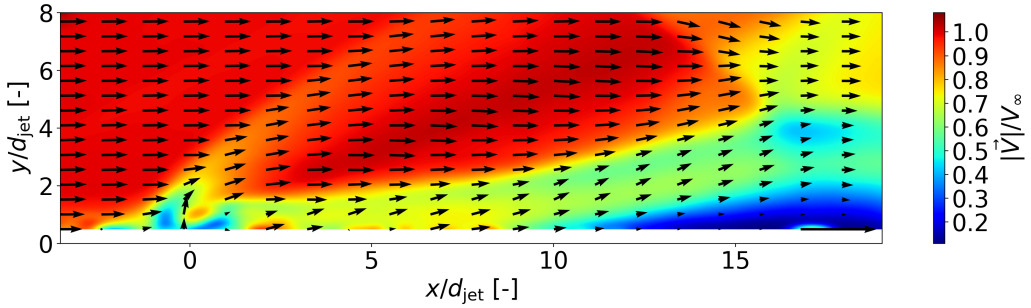

(a) θ = 12 deg

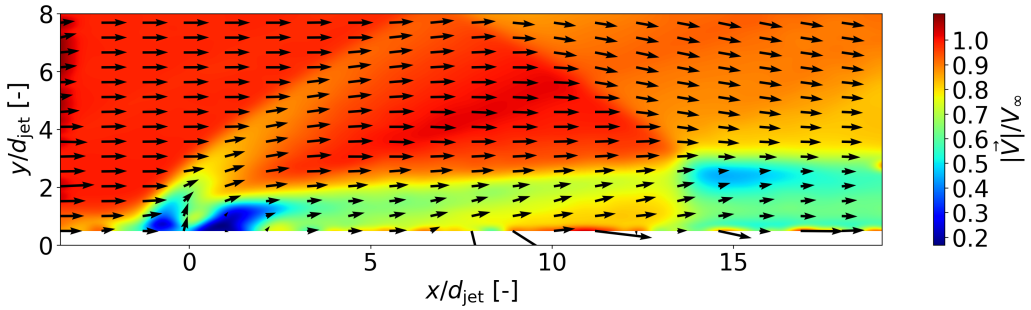

(b) θ = 9 deg

Figure 6.34: Contour plots of velocity magnitude for the flow configuration for the most downstream shock impingement position. $J = 1$.

6.3.3. Effect of the jet on the SWBLI

The mechanism behind the "classic" shock-wave boundary-layer interaction is well-known and extensively described in literature such as the work by Babinsky and Harvey (2011). As the incident shock reaches the subsonic part of the boundary layer, the subsequent compression causes an adverse pressure gradient that propagates upstream through the boundary layer below the sonic line. This forms a bubble that acts as an obstacle to the incoming flow. As a reaction to this, initially weak isentropic compression waves form that then coalesce into a shock wave. This secondary shock then propagates into the external flow as the reflected wave. The higher the shock strength of the impinging wave, the greater the adverse pressure gradient and, hence, the more massive the interaction, as it clearly emerges from the figures mentioned in the above. A quantification of the interaction length is in order, as that is the region where most of the turbulence is generated and, for engineering purposes, the region responsible for most of the turbulent drag. A brief digression on how velocity data was converted to Mach number is given below.

The total enthalpy H of the flow is expressed as in Equation 6.6.

$$H = h + \frac{|\vec{V}|^2}{2} = c_p T + \frac{|\vec{V}|^2}{2} \tag{6.6}$$

where h is the "static" enthalpy, c_p the specific heat at constant pressure and T the static temperature. Now, for adiabatic flow, total enthalpy is constant and, thus, its value in the freestream should be conserved throughout the entire field. Having this conservation law allows for a rather brisk estimation of the temperature field as in Equation 6.7.

$$T = \left(H_\infty - \frac{|\vec{V}|^2}{2} \right) \frac{1}{c_p} \tag{6.7}$$

Once the temperature field is available, the Mach number is readily computed as of Equations 2.5 and, more in details, 6.8.

$$M = \frac{|\vec{V}|}{a} = \frac{|\vec{V}|}{\sqrt{\gamma R T}} \tag{6.8}$$

An error source for this estimation technique lies in the fact that only the freestream total enthalpy is taken as a datum value. However, as the jet does not possess the same conditions as the main stream, its total enthalpy will be different too. As the ratio of jet mass flow to the crossflow's is rather weak, the error is deemed negligible. Yet, Figure 6.35 reports the relative uncertainty for the Mach number field. Please note that the scenario depicted in the Figure is an extreme one: it reports a situation analyzing the error where the estimated total enthalpy is taken as the jet injection conditions, and not the freestream's. The consequent ΔT is propagated through the processing steps to obtained Figure 6.35, reporting the relative error. The figure then shows an uncertainty level to be well below 5%, which is deemed acceptable for the study. Please note the interpretation of the data in the figure. The relative error was defined as the ratio of the Mach number computed by taking the freestream total enthalpy as reference to the Mach number computed by taking the jet total enthalpy as the reference. Thus, a value of e.g. 4% means that, if the Mach number were to be computed by applying adiabatic flow equations with the jet total enthalpy as the quantity to conserve, than the result would be 4% higher than if it were computed with the freestream value.

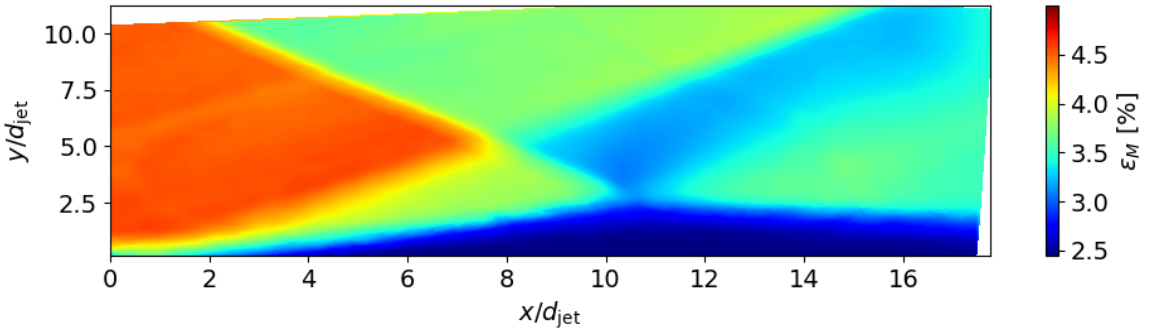

Figure 6.35: Relative error in the estimation of Mach number. Shown for the field generated by $\theta = 12\,\text{deg}$ and no jet.

Figure 6.36 reports the distribution of the Mach number, with a highlight on the sonic line, marked in black. By comparison with Figure 6.37, it is possible to notice how the weak shock causes a smaller separation zone compared to the 12-degree case. The reader is kindly invited to note that, for either case, it was not the intention the shocks would hit at the same location, but rather to demonstrate the difference in the extension of the separated flow bubble. The effect of the jet on the SBLI is also mentioned in some work of

literature, but to a lesser extent. Publications such as the one by Barzegar Gerdroodbary et al. (2015) or the ones by Nakamura et al. (2008) and Nakamura et al. (2009) focus more on the effect that the shock has on the mixing more than the effect on the SBLI itself. But what is the effect of the jet on the plain interaction, and not the opposite? Figures 6.38 and 6.39 provide some initial insight.

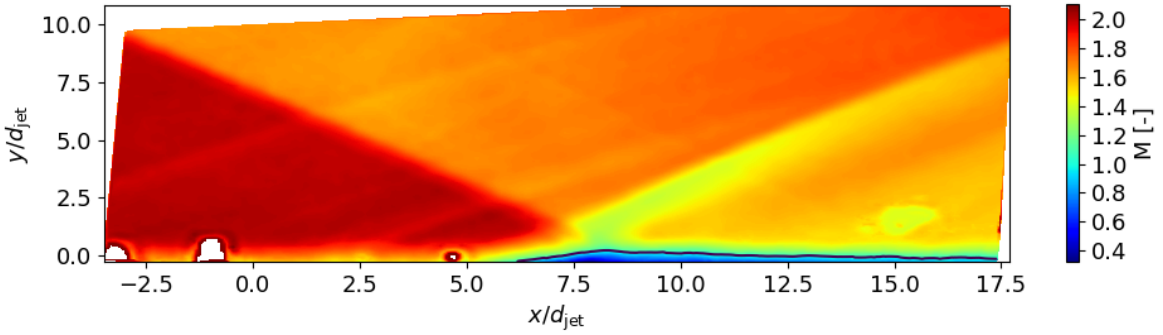

Figure 6.36: Contour plot of Mach number for the baseline flow cases without the jet. $\theta = 9\,\text{deg}$

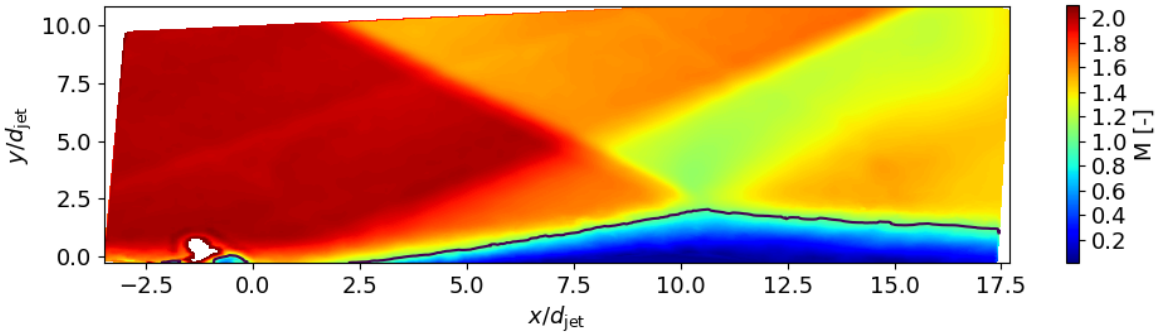

Figure 6.37: Contour plot of Mach number for the baseline flow cases without the jet. $\theta = 12\,\text{deg}$

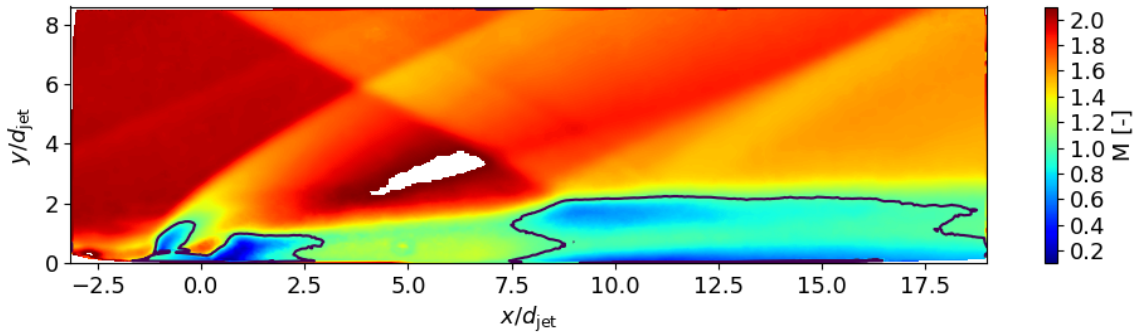

Figure 6.38: Contour plot of Mach number for the baseline flow cases without the jet. $\theta = 9\,\text{deg}$ and $x/d = 13$

The contour plot reporting the distribution of Mach number is a familiar sight. Yet, a fundamental difference emerges, as the separation zone caused by the shock is now substantially greater in size than the baseline cases. It is, in fact, possible to see some

notable differences in the behaviour of the sonic line. First, the region upstream of the jet is also wrapped in the thin black line: this is where the bow shock interacts with the incoming boundary layer. The downstream region too appears subsonic until a point where presumably the flow reattaches to the wall. Then, as the incoming shock meets the wall layer, air undergoes a second sharp deceleration that assumes the form of almost a normal shock wave. The flow remains subsonic until almost the end of the field of view.

The configuration for the stronger oblique shock also shows a larger than baseline separation region. The change here is, in fact, massive. Not only the jet's wake has the effect of enlarging the separation zone beneath the point of impingement, but the adverse pressure gradient induced by the wave is so strong that perturbations are able to travel all the way up to the jet location. This allows the two flow bubbles to connect forming one single massive separation zone, as depicted in Figure 6.39.

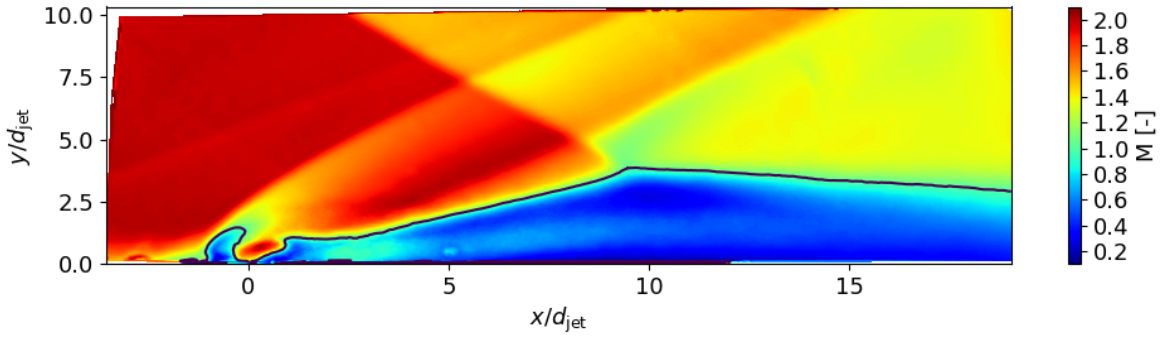

Figure 6.39: Contour plot of Mach number for the baseline flow cases without the jet. $\theta = 12$ deg and $x/d = 13$

As the shock is moved more downstream, the flow is then able to reattach before turning subsonic again, as demonstrated in Figure 6.40.

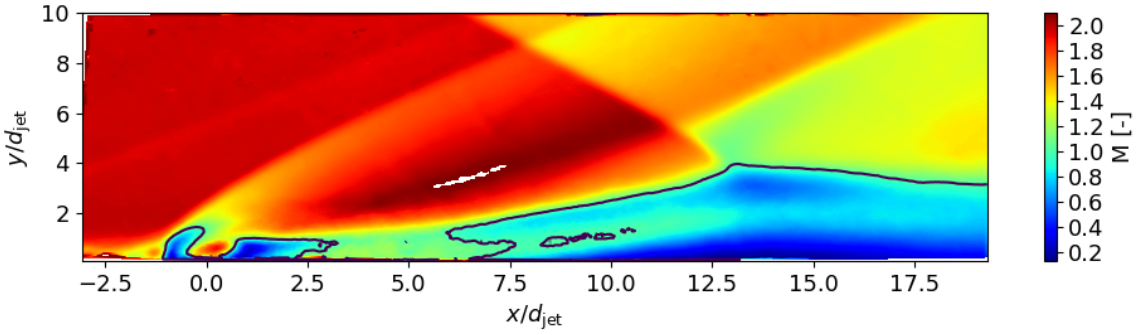

Figure 6.40: Contour plot of Mach number for the baseline flow cases without the jet. $\theta = 12$ deg and $x/d = 16$

The effect on increasing momentum flux ratio on the interaction also appear rather clear, although not visualized in a contour plot such as the ones in the above. By pumping more momentum into the crossflow, an increased-J scenario leads to a increase in the size of the separated flow bubble. Table 6.3 reports data on the geometry of the interaction zone (i.e. below the sonic line).

J	θ [deg]	x_{shock}/d [x/d]	Δx	$\Delta x/\Delta x_{baseline}$
-	*9*	-	*11.74*	-
1	9	13	10.50	0.89
2	9	13	12.00	1.02
-	*12*	-	*27.52*	-
1	12	13	49.43	1.80
1	12	16	61.99	2.25
2	12	13	96.96	3.52
2	12	16	70.10	2.55

Table 6.3: Table reporting the variations in height and length of the interaction zone.

In the table above, the length parameter Δx refers to the length subtended along the wall by the sonic line. As the flow there is subsonic, the Navier-Stokes assume an elliptical behaviour, thus allowing perturbations to travel both down- and upstream. It is necessary to note that the values for the Δx for the 12-degree cases were estimated by taking the average slope of the degrading sonic line and computing a tentative reattachment point.

Some notable results emerge from Table 6.3.

- **The weak shock case causes little change.** By comparing the figures for the change in interaction length and height of the sonic flow bubble, one can see how the 9-degree case causes little to no variation compared to the 12-degree shock generator. As the shock is weaker, a weaker opposing pressure gradient is generated, thus allowing air to remain more closely attached to the wall.
- ***J* worsens the interaction.** By increasing the momentum flux ratio an immediate repercussion on the separated "triangle" is seen, as the Δx increases as a consequence.

The last aspect that needs to be discussed for this section is the one three-dimensionality. The "classical" SBLI mechanism is mainly two-dimensional, in fact. However, the addition of normal blowing jet upstream of the interaction zone causes the resulting field to be everything but 2D. From the large-scale vortices appearing in the oil flow visualization and in the PIV imaging of wall-normal planes to strong out-of-plane velocity components, the resulting field is highly 3D. An example (indicative of all cases) is shown in Figure 6.41.

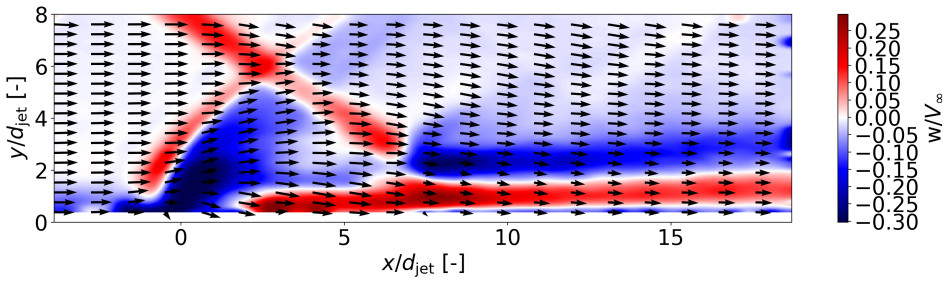

Figure 6.41: Vector field for flow configuration where $J = 1$, $\theta = 9$ deg, $x/d = 16$. Imaged at $z/d = -2$. Coloured by w-component of velocity (out-of-plane).

The combined action of the bow shock wave, the CVP-induced velocity field and the action of the expanding plume all contribute to the definition of the out-of-plane velocity

component distribution seen in the above graphic. One would expect the field to be two-dimensional even if the jet were present, especially because the field shown corresponds to the centre-plane. In light of this fact, this can be only explained by a slight misalignment of the laser sheet, slightly to the port side of the mid-plane. This being said, it is maybe more interesting to look at the distribution of the same component of velocity, but this time on a wall-parallel view: Figure 6.42.

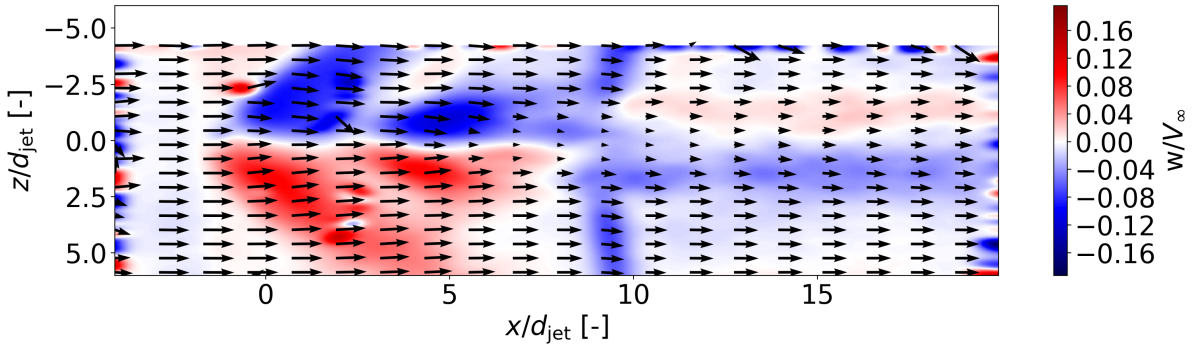

Figure 6.42: Vector field for flow configuration where $J = 1$, $\theta = 12\,\text{deg}$, $x/d = 16$ imaged at $y/d = 2$. Coloured by w-component of velocity (across-plane).

The figure shows an obvious divergence of the incoming flow around the centre line due to the bow shock. This feature imparts a deviation to the incoming flow in accordance with its local inclination angle to the symmetry line of the test section. The same flow deviation is also observed just downstream of the shock as air is pushed around the barrel shock by the expansion fan. As the shock front is crossed, the tail of the CVP vortices is still visible and imparts a deviation in the direction of the centre line on either side of it.

6.3.4. The instantaneous field

In the context of the design of a SCramjet-powered vehicle, the flight Mach number of interest is usually placed in 8-15 range. As thoroughly explained in the work by Ben-Yakar and Hanson (1998), the burner entry total enthalpy is usually much greater than the current experiment's value. In flight, with higher temperature, higher speed of sound and, thus, higher flow velocity, the value for H sets itself at about one order of magnitude higher. As the combustor system characterized by a jet in crossflow fully relies on self-ignition for combustion, four main variables need to attain high-enough values: static temperature, static pressure, fuel-air mixture and residence time. Now, concerning the present work, clear regions where this can occur coincide with the flow separation and recirculation regions both upstream and downstream of the jet injection point. Here, lower velocity allows for longer residence time, while conservation of momentum laws dictate and increase in static pressure and, thus, static temperature. This makes the regions in question rather suitable for holding a flame. In addition to providing "momentum" to flow state variables such as temperature and pressure, these are the loci where most of the large-scale turbulent motions and coherent structures are created. According to Liu et al. (2015), these carry batches of unmixed fuel and air which enables the formation of a diffusion that gets convected downstream. A similar conclusion had been drawn by Nakamura et al. (2009), who indicated how the incident oblique shock allows for proliferation of vorticity-driven structures that tend to enhance mixing.

A mention is made on the publication by Ben-Yakar and Hanson (1998) specifically addressing the importance of the shock in potentially corroborating the flameholding capability of the system. Figure 6.43 displays the instantaneous flow field for one of the baseline cases.

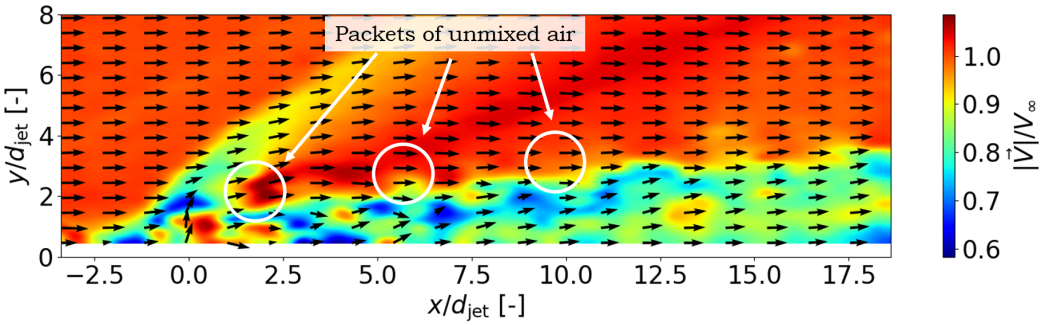

Figure 6.43: Instantaneous snapshot of flow field for $J = 1$ taken 6.67 [s] after the beginning of the corresponding acquisition sequence. Coloured by velocity magnitude. Highlighting packets in the shear layer.

As the air stream being exhausted from the wall passes the normal Mach disk and decelerates, a shear layer is formed between the jet's flow and the crossflow. Shear induces deformation and large-scale coherent structures, which form "packets" which enlarge the contact area between the two entraining fluids. This allows for greater mixing performance and, thus, the achievement of the proper stoichiometric ratio for combustion (i.e. the fuel-to-air ratio, φ). Auto-ignition is then obtained with the achievement of sufficient static pressure and temperature.

Figure 6.44 shows, instead, the development of vortices on a wall-parallel plane, whereby the intensity of the vortical motions appear to fade the further downstream. This is a com-

bined effect of the plume rising above the actual plane of the laser and the fact that “fuel” mixes with and diffuses into the crossflow.

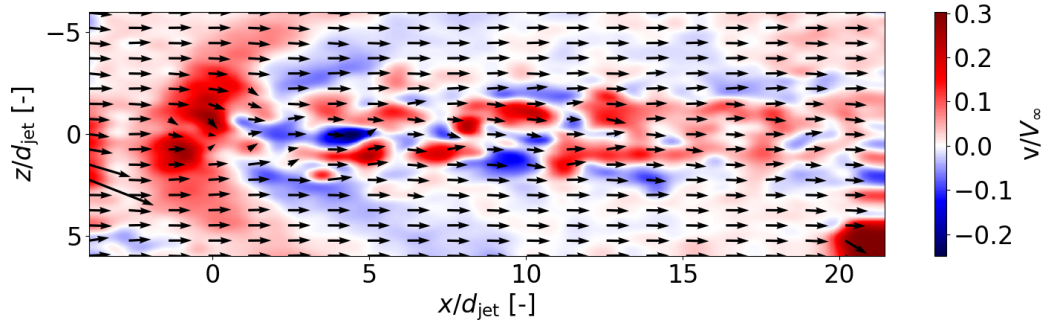

Figure 6.44: Instantaneous snapshot of flow field for $J = 1$ at $y/d = 1$ taken 6.67 [s] after the beginning of the corresponding acquisition sequence. Coloured by velocity v-component (out-of-plane).

But what happens when an incident shock is introduced into the field? Figure 6.45 introduces the situation on a wall-normal plane.

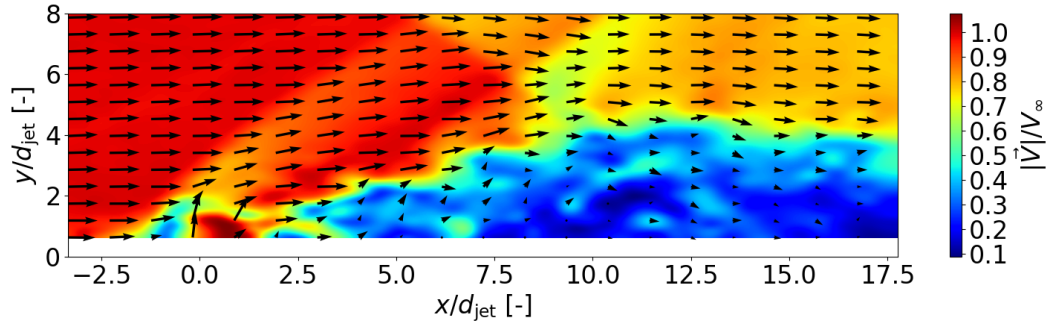

Figure 6.45: Instantaneous snapshot of flow field for $J = 1$, $\theta = 12\,\text{deg}$ and $x/d = 13$ taken 6.67 [s] after the beginning of the corresponding acquisition sequence. Coloured by velocity magnitude.

Before discussing the effect of it any further, the introduction of the situation on a wall-parallel plane is in order (see Figure 6.46), as the effects on both planes are complementary.

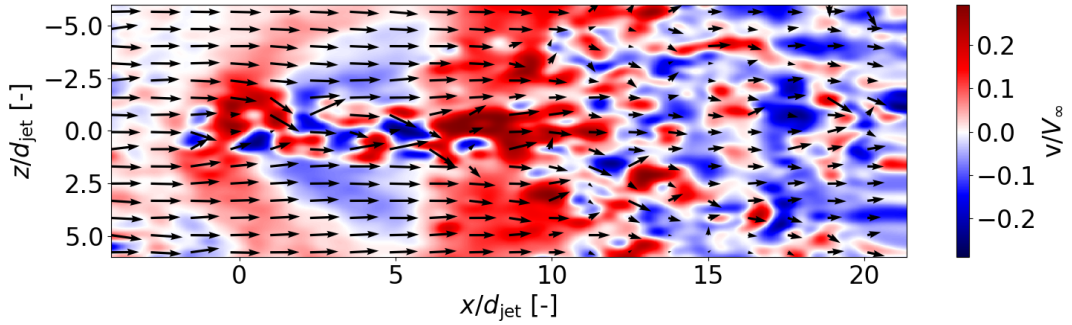

Figure 6.46: Instantaneous snapshot of flow field for $J = 1$, $\theta = 12\,\text{deg}$ and $x/d = 13$ at $y/d = 1$ taken 6.67 [s] after the beginning of the corresponding acquisition sequence. Coloured by velocity v-component (out-of-plane).

6.4. Discussion

The chapter that is just coming to an end reported the findings of an experimental test campaign that had the goal to the investigate the interaction between a sonic jet and an incident oblique shock wave in a supersonic crossflow. The relevance of this set-up is particularly clear in the context of the design of a combustor for SCramjet engines. The plain jet in crossflow configuration has been extensively studies in the literature as an effective method of injecting fuel inside the combustion chamber of a SCramjet engine. The introduction of an oblique shock impinging on the plume serves as a mean to enhance mixing of fuel and air in preparation for combustion.

Three main control parameters were taken into consideration for the study of the resulting field: the momentum flux ratio, the flow deflection angle (dictating the shock strength) and the location of the inviscid impingement point downstream of the jet exit's position. A quantification was then performed for the velocity, vorticity and Reynolds stress fields (i.e. turbulent kinetic energy). Furthermore, it was possible to quantify both the vertical penetration of fuel in the crossflow and the lateral expansion of the plume. Downgrading effects of this interaction reside in the separation caused within the interaction region of the SBLI, which is expected to cause a significant increase in wave drag.

It was observed how the different control variables each have a different and not necessarily intuitive effect on the mixing patterns. The introduction of the shock itself causes unexpected effects. The baseline images reporting the field generated by a jet not interacting with a shock show a sharp increase in the scalar value of Reynolds stresses along a diagonal region rising from the jet exit location. An addition high-mixing region is observed in the near-wall region in the mid-field, where high-intensity turbulent stresses are observed. As the shock is introduced in the field, it appears as the turbulent stresses concentrated mainly in the downstream near-field of the jet and along the developing shear layer resulting from the SBLI's compression wave. High-intensity turbulent kinetic energy is no longer visible in the near-wall region. This is a result of the shock stabilizing the flow downstream of its impingement point and is a similar result compared to the one obtained by Pasquariello et al. (2014).

Anyhow, the shock does prove to be effective in the enhancement of mixing by other means. To begin with, the shock increases the penetration height of the plume and its lateral expansion. A word of caution must be mentioned, though, as only the strong wave was seen to have this effect. The 9-degree cause little to no difference on the field. Furthermore, the formation of a shear layer further helps in increasing vorticity in the jet's near- to mid-fields. Not to mention the vortical features that are expected to provide an additional helping hand. Large-scale vortices were observed both in oil flow visualization and wall-parallel PIV measurements, especially in the strong shock configurations. These provided additional vorticity sources and particularly strong in the configurations with a 12-degree flow deflection. In fact, 9-degree cases were also observed to generate this kind of vortices as of oil flow friction lines, but of lesser intensity.

Finally, in terms of combustion enhancement, a brief digression is made in the foregoing. As one of the fundamental variables that one needs to look out for in the context of the design of a combustor, an increased transit time through the field allows thorough combustion. The longer the transit time, the better. As expected, by inspection of Table 6.4, the case where the shock impinges the closest to the jet for the strong shock case is

the one with the longest time. Transit time is defined as the ratio of the average velocity along the streakline originating at the point (0,0.5) to the distance travelled along that same streakline all the way to the end of the visible field of view (Equation 6.9).

$$\tau = \frac{\overline{L}}{\overline{V}} \tag{6.9}$$

In the above, $\overline{L}$ and $\overline{V}$ are the distance travelled and the average stream speed along the flow locus.

J	θ [deg]	$x_{\text{shock}}/d_{\text{jet}}$	$\overline{V}$ [m/s]	$\overline{L}$ [mm]	τ [μs]
1	-	-	392.85	62.07	158.03
2	-	-	393.97	63.24	160.52
1	**12**	**13**	**280.53**	**63.04**	**224.71**
2	12	13	297.86	64.20	215.54
1	12	16	329.58	61.56	186.78
2	12	16	350.50	63.32	180.66
1	9	13	336.93	63.12	182.95
2	9	13	369.22	63.32	170.96
1	9	16	302.74	61.64	203.61
2	9	16	322.37	62.60	194.18

Table 6.4: Table reporting average transit speed, transit length and time for a particle along a streakline originating at (0,0.5) [d_{jet},d_{jet}].

By analysing Figures 6.46 and 6.46, it is possible to conclude that the shock can have the following effects relating to the promotion of combustion.

- **Favourable flow variables.** As the flow over the shock decelerates, both static temperature and pressure undergo an increase, which are both factors that ease autoignition.
- **The introduction of vorticity.** As the shock acts as a source of baroclinic vorticity ($\omega \propto \nabla p \times \nabla \rho$) it favours entrainment. This promotes mixing of fuel and air on a molecular level. In turn, this allows for the setting of a fuel-to-air ration that is adapt for combustion.
- **Formation of large-scale structures.** As the shock effectively slows down the flow even more than the upstream bow shock, another "new" shear layer is added to the flow field, promoting the formation of even more vortical structures and "packets" of unmixed flow.
- **Plume expansion.** As per the combined action of the CVP and the compression wave upstream of the interaction region, the plume rises from the wall and, due to the deceleration imparted by the shock front, the plume expands laterally due to continuity (Figure 6.46).
- **Increased residence time.** Taking a streakline originating at some distance above the jet exit, Table 6.4 points to the fact that the most convenient solution is having the strong shock interacting with the jet at the closest distance downstream.

7

Conclusion

The development of high-speed air-breathing engines as a mean to propel single-stage-to-orbit (SSTO) launchers, high-speed transport aircraft and, eventually, space-planes is returning to act as an alternative to chemical propulsion for (trans-)atmospheric flight. As the flight regime turns hypersonic ($M_\infty > 5$), ramjet engines no longer provide high enough efficiency for sustained super- and hyper-cruise. Supersonic combustion engines thus make the only propulsion system that the state-of-the-art can offer. An experimental research project was conducted with the goal of analysing the interaction of a sonic transverse jet with a supersonic Mach-2 crossflow and an incident oblique shock wave. Being this flow system mostly in use as a fuel injector for supersonic combustion ramjet engines, the intent was to study how an impinging oblique shock could enhance mixing of fuel and air in light of the combustion processes that take place within the chamber. As a result, though, a shock-wave boundary-layer interaction forms inside the section due to the presence of the flow discontinuity. Depending on the strength of the impinging shock, flow separation thereby introduced could cause losses in terms of total pressure, section chocking and increased friction. The aim of this research was therefore to attempt a quantification of these counter-playing effects to provide information for the design of SCramjet engines and, specifically, the combustion chamber.

ST-15 is a high-speed, blow-down wind tunnel located in the Aerodynamics High-Speed Laboratory (HSL) at the Faculty of Aerospace Engineering of Delft University of Technology. Its test section is 15x15 [cm] in cross-section and allows for insertion of different nozzle geometries. This facility was the one in use for the work presented in this document. The testing conducted for this work made use of a Mach-2 converging-diverging nozzle. Simultaneous oil flow visualization and Schlieren photography have been used to get an understanding of the flow behaviour for the complex interaction taking place in the test section. These preliminary measurement also served as a starting point to select which conditions should have been tested with stereo PIV and to allow for re-design of some necessary components. Testing was conducted varying three main parameters: the jet's momentum flux ratio (J), the flow deflection angle (θ) and the shock impingement location downstream of the jet ($x_{\mathrm{shock}}/d_{\mathrm{jet}}$). Additionally, PIV measurements were acquired both on wall-normal and wall-parallel planes.

Schlieren photography images allows for basic quantification of the flow field and the characterization of baseline results. Concerning the behaviour of the flow in the near-field of the jet, a barrel shock forms enveloping the exhaust of the nozzle. The position of

the Mach disk, of fundamental importance for momentum-driven mixing in the near-field, rises linearly from the bottom wall with increasing J, as it shifts downstream. The further the Mach disk is located from the exit location, the better the mixing, as mentioned by Kawai and Lele (2009). Furthermore, it was noticed that, for the lowest momentum flux ratio in testing and, especially for the cases where the incident shock strength was the highest, the barrel shock assumes a concave shape. Most probably, this is caused by the perturbation travelling upstream below the sonic line due to large-scale separation caused by the incident shock. As J is increased from 1 to 2, x- and y-positions see an increment of $\approx 0.66 d_{\mathrm{jet}}$ and $\approx 0.45 d_{\mathrm{jet}}$, respectively. The addition of the incident shock wave has no particular effect on the location of the Mach disk, as the barrel shock lies well outside the elliptical region induced by the shock. The incident OSW does, however, have an effect on the point where the flow separates as a result of the compression wave induced by the SBLI. When the shock impinges at the most upstream location, $x/d = 13$ for the 12-degree and $x/d = 16$ for the 9-degree case (for the preliminary runs) the difference on the point of onset of the compression wave barely varies. As the shock impinges at the downstream location, though, the variation is of 8.3% for the 12-degree and 5.8% for the 9-degree wedge for an increasing J. Both cases extend the separation bubble.

The question as to how the shock affects mixing has a complicated answer. Depending, in fact, on the shock strength (i.e. the deflection angle) and the downstream impingement point, different flow features arise. Starting from the abrupt expansion of the separated flow bubble and the extension of the size of vortices visible in the instantaneous snapshots to the formation of discontinuities in the shock-affected portion of the wall-layer. The presence of low-speed flow is beneficial for entrainment of the two air flows as, in general, this leads to greater velocity gradients and, thus, vorticity and strain. The formation of a large-scale shear layer is deemed by literature, in fact, of great importance for mixing of fuel and air. Three variables are the ones to monitor for the quantification of this interaction: the plume's penetration, its lateral expansion and the Reynolds stresses (or the sum of the diagonal components: the turbulent kinetic energy).

Jet penetration was shown to increase as a strong oblique shock is introduced into the field. Due to the combined action of the CVP and the upward deflection caused by the compression wave upstream of the SBLI region, the plume showed an increase in height above the wall. In particular, for $J = 1$ and $J = 2$, it showed a 44.5% and 66.3% increase in height above the wall at $x/d_{\mathrm{jet}} = 10$, respectively. This was for the case where $\theta = 12$ deg and $x_{\mathrm{shock}}/d_{\mathrm{jet}} = 13$. A milder improvement, as compared to baseline, was shown for the case where $x_{\mathrm{shock}}/d_{\mathrm{jet}} = 16$ and little to no improvement was instead shown for the weakly interacting shock and boundary layer (i.e. $\theta = 9$ deg). If the weak shock did not show much improvement for the vertical penetration, it certainly showed gains for the plume's lateral expansion. It enables a 33% gain in the plume's width on wall-parallel images for the case where $x_{\mathrm{shock}}/d_{\mathrm{jet}} = 13$. The more downstream case reported a gain of 29.8% in width. The 12-degree case certainly still provides more lateral expansion, as large-scale vortices are shown to form both on the $y/d_{\mathrm{jet}} = 1$ and $y/d_{\mathrm{jet}} = 2$ planes, which greatly contribute to entrainment enhancements. This configuration reports a 59.6% increase for the shock's upstream position and a 48.9% one for the downstream scenario.

The distribution of turbulent kinetic energy is greatly altered by the introduction of the incident shock. The baseline cases show the development a large "streak" of medium-intensity turbulent kinetic energy that propagates up and away from the wall. This no longer appears visible in the cases where the shock hits the plume. Instead, a very high-intensity region is seen in the immediate near field of the jet, followed downstream by

medium-to-low-intensity flow parcels that distribute around the sonic line. Even though instantaneous frames still show the abundant presence of shear layer vortices, the turbulent kinetic energy appears to be lower as compared to no-shock cases. Certainly, this is compensated by greater penetration and expansion and higher residence time in the combustor dictated by lower chamber velocity.

A performance-downgrading phenomenon is certainly introduced by the shock in the form of shock-wave boundary-layer interactions. The cases with no shock impinging on the flow report little separation in the proximity of the jet exit. As a shock is added to the field, the consequent SBLI causes large-scale separated flow bubbles, which certainly hinder overall combustor performance as they translate into a notable increment in wave drag. In some cases, the separation region induced by the discontinuity joins with the jet-induced one downstream of it to form a massive recirculating flow bubble. For the strong shock cases this obviously constitutes a greater issue compared to the weak shock configurations. An increment of 80% to as much as 252% of the length of the interaction zone. Milder separation is seen for the 9-degree deflection cases, which only report a significant increase in the bubble's height, but not in length.

On a positive note, the introduced shock wave increases the residence time of air inside the combustion chamber. In particular, the configuration that also provided the maximum expansion and penetration ($\theta = 12\,\mathrm{deg}$ and $x_{\mathrm{shock}}/d_{\mathrm{jet}} = 13$ for $J = 1$) also appears to be the one slowing air down the most, by 42.1% compared to the baseline. As the strong shock provides the most deceleration, the highest increase in static pressure and static temperature, it is deemed the configuration that, purely for flame holding provides the most gains for the design of the combustor.

7.1. Recommendations for future work

Based on the conclusions that have been drawn from the present work, the author feels necessary to recommend future research endeavours to attempt and solve the outstanding issues by taking on further experimental work. The foregoing highlights a few points that are deemed of importance to accomplish this goal. The foregoing highlights factors that are within the technical possibilities of ST-15 or, in general, the high-speed experimental facilities of the HSL.

The present work focused on the quantification of the flow field using air being injected into more air. If a more thorough investigation of mixing is to be conducted, than a using a different injectant might be of interest. This is particularly relevant for Schlieren measurement, where the almost uniform density field in the region of injection does not allow for proper clarification of the jet's shear layer developing.

The employment of a different species for the injectant also allows for vortex-tracking techniques to be implemented in an attempt to quantify the unsteadiness induced by the interaction. The present study indeed attempted a quantification based on the empirical evidence that the deformation of the barrel shock is periodic. However, the hypothesis that its unsteadiness is purely due to shear layer vortices being shed at the orifice could not be verified. Vortex tracking allows for better quantification of this phenomenon. Furthermore, the question remains as to how exactly the unsteadiness caused by shear layer vortices affects the combustion process.

Even though literature suggests that having a shock impinge upstream of the jet is not ideal for the enhancement of combustion, the study of flow cases where this is indeed

the case might provide definitive answers as to why this is actually the case. Still, it is though that the upstream shock impingement position might benefit the flow in reducing the strength of the bow shock (as the incoming Mach number is now lower than freestream) and thus causes lower losses in terms of total pressure. So the study of such configuration could provide additional information when the time comes to execute a trade-off.

In terms of PIV measurements, three are thought to be the improvements to the measurement set-up that has been employed in the present study. First: tomographic PIV. As the flow field is highly three-dimensional and stereo PIV is only able to capture the out-of-plane velocity component, the quantification of the full velocity gradient tensor will provide more accurate characterization of the vortical motions caused by the interaction. Vortex reconstruction with identification techniques such as the λ_2 criterion will come in handy for the quantification of the development of the shear layer. A second improvement that can be made is the acquisition frequency of the PIV system. As the freestream velocity is rather high, increased acquisition frequency will enable more accurate tracking of the development of flow features. Third and final: the analysis of the last remaining plane: the wall-normal, flow-normal plane. This is the plane that will depict in detail the development of the CVP and will enable the description of the velocity field it induces.

The last recommendation that the authors feels is needed to mention is the application of pressure reconstruction techniques. The present research could only make speculations in regards to the effects each flow configuration has on the wave drag based on the size of the separation zone. Pressure reconstruction, maybe combined with Pitot tube measurements for the acquisition of total pressure readings will give a clear overview in regards to a change in wave drag. The configurations in study, in fact, are thought to produce a large component of wave drag. For the design of SCramjet engines, the definition of this factor is key.

A

Technical Drawings

This appendix presents the technical drawings of the components that went into the test section of ST-15, making up the main experimental set-up.

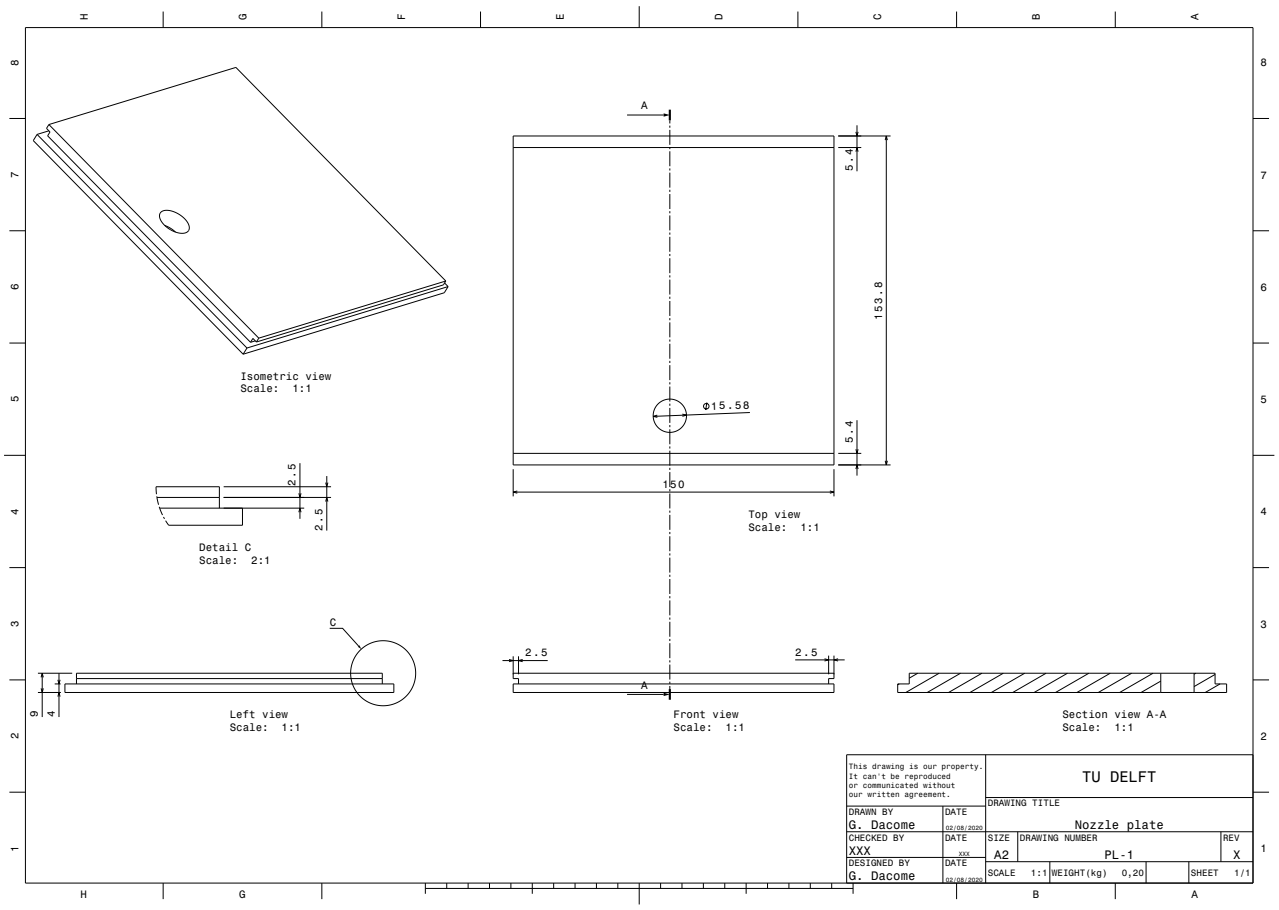

Figure A.1: The plate holding the sonic nozzle on the bottom liner of ST-15

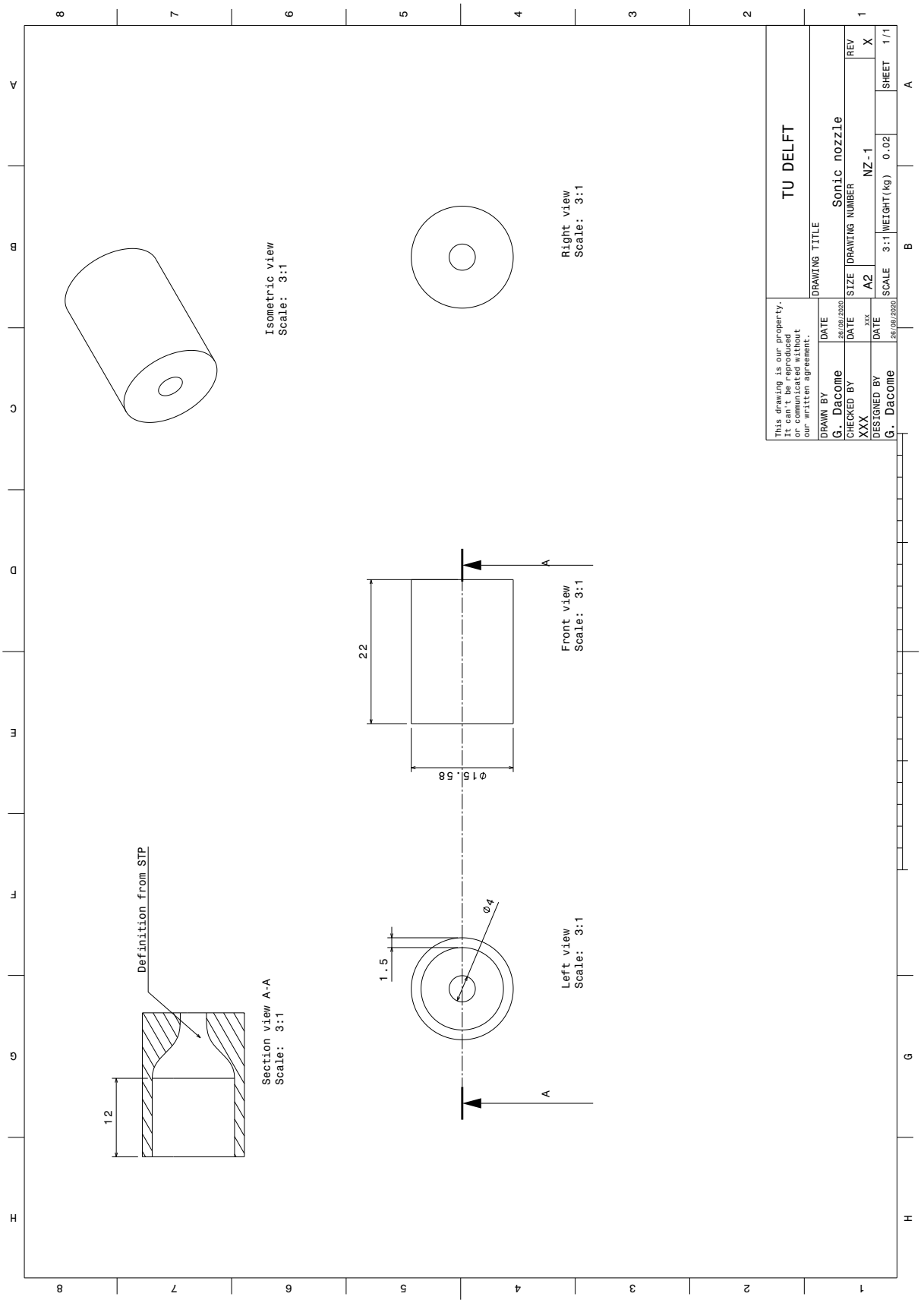

Figure A.2: The plate holding the sonic nozzle on the bottom liner of ST-15

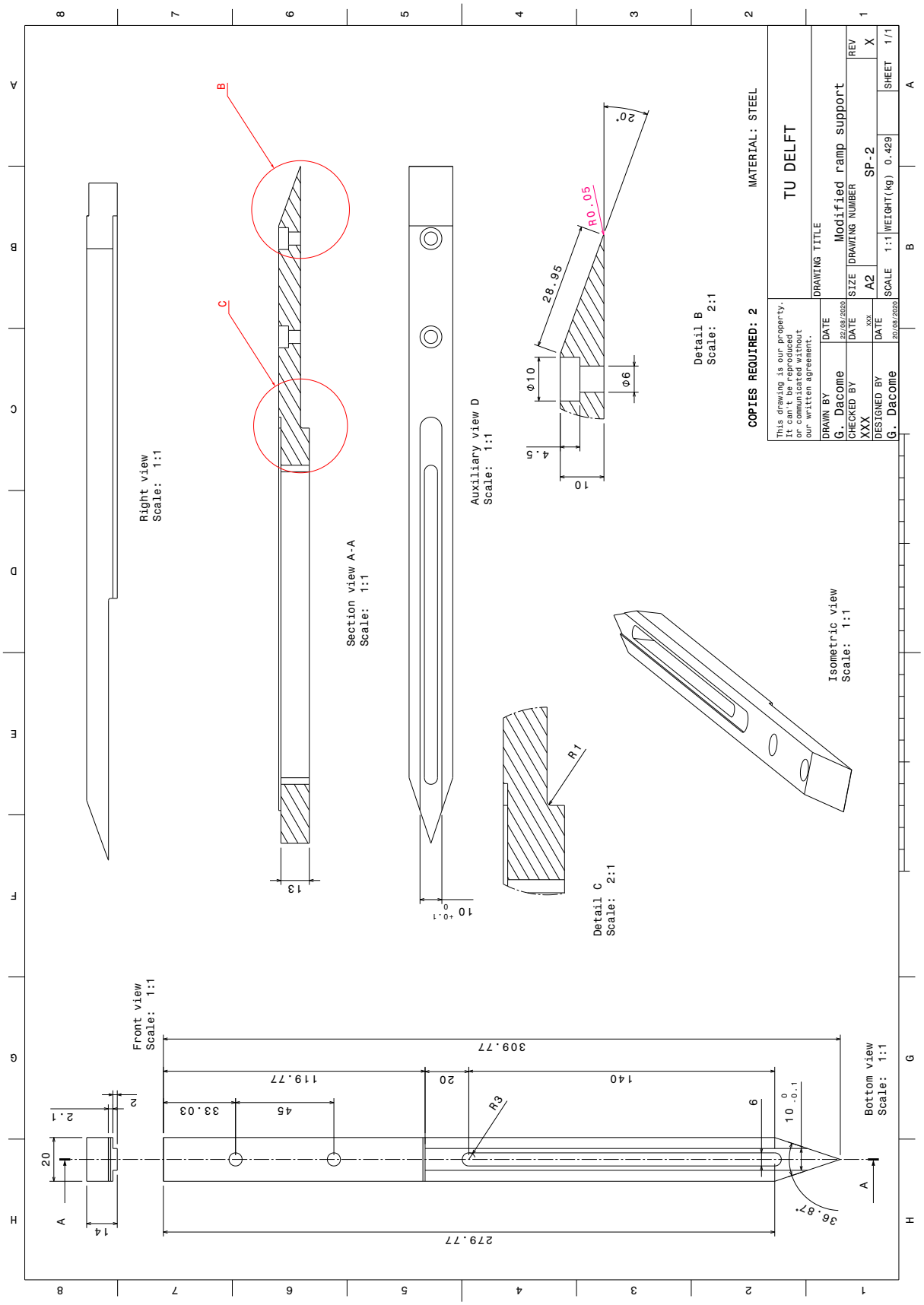

Figure A.3: Re-designed supports for the shock generators

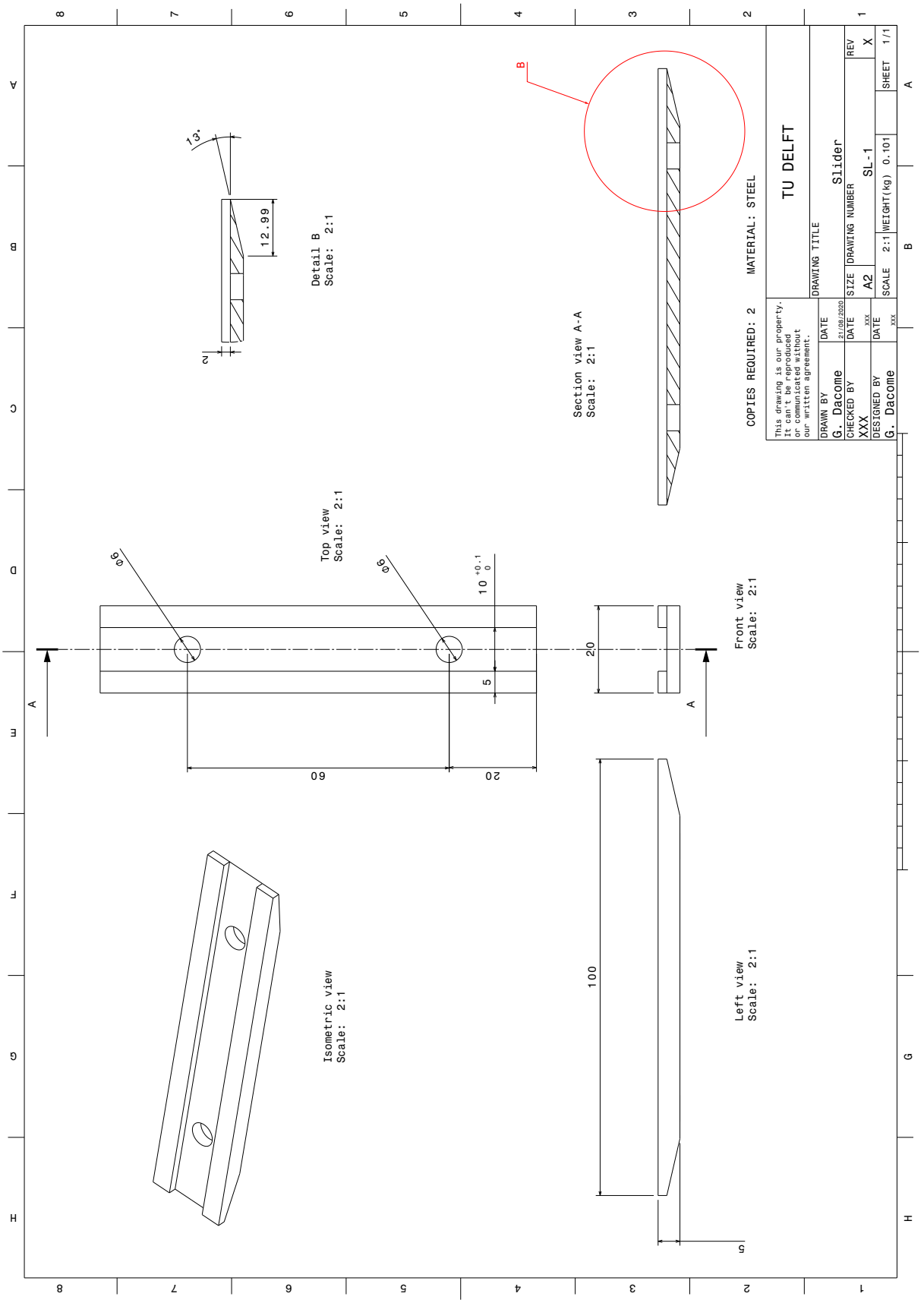

Figure A.4: Slider for securing bolts to pylons

B

Test Matrices

Table B.1 reports the test matrix that was executed in the first testing campaign in ST-15. The goal of this was obtain an understanding of the flow physics underlying the complex interaction.

Table B.2, instead, reports the test matrix for the PIV campaign. Please note that it includes some measurement points that had to be repeated due to poor acquisition quality in the first experimental effort.

#	M	J	θ [deg]	$x_{\text{shock}}/d_{\text{jet}}$	Oil	Measurement Technique
1	2	1	-	-	-	Schlieren
2	2	1.5	-	-	-	Schlieren
3	2	2	-	-	-	Schlieren
4	1	1	-	-	-	Schlieren
5	1	1.5	-	-	-	Schlieren
6	1	2	-	-	Yes	Schlieren
7	-	-	9	16	Yes	Schlieren
8	1	1	9	16	-	Schlieren
9	1	2	9	16	Yes	Schlieren
10	1	1	9	24	-	Schlieren
11	1	2	9	24	Yes	Schlieren
12	-	-	12	13	Yes	Schlieren
13	1	1	12	13	-	Schlieren
14	1	2	12	13	Yes	Schlieren
15	1	1	12	21	-	Schlieren
16	1	2	12	21	Yes	Schlieren
17	1	1	12	30	-	Schlieren
18	1	2	12	30	Yes	Schlieren
19	1	1	-	-	-	High frame rate Schlieren
20	1	2	-	-	-	High frame rate Schlieren
21	1	1	-	-	-	Shadowgraph
22	1	2	-	-	-	Shadowgraph
23	1	1	9	16	-	Shadowgraph
24	1	2	9	16	Yes	Shadowgraph
25	1	1	12	13	-	Shadowgraph
26	1	2	12	13	-	Shadowgraph
27	1	1	12	13	-	High frame rate Schlieren
28	1	1.5	-	-	-	High frame rate Schlieren
29	1	2	12	13	-	High frame rate Schlieren
30	1	-	12	13	-	High frame rate Schlieren
31	1	1	-	-	-	High frame rate shadowgraph
32	1	2	-	-	-	High frame rate shadowgraph
33	1	1	12	13	-	High frame rate shadowgraph
34	1	2	12	13	-	High frame rate shadowgraph
35	1	2	-	-	Yes	Just oil, no imaging
36	1	1	9	16	-	High frame rate Schlieren
37	1	2	9	16	-	High frame rate Schlieren

Table B.1: Test matrix for Schlieren campaign

#	J	θ [deg]	$x_{\text{shock}}/d_{\text{jet}}$	Oil	Plane – z/d_{jet} or y/d_{jet}
Wall-parallel measurements					
1	1	12	13	YES	-
2	2	12	13	YES	-
3	2	9	16	YES	-
4	1	-	-	-	0
5	2	-	-	-	0
6	1	9	16	-	0
7	2	9	16	-	0
8	1	9	13	-	0
9	2	9	13	-	0
10	1	12	16	-	0
11	2	12	16	-	0
12	1	12	13	-	0
13	2	12	13	-	0
14	1	9	16	-	-2
15	2	9	16	-	-2
16	1	9	13	-	-2
17	2	9	13	-	-2
Wall-parallel measurements					
18	1	-	-	-	2
19	1	12	16	-	2
20	1	12	13	-	2
21	1	9	16	-	2
22	1	9	13	-	2
23	1	-	-	-	1
24	1	9	13	-	1
25	1	12	13	-	1

Table B.2: Test matrix for PIV campaign

Bibliography

Mohd Y. Ali, Farrukh S. Alvi, Rajan Kumar, C. Manisankar, S. B. Verma, and L. Venkatakrishnan. Studies on the influence of steady microactuators on shock-wave/boundary-layer interaction. *AIAA Journal*, 51(12):2753–2762, 2013. ISSN 0001-1452 1533-385X. doi: 10.2514/1.J052201.

A. Anazadehsayed, M. Barzegar Gerdroodbary, Y. Amini, and R. Moradi. Mixing augmentation of transverse hydrogen jet by injection of micro air jets in supersonic crossflow. *Acta Astronautica*, 137:403–414, 2017. ISSN 00945765. doi: 10.1016/j.actaastro.2017.05.007.

T. J. Aubry, G. Carazzo, and A. M. Jellinek. Turbulent entrainment into volcanic plumes: New constraints from laboratory experiments on buoyant jets rising in a stratified crossflow. *Geophysical Research Letters*, 44(20):10,198–10,207, 2017. ISSN 00948276. doi: 10.1002/2017gl075069.

H. Babinsky and J. K. Harvey. *Shock Wave-Boundary-Layer Interactions*. Cambridge University Press, 2011. ISBN 9780521848527.

M. Barzegar Gerdroodbary, O. Jahanian, and M. Mokhtari. Influence of the angle of incident shock wave on mixing of transverse hydrogen micro-jets in supersonic crossflow. *International Journal of Hydrogen Energy*, 40(30):9590–9601, 2015. ISSN 03603199. doi: 10.1016/j.ijhydene.2015.04.107.

A. Ben-Yakar and R. Hanson. Experimental investigation of flame-holding capability of hydrogen transverse jet in supersonic cross-flow. In *Twenty-Seventh Symposium (International) on Combustion*, volume 27, pages 2173–2180, 1998.

A. Ben-Yakar and R. Hanson. Ultra-fast-framing schlieren system for studies of the time evolution of jets in supersonic crossflows. *Experiments in Fluids*, 32(6):652–666, 2002. ISSN 0723-4864 1432-1114. doi: 10.1007/s00348-002-0405-z.

A. Ben-Yakar, M. G. Mungal, and R. K. Hanson. Time evolution and mixing characteristics of hydrogen and ethylene transverse jets in supersonic crossflows. *Physics of Fluids*, 18 (2), 2006. ISSN 1070-6631 1089-7666. doi: 10.1063/1.2139684.

L. H. Benedict and R. D. Gould. Towards better uncertainty estimates for turbulence statistics. *Experiments in Fluids*, 22:129–136, 1996.

S. J. Beresh, J. F. Henfling, and R. J. Erven. Flow separation inside a supersonic nozzle exhausting into a subsonic compressible crossflow. *Journal of Propulsion and Power*, 19 (4):655–662, 2003. ISSN 0748-4658 1533-3876. doi: 10.2514/2.6154.

S.J. Beresh, J. T. Heineck, S. M. Walker, E. T. Schairer, and D. M. Yaste. Planar velocimetry of jet/fin interaction on a full-scale flight vehicle configuration. *AIAA Journal*, 45:1827–1840, 2007. doi: 10.2514/1.26485.

Steven J. Beresh, John F. Henfling, Rocky J. Erven, and Russell W. Spillers. Penetration of a transverse supersonic jet into a subsonic compressible crossflow. *AIAA Journal*, 43 (2):379–389, 2005. ISSN 0001-1452 1533-385X. doi: 10.2514/1.9919.

Steven J. Beresh, Justin L. Wagner, John F. Henfling, Russell W. Spillers, and Brian O. M. Pruett. Turbulent eddies in a compressible jet in crossflow measured using pulse-burst particle image velocimetry. *Physics of Fluids*, 28(2), 2016. ISSN 1070-6631 1089-7666. doi: 10.1063/1.4940677.

C. H. Bosanquet and J. L. Pearson. The spread of smoke and gases from chimneys. *Transactions of the Faraday Society*, 32:1249–1263, 1936.

J. E. Broadwell and R. E. Breidenthal. Structure and mixing of a transverse jet in incompressible flow. *Journal of Fluid Mechanics*, 148:405–412, 1984. ISSN 0022-1120 1469-7645. doi: 10.1017/s0022112084002408.

X. Chai and K. Mahesh. Simulations of high speed turbulent jets in crossflows. 49th AIAA Aerospace Sciences Meeting including the New Horizons Forum and Aerospace Exposition, 2011.

Sergio L. V. Coelho and J. C. R. Hunt. The dynamics of the near field of strong jets in crossflows. *Journal of Fluid Mechanics*, 200:95–120, 1989. ISSN 0022-1120 1469-7645. doi: 10.1017/s0022112089000583.

Edward T. Curran. Scramjet engines: The first forty years. *Journal of Propulsion and Power*, 17(6):1138–1148, 2001. ISSN 0748-4658 1533-3876. doi: 10.2514/2.5875.

J. Delery and J.G. Marvin. Turbulent shock-wave/boundary-layer interaction. Report, AGARD, 1986.

Akshay S. Deshpande and Jonathan Poggie. Flow control of swept shock-wave/boundary-layer interaction using plasma actuators. *Journal of Spacecraft and Rockets*, 55(5):1198–1207, 2018. ISSN 0022-4650 1533-6794. doi: 10.2514/1.A34114.

Dean A. Dickmann and Frank K. Lu. Shock/boundary-layer interaction effects on transverse jets in crossflow over a flat plate. *Journal of Spacecraft and Rockets*, 46(6):1132–1141, 2009. ISSN 0022-4650 1533-6794. doi: 10.2514/1.39297.

F.J. Donker Duyvis. Laser sheet probe design for piv in high-speed wind tunnels. In *PIVNET II International Workshop on the Application of PIV in Compressible Flows*, 2005.

Houshang B. Ebrahimi. Numerical investigation of jet interaction in a supersonic freestream. *Journal of Spacecraft and Rockets*, 45(1):95–103, 2008. ISSN 0022-4650 1533-6794. doi: 10.2514/1.29847.

Erinc Erdem, Selvaraj Saravanan, Jingzhou Lin, and Konstantinos Kontis. Experimental investigation of transverse injection flowfield at march 5 and the influence of impinging shock wave. In *18th AIAA/3AF International Space Planes and Hypersonic Systems and Technologies Conference*, 2012. doi: 10.2514/6.2012-5800.

F.H. Falempin. *Scramjet Developments in France*, pages 47–117. Elsevier, 2001. ISBN 978-1-56347-322-7 978-1-60086-660-9. doi: 10.2514/5.9781600866609.0047.0117.

T. F. Fric and A. Roshko. Vortical structure in the wake of a transverse jet. *Journal of Fluid Mechanics*, 279:1–47, 1994. ISSN 0022-1120 1469-7645. doi: 10.1017/s0022112094003800.

F. Gnani, H. Zare-Behtash, and K. Kontis. Pseudo-shock waves and their interactions in high-speed intakes. *Progress in Aerospace Sciences*, 82:36–56, 2016. ISSN 03760421. doi: 10.1016/j.paerosci.2016.02.001.

R.K. Grandhi and A. Roy. Effectiveness of a reaction control system jet in a supersonic crossflow. *Journal Of Spacecraft And Rockets*, 54:883–891s, 2017. doi: 10.2514/1.A33770.

J.E. Green. Interactions between shock waves and turbulent boundary layers. *Progress in Aerospace Sciences*, 11:235–260, 1970.

M. R. Gruber, A. S. Nejad, T. H. Chen, and J. C. Dutton. Compressibility effects in supersonic transverse injection flowfields. *Physics of Fluids*, 9(5):1448–1461, 1997. ISSN 1070-6631 1089-7666. doi: 10.1063/1.869257.

Martin Hersch, Louis A. Povinelli, and Frederick P. Povinelli. A schlieren technique for measuring jet penetration into a supersonic stream. *Journal of Spacecraft and Rockets*, 7(6):755–756, 1970. ISSN 0022-4650 1533-6794. doi: 10.2514/3.30033.

Wei Huang. Transverse jet in supersonic crossflows. *Aerospace Science and Technology*, 50:183–195, 2016. ISSN 12709638. doi: 10.1016/j.ast.2016.01.001.

Wei Huang, Han Wu, Yan-guang Yang, Li Yan, and Shi-bin Li. Recent advances in the shock wave/boundary layer interaction and its control in internal and external flows. *Acta Astronautica*, 174:103–122, 2020. ISSN 00945765. doi: 10.1016/j.actaastro.2020.05.001.

Yasuhiro Kamotani and Isaac Greber. Experiments on a turbulent jet in a cross flow. *AIAA Journal*, 10(11):1425–1429, 1972. ISSN 0001-1452 1533-385X. doi: 10.2514/3.50386.

S. Kawai and S. K. Lele. Dynamics and mixing of a sonic jet in a supersonic turbulent crossflow. *Annual Research Briefs, Centre for Turbulence Research*, pages 285–298, 2009.

R. M. Kelso, T. T. Lim, and A. E. Perry. An experimental study of round jets in cross-flow. *Journal of Fluid Mechanics*, 306:111–144, 1996. ISSN 0022-1120-1469-7645. doi: 10.1017/s0022112096001255.

V. R. Sanal Kumar, B. N. Raghunandan, T. Kawakami, H. D. Kim, T. Setoguchi, and S. Raghunathan. Boundary-layer effects on internal flow choking in dual-thrust solid rocket motors. *Journal of Propulsion and Power*, 24(2):224–235, 2008. ISSN 0748-4658 1533-3876. doi: 10.2514/1.30649.

Sang-Hyeon Lee. Characteristics of dual transverse injection in scramjet combustor, part 1: Mixing. *Journal of Propulsion and Power*, 22(5):1012–1019, 2006. ISSN 0748-4658 1533-3876. doi: 10.2514/1.14180.

Sang-Hyeon Lee, In-Seuck Jeung, and Youngbin Yoon. Computational investigation of shock-enhanced mixing and combustion. *AIAA Journal*, 35(12):1813–1820, 1997. ISSN 0001-1452 1533-385X. doi: 10.2514/2.56.

Lang-quan Li, Wei Huang, Li Yan, and Shi-bin Li. Parametric effect on the mixing of the combination of a hydrogen porthole with an air porthole in transverse gaseous injection flow fields. *Acta Astronautica*, 139:435–448, 2017. ISSN 00945765. doi: 10.1016/j.actaastro.2017.07.048.

Chang-hai Liang, Ming-bo Sun, Yuan Liu, and Yi-xin Yang. Shock wave structures in the wake of sonic transverse jet into a supersonic crossflow. *Acta Astronautica*, 148:12–21, 2018. ISSN 00945765. doi: 10.1016/j.actaastro.2018.04.009.

M. J. Lighthill. Attachment and separation in three-dimensional flow. *Laminar Boundary Layers, Cambridge University Press*, 1963.

Chaoyang Liu, Zhenguo Wang, Hongbo Wang, and Mingbo Sun. Numerical investigation on mixing and combustion of transverse hydrogen jet in a high-enthalpy supersonic crossflow. *Acta Astronautica*, 116:93–105, 2015. ISSN 00945765. doi: 10.1016/j.actaastro.2015.06.023.

Yuan Liu, Ming-bo Sun, Chang-hai Liang, Zun Cai, and Ya-nan Wang. Structures of near-wall wakes subjected to a sonic jet in a supersonic crossflow. *Acta Astronautica*, 151: 886–892, 2018. ISSN 00945765. doi: 10.1016/j.actaastro.2018.07.048.

Krishnan Mahesh. The interaction of jets with crossflow. *Annual Review of Fluid Mechanics*, 45(1):379–407, 2013. ISSN 0066-4189 1545-4479. doi: 10.1146/annurev-fluid-120710-101115.

C.R. McClinton. Effect of ratio of wall boundary-layer thickness on mixing of a normal hydrogen jet in a supersonic stream. Report, NASA Langley Research Center, 1974.

W. Merzkirch. *Flow Visualization, Second Edition*. Academic Press, Inc., Orlando, FL, USA, 1987. ISBN 0-12-491351-2.

J.H. Morgenthaler. Supersonic mixing of hydrogen and air. Report CR-747, NASA, 1967.

M.V. Morkovin, C.A. Pierce Jr., and C.E. Craven. Interaction of a side jet with a supersonic main stream. *Bulletin of Mechanical Engineering of the University of Michigan*, 35, 1952.

Suman Muppidi and Krishnan Mahesh. Study of trajectories of jets in crossflow using direct numerical simulations. *Journal of Fluid Mechanics*, 530:81–100, 2005. ISSN 0022-1120 1469-7645. doi: 10.1017/s0022112005003514.

S. Murugappan, E. Gutmark, and C. Carter. Control of penetration and mixing of an excited supersonic jet into a supersonic cross stream. *Physics of Fluids*, 17(10), 2005. ISSN 10706631. doi: 10.1063/1.2099027.

H. Nakamura, N. Sato, H. Kobayashi, and G. Masuya. Effect of the location of an incident shock wave on combustion and flow field of wall fuel-injection. *Trans. Japan Soc. Aero. Space Sci*, 51:170–175, 2008.

H. Nakamura, N. Sato, S. Ishida, Y. Ogami, and H. Kobayashi. A study of interaction between shock wave and cross-flow jet using particle tracking velocimetry. *Trans. Japan Soc. Aero. Space Sci*, 52:81–88, 2009.

Ashish Nedungadi and Mark J. Lewis. Numerical study of fuel mixing enhancement using an oblique shock/vortex interaction. *Journal of Propulsion and Power*, 16(6):946–955, 2000. ISSN 0748-4658 1533-3876. doi: 10.2514/2.5691.

R. C. Orth, J. A. Schetz, and F. S. Billig. The interaction and penetration of gaseous jets in supersonic flow. Report, NASA, 1969.

D. Papamoschou and D. G. Hubbard. Visual observations of supersonic transverse jets. *Experiments in Fluids*, 14:468–476, 1992.

Vito Pasquariello, Muzio Grilli, Stefan Hickel, and Nikolaus A. Adams. Large-eddy simulation of passive shock-wave/boundary-layer interaction control. *International Journal of Heat and Fluid Flow*, 49:116–127, 2014. ISSN 0142727X. doi: 10.1016/j.ijheatfluidflow.2014.04.005.

Ventsislav Viktorov Pazhev. *Experimental Investigation of Transverse Jet Injection into Supersonic Crossflow*. Msc thesis, Delft University of Technology, 2020.

A. Pizzaia and T. Rossmann. Effect of boundary layer thickness on transverse sonic jet mixing in a supersonic turbulent crossflow. *Physics of Fluids*, 30(11), 2018. ISSN 1070-6631 1089-7666. doi: 10.1063/1.5056540.

Ron Portz and Corin Segal. Penetration of gaseous jets in supersonic flows. *AIAA Journal*, 44(10):2426–2429, 2006. ISSN 0001-1452 1533-385X. doi: 10.2514/1.23541.

Hamideh Pourhashem, Iraj M. Kalkhoran, and Sunil Kumar. Interaction of vortex with bow shock wave: Computational model, experimental validation, enhanced mixing. *AIAA Journal*, 56(8):3071–3085, 2018. ISSN 0001-1452 1533-385X. doi: 10.2514/1.J056789.

F.P. Povinelli and L.A. Povinelli. Correlation of secondary sonic and supersonic gaseous jet penetration into supersonic crossflow. Report, NASA Lewis Research Center, 1971.

A.K. Prasad. Stereoscopic particle image velocimetry. *Experiments in Fluids*, 29:103–116, 2000.

Markus Raffel, Christian E. Willert, Fulvio Scarano, Christian J. Kähler, Steven T. Wereley, and Jürgen Kompenhans. *Particle Image Velocimetry A Practical Guide*. Springer, 2018. ISBN 978-3-319-68851-0.

D. Ragni, F. Schrijer, B. W. van Oudheusden, and F. Scarano. Particle tracer response across shocks measured by piv. *Experiments in Fluids*, 50(1):53–64, 2011. ISSN 0723-4864 1432-1114. doi: 10.1007/s00348-010-0892-2.

R.C. Rogers. A study of the mixing of hydrogen injected normal to a supersonic airstream. Report, NASA, 1971.

Juan Gabriel Santiago and J. Craig Dutton. Velocity measurements of a jet injected into a supersonic crossflow. *Journal of Propulsion and Power*, 13(2):264–273, 1997. ISSN 0748-4658 1533-3876. doi: 10.2514/2.5158.

Joseph A. Schetz and Frederick S. Billig. Penetration of gaseous jets injected into a supersonic stream. *Journal of Spacecraft and Rockets*, 3(11):1658–1665, 1966. ISSN 0022-4650 1533-6794. doi: 10.2514/3.28721.

Joseph A. Schetz, Paul F. Hawkins, and Harry Lehman. Structure of highly underexpanded transverse jets in a supersonic stream. *AIAA Journal*, 5(5):882–884, 1967. ISSN 0001-1452 1533-385X. doi: 10.2514/3.4095.

F. F. J. Schrijer and F. Scarano. Effect of predictor–corrector filtering on the stability and spatial resolution of iterative piv interrogation. *Experiments in Fluids*, 45(5):927–941, 2008. ISSN 0723-4864 1432-1114. doi: 10.1007/s00348-008-0511-7.

Corin Segal. *The Scramjet Engine Processes and Characteristics*. Cambridge Aerospace Series. Cambridge University Press, 2009. ISBN 978-0-521-83815-3.

G. S. Settles. *Schlieren and Shadowgraphy Techniques. Visualizing Phenomena in Transparent Media*. Experimental Fluid Mechanics. Springer-Verlag Berlin Heidelberg GmbH, 2001. ISBN 978-3-642-63034-7.

Gary S. Settles and Michael J. Hargather. A review of recent developments in schlieren and shadowgraph techniques. *Measurement Science and Technology*, 28(4), 2017. ISSN 0957-0233 1361-6501. doi: 10.1088/1361-6501/aa5748.

A. T. Sheridan. Surface entrainment of air by a water jet. *Nature*, 209:799–800, 1966. doi: 10.1038/209799a0.

Michael K. Smart and Iraj M. Kalkhoran. Effect of shock strength on oblique shock-wave/vortex interaction. *AIAA Journal*, 33(11):2137–2143, 1995. ISSN 0001-1452 1533-385X. doi: 10.2514/3.12958.

L. J Souverein, P. G Bakker, and P. Dupont. A scaling analysis for turbulent shock-wave/boundary-layer interactions. *Journal of Fluid Mechanics*, 714:505–535, 2013. ISSN 0022-1120 1469-7645. doi: 10.1017/jfm.2012.495.

L. C. Squire. The motion of a thin oil sheet under the steady boundary layer on a body. *Journal of Fluid Mechanics*, 11(2):161–179, 1961. ISSN 0022-1120 1469-7645. doi: 10.1017/s0022112061000445.

Bernhard Stahl, Hans Emunds, and Ali Gülhan. Experimental investigation of hot and cold side jet interaction with a supersonic cross-flow. *Aerospace Science and Technology*, 13 (8):488–496, 2009. ISSN 12709638. doi: 10.1016/j.ast.2009.08.002.

M. Sun, Lei Jing, Wu Hai-yan, Liang Jian-han, Liu Wei-dong, and Wang Zhen-guo. Flow patterns and mixing characteristics of gaseous fuel multiple injections in a non-reacting supersonic combustor. *Heat and Mass Transfer*, 47(11):1499–1516, 2011. ISSN 0947-7411 1432-1181. doi: 10.1007/s00231-011-0804-x.

Ming-bo Sun and Zhi-wei Hu. Mixing in nearwall regions downstream of a sonic jet in a supersonic crossflow at mach 2.7. *Physics of Fluids*, 30(10), 2018a. ISSN 1070-6631 1089-7666. doi: 10.1063/1.5045752.

Mingbo Sun and Zhiwei Hu. Formation of surface trailing counter-rotating vortex pairs downstream of a sonic jet in a supersonic cross-flow. *Journal of Fluid Mechanics*, 850: 551–583, 2018b. ISSN 0022-1120 1469-7645. doi: 10.1017/jfm.2018.455.

O. G. Sutton. A theory of eddy diffusion in the atmosphere. *Proceedings of the Royal Society*, 135:143–165, 1932. ISSN 2053-9150. doi: 10.1098/rspa.1932.0025.

Wayne M. VanLerberghe, Juan G. Santiago, J. Craig Dutton, and Robert P. Lucht. Mixing of a sonic transverse jet injected into a supersonic flow. *AIAA Journal*, 38(3):470–479, 2000. ISSN 0001-1452 1533-385X. doi: 10.2514/2.984.

Frank M. White. *Viscous Fluid Flow, Third Edition*. McGraw Hill Series in Mechanical Engineering. McGraw Hill Education, 2011.

Li Yan, Wei Huang, Hao Li, and Tian-tian Zhang. Numerical investigation and optimization on mixing enhancement factors in supersonic jet-to-crossflow flow fields. *Acta Astronautica*, 127:321–325, 2016. ISSN 00945765. doi: 10.1016/j.actaastro.2016.06.011.

Li Yan, Han Wu, Wei Huang, Shi-bin Li, and Jun Liu. Shock wave/turbulence boundary layer interaction control with the secondary recirculation jet in a supersonic flow. *Acta Astronautica*, 173:131–138, 2020. ISSN 00945765. doi: 10.1016/j.actaastro.2020.04.003.

W. Yang. *Handbook of Flow Visualization*. Taylor & Francis, 29 West 35th Street, New York, NY 10001, 2001. ISBN 1-56032-417-1.

Lester L. Yuan, Robert L. Street, and Joel H. Ferziger. Large-eddy simulations of a round jet in crossflow. *Journal of Fluid Mechanics*, 379:71–104, 1999. ISSN 0022-1120 1469-7645. doi: 10.1017/s0022112098003346.

Jun-Mei Zhang, Y. D. Cui, Jinsheng Cai, and Hua-Shu Dou. Numerical investigation of lateral jets over a body of revolution in supersonic cross-flow. *Journal of Propulsion and Power*, 28(1):33–46, 2012. ISSN 0748-4658 1533-3876. doi: 10.2514/1.B34171.

Yujie Zhang, Weidong Liu, Bo Wang, and Mingbo Sun. Effects of micro-ramp on transverse jet in supersonic crossflow. *Acta Astronautica*, 127:160–170, 2016. ISSN 00945765. doi: 10.1016/j.actaastro.2016.05.032.

Edward E. Zukoski and Frank W. Spaid. Secondary injection of gases into a supersonic flow. *AIAA Journal*, 2(10):1689–1696, 1964.